Technische Universität München
Fakultät für Chemie
Professur für Organische Chemie

Optimal control of inhomogeneous spin ensembles: Applications in NMR and Quantum optics

Quentin Ansel

Vollständiger Abdruck der von der Fakultät für Chemie der Technische Universität München zur Erlangung des akademischen Grades eines

Doktors der Naturwissenschaften

Genehmigten Dissertation.
Vorsitzender: Prof. Dr. Bernd Reif
Prüfer der Dissertation:

1. Prof. Dr. Steffen Glaser
2. Prof. Dr. Dominique Sugny

Die Dissertation wurde am 17.10.2018 bei der Technische Universität München eingereicht und durch die Fakultät für Chemie am 14.11.2018 angenommen.

Abstract **(EN)** The goal of this thesis is to apply optimal control theory to the dynamics of inhomogeneous spin ensembles. The first part focuses on the control of a spin ensemble coupled to a cavity. The theory is introduced in detail, and a general method to efficiently control spins is presented. Several pulses are derived in the bad/good cavity regimes using numerical optimal control techniques. Additionally, non-linear generalized functions are used in order to derive simple approximated solutions. In a second step, the problem of spin echo Signal to Noise Ratio maximization is investigated, and maximization conditions are derived. It is shown that new pulses are superior to state-of-the-art square pulses in terms of fidelity and SNR maximization. Moreover, they allow us to explore new situations (e.g. Free Induction Decay measurements in cavity-QED with a cavity damping longer than T_2^*). The second part focuses on standard NMR/MRI problems. Two distinct situations of selectivity are investigated. The first one consists of determining the time minimum pulse which produces the most offset-selective transformation. In the ultra-selectivity case, the optimal solution is a singular arc of constant amplitude. However, if additional robustness constraints are taken into account, the optimal solution can be a regular arc. The second situation is the optimization of databases for MR-fingerprinting experiments. In this case, a control field is designed so that it generates a fingerprint database which maximizes the recognition process between several spins with different parameters. Additionally, optimal control theory and non-linear generalized function theory are introduced.

⋆

(DE) Ziel dieser Dissertation ist die Anwendung der optimaler Steuerungs-Theorie auf die Dynamik inhomogener Spinensembles. Im ersten Teil wird die Kontrolle eines an einen Resonator gekoppelten Spinensembles behandelt. Die zugrundeliegende Theorie wird im Detail erklärt und eine generelle Methode, um Spins effektiv zu steuern, wird vorgestellt. Mehrere Pulse im schlechten bzw. guten Resonator-Limit werden mit Hilfe von numerischen Techniken aus der optimalen Steuerungs-Theorie erarbeitet. Weiterhin wird Gebrauch von nicht-linearen verallgemeinerten Funktionen gemacht, um vereinfachte Näherungslösungen zu erhalten. Im zweiten Schritt wird die Maximierung des Signal-zu-Rausch-Verhältnisses (engl.: signal-to-noise ration, SNR) eines Spin-Echos untersucht und Bedingungen zur Maximierung werden herausgearbeitet. Wir zeigen, dass neue Pulse die bisherigen Rechtecks-Pulse bezüglich Güte und SNR-Maximierung übertreffen. Diese erlauben uns weiterhin, neue Szenarien, wie Messungen des freien Induktionszerfalls (FID) in Quanten-Elektrodynamik-Messungen mit Resonator-Dämpfung länger als T_2^*, zu erforschen. Der zweite Teil der Arbeit konzentriert sich auf Probleme der Standard-Kenspinresonanz-Spektroskopie und Bildgebung, wobei Selektivitäs-Fragent in zwei verschiedenen Szenarien untersucht werden. Das Erste besteht aus der Bestimmung des Minimalzeit-Pulses, welcher die selektivste Transformation bezüglich des Offset-Parameters hervorbringt. Im ultra-selektiven Falle ist die optimale Lösung ein singulärer Puls konstanter Amplitude. Berücksichtigt man allerdings zusätzliche Einschränkungen bezüglich Robustheit, kann die optimale Lösung auch nicht-singulär sein. Das andere Szenarium ist die Optimierung von Datenbanken für Magnetresonanz-Fingerprinting-Experimente. In diesem Fall wird ein Steuerungs-Pulssequenz entworfen, welche eine Fingerprint-Datenbank erzeugt, die den Erkennungsprozess der Parameter verschiedener Spins optimiert. Zusätzlich wird die Theorie optimaler Steuerung und nicht-linearer verallgemeinerter Funktionen eingeführt.

⋆

(FR) L'objectif de cette thèse est d'appliquer la théorie du contrôle optimal à la dynamique d'ensembles inhomogènes de spins. La première partie est dévouée au contrôle d'un ensemble de spins couplé à une cavité. La théorie est introduite en détail, et une méthode générale pour contrôler efficacement les spins est présentée. Plusieurs pulses sont déterminés dans les régimes de bonne et de mauvaise cavité. De même, les fonctions non linéaires généralisées sont utilisées afin de déterminer des approximations simples. Dans un second temps, le problème de la maximisation du Signal-sur-Bruit d'un écho de spin est abordé, et des conditions d'optimisations sont établies. Il est montré que les nouveaux pulses sont supérieurs à ceux de l'état de l'art, en termes de fidélité et d'augmentation du Signal-sur-Bruit. Par ailleurs, ils permettent d'explorer de nouvelles situations (e.g. mesure de FID (Free Induction Decay) en CQED avec un taux de perte de cavité plus long que T_2^*). La seconde partie est dévouée à des problèmes de RMN/IRM standard. Deux situations de "sélectivité" sont étudiées. La première consiste à déterminer le pulse le plus court qui produit la transformation la plus sélective par rapport aux offsets. Dans le cas ultra-sélectif, la solution optimale est un arc singulier d'amplitude constante. Cependant, si des contraintes de robustesse sont ajoutées, la solution optimale peut-être un arc régulier. La seconde est celle de l'optimisation de base de données pour des expériences de MR-fingerprinting. Dans ce cas, un champ de contrôle est conçu pour générer une base de données "d'empreinte digitale" qui maximise le processus de reconnaissance entre spins de paramètres différents. De plus, des annexes présentent différents outils mathématiques, comme la théorie du contrôle optimal ou les fonctions non linéaires généralisées.

Contents

Acknowledgment

Firstly, I would like to express my sincere gratitude to my advisors, Dominique Sugny and Steffen Glaser for the continuous support during these three years, for their patience (with special attention during the writing period), motivation, and the long fruitful discussions about scientific subjects. I could not have imagined having a better supervision for my Ph.D study.

I thank J. Salomon, E.Brion and B. Reif for the reviewing of the present manuscript, and to have been a member of the examination committee.

My sincere thanks also go to all the members (scientists, but also secretaries and other staff members) of the Glaser group and the ICQ department at the ICB, for their good mood, their help and their precious support. Otherwise, it would not be possible to conduct this research.

I also address my sincere thanks to collaborators: Patrice Bertet and Sebastian Probst, for their invitation at the CEA, and all the stimulating discussions. I also thank the people from Lyon, and more generally to all collaborators of the Explosys project, and the colleagues from several horizons (Italy, Canada) met during workshops.

I thank the other PhD students (random order): Michael, Vincent, Thomas, Emilien, Bálint, Adrien, David, Moritz, Frederik, Daniella, Xavier, Manu, Valeriya for all the fun we had in the last years, and the various helps such as IT maintenance, German translations or "Coffee-breaks for brain depressurization".

Last but not the least, I would like to thank my family: my parents, my brother, my sister, and my in-laws for supporting me throughout writing this thesis, and of course, to my wonderful companion, Cécilia.

Chapter 0

Introduction

*"It is wrong to think that the task of physics is to find out how nature is. Physics concern what we say about nature."*N.Bohr said these words in the early 20th century, while he and his pairs were trying to understand the fundamental laws of nature at the atomic scale[118, 55]. But at this time, he was certainly not thinking that one day, our knowledge of nature would be great enough to control nature at this scale [45, 53, 82, 179]. As a matter of fact, the control of the environment is a natural evolution of physical theories: First humans want to understand how things are, and then, they imagine how things could be.

As soon as physicists understood basic mechanical laws and how forces influence object trajectories, they imagined an extraordinary number of situations where a system is brought/transported from an initial position to a new desired one [166, 25, 88]. This is made possible because classical mechanics tells us how an object evolves from the data of its initial conditions. However, as Bohr also noticed, *"Prediction is very difficult, especially if it's about the future"*. This is what we have learned from Quantum Mechanics: we generally cannot predict events with certainty, we can only predict at which frequency events can occur [118, 55].

In the context of a controlled object, this fundamental fact can be seen as an unpreventable limitation. Positively, the light-matter [75, 128, 4] interaction is nowadays well understood, and we can claim that we know how to control quantum systems. The control of quantum systems is slightly different from the image we usually have in mind with classical control. We do not control the position or the velocity of an object, rather we control the probability law of possible future events [45]. Quantum control tasks are difficult tasks which are experimentally challenging. Solving these challenges constitutes the core of the current research in quantum technologies [17, 53, 82, 179].

Different categories of control strategies can be emphasized. The first one, which is the simplest, consists of finding the environmental constraints which ensure that the quantum system will reach the target state after a certain time. This strategy is qualified as *static* because we do not interact with the system after the beginning of the experiment. This is analogous to the launch of an arrow to a target: we only input its initial orientation and speed. This strategy is limited and we generally prefer to use a *dynamic* control. In this case, the environment is modulated as a function of time. This allows us to reach new states, unreachable in a static way. Finding the dynamic environment constraints can be a very difficult task, and several solutions can exist. Therefore, a question naturally arises: which control is the best one? The notion of *best* is a notion to clarify, and it depends on our expectations/wishes. For example, one objective is to minimize the time or the energy required for reaching the target state. Such problems are also present in classical control, and in order to answer such questions, a field of mathematics emerged in the 50's/60's: Optimal Control Theory (OCT) [129, 166, 25, 88]. The theory proposes a mathematical framework, tools, which allow us to say: *This is the*

best solution! (Or at least, one of the bests, several optimal solutions could exist.)

In quantum technologies, we generally encode information on photons or magnetic momentums of atoms. Photons are useful to carry information on long distances (e.g. quantum cryptography, see [137, 105], for recent studies) while atoms are better to store information (e.g. quantum memories [17, 21, 124]).

The ability to control magnetic momentums was made possible at the beginning of the history of Quantum Mechanics, with the introduction of Nuclear Magnetic Resonance (NMR) during the 30/40's [52, 101, 35]. This field led to two major technologies: NMR spectroscopy, for the analysis of chemical species, and Magnetic Resonance Imaging for the visualization of the three-dimensional structure of objects (such as the human body, for medicine applications [43, 35]). During the last decade, magnetic resonance received a lot of interest for applications in quantum technologies/ quantum computing [67].

Most of MR applications require the efficient control of an ensemble of magnetic momentums (spins). As a matter of fact, experimental setups are built around a collection of quantum systems (atoms, molecules, photons...). The response of each individual entity may differ. This disparity leads to the so-called inhomogeneous effects [101],which must be taken into account in the control strategy. A lot of studies have been published on this subject with various control methods, and most of the control problems are well understood nowadays. However, most of these methods have been derived on the basis of an intuitive approach of the dynamics, or with adiabatic principles [117, 173, 80](slow variations of the system). Therefore, small imperfections can decrease the process efficiency. Improving the fidelity of these methods is generally possible, but at the price of long and energy demanding operations. Here the idea is to push processes to their physical limit by applying OCT directly in the design of control field (see [90, 91, 99, 107, 123, 27], to cite a few).

⋆

This manuscript is separated into two main parts. The first part deals with the control of an inhomogeneous spin ensemble coupled to a cavity. The study of this system is motivated by recent experiments in electron spin resonance (ESR) and quantum optics [21, 75]. In these new experiments, magnetic resonance is pushed to a regime where quantum effects become predominant.

Actually, in standard MR, a classical or semi-classical analysis is sufficient for a good mathematical description of the underlying physics (except if there is a non-negligible spin-spin coupling). In these new experiments [21], a sample (typically a crystal carefully chosen for its properties) is coupled to a microwave resonator. In a second step, the ensemble is cooled down to a very low temperature, around 10 or 20 mK, in order to avoid thermal effects. In this situation, quantum behaviors of the electromagnetic field are measurable: The resonator naturally selects photons at a specific energy, and the low temperature allows us to observe quantum fluctuations around the ground state. The coupling of the cavity ground state with a spin ensemble induces the so-called Purcell effect [154], an enhancement of the electrons' spontaneous emission. Additionally, the interaction between electrons and photons can be long enough to observe coherent effects such as super-radiance. [164, 69]. This setup is interesting for several reasons: It allows us to push MR spectrometer to its physical limit in terms of sensitivity, and it can be used as a building block in several quantum objects, such as quantum memories. Unfortunately, the presence of the cavity and the emergence of new phenomena force us to adapt the control methods. The development of these new methods constitute the core of the first part.

In this manuscript, we propose a simple and systematic procedure which allows us to apply most of the control strategies used in NMR. Moreover, the procedure is

particularly interesting for OCT applications. Several examples of optimal pulses are presented. Among all the experimental challenges, it is of particular interest to obtain the best Signal-to-Noise-Ratio (SNR) during the spin response measurement [35, 162, 146, 98]. A specific study of the SNR is made and optimal conditions are derived. Moreover, we show that optimal pulses allow us to reach the SNR physical limit.

Performing optimal control calculations on such a complex system requires numerical simulations. These simulations are not easy to perform, and specific numerical methods are necessary. The development of such methods gives the opportunity to revisit the physical effects of the system. Several paragraphs of this manuscript are devoted to their analysis, and several standard approximations are studied.

The chapter 1 is devoted to the presentation of the state of the art. The reader can find basic ideas and useful results about cavity-QED. Chapter 2 presents an original work from the numerical point of view, but the corresponding physics is well known. However, this is a necessary preliminary work to deal with chapters 3 and 4. These two chapters present my main contribution to the field.

⋆

The second part of this manuscript focuses on more standard situations in NMR. In this case, quantum behavior of light can be neglected. The electromagnetic field is given by a simple time dependent function, which represents the control field that must be determined [170]. Two different problems are considered, but in both cases, the underlying idea is to separate as much as possible the dynamics of spins with different parameters (offset, relaxation times,...).

The first problem consists of determining the control field which produces the most selective universal rotation against offset parameters [35, 127, 174, 175, 109]. In addition, we consider a time or an energy minimum constraint. This study is motivated by experiments of spins coupled to the cavity. Indeed, such controls can be useful to manipulate an extremely small number of spins. Computations have been made in a simple NMR framework in order to simplify the analysis. However, the results can be extended to a system with a cavity.

The second and last problem concerns the magnetic-resonance-fingerprinting [110, 12, 113]. This work was motivated by a recent proposition of measurement method in NMR/MRI. The idea consists of generating numerically a database of magnetization trajectories. Each trajectory is generated from the data of the control field and spin parameters (relaxation time, inhomogeneity parameters...). In a second step, a pattern recognition algorithm [3] is used to recover in a single experiment all the parameters of a system. The name "fingerprinting" comes from an analogy of human fingerprint analysis: The time-dependent magnetization is like "the fingerprint" of the spin, and the goal is to identify the latter by comparing the measurement to our database entries. The approach is particularly efficient in MRI to determine a (T_1, T_2) map of the human body. In the original paper [110], the authors considered a control field of random amplitude in order to generate a time dependent magnetization sensitive to spin parameters. The use of a random field is convenient, but nothing guarantees that the sensitivity is sufficient to distinguish accurately similar parameters in a noisy experiment. Our idea is to introduce optimal control tools in the control design and a curve recognition algorithm (in order to remove database limitations). A first work is to define a mathematical framework to perform such non-standard optimizations. We have demonstrated the efficiency of the approach by using an experimental example in NMR. We have also emphasized the physical limits inherent to the fingerprinting method.

This second part is original and two papers have been written on the basis of these

two chapters.

⋆

In order to complete this manuscript, some mathematical elements are presented in appendices. They are devoted to optimal control theory, non-linear generalized functions and non-commutative geometry.

⋆

From the results of this manuscript, the following papers have been submitted or published:

PART I:

- *Optimal control of an inhomogeneous spin ensemble coupled to a cavity*, Q. Ansel, S. Probst, P. Bertet, S.J. Glaser, D. Sugny, Phys. Rev. A 98, 023425 – 2018
- *Shaped pulses for cavity compensation in high sensitivity electron spin resonance spectroscopy*, S. Probst, Q. Ansel, S.J. Glaser, D. Sugny, P. Bertet, in preparation.
- *Optimal control of an inhomogeneous spin ensemble coupled to a cavity II: A full quantum approach*, Q.Ansel, S.J. Glaser, D. Sugny, in preparation.

PART II:

- *Optimizing Fingerprinting Experiments for Parameter Identification: Application to Spin Systems*, Q. Ansel, M. Tesch, S. J. Glaser, D. Sugny, Phys. Rev. A 96, 053419/1-9 (2017)
- *Selective $SO(3)$ transformations by optimal control theory* Q. Ansel, L. Van Damme, S.J. Glaser, D. Sugny, in preparation
- *Time-optimal selective pulses of two uncoupled spin 1/2 particles* L. Van Damme, Q. Ansel, S.J. Glaser, D. Sugny, submitted to PRA
- *Robust optimal control of two-level quantum systems* L. Van Damme, Q. Ansel, S.J. Glaser, D. Sugny, Phys. Rev. A 95, 063403 (2017)

Part I

Optimal control of an inhomogeneous spin ensemble coupled to a cavity

0.1 Notations

- $\hat{a}, \hat{a}^\dagger$: cavity creation/annihilation operators
- β: control field (circular polarization)
- $B_{X,Y}$: control fields seen by the spins on the quadratures X, Y (generally, it is equivalent to $\langle \hat{X} \rangle, \langle \hat{Y} \rangle$).
- $\mathsf{B}_{X,Y}$: integral of $B_{X,Y}$.
- Δ, $\Delta_{(n)}$: offset frequency of a spin.
- $g, g_{(n)}, g_1, g_2$: coupling factor spin/electromagnetic field. (n) denotes the label of the spin, and $1, 2$ refer respectively to the coupling with the electric and magnetic fields.
- Γ_P: Purcell rate.
- $\hbar = 1$: Planck constant, always expressed in normalized units.
- κ: cavity damping rate.
- $\vec{M}$: magnetization vector.
- N: number of spins
- N_D: number of coherent spins (number of spins/ Dicke-state).
- N_ρ: number of incoherent spins.
- η_q: mollifier of order q.
- Ω: width of the offset distribution.
- ω: frequency of the cavity.
- $\omega_S, \omega_{S,(n)}$: frequency associated to the energy transition of a spin.
- $\omega_{X,Y}$: control field on the quadratures X, Y in the rotating frame.
- $\hat{\rho}$: density matrix.
- ρ: a probability distribution
- $\rho_{purcell}$: distribution of spins induced by the Purcell effect
- ρ_1: distribution of coupling factor g.
- ρ_0: distribution of offset.
- $\mathcal{S}$: integral over time of the quadrature $X = \langle \hat{X} \rangle$.
- $\mathcal{S}^{(2)}$: integral over time of X^2.
- $\hat{\sigma}_x, \hat{\sigma}_y, \hat{\sigma}_z, \hat{\sigma}_+, \hat{\sigma}_-$: Pauli matrices and creation/annihilation spin operators.

- $\hat{S}_a$: spin operator defined by $\hat{S}_a = \frac{1}{2}\hat{\sigma}_a$
- T_1: longitudinal relaxation time.
- T_2: transverse relaxation time.
- T_1^P: repetition time of an experiment.
- T_e: time between two pulses (spin-echo and CPMG sequences).
- T_c: control (pulse) duration in a spin CPMG sequence.
- T_r: repetition time $T_e + T_c$ in a CPMG sequence.
- T, t_f: final time.
- $\hat{U}_F$: evolution operator of the free electromagnetic field.
- $\hat{U}_S$: evolution operator of the spins with a drive.
- $\hat{U}_E$: evolution operator describing the entanglement spins/cavity.
- $\hat{X}, \hat{Y}$ operators associated to the cavity quadratures.
- ΔX: quantum noise of the quadrature X.

Chapter 1

Experimental and theoretical backgrounds

This chapter aims at reviewing the state of the art of a spin ensemble coupled to a cavity in order to provide the essential tools that are used in the next chapters. First, in section 1.1, a brief presentation of the experimental setup is made. Then, the theory of an electron coupled to a single cavity mode is developed in section 1.2. Successive approximations allow us to reformulate the system with a simplified model, based on the Jaynes-Cummings interaction. Thirdly, in section 1.3, the solution of the master equation that describes the damped harmonic oscillator dynamics is derived. The damped quantum oscillator describes accurately a single electromagnetic cavity mode. The solution of the master equation (of the single E.M. field) is investigated in chapter 3. In section 1.4, the model is completed, the different theoretical building blocks are gathered in order to form the full system of an inhomogeneous spin ensemble coupled to a cavity. Several physical effects, such as the super-radiance or the Purcell effects, are described in this later section. Section 1.6 details a semi-classical approximation based on a cumulant expansion, and an analogy with the NMR radiation damping is made. Finally, section 1.7 is devoted to the spin distribution.

1.1 The experimental setup

Experiments involving few atoms coupled to a microwave resonator are performed at the Quantronics group, a research group based at the *Centre de l'Energie Atomique* in Saclay (France) [1]. The goal of our collaboration is to improve the sensitivity and the efficiency of the methods used in these experiments by applying optimal control theory.

[1] http://iramis.cea.fr/spec/Pres/Quantro/static/index.html

Current experiments are only constructed in a development spirit: the goal is to build "the best" magnetic resonance spectrometer at the quantum scale, and to play with its quantum/-classical features [17, 97, 20, 21, 19, 132]. Nevertheless, one of the long-term goal is to build quantum memories [122]. Indeed, the

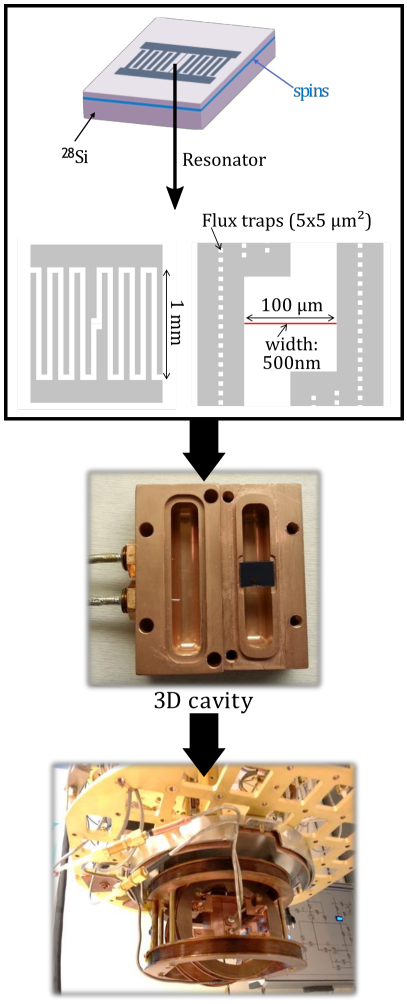

Figure 1.1: The setup is composed of a 2D microwave resonator in contact with a crystal of BiSi. They are packaged into a bigger 3D cavity, which is the support of the system inside the magnetic coils. The thin wire inside the resonator produces the control. (Credit: S. Probst. & al, poster).

[2] However, due to field inhomogeneity, all the spins do not contribute to the signal with the same intensity, and an effective number can be deduced. It is generally included between 100 and 1000.

information carried by a quantum state of light can be stored into a spin ensemble (the atoms).

In order to connect the theory developed in this manuscript to a concrete experiment, a short overview of the setup is presented in this section. The interested reader is referred to the original works of the Quantronics group [21, 132]. The technical details are omitted here in order to keep the simplest elements required for understanding the theory of a spin ensemble coupled to a cavity.

Let us have a global look on the setup (figure 1.1), and first, let us focus on the microwave resonator (the cavity). As we can see in figure (1.1), the latter is carefully designed, and a special attention is paid to the quality factor. A high quality factor allows to produce monochromatic photons, to maintain a long coherence time in the cavity and to preserve the system from decoherence effects. Here, the quality factor is chosen in order to obtain the desired amount of coherent/incoherent effects ($Q \sim 10^5$). The electromagnetic field in the cavity interacts with an ensemble of atoms. However, the setup is not exactly built like a laser: atoms are not trapped inside the cavity. The resonator is rather two-dimensional, and it is simply "put on" a crystal. Thus, we have a surface interaction and only spins near the surface can interact with the cavity field.

We now consider the spins: the crystal is not chosen randomly. Indeed, it is necessary to find a material that provides the strongest coupling and the longest coherence time for electronic spins. Bismuth donors in silicon (Si:Bi) [121] is a material that corresponds particularly well to these specifications (figure 1.2). This material is also interesting for other quantum technologies, as it is a promising option for encoding quantum information as qubits. The electronic spin 1/2 of a donor in silicon is degenerated due to hyper-fine and quadrupolar interactions. The use of a strong static magnetic field, normal to the cavity plane, allows us to lift the degeneracy and to adapt the spectrum to the bandwidth of the cavity. The transition $|9\rangle \leftrightarrow |10\rangle$ is used in experiments [21].

The number of spins involved in the experiment is very small. For example, the amount of spins in a standard NMR experiment is around the Avogadro number, but here this number is reduced to approximately 15,000 [2]. The magnetization produced by such a small number of electrons is very weak, and therefore, measurement must be performed in very specific conditions. How magnetic resonance measurement can be achieved at this scale? We briefly describe these conditions. Most of quantum effects are sensitive to temperature. Hot temperatures are related to incoherent motions of atoms and thermal states. This leads to an incoherent environment that cancels quickly most of quantum behaviors. Therefore, it is necessary to cool down the setup to a very low temperature. At the center of the setup, where the spins and the resonator are located, the temperature falls locally to 10 mK. This is far colder than the cryogenic magnet of the LHC (1.9K). However the volume is very small, a few μm^3. At this temperature, thermal photons are suppressed and the electromagnetic

field reaches its ground state. Hence, the detector receives a signal perturbed only by the ground state quantum fluctuation.

Unfortunately, this is not enough, and the signal must be considerably amplified. This amplification is not simple at all, and requires three successive amplifiers based on different technologies. The first one, a *Josephson Parametric Amplifier* (JPA), is maybe the most interesting. When set in phase preserving mode, JPAs can amplify the signal with a very little noise increase[3]. More precisely, the noise-amplification relation is given by [36]:

$$\frac{\langle \Delta \hat{S}^2_{out} \rangle}{G} \gtrapprox \langle \Delta \hat{S}^2_{in} \rangle + \frac{1}{2}, \tag{1.1}$$

where $\langle \Delta \hat{S}^2_{in/out} \rangle$ is the noise of the signal and G is the gain. The constant $1/2$ comes from the quantum noise induced by the amplifier. This one-half constant is the only source of noise. Then, the signal is amplified with an almost negligible noise increase. Of course, the process has a limit, and several amplification steps are used downstream (which are sensitive to the thermal noise). In order to visualize the gain of performance induced by a JPA, figure 1.3 shows different spin echoes recorded with or without JPA.

Without control, spins remain in their ground state and no signal can be measured. In order to produce a measurable magnetization, it is necessary to excite the spins. This is made possible by the use of a small inductor wire directly introduced inside the resonator (see the $100\mu m$ long red wire in figure 1.1). When a current is applied to the antenna, it produces electromagnetic waves similar to the one of a laser (characterized by a coherent state). Therefore, we are able to control the field inside the cavity using classical physics: the control field is parametrized by two time-dependent and continuous variables, which represent field quadratures.

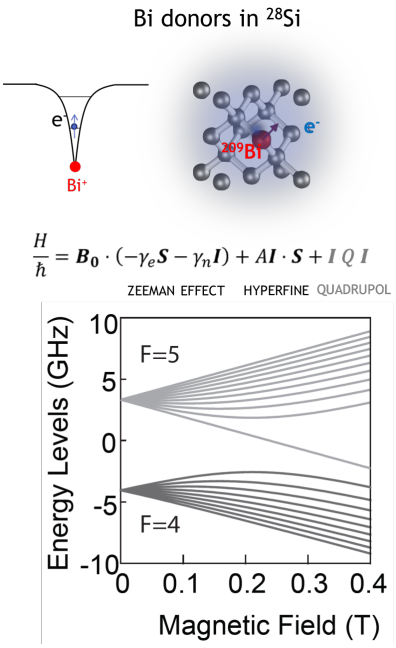

Figure 1.2: Bismuth donors in silicon (Si:Bi) is a particularly good material for quantum technologies. The selection of a specific energy transition allows us to create qubits. (Credit: S. Probst. & al, poster).

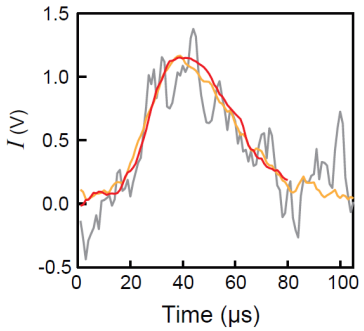

Figure 1.3: Echo signal $I(t)$ averaged 10 times without JPA (gray), with JPA in nondegenerate mode (orange), with JPA in degenerate mode (red). The gray ($\times 38$, $SNR = 2 \pm 0.5$) and orange curves ($\times 2.2$, $SNR = 14 \pm 1$) are rescaled to the red ($SNR = 22 \pm 3$) for an easy comparison. Credit: A.Bienfait [21].

[3] The JPA can also be used as a squeezer [21].

1.2 Light and electron interaction

The spectrum of BiSi is very complicated due to the hyper-fine and the quadrupolar terms in the Hamiltonian. Fortunately, several approximations are possible. First of all, ^{28}Si has zero spin, thus the lattice of silicon atoms allows us to trap bismuth atoms without perturbation of its spins. We thus have to consider only the interaction of electrons with the bismuth nucleus, but the cavity selects only one transition in the spectrum, so that we can focus on a single energy transition and neglect the others. However, we cannot restrict the study to a simple two-level system. The constant field used to lift the degeneracies is not perfectly homogeneous, due to the geometry of the coil, and the magnetic effects of surrounding objects. It results that each electron is not detuned by the same quantity, and inhomogeneous ensemble of spins must be considered. This situation is extremely similar to the one encountered in NMR [101, 35], but a few differences exist.

In order to highlight this link, a derivation of the model is given from the Dirac equation.

1.2.1 Quantum model of a non-relativistic electron coupled to the electromagnetic Field

In this section, we aim at deriving a simple model for the interaction of electronic spins with the cavity: a spin ensemble with a Jaynes-Cummings interaction with a damped quantum oscillator. This model is well known and can be postulated, as a first input in the theory. However, it is also interesting to start with a more general model, and to see how we can recover the final model from successive approximations. Then, our starting point is the Dirac equation for an interacting electron with the electromagnetic field [81, 128]. The quadrupolar structure is not taken into account here [4]. This approach has also the advantage to give a simple derivation of the Bloch equation. The Dirac equation with minimal coupling is given by:

$$i\hat{\gamma}^{\mu}(\partial_{\mu} + ieA_{\mu})\Psi_4 = m\Psi_4, \tag{1.2}$$

where Ψ_4 is a four-spinor field, γ_μ are Dirac matrices, e is the elementary electric charge, m is the electron mass and $A_\mu = (V, \vec{A})$ is the electromagnetic potential. As usual, the space-time index μ takes the values 0,1,2,3. In most of magnetic resonance experiments, particles do not move, or at least, the movement is negligible, thus one can proceed to a non-relativistic approximation [81]. This allows us to decouple and separate particles and antiparticle variables and to transform the Dirac equation into a non-relativistic Schrödinger equation [5]:

$$i\frac{d\Psi}{dt} = \left(\frac{(\hat{p} - e\hat{A})^2}{2m} - \hat{\mu}.\hat{B} + eV\right)\Psi, \tag{1.3}$$

where $\hat{p}$ is the momentum operator, $\hat{A}$ is the potential vector operator, $\hat{\mu}$ is the magnetic momentum, V is the electric potential (mostly induced by the Bi nucleus), and $\hat{B}$ is the magnetic field. Here, Ψ is a 2-spinor, so operators are 2×2 matrices.

Assuming that operators $\hat{A}$ and $\hat{p}$ commute and neglecting two photon processes, equation (1.3) becomes:

$$i\frac{d\Psi}{dt} = \left(\underbrace{\frac{\hat{p}^2}{2m} + eV}_{\hat{H}_0} \underbrace{- \frac{e}{2m}\hat{A}\hat{p} - \hat{\mu}.\hat{B}}_{\hat{H}_I}\right)\Psi. \tag{1.4}$$

The electron described here is free to move in the entire space and the corresponding Hamiltonian also depends on space variables. For the purpose of establishing a simple model, we consider fixed particles: they are trapped in the crystal's lattice or they move very slowly, so that the movement is negligible. Here, the

[4] It is not necessary to take into account this interaction to derive the simplified model.

[5] The non-relativistic limit is obtained by assuming $eA_0 \ll 2m$. Under this assumption, we can proceed to a WKB approximation, which allows us to say that particle and antiparticle parts vary proportionally. Then, all explicit dependence of antiparticle variables in the Dirac equation can be removed. Another way to describe this approximation consists of assuming that Lorentz boosts are negligible, and thus the energy exchange between electrons and positrons is also negligible.

particle is located in a small volume of space with a size smaller than the wave length. Under this condition, the electromagnetic field is assumed to be coherent on this restricted volume. These hypotheses allow us to drop the space dependence of the problem. Finally, one must choose a representation of operators. Here we use the well-known Pauli matrices:

$$\hat{\sigma}_x = \begin{pmatrix} 0 & 1 \\ 1 & 0 \end{pmatrix} ; \hat{\sigma}_y = \begin{pmatrix} 0 & -i \\ i & 0 \end{pmatrix} ; \hat{\sigma}_z = \begin{pmatrix} 1 & 0 \\ 0 & -1 \end{pmatrix}.$$

Let us start with $\hat{H}_0$. The Schrödinger equation describes the time evolution of a two-level system and the quantization of $p^2/2M + eV$ leads naturally to:

$$\hat{H}_0 = \frac{\omega_S}{2}\hat{\sigma}_z, \tag{1.5}$$

where ω_S is the difference of energy between the two states $|\uparrow\rangle$ and $|\downarrow\rangle$. Next, one must use a quantized electromagnetic field. We consider experiments in cavities, thus we can suppose that the system interacts only with the mode of energy ω with a wave vector aligned along a single direction. This simplification provides simple expressions of electromagnetic field operators:

$$\hat{A} = \begin{pmatrix} \hat{a}_x + \hat{a}_x^\dagger \\ \hat{a}_y + \hat{a}_y^\dagger \\ 0 \end{pmatrix} \equiv \sqrt{2} \begin{pmatrix} \hat{Q}_x \\ \hat{Q}_y \\ 0 \end{pmatrix} \tag{1.6}$$

$$\hat{B} = i \begin{pmatrix} -\hat{a}_y + \hat{a}_y^\dagger \\ \hat{a}_x - \hat{a}_x^\dagger \\ 0 \end{pmatrix} \equiv \sqrt{2} \begin{pmatrix} -\hat{P}_y \\ \hat{P}_x \\ 0 \end{pmatrix}. \tag{1.7}$$

With these equations, the interaction with the magnetic field is straightforward to compute:

$$\hat{\mu}.\hat{B} = \frac{ie}{\sqrt{2}m}\left(-\hat{\sigma}_x\hat{P}_y + \hat{\sigma}_y\hat{P}_x\right). \tag{1.8}$$

The last term in the interaction Hamiltonian is:

$$\frac{e}{2m}\hat{A}\hat{p} = -\frac{D\omega_S}{2}(\hat{Q}_x\hat{\sigma}_x + \hat{Q}_y\hat{\sigma}_y), \tag{1.9}$$

where we have introduced the amplitude of the dipole D [128]. To complete this first model, the Hamiltonian of the free electromagnetic field is introduced:

$$\begin{aligned} \hat{H} =& \omega\hat{N} + \frac{\omega_S}{2}\hat{\sigma}_z \\ &+ g_1(\hat{Q}_x\hat{\sigma}_x + \hat{Q}_y\hat{\sigma}_y) \\ &- g_2(-\hat{P}_y\hat{\sigma}_x + \hat{P}_x\hat{\sigma}_y). \end{aligned} \tag{1.10}$$

1.2.2 Recovering the spin-boson and the Jaynes Cummings models

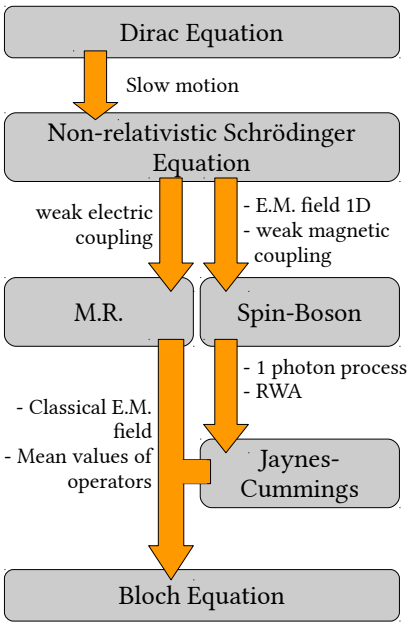

Figure 1.4: Summary of the successive approximations to derive the models.

Depending on the situation, the Hamiltonian (1.10) can be simplified. In the context of two-level systems coupled to a cavity, the dynamics are constrained in a single dimension. Consequently, we can proceed further by choosing a cavity aligned along the x-axis and by eliminating $\hat{a}_y$ and $\hat{a}_y^\dagger$. In order to simplify notations, the space index of field operators is dropped: $\hat{a}_x \to \hat{a}$ and $\hat{a}_x^\dagger \to \hat{a}^\dagger$. Additionally, in optics, the interaction with the magnetic field is generally neglected, this leads to set $g_2 = 0$. Notice that in Magnetic Resonance, it is the opposite.

These two simplifications conduct to the famous spin-Boson Hamiltonian [181] :

$$\hat{H}_{SB} = \omega\hat{N} + \frac{\omega_S}{2}\hat{\sigma}_z + g_1\hat{Q}_x\hat{\sigma}_x. \tag{1.11}$$

This Hamiltonian can be still approximated by expanding the interaction term:

$$\hat{Q}_x\hat{\sigma}_x = \hat{a}^\dagger\hat{\sigma}_+ + \hat{a}^\dagger\hat{\sigma}_- + \hat{a}\hat{\sigma}_+ + \hat{a}\hat{\sigma}_-, \tag{1.12}$$

with $\hat{\sigma}_x = \hat{\sigma}_+ + \hat{\sigma}_-$ and $\hat{\sigma}_y = -i(\hat{\sigma}_+ - \hat{\sigma}_-)$. In most of cavity QED experiments, the Rotating Wave Approximation [56] is valid. This allows us to neglect counter rotating terms, so that: $\hat{Q}_x\hat{\sigma}_x \simeq \hat{a}^\dagger\hat{\sigma}_- + \hat{a}\hat{\sigma}_+$ and the Hamiltonian becomes the Jaynes Cummings Hamiltonian [83, 155]:

$$\hat{H}_{JC} = \frac{\Delta}{2}\hat{\sigma}_z + g_1(\hat{a}^\dagger\hat{\sigma}_- + \hat{a}\hat{\sigma}_+), \tag{1.13}$$

where the offset $\Delta = \omega_S - \omega$ is introduced. In order to emphasis the link (and the differences) between usual magnetic resonance and quantum optic models, we write the Hamiltonian when the magnetic interaction is dominant:

$$\hat{H}_{MR} = \omega\hat{N} + \frac{\omega_S}{2}\hat{\sigma}_z - g_2(-\hat{P}_y\hat{\sigma}_x + \hat{P}_x\hat{\sigma}_y). \tag{1.14}$$

A summary of the relations between the different models is presented in figure 1.4.

1.2.3 Towards the unitary Bloch equation

The Bloch equation is determined by computing mean values of spin operators (proportional to the magnetization vector). By assuming a classical electromagnetic field, and using the Ehrenfest theorem on Hamiltonians (1.13) and (1.14), we are able to determine that in both cases, the time evolution of the magnetization vector is of the form [6]:

$$\frac{d}{dt}\vec{M} = g(B^x\hat{\epsilon}_x + B^y\hat{\epsilon}_y + B^z\hat{\epsilon}_z)\vec{M}, \tag{1.15}$$

[6] The equation is not written with usual conventions in NMR. Indeed, standard notations use physical units. **Here, units and notations might change with the context, we are only interested in the mathematical structure of the Bloch equation.**

where B^x and B^y are two components of the field (electric or magnetic) in the transverse direction of the static field (the z-axis), $B^z = \Delta/g$ is the offset term and $\hat{e}_a$ are generators of the $\mathfrak{so}(3)$ algebra [72, 45]. They verify the commutation relations $[\hat{e}_a, \hat{e}_b] = -\epsilon_{ab}{}^c \hat{e}_c$, where $\epsilon_{abc} = \epsilon_{ab}{}^c$ is the Levi-civita symbol. Generators are defined such that $(\hat{e}_c)_{ab}$ are matrix elements of ϵ_{abc}. These matrices are related to the wedge product with the relation: $-\vec{A} \wedge \vec{B} = \left(\sum_a \vec{A}_a \hat{e}_a\right) \vec{B}$.

The two models lead to the Bloch equation. This is not surprising since Hamiltonians are defined on $\mathfrak{su}(2)$. *However, the sign of the interaction constant is not the same: controls produce rotations in two different senses! This fact must be taken into account when relaxation mechanisms are introduced.* The action of the Bloch equation is represented in figure 1.5.

The symmetry group of the Bloch equation is $SO(3)$. This can be expected since a representation of $SU(2)$ on a 3 dimensional space is given by $SO(3)$ [72]. Therefore, the Bloch equation and the Schrödinger equation for a spin coupled to the electromagnetic field contain the same information (except for an irrelevant phase for representations in spaces of odd dimensions [72]). Without relaxation processes, considering the Bloch or the Schrödinger equation is almost equivalent. In this manuscript, the two representations are used. The $SO(2)$ version is chosen for quantum systems (Schrödinger and master equations) and the $SO(3)$ is preferred for classical or semi-classical dynamics (Bloch equation).

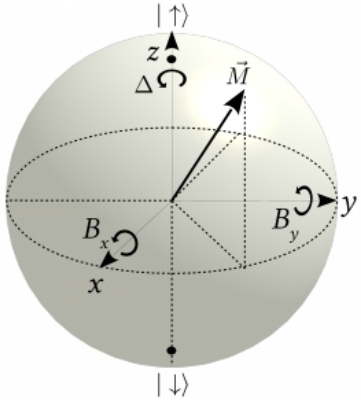

Figure 1.5: Action of the Bloch equation on the magnetization vector $\vec{M}$. We observe a rotation around the axis z, due to the offset Δ. The field B_a produces rotations in the two transverse (normal) directions. In order to underline the mapping between the magnetization vector representation and the quantum state, the two basis states $|\uparrow\rangle$ and $|\downarrow\rangle$ are represented (north and south poles).

The Bloch equation is not restricted to electrons, it is a good modeling for any magnetic moment in presence of a strong static field. For instance, nucleus of atoms can admit a magnetic moment, and its study is the core of Nuclear Magnetic Resonance.

Since we consider a time dependent linear differential equation, it is possible to use bundle theory and geometric tools for its analysis [139, 42]. B can be seen as a base manifold (the control manifold) and at each point of this space is attached a fiber: $\mathbb{R}^3$ if we consider the magnetization, or $SO(3)$ if we consider the evolution operator. The connection between the base manifold and the fiber is given by the Bloch equation. A solution of the equation is given by the parallel transport of a vector along a path. Here, the path is simply given by the function $B_a(t)$. The parallel transport along this path is given by the evolution operator:

$$\hat{U} = \mathbb{P}\exp\left(g \int B^a(s)\hat{e}_a ds\right), \tag{1.16}$$

where $\mathbb{P}\exp$ denotes the *path-ordering exponential*. We also use the notation $\mathbb{T}\exp$ for *time-ordering*, when the integration parameter is the physical time.

Since $SO(3)$ is not abelian, it is generally very difficult to determine explicitly a time ordered exponential. However, calculations are direct for a constant field or with a Dirac distribution[7]. We

[7] More information about these computations is provided in appendix B.

obtain respectively:

$$\mathbb{T}\exp\left(g\int_0^T B^a\hat{\epsilon}_a dt\right) = \exp\left(gTB^a\hat{\epsilon}_a\right), \tag{1.17}$$

$$\mathbb{T}\exp\left(g\int_0^T B^a\hat{\epsilon}_a\delta_\tau(t)dt\right) = \exp\left(gB^a\hat{\epsilon}_a\right). \tag{1.18}$$

1.3 Dynamics of the damped harmonic oscillator

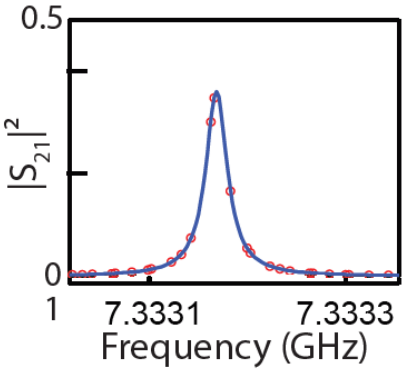

Figure 1.6: Examples of frequency response of the microwave resonator used by A. Bienfait [21].

Cavities used during experiments are quite good, but they are far from being perfect since they admit a non-negligible spectral width (figure 1.6). Several approaches can be used to tackle the problem: the electromagnetic field can be considered as a continuum of modes and at each mode is associated a quantum harmonic oscillator. In this case, it is necessary to couple the spin ensemble to the continuum and a density of state/correlation function must be chosen in order to compute the dynamics [81, 176]. This approach is elegant but quite difficult to solve. Another approach consists of expanding quantum excitations on a single Fock space, but with non-unitary dynamics. This approach has been formalized rigorously by Garraway in [62]. Here, we propose an intuitive derivation of the Lindblad equation based on phenomenological arguments [31].

We consider an imperfect cavity surrounded by a "perfect detector". A perfect detector means that photons are measured with certainty if they escape from the cavity. Now if we input very quickly an excitation inside the cavity, we know that the field intensity should decay exponentially with a rate κ. In the Fock-space representation, the intensity is replaced by the number of photons [8]. Then, at time $t+dt$, we have the probability $P_1 = n\kappa dt$ to detect a photon outside the cavity and a probability $P_2 = 1 - n\kappa dt$ to detect nothing. These two events are characterized by two operators $\hat{O}_1$ and $\hat{O}_2$, which act on the density matrix. More precisely, one must have:

[8] We assume that we "input" n photons at time t.

$$\hat{O}_1[|n\rangle\langle n|] = n\kappa dt|n-1\rangle\langle n-1| \tag{1.19}$$

$$\hat{O}_2[|n\rangle\langle n|] = (1-n\kappa dt)|n\rangle\langle n|. \tag{1.20}$$

These relations are very restrictive on the possible form of the operators. We verify that they are described by:

$$\hat{O}_1[\hat{\rho}(t)] = n\kappa dt\ \hat{a}\hat{\rho}(t)\hat{a}^\dagger \tag{1.21}$$

$$\hat{O}_2[\hat{\rho}(t)] = \hat{\rho}(t) - \frac{\kappa dt}{2}\hat{N}\hat{\rho}(t) - \frac{\kappa dt}{2}\hat{\rho}(t)\hat{N}. \tag{1.22}$$

Adding the two operators allows us to determine the non-unitary part of the Linblad equation:

$$\frac{d\hat{\rho}}{dt} = \kappa\left(\hat{a}\hat{\rho}\hat{a}^\dagger - \frac{1}{2}\hat{N}\hat{\rho} - \frac{1}{2}\hat{\rho}\hat{N}\right). \tag{1.23}$$

A more general expression of the Lindblad term can be determined if thermal effects are taken into account [58]. In this thesis, thermal effects are assumed to be negligible.

We recognize here that the equation follows the general form of a differential equation for a trace preserving positive density matrix [106, 31, 75]. More precisely, the evolution is Markovian, because operators $\hat{O}_1$ and $\hat{O}_2$ are constant in time. We can connect this situation to a quantum system coupled to a bath: here, the outside of the cavity is the bath, and since we assume that photons cannot re-enter the cavity, the information given to the bath cannot interact again with the quantum system.

In order to provide the full model system, one must include in the Hamiltonian, a term that describes the action of the inductive wire (the source of control), and of course, the Hamiltonian of the oscillator. The full Linblad equation of the damped quantum oscillator with a drive is therefore given by:

$$\begin{aligned} \frac{d\hat{\rho}}{dt} &= -i[\hat{H},\hat{\rho}] + \kappa\hat{D}\hat{\rho} \\ \hat{H} &= \underbrace{\omega\left(\hat{a}^\dagger\hat{a} + \frac{\hat{\mathbb{I}}}{2}\right)}_{\hat{H}_{osc}} + \underbrace{i(\beta(t)\hat{a}^\dagger - \beta^*(t)\hat{a})}_{\hat{H}_{control}} \\ \hat{D}\hat{\rho} &= \underbrace{\left(\hat{a}\hat{\rho}\hat{a}^\dagger - \frac{1}{2}(\hat{a}^\dagger\hat{a}\hat{\rho} + \hat{\rho}\hat{a}^\dagger\hat{a})\right)}_{damping}. \end{aligned} \tag{1.24}$$

The constant κ is the relaxation rate and ω is the frequency of an electromagnetic mode of the cavity. β is the control and is a complex function. Its real and imaginary parts describe the control on each quadrature. $\hat{D}$ is the relaxation operator, which is trace preserving (to conserve the properties of the density matrix) and it represents the amplitude decay [9].

The gauge group of the electromagnetic field being abelian, it is not too complicated to solve the dynamics of this system. However, the presence of relaxation complexifies the calculations. The next paragraphs are dedicated to the integration of the master equation by using an evolution operator. The final solution has a simple form in terms of coherent states or photon states.

Since the rest of this section is aimed at exhibiting the solution of the Lindblad equation, it is presented in a very Mathematical way. The reader who is not interested in the details can easily skip the proofs.

[9] The master equation is valid only if $|\beta| \ll \omega$. Otherwise, the cavity can enter in a non-linear regime, and the damping operator can become non-Markovian [31].

1.3.1 Free evolution of the damped oscillator

General solution of the master equation

In a first step, the case without control is studied. The following proposition is a specific case of a more general solution derived by Fujii [58].

Proposition 1 (Propagator of the free field): *Let the following Lindblad equation define the time evolution of the free electromagnetic field* [a]

$$\frac{d\hat{\rho}}{dt} = -i\omega[\hat{a}^\dagger\hat{a}, \hat{\rho}] + \kappa\hat{D}\hat{\rho}.$$

Then, given an initial condition $\hat{\rho}(0)$, the state at time t is given by:

$$\hat{\rho}(t) = e^{-(\kappa/2+i\omega)t\hat{N}} \left(\sum_{n=0}^{\infty} \frac{(1-e^{-\kappa t})^n}{n!} \hat{a}^n \hat{\rho}(0) (\hat{a}^\dagger)^n \right) e^{-(\kappa/2-i\omega)t\hat{N}}, \tag{1.25}$$

where we introduce the number operator $\hat{N} = \hat{a}^\dagger\hat{a}$.

[a] Notice that a term $\omega\hat{\mathbb{I}}/2$ has been removed from the Hamiltonian. This can be done without loss of generality because it induces a phase, which is canceled by the commutator.

Proof. First, let us use theorem 11 (appendix C) to express $D\hat{\rho}$ in its vector form:

$$D\tilde{\rho} = \left(\hat{a} \otimes (\hat{a}^\dagger)^T - \frac{1}{2}\hat{a}^\dagger\hat{a} \otimes \hat{\mathbb{I}} - \frac{1}{2}\hat{\mathbb{I}} \otimes (\hat{a}^\dagger\hat{a})^T \right) \tilde{\rho}.$$

Notice that in matrix representation, operators are real: $(\hat{a})^T = \hat{a}^\dagger$ and $\hat{a}^\dagger\hat{a} = \hat{N} = \hat{N}^T$, so the previous equation becomes:

$$D\tilde{\rho} = \left(\hat{a} \otimes \hat{a} - \frac{1}{2}\hat{a}^\dagger\hat{a} \otimes \hat{\mathbb{I}} - \frac{1}{2}\hat{\mathbb{I}} \otimes \hat{a}^\dagger\hat{a} \right) \tilde{\rho},$$

and it results that the master equation could be written in the form:

$$\begin{aligned} \frac{d\tilde{\rho}}{dt} = \Big[& -i\omega \left(\hat{a}^\dagger\hat{a} \otimes \hat{\mathbb{I}} - \hat{\mathbb{I}} \otimes \hat{a}^\dagger\hat{a} \right) \\ & + \kappa\hat{a} \otimes \hat{a} - \frac{\kappa}{2} \left(\hat{a}^\dagger\hat{a} \otimes \hat{\mathbb{I}} + \hat{\mathbb{I}} \otimes \hat{a}^\dagger\hat{a} \right) \Big] \tilde{\rho} \end{aligned}$$

The next step consists of solving the equation with a group homomorphism. Here we present only the main steps and additional details are given in [58], such as the existence of the group homomorphism. For that purpose, we are going to see that operators form a Lie algebra with the same commutation relations as $\mathfrak{su}(1,1)$. So we solve the problem in $SU(1,1)$ and finally, we transpose the solution to the initial problem. Let us define:

$$K_0 = \hat{N} \otimes \hat{\mathbb{I}} - \hat{\mathbb{I}} \otimes \hat{N} \qquad K_1 = \hat{a}^\dagger \otimes \hat{a}^\dagger \tag{1.26}$$

$$K_2 = \hat{a} \otimes \hat{a} \qquad K_3 = \frac{1}{2}(\hat{N} \otimes \hat{\mathbb{I}} + \hat{\mathbb{I}} \otimes \hat{N} + \hat{\mathbb{I}} \otimes \hat{\mathbb{I}}) \tag{1.27}$$

We have the resulting algebra (note that generally, 1,2 are replaced by +,-):

$$[K_3, K_2] = -K_2 \qquad [K_3, K_1] = K_1 \tag{1.28}$$

$$[K_1, K_3] = -2K_3 \qquad [K_0, K_{j>0}] = 0 \tag{1.29}$$

and consequently :

$$\begin{aligned}\tilde{\rho}(t) &= \exp([-i\omega K_0 + \kappa(K_2 - K_3 + \hat{\mathbb{I}} \otimes \hat{\mathbb{I}}/2]t)\tilde{\rho}(0) \\ &= e^{\kappa t/2} e^{-i\omega K_0 t} \exp(\kappa t[K_2 - K_3])\tilde{\rho}(0).\end{aligned} \tag{1.30}$$

The difficulty is to compute exponentials with K_2 and K_3. Several methods can be used to simplify this term. The original methods used by Fujii consist of recognizing that the commutation relation given in (1.28-1.29) are the ones of the $\mathfrak{su}(1,1)$ algebra, where the generators are given by:

$$k_1 = \begin{pmatrix} 0 & 1 \\ 0 & 0 \end{pmatrix} \; ; \; k_2 = \begin{pmatrix} 0 & 0 \\ -1 & 0 \end{pmatrix} \; ; \; k_3 = \begin{pmatrix} 1/2 & 0 \\ 0 & -1/2 \end{pmatrix},$$

and we assume the existence of an algebra homomorphism such that $K_i = d\phi(k_i)$. The proposition 13 connects the algebra homomorphism to the group homomorphism such as:

$$\exp(\kappa t[K_2 - K_3]) \;=\; \exp(\kappa t[d\phi(k_2 - d\phi(k_3)]) \;=\; \phi(\exp(\kappa t[k_2 - k_3])),$$

and the problem can be solved by computing the exponential of a 2 by 2 matrix. Replacing k_2 and k_3 by their matrix form, we get:

$$\begin{aligned}\exp(\kappa t[k_2 - k_3]) &= \exp\left(\kappa t \begin{pmatrix} -1/2 & 0 \\ -1 & 1/2 \end{pmatrix}\right) \\ &= \begin{pmatrix} e^{-\kappa t/2} & 0 \\ -2\,\mathrm{sh}(\kappa t/2) & e^{\kappa t/2} \end{pmatrix}.\end{aligned} \tag{1.31}$$

To recover the expression with K_i, we have to express the last equation as a product of matrix exponentials, with only basis vectors of the algebra as phase generators. For that purpose we use the Gauss decomposition of $SL(2,\mathbb{C})$:

$$\begin{pmatrix} a & b \\ c & d \end{pmatrix} = \begin{pmatrix} 1 & b/d \\ 0 & 1 \end{pmatrix} \begin{pmatrix} 1/d & 0 \\ 0 & d \end{pmatrix} \begin{pmatrix} 1 & 0 \\ c/d & 1 \end{pmatrix},$$

with, $ad - bc = 1$. Such a decomposition is possible because $SU(1,1) \subset SL(2,\mathbb{C})$. Here we simply have:

$$\begin{aligned}\begin{pmatrix} e^{-\kappa t/2} & 0 \\ 2\,\mathrm{sh}(\kappa t/2) & e^{\kappa t/2} \end{pmatrix} &= \begin{pmatrix} e^{-\kappa t/2} & 0 \\ 0 & e^{\kappa t/2} \end{pmatrix} \begin{pmatrix} 1 & 0 \\ e^{-\kappa t} - 1 & 1 \end{pmatrix} \\ &= \exp\begin{pmatrix} -\kappa t/2 & 0 \\ 0 & \kappa t/2 \end{pmatrix} \exp\begin{pmatrix} 0 & 0 \\ e^{-\kappa t} - 1 & 0 \end{pmatrix} \\ &= \exp(-\kappa t k_3) \exp\left((1 - e^{-\kappa t})k_2\right).\end{aligned} \tag{1.32}$$

We go back to the initial problem and we get:

$$\tilde{\rho} = e^{\kappa t/2} e^{-i\omega K_0 t} e^{-\kappa t K_3} \exp\left((1 - e^{-\kappa t})K_2\right) \tilde{\rho}(0). \tag{1.33}$$

Finally, the solution is expressed in the initial representation:

$$\hat{\rho}(t) = e^{-(\kappa/2 + i\omega)t\hat{N}} \left(\sum_{n=0}^{\infty} \frac{(1 - e^{-\kappa t})^n}{n!} \hat{a}^n \hat{\rho}(0) (\hat{a}^\dagger)^n \right) e^{-(\kappa/2 - i\omega)t\hat{N}}. \tag{1.34}$$

The methods based on the group homomorphism is beautiful and helpful in complicated groups, but in this case, it is also possible to do a straightforward computation:

$$e^{\kappa t(K_2-K_3)} = \mathbb{T}e^{-\kappa t K_3}e^{\int_0^t e^{\kappa t' K_3}K_2 e^{-\kappa t' K_3}dt'}$$

By using the identity: $e^{-F}Ge^{F} = \sum_n \frac{(-1)^n}{n!}[F,G]_n$, with $[F,G]_{n+1} = [F,[F,G]_n]$ and $[F,G]_0 = G$, we can determine:

$$e^{\kappa t' K_3}K_2 e^{-\kappa t' K_3} = e^{-\kappa t' K_2}$$

Thus we have,

$$e^{\kappa t(K_2-K_3)} = e^{-\kappa t K_3}e^{(1-e^{-\kappa t})K_2}$$

□

Note: The proof can be generalized to an oscillator at high temperature (the steady state is a thermal state).

Study of Specific Examples

The previous proposition gives an exact analytic solution of the Lindblad equation but the latter is not very friendly. In this section, few specific cases are studied.

Proposition 2 (specific cases): *Let the following Lindblad equation define the time evolution of the free electromagnetic field:*

$$\frac{d\hat{\rho}}{dt} = -i\omega[\hat{a}^\dagger\hat{a},\hat{\rho}] + \kappa D\hat{\rho}.$$

1) *Assume,* $\hat{\rho}(0) = |\alpha\rangle\langle\alpha|$. *Then,*

$$\hat{\rho}(t) = |\alpha e^{-t(\kappa/2+i\omega)}\rangle\langle\alpha e^{-t(\kappa/2+i\omega)}|. \tag{1.35}$$

2) *Assume,* $\hat{\rho}(0) = |\alpha\rangle\langle\xi|$. *Then,*

$$\hat{\rho}(t) = \exp\left(-\frac{1}{2}(|\alpha|^2+|\xi|^2-2\alpha\xi^*)\left(1-e^{-\kappa t}\right)\right)|\alpha e^{-\gamma t}\rangle\langle\xi e^{-\gamma t}|, \tag{1.36}$$

with $\gamma = \kappa/2 + i\omega$.
3) *Assume,* $\hat{\rho}(0) = \sum_n |c_n|^2|n\rangle\langle n|$ *and* $\omega = 0$ *(rotating frame). Then,*

$$\hat{\rho}(t) = \sum_{n>m}|c_n|^2\binom{n}{m}e^{-\kappa m t}\left(1-e^{-\kappa t}\right)^{n-m}|m\rangle\langle m|. \tag{1.37}$$

As an example, the time evolution of a coherent state is computed numerically. The time evolution of the density matrix diagonal elements is presented in figure 1.7.

Proof. **1)** The starting point is the proposition 1, which gives :

$$\hat{\rho}(t) = e^{-(\kappa/2+i\omega)t\hat{N}}\left(\sum_{n=0}^{\infty}\frac{(1-e^{-\kappa t})^n}{n!}\hat{a}^n\hat{\rho}(0)(\hat{a}^\dagger)^n\right)e^{-(\kappa/2-i\omega)t\hat{N}}.$$

Then, it is a straightforward computation. First we compute the part into brackets:

$$\frac{1-(e^{-\kappa t})^n}{n!}\hat{a}^n|\alpha\rangle\langle\alpha|(\hat{a}^\dagger)^n = \frac{(1-e^{-\kappa t})^n}{n!}\alpha^n|\alpha\rangle\langle\alpha|(\alpha^*)^n$$

$$\rightarrow \exp(|\alpha|^2(1-e^{-\kappa t}))|\alpha\rangle\langle\alpha|.$$

Now, the second part can be computed. The effect of the exponential of the photon-number operator on a coherent state is given by:

$$e^{\gamma\hat{N}}|\alpha\rangle = e^{-|\alpha|^2/2}\sum_{n,k}\frac{(\gamma\hat{N})^n}{n!}\frac{\alpha^k}{\sqrt{k!}}|k\rangle = e^{-|\alpha|^2(1-|\exp(\gamma)|^2)/2}|\alpha e^{\gamma}\rangle \tag{1.38}$$

and a similar computation for the adjoint state allows us to determine:

$$\hat{\rho}(t) = |\alpha e^{-t(\kappa/2+i\omega)}\rangle\langle\alpha e^{-t(\kappa/2+i\omega)}|. \tag{1.39}$$

2) By using the linearity of the propagator, the state of any density matrix in the coherent state representation can be computed:

$$\hat{\rho}(0) = \int d\alpha d\xi.\hat{\rho}_0(\alpha,\xi)|\alpha\rangle\langle\xi|$$

$$\hat{\rho}(t) = \int d\alpha d\xi.\hat{\rho}_0(\alpha,\xi)\exp\left(-\frac{1}{2}(|\alpha|^2+|\xi|^2-2\alpha\xi^*)\left(1-e^{-\kappa t}\right)\right) \times |\alpha e^{-\gamma t}\rangle\langle\xi e^{-\gamma t}|.$$

3) The proof of the last statement is a long but straightforward calculation. □

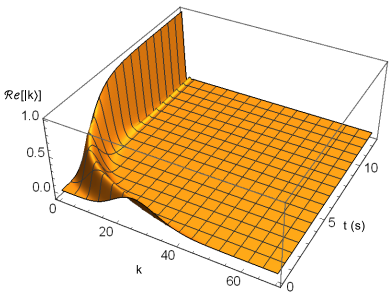

Figure 1.7: We observe that the maximum of the peaks increases as its position moves to zero. As expected, it reaches a steady state with an amplitude of 1 for the vacuum. The initial state is a coherent state with amplitude $\alpha = 5$ and the relaxation parameter is $\kappa = 1$ rad/s. This graph is made by using proposition 1), but the same result can be obtained by computing the coherent state $|5e^{-t/2}\rangle$ in the Fock basis.

1.3.2 Damped quantum oscillator with a drive

This section is devoted to the integration of the master equation (1.24). We recall that [10]:

$$\frac{d\hat{\rho}}{dt} = -i\left[\omega\hat{a}^\dagger\hat{a} + i(\beta\hat{a}^\dagger - \beta^*\hat{a}), \hat{\rho}\right] + \kappa\left(\hat{a}\hat{\rho}\hat{a}^\dagger - \frac{1}{2}(\hat{a}^\dagger\hat{a}\hat{\rho} + \hat{\rho}\hat{a}^\dagger\hat{a})\right).$$

The most difficult part has been computed in the previous section and it remains to include the drive. We could solve the master equation as in proposition 1, but the number of generators of the algebra increases significantly and the computation becomes more involved. We rather prefer an approach using split operators. First, we assume that the control field β is a sum of Dirac

[10] The irrelevant part $\omega\mathbb{I}/2$ has been removed.

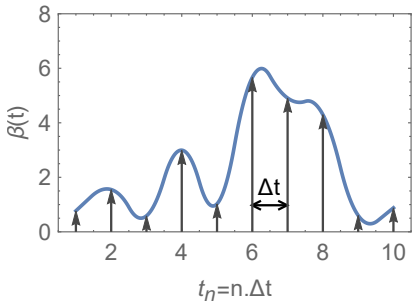

Figure 1.8: A series of Dirac distributions with different amplitudes converges vaguely toward L^2 functions when the distance between each distribution goes toward 0. Consequently, we can approximate any control field β with this parameterization.

pulses with different amplitudes β_n. Each pulse is separated by a time step Δt (figure 1.8). The formal expression is:

$$\beta(t) = \sum_{n=0}^{N} \beta_n \delta(t - n\Delta t). \tag{1.40}$$

This parameterization allows to use a pseudo-periodic point of view and the study of the system is reduced to the subsystem: kick +relaxation. We can prove that for any sequence of symmetric functions, which converges toward a Dirac distribution, the propagator of "kick + relaxation" is a product of propagators (see appendix B):

$$\hat{\rho}(t_{n+1}) = \hat{\mathcal{U}}_R(t, t_{n+1})[e^{\beta_n \hat{a}^\dagger - \beta_n^* \hat{a}} \hat{\rho}(t_n) e^{-\beta_n \hat{a}^\dagger + \beta_n^* \hat{a}}],$$

where $\hat{\mathcal{U}}_R$ is an operator defined by the propagator in equation (1.25) (proposition 1). The use of proposition 3 allows us to show that a Dirac pulse generates coherent states and the dynamics can be expressed as a pure coherent state with a time-dependent amplitude.

$$\hat{\rho}(t) = |\alpha(t)\rangle\langle\alpha(t)|.$$

Proposition 3 (Displacement of pure coherent states): *Let $D_\beta = e^{\beta\hat{a}^\dagger - \beta^*\hat{a}}$ be a displacement operator, then, for any density matrix, which is a pure coherent state $\hat{\rho} = |\alpha\rangle\langle\alpha|$:*

$$D_\beta |\alpha\rangle\langle\alpha| (D_\beta)^\dagger = |\alpha + \beta\rangle\langle\alpha + \beta|.$$

Proof. First, we start with:

$$e^{\beta\hat{a}^\dagger - \beta^*\hat{a}}|\alpha\rangle = e^{\beta\hat{a}^\dagger - \beta^*\hat{a}} e^{\alpha\hat{a}^\dagger - \alpha^*\hat{a}}|0\rangle.$$

Then, we compute the commutator of two coherent state propagators in order to use the Baker-Campbell-Hausdorff formula:

$$[\beta\hat{a}^\dagger - \beta^*\hat{a}\ ,\ \alpha\hat{a}^\dagger - \alpha^*\hat{a}] = (\beta\alpha^* - \beta^*\alpha)\hat{\mathbb{I}}.$$

The commutator commutes with all operators, so we have a relation of the form: $e^X e^Y = e^{X+Y+[X,Y]/2}$, which leads to:

$$e^{\beta\hat{a}^\dagger - \beta^*\hat{a}}|\alpha\rangle = e^{(\beta\alpha^* - \beta^*\alpha)/2}|\alpha + \beta\rangle.$$

Finally, the density matrix under the action of Dirac pulse of amplitude β is given by:

$$e^{\beta\hat{a}^\dagger - \beta^*\hat{a}}|\alpha\rangle\langle\alpha|e^{-\beta\hat{a}^\dagger + \beta^*\hat{a}} = |\alpha + \beta\rangle\langle\alpha + \beta|. \tag{1.41}$$

□

We have to determine the function $\alpha(t)$ in order to determine completely the dynamics of the density matrix. From propositions 2 and 3, the computation is straightforward:

$$\alpha(t) = \sum_{n=0}^{N} \beta_n e^{-(N-n)\Delta t(\kappa/2+i\omega)}. \tag{1.42}$$

Nevertheless, it is generally more convenient to work with an integral form. The change of formalism is direct because the control is a sum of Dirac distributions:

$$\alpha(t) = \int_0^T \beta(t') e^{-(\kappa/2+i\omega)(T-t')} dt'. \tag{1.43}$$

Using (1.40), we can show that this equation is always true. But, when Δt goes toward zero, we can reasonably extend the result to functions. To do so, we approximate the Dirac distribution by indicator functions of support size Δt so that the control becomes a stepwise constant function [141, 84]:

$$\beta(t) = \sum_{n=0}^{N} \beta_n \delta(t - n\Delta t) = \lim_{\Delta t \to 0} \sum_{n=0}^{N} \beta'_n . \Delta t . \mathbb{I}_{](n-1/2)\Delta t;(n+1/2)\Delta t]}(t). \tag{1.44}$$

This allows us to replace β_n by $\beta'_n . \Delta t$ in equation (1.42) and we finally obtain an expression for continuous functions:

$$\alpha(t) = \int_0^T \beta'(t') e^{-(\kappa/2+i\omega)(T-t')} dt'. \tag{1.45}$$

A similar result has been derived in a simpler case (without decoherence) by using the holomorph representation and without any assumption on the control (see [60], p 124).

For the sake of simplicity, the distinction between β and β' will be forgotten in the rest of the manuscript.

1.3.3 Semi-classical model

The semi-classical model is obtained by taking the mean value of the field variables. The system of differential equations, which governs the evolution of such mean values is computed with
$d_t \langle \hat{A} \rangle = Tr[\hat{A} . d_t \hat{\rho}]$. From master equation (1.24), we determine:

$$\frac{d}{dt}\langle a \rangle = \beta - \left(i\omega - \frac{\kappa}{2}\right) \langle a \rangle \tag{1.46}$$

$$\frac{d}{dt}\langle a^\dagger \rangle = \beta^* + \left(i\omega - \frac{\kappa}{2}\right) \langle a^\dagger \rangle. \tag{1.47}$$

These equations are solved by using Green functions, and we obtain for the first one: $\langle a \rangle(t) = \int_{-\infty}^{T} \beta(t') e^{-(\kappa/2+i\omega)(T-t')} dt'$. As could be expected, we recover the function $\alpha(t)$, defined in (1.45).

This shows the consistency of the two approaches [11]. This result is interesting if the electromagnetic field does not interact with another field, then, classical equations of motion are sufficient to describe exactly the cavity dynamics.

1.4 Ensemble of spins coupled to a cavity

1.4.1 Definition of the system

All the building blocks of a spin ensemble coupled to a cavity have been introduced, and the full model is determined by considering the contribution of each spin and by introducing the cavity damping (figure 1.9). In practical applications, the Jaynes Cummings interaction is used and it provides a very good agreement with experiments [75, 163, 85, 119, 21]. Therefore we have:

$$\hat{H}_{tot} = \omega\hat{N} + i(\beta\hat{a}^\dagger - \beta^*\hat{a}) + \sum_{n=1}^{N} \frac{\omega_{S,(n)}}{2}\hat{\sigma}_z^{(n)} + g_{(n)}(\hat{a}^\dagger\hat{\sigma}_-^{(n)} + \hat{a}\hat{\sigma}_+^{(n)}) \tag{1.48}$$

$$\frac{d\hat{\rho}}{dt} = -i\left[\hat{H}_{tot}, \hat{\rho}\right] + \kappa\left(\hat{a}\hat{\rho}\hat{a}^\dagger - \frac{1}{2}(\hat{a}^\dagger\hat{a}\hat{\rho} + \hat{\rho}\hat{a}^\dagger\hat{a})\right), \tag{1.49}$$

where ω is the fundamental energy of the cavity, β is a time-dependent control, $\omega_{S,(n)}$ is the energy transition of the spin n (in many applications, we prefer to use the offset $\Delta_{(n)} = \omega_{S,(n)} - \omega$), $g_{(n)}$ is the coupling constant of the spin n, and κ is the damping rate of the cavity. The Hilbert space of the system is defined by the tensor product of each sub-entity: $\mathcal{H} = \mathcal{F} \otimes (\mathbb{C}^2)^{\otimes N}$.

1.4.2 Dick-States and super-radiance

Depending on the values of $\Delta_{(n)}$, $g_{(n)}$, the spin ensemble could behave differently. Since the work of R.H. Dicke [47] in 1954, it is well known that an ensemble of N spin 1/2-particles located in a small space area, with the same parameters (offset, coupling) can interact coherently with the electromagnetic field, and they can be described by an effective spin $N/2$ (figure 1.10) [12]. More precisely, a mapping is made between a fully symmetrical superposition of states and the state of a spin $N/2$ [57]:

$$\begin{aligned} |\frac{N}{2}, m\rangle &= \sqrt{\frac{(N/2+m)!(N/2-m)!}{N!}} \sum_P |\underbrace{\uparrow,...,\uparrow}_{N/2+m}, \underbrace{\downarrow,...,\downarrow}_{N/2-m}\rangle \\ &= c_m \sum_P |\underbrace{\uparrow,...,\uparrow}_{N/2+m}, \underbrace{\downarrow,...,\downarrow}_{N/2-m}\rangle, \end{aligned} \tag{1.50}$$

where $\sum_P$ means "the sum over all possible permutations".

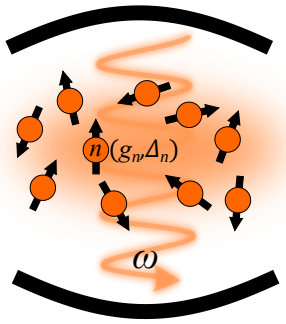

Figure 1.9: The spin ensemble is located in a small volume, defined by the cavity. Due to this small size, we can assume that each spin experiences the same field, and hence, the coupling is introduced with the same operator.

[11] A coherent state ψ is entirely described by the mean value $\langle\psi|\hat{a}|\psi\rangle$. Therefore, if the system evolves accordingly to a continuous transformation of coherent state, it is sufficient to determine the time evolution of its mean value.

[12] Dicke states form a closed subspace of the spin ensemble Hilbert space under the action of the Hamiltonian. Then, if the initial state is a Dicke state, the ensemble remains on a Dicke state. If it is not, the full ensemble of states must be considered.

For example, for two spins, the Dicke subspace is spanned by:

$$\left\{ |\uparrow,\uparrow\rangle \ , \ \frac{1}{\sqrt{2}}(|\uparrow,\downarrow\rangle + |\downarrow,\uparrow\rangle) \ , \ |\downarrow,\downarrow\rangle \right\}. \tag{1.51}$$

Moreover, momentum operators are given by the usual operators in the $N/2$-representation of $SU(2)$:

$$\begin{aligned} \hat{\sigma}_{\pm}|j,m\rangle &= \sqrt{j(j+1) - m(m\pm 1)}|j,m\pm 1\rangle \\ \hat{\sigma}_{z}|j,m\rangle &= m|j,m\rangle. \end{aligned} \tag{1.52}$$

For states with $m \simeq 0$, spins have the highest probability to emit a photon. This probability increases with N, therefore, even if the coupling is low, the coherence of the spins can induce a very high probability of emission (the rate is given by Ng). In these conditions, the spins can release suddenly their energy, producing a short and intense radiation pulse. This effect is known under the name of "*super-radiance*". It is illustrated in chapter 2, in the context of the Purcell relaxation.

The presence of cooperative effects such as superradiance can be estimated by computing the cooperativity parameter [164]:

$$C = \frac{4Ng^2}{\kappa\Omega}, \tag{1.53}$$

where Ω is the width of the offset distribution. In the low cooperativity regime ($C \ll 1$), we expect an uncorrelated spin ensemble and the absence of collective effect. On the opposite, in the high cooperativity regime ($C \gg 1$), we expect a noticeable interaction between the spins, which influences their individual dynamics.

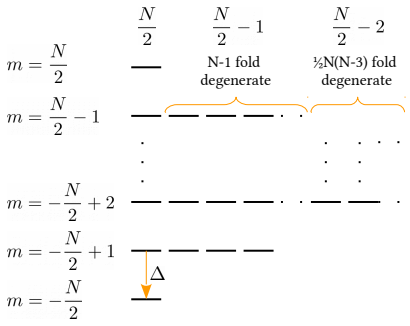

Figure 1.10: Energy diagram of N coherent spins 1/2 as presented in [47]. The idea is to gather degenerated states into a symmetric superposition of states, which follow the same rules as spin $N/2$ states.

1.5 Relaxation mechanisms

In general, for an accurate experimental description, it is necessary to consider the quantum system coupled to its environment. Previously, we have introduced such a theory for the photons trapped inside the cavity, but magnetic momentums are also subjected to non-unitary effects. In this section, a brief description of the different relaxation processes are presented [31, 71, 154].

1.5.1 T_1 and T_2 relaxations

These relaxations are induced by the random fluctuations of the electromagnetic field. Such fluctuations are due to surrounding atoms, which emit photons (or phonons) randomly. Generally, these relaxations are introduced with phenomenological claims [101, 35], by adding terms in the Bloch equation. These terms produce an exponential relaxation toward the ground state. We observe two contributions, called T_1 and T_2 relaxations. Notice that T_1 and T_2 are process characteristic times. Their difference can be understood qualitatively: The first one is induced by the

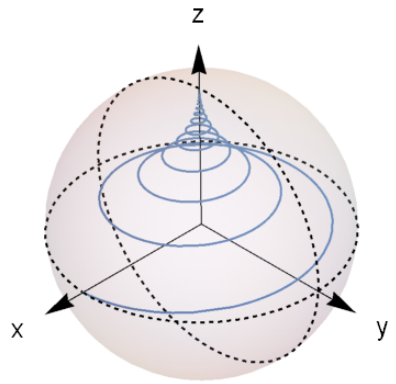

Figure 1.11: An example of trajectory with relaxation (blue solid line). The Bloch vector is initially aligned along x and it relaxes toward the z axis. Due to the presence of an offset, the vector spins around z.

constant magnetic field used for the Zeeman splitting. Indeed, this field forces the spins to be aligned along its direction. The second relaxation occurs in the transverse plane, it comes from the relative dephasing of the spins in the sample. This dephasing is produced randomly, hence, it is an irreversible mechanism.

A full quantum derivation of these relaxations is possible by determining a master equation from a many-body Hamiltonian [71]. This theory is not developed in this manuscript, T_1 and T_2 relaxation are considered only at the classical level, with the introduction of damping terms in the Bloch equation. More precisely, the differential equation becomes:

$$\frac{d}{dt}\vec{M} = \begin{pmatrix} 1 & 0 & 0 & 0 \\ 0 & -\frac{1}{T_2} & \Delta & -g\omega_y(t) \\ 0 & -\Delta & -\frac{1}{T_2} & g\omega_x(t) \\ \frac{1}{T_1} & g\omega_y(t) & -g\omega_x(t) & -\frac{1}{T_1} \end{pmatrix} \vec{M}, \tag{1.54}$$

where $\vec{M} = (M_0, M_x, M_y, M_z)$ is the extended Bloch vector, the component M_0 corresponds to the amplitude of the magnetization along z in the ground state (it is a constant of motion) [135]. $M_{x,y,z}$ are the usual components of the magnetization vector along the x, y, z- directions. An example of trajectory in the Bloch ball is presented in figure 1.11. Equation (1.54) can be written in the form $d_t\vec{M} = A.\vec{M} + \vec{B}$, where $\vec{M}$ is 3 dimensional and $\vec{B}$ contains M_0. Equation (1.54) is an affine equation, and a solution is computed easily with an evolution operator. Notice that depending on the coupling sign, the magnetization relaxes toward different poles. In usual NMR, it is the north pole, but in cavity QED it is the south pole.

T_1 and T_2 relaxations can be introduced in the master equation using Lindblad terms [31]. However, we consider these relaxations only at the Bloch equation level. We use Lindblad equation only in situations where the two relaxation terms are negligible.

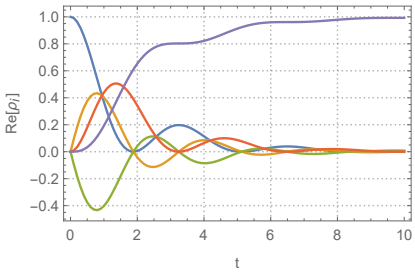

Figure 1.12: Time evolution of the five density matrix elements (real part) involved in equation (1.55). The dynamics are computed in the rotating frame, with a spin at resonance, and $g = \kappa = 1$. In this case, we observe relaxation at the rate 1/2 and small Rabi oscillations.

1.5.2 The Purcell effect

The Purcell effect [154, 75, 83] is a cavity enhancement of spontaneous emission. Let us consider a single spin in its excited state and a cavity in the ground state. Due to the spin-field coupling, the spin can return to its ground state by emitting a photon. This emitted photon has two possible futures: it can be absorbed again by the spin or it can escape from the cavity. If the photon is absorbed, the spin returns to its initial state, otherwise the photon is lost and the full system remains in its lowest energy state. In this simple situation, the dynamics can be solved analytically. Due to the assumption on the initial state, the number of degrees of freedom is reduced to only five variables, and we can rewrite the master equation (1.49) in a matrix form of smaller dimensions. Here, we consider a spin at resonance ($\Delta = 0$) and no control

term ($\beta = 0$). The reduced system is the following:

$$\frac{d}{dt}\begin{pmatrix} \hat{\rho}_{\uparrow 0 \uparrow 0} \\ \hat{\rho}_{\uparrow 0 \downarrow 1} \\ \hat{\rho}_{\downarrow 1 \uparrow 0} \\ \hat{\rho}_{\downarrow 1 \downarrow 1} \\ \hat{\rho}_{\downarrow 0 \downarrow 0} \end{pmatrix} = \begin{pmatrix} 0 & ig & -ig & 0 & 0 \\ ig & -\frac{\kappa}{2} & 0 & -ig & 0 \\ -ig & 0 & -\frac{\kappa}{2} & ig & 0 \\ 0 & -ig & ig & -\kappa & 0 \\ 0 & 0 & 0 & \kappa & 0 \end{pmatrix} \begin{pmatrix} \hat{\rho}_{\uparrow 0 \uparrow 0} \\ \hat{\rho}_{\uparrow 0 \downarrow 1} \\ \hat{\rho}_{\downarrow 1 \uparrow 0} \\ \hat{\rho}_{\downarrow 1 \downarrow 1} \\ \hat{\rho}_{\downarrow 0 \downarrow 0} \end{pmatrix}. \tag{1.55}$$

This equation is solved by a simple diagonalization method. The computation of eigenvalues is straightforward:

$$0\,;\quad -\tfrac{\kappa}{2}\,;\quad -\tfrac{\kappa}{2}\,;\quad \tfrac{1}{2}\left(-\kappa \pm \sqrt{\kappa^2 - 16g^2}\right). \tag{1.56}$$

An example of dynamics is shown in figure 1.12. In the strong coupling regime, $\frac{1}{2}\sqrt{\kappa^2 - 16g^2}$ is complex. Hence, we observe oscillations at this frequency and a damping at rate $\kappa/2$. In the weak coupling regime, $\frac{1}{2}\sqrt{\kappa^2 - 16g^2}$ is real and a first order Taylor expansion gives: $4g^2/\kappa = \Gamma_p$, which is the well-known Purcell rate for a spin at resonance. In the semi-classical model (see next section), the Purcell relaxation is not naturally taken into account. This later is introduced as a T_1 relaxation term, like a phenomenological input. Since we do not consider spins only at resonance, we use the more general formula [154]:

$$\Gamma_p = \frac{\kappa g_{(n)}^2}{\Delta_{(n)}^2 + \kappa^2/4}. \tag{1.57}$$

Considering an ensemble of spins (instead of a single spin) has an influence on the Purcell rate: if every spin is at resonance, a super-radiance effect can occur and spins can relaxe suddenly, in a very short time $\ll 2/\kappa$ [164]. For weakly inhomogeneous ensemble, we observe an intermediate behavior. This effect is illustrated in chapter 2, section 2.7.1.

1.6 Semi-classical approximation and the bad cavity limit

1.6.1 Cumulant expansion

When the different time scales are dominated by the cavity damping, it is possible to proceed to a semi-classical approximation. By semi-classical, we mean that the entanglement between photons and spins is negligible [13]. This allows us to neglect quantum correlations. In physics, this approximation is usually called "*mean field approximation*". The name is due to the fact that the electromagnetic field is replaced by its mean value. In this manuscript, the approximation is called with the name of the underlying mathematical theory: *the cumulant expansion* [95, 148]. As suggested by its name, mean values of operators are expanded in a series,

[13] It follows that spin-spin entanglement is also negligible, because spins interact through the electromagnetic field.

and their high order terms allow us to describe more accurately quantum behaviors [14].

From the *moment generating function* of a random variable $M_X(t) = \langle e^{tX} \rangle$ [15], we define the cumulant $\langle X \rangle_c = \log M_X(t)$. Cumulant are related to the moment of a probability measure, then it is a way to encode the information of a probabilistic system. Introducing in detail the theory of cumulant is not our purpose here (it requires a too long digression). We only highlight that the mean value of a product of operators can be expressed as a function of a cumulant, that is a quantity that can be neglected:

$$\langle \hat{A}\hat{B} \rangle = \langle \hat{A} \rangle \langle \hat{B} \rangle + \langle \hat{A}\hat{B} \rangle_c \tag{1.58}$$

$$\begin{aligned} \langle \hat{A}\hat{B}\hat{C} \rangle =& \langle \hat{A}\hat{B} \rangle \langle \hat{C} \rangle + \langle \hat{A}\hat{C} \rangle \langle \hat{B} \rangle + \langle \hat{C}\hat{B} \rangle \langle \hat{A} \rangle \\ & - 2\langle \hat{A} \rangle \langle \hat{B} \rangle \langle \hat{C} \rangle + \langle \hat{A}\hat{B}\hat{C} \rangle_c. \end{aligned} \tag{1.59}$$

This corresponds to expansions of orders 2 and 3. Similar relations can be deduced as well for products of higher degrees. We observe that the cumulant describes in which quantity observables commute. Since the expansion uses products of lower degrees, the cumulant of order $n+1$ is generally smaller the one of order n. The classical limit of quantum mechanics is recovered with the second order expansion. Indeed, when $\hbar \to 0$, $[\hat{x}, \hat{p}] \to 0$, and $\langle \hat{x}\hat{p} \rangle_c \to 0$. This describes the fact that in classical mechanics, observables commute.

The number of terms required at each order is given by $2^N - 2$. Therefore, the approximation is interesting only at the lowest orders, since the total number of variables should be smaller than the dimension of the density matrix.

This approximation is useful to derive an ensemble of ODEs for mean values of operators [16]. Unfortunately, an infinite number of differential equations is generally required to determine the full dynamics. Therefore, the use of a cumulant expansion allows us to express correlations in terms of products of lower degree. By assuming that the cumulant is negligible, we obtain a closed ensemble of ODEs. The validity of the approximation can be verified by evaluating the cumulant explicitly. It can be estimated by integrating the next order. If the approximation is valid, we should observe a convergence of the results. In this manuscript, another option is chosen and the full Lindblad equation is integrated in order to verify the approximation. The range of validity of the semi-classical approximation is given from exact integration.

Using Linblad equation (1.49) in the rotating frame, and the expansion (1.58) give the following $3N + 2$ differential equations [85]:

[14] In practice, we consider only the lowest orders. Otherwise, an infinite number of terms could be required to describe exactly quantum dynamics.

[15] A generalization to several random variables $X_1, ..., X_N$ is defined by: $\langle \exp\left(\sum_{n=1}^{N} t_n X_n\right) \rangle$.

[16] By using the relation $d_t \langle \hat{A} \rangle = Tr[\hat{A} d_t \hat{\rho}]$.

$$
\begin{aligned}
\frac{d}{dt}\langle\hat{X}\rangle &= -\frac{\kappa}{2}\langle\hat{X}\rangle + \omega_X - \sum_j 2g_{(j)}\langle\hat{S}_y^{(j)}\rangle \\
\frac{d}{dt}\langle\hat{Y}\rangle &= -\frac{\kappa}{2}\langle\hat{Y}\rangle + \omega_Y + \sum_j 2g_{(j)}\langle\hat{S}_x^{(j)}\rangle \\
\frac{d}{dt}\langle\hat{S}_x^{(j)}\rangle &= -\Delta_{(j)}\langle\hat{S}_y^{(j)}\rangle + g_{(j)}\langle\hat{Y}\hat{S}_z^{(j)}\rangle \\
\frac{d}{dt}\langle\hat{S}_y^{(j)}\rangle &= \Delta_{(j)}\langle\hat{S}_x^{(j)}\rangle - g_{(j)}\langle\hat{X}\hat{S}_z^{(j)}\rangle \\
\frac{d}{dt}\langle\hat{S}_z^{(j)}\rangle &= g_{(j)}\langle\hat{X}\hat{S}_y^{(j)}\rangle - g_{(j)}\langle\hat{Y}\hat{S}_x^{(j)}\rangle,
\end{aligned}
\tag{1.60}
$$

where we introduce the spin operators $\hat{S}^{(j)}_{x,y,z,\pm} = \sigma^{(j)}_{x,y,z,\pm}/2$, $\hat{X} = a + a^\dagger$ and $\hat{Y} = -i(a^\dagger - a)$ in order to get more symmetrical expressions. The control fields $\omega_{X,Y}$ are the projections of the control β onto the two field quadratures, in the rotating frame: $\omega_X = e^{i\omega t}(\beta + \beta^*)$ and $\omega_Y = ie^{i\omega t}(\beta - \beta^*)$.

At order 3, the number of equations increases considerably. For the sake of conciseness, the equations are derived for a single spin coupled to a cavity [17][148]:

$$
\begin{aligned}
d_t\langle\hat{\sigma}_-\rangle &= -i\Delta\langle\hat{\sigma}_-\rangle + ig\langle\hat{\sigma}_z\hat{a}\rangle \\
d_t\langle\hat{\sigma}_-\hat{a}\rangle &= (-i\Delta + \beta - \kappa/2)\langle\hat{\sigma}_-\hat{a}\rangle - ig\langle\hat{\sigma}_z\hat{a}\hat{a}\rangle \\
d_t\langle\hat{\sigma}_-\hat{a}^\dagger\rangle &= (-i\Delta + \beta^* - \kappa/2)\langle\hat{\sigma}_-\hat{a}^\dagger\rangle + ig\left(\frac{1}{2}(\langle\hat{\sigma}_z\rangle + 1) - \langle\hat{\sigma}_z\hat{a}^\dagger\hat{a}\rangle\right)
\end{aligned}
$$

$$
\begin{aligned}
d_t\langle\hat{\sigma}_+\rangle &= i\Delta\langle\hat{\sigma}_+\rangle + ig\langle\hat{\sigma}_z\hat{a}^\dagger\rangle \\
d_t\langle\hat{\sigma}_+\hat{a}\rangle &= (i\Delta + \beta - \kappa/2)\langle\hat{\sigma}_+\hat{a}\rangle - ig\left(\frac{1}{2}(\langle\hat{\sigma}_z\rangle + 1) + \langle\hat{\sigma}_z\hat{a}^\dagger\hat{a}\rangle\right) \\
d_t\langle\hat{\sigma}_+\hat{a}^\dagger\rangle &= (i\Delta + \beta^* - \kappa/2)\langle\hat{\sigma}_+\hat{a}^\dagger\rangle - ig\langle\hat{\sigma}_z\hat{a}^\dagger\hat{a}^\dagger\rangle
\end{aligned}
$$

$$
\begin{aligned}
d_t\langle\hat{\sigma}_z\rangle &= 2ig(\langle\hat{\sigma}_-\hat{a}^\dagger\rangle - \langle\hat{\sigma}_+\hat{a}\rangle) \\
d_t\langle\hat{\sigma}_z\hat{a}\rangle &= (\beta - \kappa/2)\langle\hat{\sigma}_z\hat{a}\rangle - ig(2\langle\hat{\sigma}_+\hat{a}\hat{a}\rangle - \langle\hat{\sigma}_-\rangle - 2\langle\hat{\sigma}_-\hat{a}^\dagger\hat{a}\rangle) \\
d_t\langle\hat{\sigma}_z\hat{a}^\dagger\rangle &= (\beta^* - \kappa/2)\langle\hat{\sigma}_z\hat{a}^\dagger\rangle + ig(2\langle\hat{\sigma}_-\hat{a}^\dagger\hat{a}^\dagger\rangle) - \langle\hat{\sigma}_+\rangle - 2\langle\hat{\sigma}_+\hat{a}^\dagger\hat{a}\rangle
\end{aligned}
$$

$$
\begin{aligned}
d_t\langle\hat{a}\rangle &= \beta - \kappa/2\langle\hat{a}\rangle - ig\langle\hat{\sigma}_-\rangle \\
d_t\langle\hat{a}^\dagger\rangle &= \beta^* - \kappa/2\langle\hat{a}^\dagger\rangle - ig\langle\hat{\sigma}_+\rangle \\
d_t\langle\hat{a}^\dagger\hat{a}\rangle &= \beta\langle\hat{a}^\dagger\rangle + \beta^*\langle\hat{a}\rangle - \kappa\langle\hat{a}^\dagger\hat{a}\rangle - ig(\langle\hat{\sigma}_-\hat{a}^\dagger\rangle - \langle\hat{\sigma}_+\hat{a}\rangle) \\
d_t\langle\hat{a}\hat{a}\rangle &= -\kappa\langle\hat{a}\hat{a}\rangle - 2ig\langle\hat{\sigma}_-\hat{a}\rangle) + 2\beta\langle\hat{a}\rangle \\
d_t\langle\hat{a}^\dagger\hat{a}^\dagger\rangle &= -\kappa\langle\hat{a}^\dagger\hat{a}^\dagger\rangle - 2ig\langle\hat{\sigma}_+\hat{a}^\dagger\rangle) + 2\beta^*\langle\hat{a}^\dagger\rangle.
\end{aligned}
$$

It should be noted that the ensemble of differential equations is not strictly closed. The complete set is determined by replacing mean values of products of three operators by their expansion (1.59), and to neglect the cumulant. In the case of several spins, other quantities such as $\langle\hat{\sigma}_a^{(n)}\hat{\sigma}_b^{(m)}\rangle$ must be accounted for.

[17] In order to simplify equations, we have replaced β by its analogue in the rotating frame: $\beta(t) \to \beta(t)e^{i\omega t}$.

1.6.2 The (very) bad cavity limit

Performing a semi-classical approximation requires a bad cavity in order to neglect entanglement. However, if the quality factor is very low, the cavity damping dominates the dynamics in (1.60), and an additional approximation can be performed. The idea is to integrate with Green functions the E.M. field ODEs in (1.60), and to invoke the limit of the integration kernel $e^{\kappa(t'-t)/2}$ as a Dirac distribution[18]. This allows us to determine a new ensemble of differential equations [9]

[18] A general description of the method is presented in section B.4.2.

$$\begin{aligned}
\frac{d}{dt}\langle S_x^{(j)}\rangle &= -\Delta_j\langle S_y^{(j)}\rangle + \frac{2g}{\kappa}\omega_Y\langle S_z^{(j)}\rangle + \frac{4g^2}{\kappa}\bar{S}_x\langle S_z^{(j)}\rangle \\
\frac{d}{dt}\langle S_y^{(j)}\rangle &= \Delta_j\langle S_x^{(j)}\rangle - \frac{2g}{\kappa}\omega_X\langle S_z^{(j)}\rangle + \frac{4g^2}{\kappa}\bar{S}_y\langle S_z^{(j)}\rangle \\
\frac{d}{dt}\langle S_z^{(j)}\rangle &= \frac{2g}{\kappa}(\omega_X\langle S_y^{(j)}\rangle - \omega_Y\langle S_x^{(j)}\rangle) - \frac{4g^2}{\kappa}(\bar{S}_x\langle S_x^{(j)}\rangle + \bar{S}_y\langle S_y^{(j)}\rangle),
\end{aligned} \tag{1.61}$$

where $\bar{S}_x = \sum_k\langle S_x^{(k)}\rangle$, $\bar{S}_y = \sum_k\langle S_y^{(k)}\rangle$. We recover a relaxation mechanism with a rate $\frac{4g^2}{\kappa}$, which is the Purcell rate at resonance (equation (1.57)). Notice that we assume the same value $g_{(j)} = g$ for each spin.

1.6.3 Discussion and analogy with the NMR radiation damping

NMR radiation damping

The radiation damping in NMR is a collective effect of the mean magnetization interacting with the detection coil. The magnetization produces in the coil a detectable current, but due to the Lorentz force, a back action is produced in the opposite direction, which is not negligible for a strong magnetic field [94, 101]. This new field interacts again with the spins and since its amplitude depends on the average magnetization, it is the source of a non-linear dynamics.

In order to introduce the effect, we neglect propagation effects inside the apparatus and the Lorentz force is assumed to follow instantaneously the magnetization. The inhomogeneous Maxwell equation [170] in its steady state gives:

$$\partial_a \wedge \vec{H} = \star\vec{j} = \frac{1}{\mu_0}\partial_a \wedge \star\vec{B} - \partial_a \wedge \vec{M}. \tag{1.62}$$

We introduce ∂_a the partial derivative in direction $a = x, y, z$, and $\star$ is the Hodge dual. $\vec{B}$ is the magnetic field, $\vec{M}$ is the total magnetization and $\vec{j}$ is the current in the coil. Equation (1.62) being an equation of a differential 2-form, it can be integrated over a surface:

$$\int_{S'}(\partial_a \wedge \star\vec{B})d\vec{S} = \mu_0\int_{S'}\left(\partial_a \wedge \vec{M} + \star\vec{j}\right)d\vec{S}. \tag{1.63}$$

Let us suppose that $\star\vec{B}$ and $\vec{M}$ are constants on $\delta S'$:

$$B = \mu_0 \left(M + \frac{1}{\delta S'} \int_{S'} (\star\vec{j}) d\vec{S} \right), \tag{1.64}$$

where B and M are respectively the amplitude of the magnetic field and the magnetization normal to the surface. This equation describes the current induced by the spin magnetization in the detection coil, and the magnetic field it produces. We analyze the dynamics along the direction normal to this surface, called x. We express the radiation damping as a first order effect of the magnetization back action. For this purpose, the magnetic field is expressed as a function of a loop $\mathcal{C}$ (materialized by the coil). In the x direction we have:

$$B_x = \frac{1}{S} \left(\oint_{\mathcal{C}_{\perp x}} \vec{A} d\vec{l} \right), \tag{1.65}$$

where the loop $\mathcal{C}_{\perp x}$ is a loop of current in the coil, normal to x, and $\vec{A}$ is the magnetic potential. The magnetic field is assumed to be constant along the loop. In the case of a conductor, we have the well-known relation:

$$\frac{d}{dt} \left(\oint_{\mathcal{C}} \vec{A} d\vec{l} \right) = -\sigma \oint_{\mathcal{C}} \vec{j} d\vec{l}, \tag{1.66}$$

where σ is the conductivity of the material of the coil, and $\mathbf{j}$ is the current 1-form in $\mathcal{C}$. By using again the Maxwell equation, assuming that the current is in a steady state [19], and inserting alternatively (1.64), (1.65) into (1.66), we obtain:

$$\oint_{\mathcal{C}_{\perp x}} \vec{j} d\vec{l} = -\frac{1}{\sigma} S \frac{dM}{dt}, \tag{1.67}$$

and finally we deduce:

$$B_x = -\tilde{\kappa} \frac{dM_x}{dt} + \mu_0 M_x, \tag{1.68}$$

where $\tilde{\kappa}$ is a positive constant, which depends on μ_0 and σ. Now, we focus on the local description of a spin, and we express the *average* magnetization with spherical parameters,

$$\vec{M}_x = M_0 \begin{pmatrix} \sin(\theta)\cos(\phi.t) \\ \sin(\theta)\sin(\phi.t) \\ \cos(\theta) \end{pmatrix}. \tag{1.69}$$

For the sake of simplicity, we neglect field inhomogeneity. Thus, by inserting equation (1.68) into the Bloch equation ($d_t\vec{M} = -\gamma\vec{B} \wedge \vec{M}$), we notice the introduction of a non-vanishing term: $\vec{M} \wedge d_t\vec{M}$. Therefore, the computation of $d_t M_z$ leads to the equation:

$$\frac{d\theta}{dt} = -\frac{\gamma}{\tilde{\kappa}} M_0 \sin(\theta), \tag{1.70}$$

[19] The origin of this approximation is questionable as we mix Maxwell's equations with and without steady state. Heuristically, we can expect that it should work this way, but a rigorous explanation of this approximation is not straightforward. The radiation damping phenomenon can be explained more rigorously with the QFT and an ordered interaction of particles [51].

and finally, the radiation damping term is determined by inserting (1.70) into the Bloch equation:

$$\frac{d\vec{M}^{(i)}}{dt} = \frac{\gamma^2}{\tilde{\kappa}} \begin{pmatrix} -M_z^{(i)}.M_x \\ -M_z^{(i)}.M_y \\ M_x.M_x^{(i)} + M_y.M_y^{(i)} \end{pmatrix}. \tag{1.71}$$

This equation describes the non-linear effect of the mean magnetization on *a single spin* (i), through the coupling with the detection coil. The effect is summarized in figure 1.13.

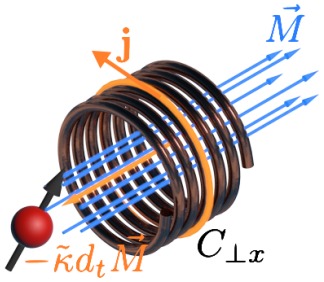

Figure 1.13: Principle of the radiation damping effect in NMR. The spins produce a magnetization field $\vec{M}$, which induces a current **j** in the detection coil. The electron inertia leads to the creation of a magnetic field with the opposite direction and amplitude $-\tilde{\kappa} d_t \vec{M}$.

Cavity and Spins v.s. NMR

By comparing equations (1.61) and (1.71), we immediately recognize a similar structure. In the bad cavity limit, the semi-classical equations take the form of NMR radiation damping equations, where the radiation damping rate is the Purcell rate (with a negative sign). The sign change comes from the sign difference mentioned in section 1.2.3. Then, the radiation damping effect can be understood as a general effect of a spin coupled to a damped oscillator. In quantum optics, the oscillator is a cavity, and in NMR, it is the detection coil.

The fact that the damping rate is the same as the Purcell rate leads us naturally to think that we observe a Purcell effect. However, the radiation damping is a unitary effect: it does not change the amplitude of the Bloch vector. On another side, the Purcell effect can be viewed as a T_1 relaxation. Then, the two effects have totally different properties. More precisely, the Purcell effect is removed in semi-classical equations by the cumullant expansion at order 2 (the north pole of the Bloch sphere is an unstable stationary point, but it is not stationary in the Lindblad equation). The effect is recovered partially at order 3.

The analogy is better with the super-radiant effect because they are both unitary, and they are both important when the spins are in phase on the equatorial plane.

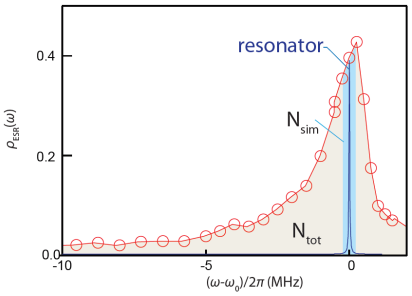

Figure 1.14: Distributions obtained by A. Bienfait in her experiments [21]. The red curve is the full distribution of spins. Due to the Purcell effect, an effective distribution is defined (black curve). The blue area corresponds to the interval of offsets accessible in the experiment.

1.7 Experimental distribution of spins

In order to describe accurately the spin ensemble, one must specify the sets of coupling $\{g_{(i)}\}$ and offset $\{\Delta_{(i)}\}$. In the limit of a large ensemble, one could consider a continuous ensemble characterized by continuous probability distributions. The width of the spectrum induced by the field inhomogeneity broadening is very large. However, only a small portion of this distribution is accessible. This restriction is induced by the repetition of the experiment (in order to increase the SNR). In order to understand the origin of this distribution, we can assume in a first step that the spins are excited only within the spectrum of the excitation pulse. We do not specify the width of this spectrum for the moment, but we assume that this latter is sufficiently large compared

to the following additional restrictions. After excitation, spins are subjected to relaxation. The T_2 relaxation cancels the transverse magnetization and the T_1 relaxation induces a return to the initial state. In the experiment, the Purcell effect is the most important contribution to the longitudinal relaxation. According to equation (1.57), spins near the resonance can relax faster than spins far from resonance. Therefore, after few measurement iterations, spins far from the resonance never return to the initial state and their magnetizations are canceled due to the T_2 relaxation. Inversely, resonant spins have time to return to the ground state and they participate at each measurement. As a consequence, the spin offset distribution is defined by the Purcell rate and the repetition time [21]:

$$\rho_{Purcell}(g,\Delta) \propto 1 - \exp\left(-\Gamma_P(g,\Delta)T_1^p\right), \tag{1.72}$$

where Γ_p is defined in (1.57) and T_1^p is the repetition time of experiments. The restriction of the spin distribution is illustrated in figure 1.14.

When T_1^p is small, the distribution $\rho_{Purcell}$ is well approximated by a Lorentzian or a Gaussian distribution [85, 93]. Therefore, in many applications an approximated distribution is used. The choice of the approximation depends on the context. The distribution (1.72) depends on g. Then, $\rho_{Purcell}$ is correlated to the distribution of coupling factors $\rho_1(g)$. As a first approximation, we could neglect this distribution and write:

$$\rho_1(g) = \delta(g - g_0).$$

Otherwise, a uniform distribution is used:

$$\rho_1(g) = \frac{1}{g_{max} - g_{min}} \mathbb{I}_{[g_{min}, g_{max}]}(g).$$

1.8 Conclusion

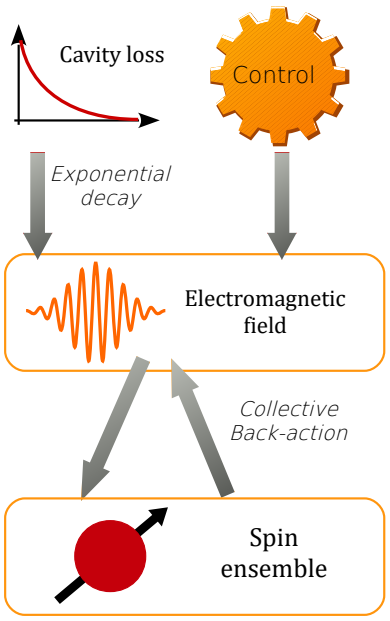

Figure 1.15: Summary of the physical model considered in the first part of this thesis.

Experiments which consist of connecting a crystal to a microwave resonator at an extremely low temperature allow us to reproduce magnetic resonance experiments at the quantum limit.

We have derived a theoretical model to describe experiments. It consists of an inhomogeneous ensemble of spins coupled to a cavity with a Jaynes-Cummings interaction. The spins are distributed over the space of parameters, composed of offsets (difference of frequency with the cavity fundamental mode) and coupling strengths. The cavity is not perfect, and due to the very low temperature of the setup, the electromagnetic field relaxes to its ground state. Additionally, a control allows us to input coherent states in the cavity. The physical model is illustrated in figure 1.15.

The main physical effects have been introduced: the many-body effects such as the super-radiance, and the relaxation mechanisms (T_1, T_2, the Purcell effect).

The integration of the master equation is a difficult problem. In this chapter, the dynamics of the quantum electromagnetic field with a drive have been solved, and a semi-classical approximation has been introduced in order to simplify the general problem in the bad cavity limit. In this limit, photons emitted by the spins can escape from the cavity before their reabsorption. Then, the entanglement spins-cavity is negligible, and we can express the dynamics using the classical formalism.

Due to cavity losses, spins experience a new source of relaxation, called the Purcell effect. This relaxation takes the form of NMR radiation damping effect in the limit of a very bad cavity. However, the analogy has some limits (differences). For instance, the bad cavity limit induces a unitary relaxation, which is closer to a super-radiance relaxation.

The approximation is convenient for the calculations (numerical or analytic), but unfortunately, it removes many quantum features which can be important. This point must be studied in detail, using numerical integration. Even with powerful computers, the simulation of a many-body quantum system is a difficult task. Therefore, studies of the semi-classical approximation and quantum effects are described in chapter 2.

The understanding of the quantum effects, the semi-classical approximation and the analogy with the radiation damping is important for the purpose of controlling the spin ensemble. The control of spin systems is well known in NMR, and the semi-classical approximation allows us to generalize the standard methods where the spin ensemble is coupled to a cavity. The control strategy and several applications are investigated in chapters 3 and 4.

Chapter 2

Numerical simulation of an inhomogeneous spin ensemble

This second chapter can be interpreted as a transition between the state of the art of cavity-QED and original results. The physics of an inhomogeneous spin ensemble coupled to a cavity is revisited with numerical simulations, by using a minimum of additional approximations. To the best of our knowledge, this is the first time that the dynamics are computed for large and inhomogeneous spin ensembles with a significant number of photons.

First, the issues of this study are presented in section 2.1. Then, the numerical algorithms are detailed in section 2.2. Sections 2.3, 2.4, 2.5 and 2.6 are devoted to the presentation of different representations of the spin ensemble (discretized and continuous distributions, semi-classical system), and it is shown how information can be extracted from these models, with partial trace operations. Finally, two physical effects are revisited in section 2.7: the Purcell relaxation of an inhomogeneous spin ensemble, and the Free Induction Decay. The dynamics are visualized for the entire ranges of parameters and each regime is compared within the same framework. The standard limit cases are recovered and we highlight non-trivial situations when $g \simeq \kappa \simeq \Omega$. Moreover, the quantum and the semi-classical approaches are compared. These numerical simulations are crucial for the applications of optimal control techniques.

2.1 Motivation

Computing numerically the dynamics of a quantum many-body system requires a huge amount of computational resources (speed, memory) and it is a problem investigated for decades by physicists [54]. The system presented in section 1.4 is a benchmark example of this class of systems: hundred of photons and thousand of spins are involved in an experiment. If Lindblad equation (1.49) is integrated in a naive way (like we integrate usual ODEs, with

an RK4 algorithm, for example), *a computer with 32 GB of memory cannot integrate a system larger than 6 spins and 4 photons... Therefore, an efficient algorithm is required to simulate a realistic system*. This is also necessary in order to use in a second step an optimal control algorithm for control field design.

In order to avoid the rapid increase of the Hilbert space dimension and hence, the complexity of the problem, one generally performs a cumulant expansion approximation (section 1.6.1).The effect of this truncation is to neglect quantum correlations [20]. Another standard approximation in spin wave theory is the Holstein Primakoff approximation [78, 92, 85, 86]. This approximation is of particular interest when the number of photons involved in the experiment is small compared to the number of spins. In this case, only the first energy levels are reachable and a part of the dynamics can be neglected.

[20] Only the classical part is preserved, so that observables commute.

Several studies have applied with success these approximations to spin ensembles coupled to cavities [21, 92]. The agreement theory/experiment is generally very good, which justifies these approximations. However, we can experimentally reach regimes where these approximations cannot be used [28]. In particular, a pulse optimized under the semi-classical approximation might not work efficiently in the good cavity limit. The application of a control and the entanglement between the electromagnetic field and a spin ensemble open the doors to new situations in quantum technologies, which are of particular interest. **Therefore, it is necessary to perform numerical simulations of a full-quantum system, composed of many spins and many photons, without using standard approximations**.

One of the main goals emphasized in the roadmap paper [67] for quantum optimal control is the *control of quantum systems coupled to Markovian and Non-Markovian baths*. Recently, several papers were published on the subject [138, 29, 115]. However, the problem is still restricted to very simple models and a lot of work is still required in this direction.

The problem of quantum control with a non-markovian environment is closely related to an inhomogeneous ensemble of spins coupled to a cavity. Actually, in our model, a Markovian damping acts only on the electromagnetic field. But if we focus on the dynamics of a single spin, by tracing out other degrees of freedom, *the problem is equivalent to a spin coupled to a non-Markovian bath* [30, 31]. For our system, the bath is composed of the electromagnetic field and the other surrounding spins. Therefore, the control of the dynamics of the full ensemble is a crucial step toward the control of general non-Markovian quantum systems.

In this chapter, numerical simulations are investigated in detail. With the methods introduced below, we are able to perform computations with a relatively small numerical cost. For example, simulating the Purcell relaxation of an inhomogeneous ensemble of 20 spins coupled with a Foch space of 25 photons requires between 30 min and 5 hours (depending on the parameters, and thus the number of time steps). The key to perform efficient compu-

tations is to choose a good numerical algorithm (such as the low rank approximation [34]), and to choose a good representation of the spin ensemble. In this chapter, we distinguish the following models:

1. **Model 1:** *Discretized spin distribution*. As usual in NMR, the spin ensemble is discretized into bins of equal detuning frequencies. For spin ensembles coupled to a cavity, a "smart" discretization can reduce the dynamics in a small subspace (see figure 2.1).

2. **Model 2:** *Continuous spin ensemble*. The spin ensemble is considered as a classical field over the detuning parameter. This model allows to deal with a small Hilbert space dimension and describes most important quantum effects (Purcell relaxation, super-radiance,...). It is an approximate model because it neglects the entanglement of spins with different detunings.

3. **Model 3:** *Semi-classical model*. This is the model presented in section 1.6, with a truncation at order two in the cumulant expansion. In this model, entanglement of subsystems is neglected.

As illustrative examples, the Purcell effect and the free induction decay are investigated in four different regimes: bad/good cavity regime [21] and the weak/strong cooperativity regime. Model predictions are compared and the convergence toward the semi-classical dynamics is studied. As far as we know, it is the first time that all dynamical regimes are explored numerically, with a full-quantum system. In order to extend this work to non-Markovian systems, the Purcell effect is investigated from the point of view of a single spin. This way, we clearly see the effect of the spin ensemble on the relaxation of a single spin.

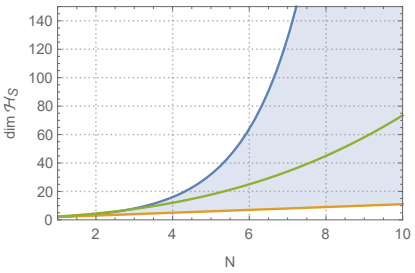

Figure 2.1: Dimension of the spin ensemble Hilbert space as a function of the number of spins. The blue curve is the full size 2^N, but this size can be reduced with an appropriate representation of the system. The blue area is the accessible ensemble of values for the space dimension. The orange curve is the lower bound, which corresponds to a situation where all the spins have the same offset frequency. The green curve corresponds to an approximation of a Gaussian distribution.

2.2 Numerical algorithms

Many algorithms are used to integrate the time evolution of a quantum system: split operators [14], RK4 (or other similar algorithms), stochastic integration [120, 75], path integrals [160, 114, 153],... The stochastic approach is well known because a single integration of the stochastic wave function gives a measurable quantum trajectory, and it is easily parallelizable. However, our final goal being to compute optimal control field, we rather use exact algorithms, in the sense that the solution does not have random fluctuations. Several algorithms are used to integrate the dynamics. Semi-classical dynamics are determined with a RK4 algorithm. Meanwhile, quantum dynamics are computed with a hybrid algorithm composed of a split operator scheme for unitary operations, and an Euler scheme for the relaxation. The latter is given by:

[21] **Vocabulary remark:** in this manuscript, the term *weak/strong coupling* is used as a synonym of *bad/good cavity*. Actually, the difference is made by comparing g and κ. This should not be confused with the *ultra-strong regime*, where g and ω are compared. In this latter regime, the RWA cannot be used and the spin-boson Hamiltonian must replace the J.C. Hamiltonian [28, 93]. In this manuscript, the RWA is assumed to be valid.

Definition 1 (Euler-Split-operator algorithm [*]):

- *compute* $U = e^{-i.dt.\hat{H}/2}$
- *compute* $L_1 = \sqrt{\kappa} * \hat{a}$
- *compute* $L_2 = \sqrt{\kappa} * \hat{a}^\dagger$
- *compute* $S = -(L_1^T.L_1 + L_2^T.L_2)/2$
- *at each time step, compute* $\hat{\rho}(t+dt)$ *with:*

$$\hat{\rho} = U.\hat{\rho}.U^\dagger$$
$$\hat{\rho} = \hat{\rho} + dt * (L_1.\hat{\rho}.L_1^T + L_2.\hat{\rho}.L_2^T)$$
$$\hat{\rho} = (\mathbb{I} + dt * S).(\hat{\rho}.(\mathbb{I} + dt * S)^T)$$
$$\hat{\rho} = U.\hat{\rho}.U^\dagger$$
$$\hat{\rho} = \frac{\hat{\rho}}{Tr[\hat{\rho}]}$$

[*] In this algorithm, the Hamiltonian is integrated with the unitary operator U, and the quantum jumps are made with operators L_1, L_2, and S. These three operators allow us to encode the Lindblad term efficiently $\kappa\hat{D}$ in master equation (1.49). The relaxation process is computed with an Euler-scheme, which does not preserve the norm. Thus, the density matrix is normalized at each iteration.

However, the computation speed can be enhanced by the Low-rank-approximation algorithm developed by Claude Le-Bris and Pierre Rouchon [34]. Their idea was to adapt the previous algorithm with a low-rank-approximation of $\hat{\rho}$. Dynamics are generally encoded in a few degrees of freedom, and it is sufficient to calculate their time evolution. The main idea is to project the density matrix $\hat{\rho}$ on a matrix of smaller size r, which encodes these degrees of freedom [22], and to integrate the dynamics with r. The two matrices are related by:

$$\hat{\rho} = M.r.M^\dagger \tag{2.1}$$

If $rank(\hat{\rho}) = n$ and $rank(r) = m$, then M is a matrix of size $n \times m$, which verifies the identity $M^\dagger.M = \mathbb{I}_m$. However, the projection is time dependent, then we also have to propagate the evolution of M. One can show that the differential equation for these two new matrices are given by [23]:

$$\begin{aligned}
\frac{dM}{dt} &= -i\hat{H}.M + \kappa(\hat{\mathbb{I}}_n - M.M^\dagger) \\
&\quad \times \left(-\frac{1}{2}\hat{N} + \hat{a}M.r.M^\dagger\hat{a}^\dagger M.r^{-1}.M^\dagger\right) M \\
\frac{dr}{dt} &= \frac{-\kappa}{2}(M^\dagger.\hat{N}.M.r + r.M^\dagger.\hat{N}.M) \\
&\quad + \kappa M^\dagger.\hat{a}.M.r.M^\dagger.\hat{a}^\dagger.M \\
&\quad + \frac{\kappa}{m}Tr\left[\hat{a}^\dagger(\mathbb{I}_n - M.M^\dagger)\hat{a}M.r.M^\dagger\right].\mathbb{I}_m
\end{aligned}$$

These equations can be integrated using an Euler/ Runge–Kutta method. In the original version of the algorithm, a third order scheme is used. Since this algorithm requires product of matrices of small dimensions [24], the computation is generally faster. How-

[22] Such that : $rank(r) < rank(\hat{\rho})$.

[23] We do not give a detailed derivation of these equations because the calculations are long and technical. dM/dt and dr/dt are given only to provide an idea of how the set of differential equations is transformed. We refer to [34] for further details.

[24] compared to rank(ρ).

ever, it is important to keep in mind that the low rank approximation does not reduce the size of the problem, and it cannot integrate the dynamics of a larger system than the one allowed by the standard algorithm. This is due to the fact that the density matrix has to be reconstructed at different stages of the process. The gain of speed also depends on the number of observables evaluated at each time step. Indeed, computing several times a quantity of the form $Tr\left[M.r.M^{\dagger}.O\right]$ takes time. We have observed that the gain of speed is negligible for a number of observables $\gtrsim 7$.

2.3 First model: Discretized density of spins

The key to reduce the Hilbert space is the discretization of the spin distribution. It is common in experiments to have an ensemble of spins with a Lorentzian/Gaussian offset distribution of half width [25] Ω (see section 1.7). We thus have to discretize the distribution. One of the best choices is to gather spins of similar offsets into spins of higher dimensions. This approach is based on the Dicke state formalism where N identical spins $1/2$ are gathered into a single $N/2$ spin (see section 1.4.2). Therefore, the dynamics is reduced to a subspace of dimension $N+1$ instead of 2^N. Then, we consider an ensemble of "*Dicke spin*" with different offset frequencies. The resulting size of the Hilbert subspace is finally: $\mathrm{Dim}(\mathcal{H}) = \prod_i^{N_{bins}}(N_i+1)$. It remains to choose the best arrangement (number of bins, and number of spins per bins) that reproduces qualitatively the behavior of the system under study. In this manuscript, the discretization step Δ_D is chosen constant, with an odd number of bins. Then, we parametrize the distribution by a set $\rho_0 := \{\Delta_D, \{N_1, N_2, ..., N_f\}\}$. The median bin is always associated with the offset 0. On both sides of this bin, we have respectively the offsets $-\Delta_D$ and $+\Delta_D$. The same rule is applied recursively on both sides. Figure 2.2 shows a possible approximation of a Gaussian ensemble.[26]

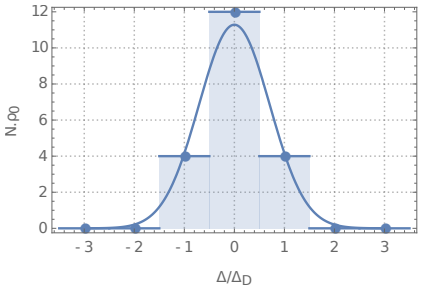

Figure 2.2: Example of discretization of a Gaussian ensemble for $N = 20$ spins. The discretization step is given by Δ_D. At each frequency of the discretized ensemble is associated a sub-ensemble parametrized by Dicke states. This discretized distribution is defined by: $\rho_0 := \{\Delta_D, \{4, 12, 4\}\}$.

[25] Depending on the context, the half width is the HWHM of the Lorentzian or the standard deviation of a Gaussian.

[26] Generally, Δ_D is of the same order of magnitude as Ω.

Plotting the energy density can help to design the spin ensemble. Such a graph can be produced quickly by first diagonalizing the Hamiltonian and then by computing the histogram of eigenvalues. Three examples of energy density are plotted in figure 2.3. They are computed with an ensemble of 13 spins but the respective sizes of the Hilbert space are: 8192, 128 and 14. This shows the importance of the discretization procedure: with the first case, it is difficult to perform a quick integration, but it is straightforward with the two other cases. Energy densities are plotted as a function of the number of photons. More precisely, we plot:

$$\rho_n(E) = \mathrm{hist}\left(\{E\} = \mathrm{spect}\left(\sum_m \Delta_{(m)}\hat{\sigma}_z^{(m)} + ng\hat{\sigma}_x^{(m)}\right)\right). \qquad (2.2)$$

This corresponds to the semi-classical Jaynes-Cummings Hamiltonian [27] when the cavity is filled with an average of n photons in

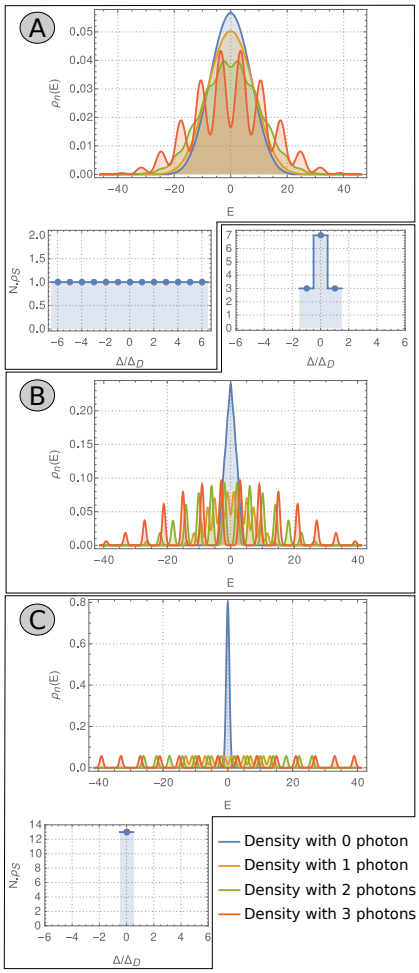

Figure 2.3: Energy density $\rho_n(E)$ and spin distribution $\rho_0(\omega)$ for 3 different systems. We have used the parameters $\Delta_D = g = 1$. The energy density is plotted for different numbers of photons n (curves of different colors). This allows us to see the difference of structures between the ground state of the cavity and the first excited states. In each case, the ensemble is composed of 13 spins: (**A**) Uniform distribution of offsets, and $\dim\mathcal{H} = 8192$. (**C**) All spins have the same offset frequency, $\dim\mathcal{H} = 14$. (**B**) Intermediate case, $\dim\mathcal{H} = 128$.

[27] This Hamiltonian is used only during the computation of spectra presented in 2.3. It is not used during the integration of $\hat{\rho}$.

the quadrature $\hat{X} = \frac{1}{2}(\hat{a}^\dagger + \hat{a})$. We see in figure 2.3 that the effect of photons is to "spread" and to "discretize" the density. These distributions are similar to the ones encountered with spin baths [134]. On the opposite, the inhomogeneous broadening makes the density smoother, wider and it reduces the difference between the ground state and the first excited states.

Gathering spins with similar offsets into few ensembles allows us to describe simultaneously all physical effects with a reasonable numerical cost. The non-trivial point here is to find a good compromise between the Hamiltonian structure and the size of the Hilbert space. A case-by-case study is required to determine the best discretization. A fit with experimental data can validate the distribution sampling.

To conclude, the Hamiltonian of the discretized model used in the numerical integration is the following:

$$\hat{H}_{M1} = i(\beta\hat{a}^\dagger - \beta^*\hat{a}) + \sum_{i=1}^{N_{bins}} \frac{\Delta_i}{2}\hat{\sigma}_z^{(i)} + g(\hat{a}^\dagger\hat{\sigma}_-^{(i)} + \hat{a}\hat{\sigma}_+^{(i)}) \tag{2.3}$$

where $\hat{\sigma}_z^{(i)}, \hat{\sigma}_-^{(i)}, \hat{\sigma}_+^{(i)}$ are $\mathfrak{su}(2)$ generators in the spin $N_i/2$ representation, and $\hat{a}^\dagger, \hat{a}$ are expressed with matrices of finite dimension. The dimension of these matrices is given by a cutoff of the number of photons allowed in the simulation. This number is chosen sufficiently large to avoid numerical artifacts. Notice that for simplicity, we neglect the inhomogeneity in g with this model.

2.4 Second model: Continuous spin ensemble

2.4.1 Basic idea

Using Dicke states in a discretized model allows us to decrease the Hilbert space dimension, but the distribution sampling must be small to be advantageous. This could be a problem when the integration time is longer than the inverse of the discretization step. In order to overcome this difficulty, it is possible to describe the spin ensemble as a global system, which interacts with the electromagnetic field. More precisely, the idea is to describe the spin ensemble by an effective field.

First of all, we notice that in the NMR framework, the density matrix of a spin ensemble can be given by:

$$\hat{\rho} = \sum_{n=1}^{N} c_n \mathbb{I} \otimes ... \otimes \hat{\rho}_n \otimes ... \otimes \mathbb{I}. \tag{2.4}$$

This form of the density matrix is valid in the semi-classical regime: when the correlation between observables of different spin is negligible: $\langle\hat{\sigma}_a^{(n)}\hat{\sigma}_b^{(m)}\rangle = \langle\hat{\sigma}_a^{(n)}\rangle\langle\hat{\sigma}_b^{(m)}\rangle$, $n \neq m$.

Therefore, in the case $N \to \infty$, we can use a function $\psi(\Delta) : \mathbb{R} \to \mathbb{C}^2$ to describe the state of the ensemble as a function of the offset parameter. Different spins with the same offset have the same state because their initial state are the same and they interact similarly with their environment. We restrict the study to offset distributions and we neglect the g-distribution. However the method can be generalized without technical difficulty if $\rho(g, \Delta) = \rho_0(\Delta)\rho_1(g)$.

The function ψ is therefore a field over the space of offset, and the idea is to replace the spin ensemble by this field. It is coupled to the cavity in a second step. Unfortunately ψ is unbounded and we cannot use it to define a Hilbert space, but the function:

$$|q\rangle = \sqrt{\rho(\Delta)}|\psi(\Delta)\rangle, \tag{2.5}$$

has all the desired properties since $\int d\Delta \langle q|q\rangle = 1$. The ensemble is classical, and the mean value of an operator is given by the integration over the measure ρ:

$$\langle \hat{A} \rangle = \int d\Delta \rho(\Delta) \langle \psi(\Delta)|\hat{A}(\Delta)|\psi(\Delta)\rangle. \tag{2.6}$$

This definition coincides with the mean value of a local operator $\hat{A} = \bigotimes_n \hat{A}_n$, such that $\langle \hat{A} \rangle = \sum_n c_n Tr[\hat{\rho}_n \hat{A}_n]$. The field q can be assimilated to a wave function. It is analogous to the Dirac field that describes the wave function of electrons and positrons.

"First quantization" A quantum representation is expressed by expanding the wave function over orthogonal modes defined by the measure ρ. For example, we can use Hermite or Lengendre polynomials. Such an expansion allows us in a second step to express the Hamiltonian with operators acting on these modes (polynomials).

For a Gaussian distribution of spins, we obtain:

$$\begin{aligned} |q(\Delta, t)\rangle &= \sum_{A,n} q_{A,n}(t)|A, n(\Delta)\rangle \\ &= \sum_{A,n} q_{A,n}(t)|A\rangle \otimes \left| \frac{e^{-\Delta^2/4\Omega^2}}{\sqrt{\pi 2^n n!}} H_n\left(\frac{\Delta}{\sqrt{2}\Omega}\right) \right\rangle. \end{aligned} \tag{2.7}$$

The general form of the Schrödinger equation is given by

$$\frac{d}{dt}|q(\Delta, t)\rangle = \frac{-i}{2}(B_x(t)\hat{\sigma}_x + B_y(t)\hat{\sigma}_y + \Delta\hat{\sigma}_z)|q(\Delta, t)\rangle, \tag{2.8}$$

where B_x and B_y are magnetic fields, which are replaced by field operators when the system is coupled with the cavity. The variable Δ acts as an operator on the function q. In order to remove any dependence on this variable in the equation, it is expressed as a function of creation/annihilation operators on Hermit polynomials: $\Delta \to (\hat{b}^\dagger + \hat{b})/\sqrt{2}$, with

$$\hat{b}^\dagger|n\rangle = \sqrt{n+1}|n\rangle \ , \ \hat{b}|n\rangle = \sqrt{n}|n-1\rangle.$$

Notice that $\hat{b}^\dagger, \hat{b}$ operators are different than usual creation/annihilation operators $\hat{a}, \hat{a}^\dagger$ in quantum optics, which are "inner" in a mode: they destroy/create excitations in a specific mode, while $\hat{b}, \hat{b}^\dagger$ move the excitation to adjacent modes. In this theory, $\hat{a}, \hat{a}^\dagger$ are rather replaced by Pauli matrices.

Finally, we arrive at the following Hamiltonian:

$$\hat{H} = \frac{1}{2}\left(B_x(t)\hat{\sigma}_x \otimes \mathbb{I} + B_y(t)\hat{\sigma}_y \otimes \mathbb{I} + \Omega\hat{\sigma}_z \otimes (\hat{b}^\dagger + \hat{b})\right). \tag{2.9}$$

In the first quantization picture, the continuous ensemble is thus a single spin coupled to a harmonic oscillator of frequency 0 (due to the RWA, it does not contribute to the total energy). From the opposite point of view, the ensemble can be seen as a "*boson field with a spinor polarization*".

The quantum number of the boson field can be physically interpreted as a disorder parameter that characterizes the inhomogeneity of the ensemble. Whereby, the boson field is called *the disorder field*.

This system is exactly equivalent to a semi-classical system, it is in one to one mapping with the initial system. From a numerical point of view, we can simulate this system by integrating (2.8), for several values of Δ. we thus have to simulate N_{bins} Schrödinger equation. Otherwise, we can integrate the system using (2.9), and truncate the Hilbert space at an order sufficiently large. The advantage of the second representation is that we can couple the system to a cavity. This step is straightforward, we just have to replace operators in $\hat{\sigma}_x$ and $\hat{\sigma}_y$ by the Jaynes-Cummings interaction:

$$\hat{H}_{M2} = i(\beta\hat{a}^\dagger - \beta^*\hat{a}) + \frac{\Omega}{2}\hat{\sigma}_z(\hat{b}^\dagger + \hat{b}) + g(\hat{a}^\dagger\hat{\sigma}_- + \hat{a}\hat{\sigma}_+) \tag{2.10}$$

This model has the advantage to use a smaller Hilbert space than the discretized model, because we can truncate the system at a relatively small dimension. It is also more accurate than just a semi-classical model because it can describe the Purcell effect, in a full-quantum way, even in the good cavity regime (see section 2.7.1). However, this model cannot describe coherent effects as well as the discretized one. Nevertheless, numerical simulations have shown that spins with a large difference of offset are weakly correlated, and only the number of coherent spins at resonance is a dominant factor (upper bound on the number of coherent spins). Therefore, we can replace the spin $1/2$ of the effective field by a $N_D/2$-spin in order to recover coherent effects. By construction, the models 1 and 2 are equivalent when $\Omega \to 0$ and N_D is the total number of spins. Furthermore, in the bad cavity limit, it is equivalent to the semi-classical model when $N_D = 1$. Further comparison details are given in section 2.7.

Second quantization We can continue the analogy with the Dirac equation by doing a second quantization. [48, 11, 10]. The state of the system can be described with a Fock-space of the classical field q, and observable quantities become operators on this space. *This step is not strictly compulsory for the numerical point of view, because the Hamiltonian conserves the number of excitation (there is always a "single particle" in the system: the spin ensemble that interacts with the cavity), and in all applications, we are restricted to a case where the two approaches are equivalent.* However the second quantization is very interesting from the physical point of view, because it puts on the same level the spin system and the electromagnetic field.

Quantization with other distributions

The formalism of continuous spin ensemble is not restricted to Gaussian distributions. Many other distributions can be used to improve the agreement with an experiment. For example, it is possible to use uniform distributions. In this case, Legendre polynomials are used and creation/annihilation operators are defined such as [108]:

$$\hat{a}^\dagger|k\rangle = \frac{k+1}{\sqrt{(2k+1)(2k+3)}}|k+1\rangle \tag{2.11}$$

$$\hat{a}|k\rangle = \frac{k}{\sqrt{(2k-1)(2k+1)}}|k-1\rangle. \tag{2.12}$$

Another possibility is to use q-deformed Gaussian distributions (used in spectroscopy or cold atoms). This leads to a wave function decomposition in terms of q-Hermite polynomials. In this case creation/annihilation operators must satisfy a commutation constraint of the form:

$$\hat{a}\hat{a}^\dagger - q\hat{a}^\dagger\hat{a} = \hat{\mathbb{I}}. \tag{2.13}$$

However, caution must be taken in the definition of these operators. We do not discuss such details here, and we refer the interested reader to the literature [100, 76, 126].

2.4.2 The number of spins

Since continuous ensembles are defined with a probability measure, we must define the number of spins N as another input. Two nonequivalent choices are possible:

- The first and the easiest choice consists of artificially multiplying the norm of the wave function by N. This induces a rescaling of the amplitude of physical observables, like in a semi-classical model.
- The second choice consists of choosing a space $\mathcal{H}$ spanned by a Dicke state of N spins.

The difference of behaviors can be understood by plotting the energy density (see figure 2.4). We see that the use of spins with higher order induced "peaks" in the spectrum which are similar to the ones encounter with true quantum ensembles.

Notice that transforming a discrete ensemble of many spins into a continuous ensemble is not trivial at all, and the parameters Ω, N_ρ, N_D are correlated (see section 2.7). Moreover, some configurations could be non-physical.

In practice, the two approaches are mixed together. Alike discretized distributions, a compact notation is required in order to specify continuous spin distributions. We adopt the following notation: $\rho_0 := \{\Omega, N_\rho, N_D\}$, where N_ρ is the trace of the density matrix and N_D the number of spins in a Dicke state.

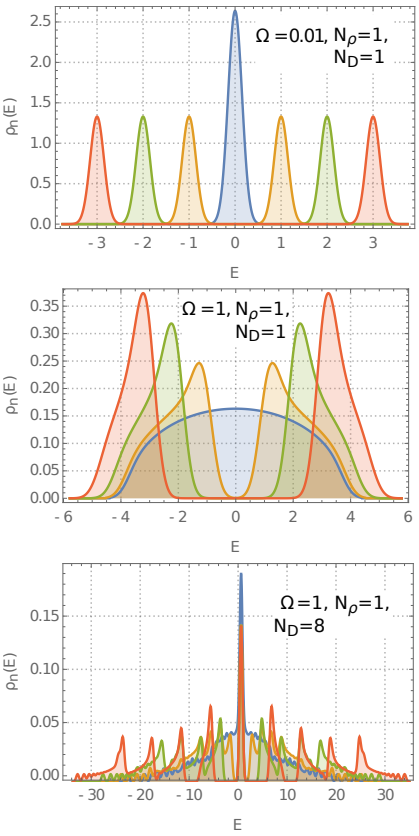

Figure 2.4: Energy density $\rho_n(E)$ for effective spin ensemble with different bandwidths. The first 2 cases have been computed with spin 1/2 as basic entities of the ensemble. The last one corresponds to a spin 8/2, i.e. an ensemble of 8 spins. For a spin 1/2 coupled to a disorder field with 61 modes, $dim\mathcal{H} = 122$. Notice that small oscillations come from the discretization of the histogram.

2.5 Partial Trace

In the representations described above, there is no explicit dependence on single spin states. However, in the context of non-Markovian dynamics, it is necessary to trace out all degrees of freedom constituing a bath. This section presents how trace operations [31] are performed on the two models.

2.5.1 Dicke state

In order to recover a single spin state from a Dicke state, we need to introduce its expression as a function of symmetrized spin states (see section 1.4.2). We recall:

$$\begin{aligned} |\frac{N}{2},m\rangle &= \sqrt{\frac{(N/2+m)!(N/2-m)!}{N!}} \sum_P |\underbrace{\uparrow,...,\uparrow}_{N/2+m},\underbrace{\downarrow,...,\downarrow}_{N/2-m}\rangle \\ &= c_m \sum_P |\underbrace{\uparrow,...,\uparrow}_{N/2+m},\underbrace{\downarrow,...,\downarrow}_{N/2-m}\rangle \end{aligned}, \tag{2.14}$$

where $\sum_P$ means "sum over all possible permutations". With this definition, the density matrix of Dicke states can be expressed as:

$$\hat{\rho} = \sum_{m,n} c_n c_m \rho_{mn} \sum_{P_m}\sum_{P_n} |\underbrace{\uparrow,...,\uparrow}_{N/2+m},\underbrace{\downarrow,...,\downarrow}_{N/2-m}\rangle\langle\underbrace{\uparrow,...,\uparrow}_{N/2+n},\underbrace{\downarrow,...,\downarrow}_{N/2-n}|. \tag{2.15}$$

The density matrix of a single spin is determined by computing $\langle\uparrow|\hat{\rho}|\uparrow\rangle$, $\langle\uparrow|\hat{\rho}|\downarrow\rangle$, $\langle\downarrow|\hat{\rho}|\uparrow\rangle$, $\langle\downarrow|\hat{\rho}|\downarrow\rangle$. Since spins are undistinguishable (due to the sum over permutations), we have the following relations:

$$\langle\uparrow|\sum_P |\underbrace{\uparrow,...,\uparrow}_{N/2+m},\underbrace{\downarrow,...,\downarrow}_{N/2-m}\rangle \propto N/2+m \tag{2.16}$$

$$\langle\downarrow|\sum_P |\underbrace{\uparrow,...,\uparrow}_{N/2+m},\underbrace{\downarrow,...,\downarrow}_{N/2-m}\rangle \propto N/2-m. \tag{2.17}$$

So we deduce:

$$\begin{aligned} \langle\uparrow|\hat{\rho}|\uparrow\rangle &\propto \sum_{m,n} c_n c_m \rho_{mn} (\frac{N}{2}+m)(\frac{N}{2}+n) \\ \langle\uparrow|\hat{\rho}|\downarrow\rangle &\propto \sum_{m,n} c_n c_m \rho_{mn} (\frac{N}{2}+m)(\frac{N}{2}-n) \\ \langle\downarrow|\hat{\rho}|\uparrow\rangle &\propto \sum_{m,n} c_n c_m \rho_{mn} (\frac{N}{2}-m)(\frac{N}{2}+n) \\ \langle\downarrow|\hat{\rho}|\downarrow\rangle &\propto \sum_{m,n} c_n c_m \rho_{mn} (\frac{N}{2}-m)(\frac{N}{2}-n). \end{aligned} \tag{2.18}$$

We use the relation $\propto$ because it depends on the Dicke state normalization. In practice, it is not useful to determine explicitly this factor since it is canceled by a normalization of the reduced density matrix $\hat{\rho} \to \hat{\rho}/Tr[\hat{\rho}]$.

2.5.2 Continuous ensemble

The notion of individual spin is less clear for continuous ensembles, therefore, the notion of trace must be defined carefully. Since two numbers N_D and N_ρ define the total number of spins, it is necessary to take them into account to derive single spin states. The underlying idea is to discretize the continuous ensemble, therefore we naturally focus on spins with a particular offset Δ_0. The question is how can we extract a quantum state from the continuous field at a specific point? This is done with a Dirac distribution. At a specific frequency, the number of spins is determined by a Dicke state (with N_D) and a re-normalization of the density matrix (with N_ρ). It is obvious that the normalization does not affect the state, so it is sufficient to extract the information from a Dicke state. This issue has been presented in the previous section. It remains to specify how the information for a particular offset can be extracted from the continuous state. For the sake of clarity, we present the evaluation of an observable mean value. Such a development can be extended straightforwardly to the density matrix formalism and partial trace operations. Suppose that we are interested in an observable $\hat{O}_{\Delta_0} \equiv \hat{O} \otimes \delta_{\Delta_0}(\Delta)$. For instance, this observable can be the magnetization in the x direction for a spin at resonance. Under the formalism presented in section 2.4.1, moments of this operator are calculated with usual quantum mechanical relations:

$$\begin{aligned}
\langle \hat{O}_{\Delta_0} \rangle &= \int d\Delta q^\dagger(\Delta) \left(\hat{O} \otimes \delta_{\Delta_0}(\Delta) \right) q(\Delta) \\
&= \sum_{A,n,m} q^*_{A,n} q_{A,m} \langle A|\hat{O}|A\rangle \int d\Delta \delta_{\Delta_0}(\Delta) \frac{e^{-\Delta^2/2\Omega^2}}{\pi\sqrt{2^n n! 2^m m!}} H_n\left(\frac{\Delta}{\sqrt{2}\Omega}\right) H_m\left(\frac{\Delta}{\sqrt{2}\Omega}\right) \\
&= \sum_{A,n,m} \frac{q^*_{A,n} q_{A,m} \langle A|\hat{O}|A\rangle e^{-\Delta_0^2/2\Omega^2}}{\pi\sqrt{2^n n! 2^m m!}} H_n\left(\frac{\Delta_0}{\sqrt{2}\Omega}\right) H_m\left(\frac{\Delta_0}{\sqrt{2}\Omega}\right).
\end{aligned} \tag{2.19}$$

2.6 Third model: Semi-classical approximation

The third model is derived from the semi-classical equations(1.60) (section 1.6) with additional terms:

$$\begin{aligned}
\frac{d}{dt}\langle \hat{X} \rangle &= -\frac{\kappa}{2}\langle \hat{X} \rangle + \omega_X - \sum_j 2 g_{(j)} \langle \hat{S}_y^{(j)} \rangle \\
\frac{d}{dt}\langle \hat{Y} \rangle &= -\frac{\kappa}{2}\langle \hat{Y} \rangle + \omega_Y + \sum_j 2 g_{(j)} \langle \hat{S}_x^{(j)} \rangle \\
\frac{d}{dt}\langle \hat{S}_x^{(j)} \rangle &= -\Gamma_2 \langle \hat{S}_x^{(j)} \rangle - \Delta_{(j)} \langle \hat{S}_y^{(j)} \rangle + g_{(j)} \langle \hat{Y} \hat{S}_z^{(j)} \rangle \\
\frac{d}{dt}\langle \hat{S}_y^{(j)} \rangle &= -\Gamma_2 + \langle \hat{S}_y^{(j)} \rangle \Delta_{(j)} \langle \hat{S}_x^{(j)} \rangle - g_{(j)} \langle \hat{X} \hat{S}_z^{(j)} \rangle \\
\frac{d}{dt}\langle \hat{S}_z^{(j)} \rangle &= -\Gamma_p (\langle \hat{S}_z^{(j)} \rangle + 1) + g_{(j)} \langle \hat{X} \hat{S}_y^{(j)} \rangle - g_{(j)} \langle \hat{Y} \hat{S}_x^{(j)} \rangle,
\end{aligned} \tag{2.20}$$

where $\Gamma_2 = 1/T_2$ is the rate associated with the transverse relaxation. Notice a sign difference with respect to the usual Bloch equation for the T_1 relaxation.

Contrary to standard NMR, the ground state is the south pole of the Bloch ball. It is not necessary to use N magnetization vectors to describe the ensemble, it can be described by a discretization of the spin distribution. At each discretization bin is associated a Bloch vector with a length corresponding to the number of spins in the bin. Contrary to other models, equations are non-linear. Then a RK4 algorithm is used for the numerical integration. From the numerical point of view, the way we encode numerically the semi-classical model is closer to the discretized ensemble, because the distribution is discretized in the same way. Then, we use the same notation as the model one to describe the spin ensemble. However, we also use sometime the notation of the model two. In this case, the distribution is a Gaussian with a very small discretization step, and $N_D/2$ is assimilated to the maximum amplitude of the Bloch vector [28].

[28] In the semi-classical model, N and N_D are related since N is given by the integral of the Bloch vector over the spin distribution. This is because there is no difference between coherent spins and other spins in the semi-classical model.

2.7 Numerical study

In order to compare the three models, two physical situations are revisited. The first one is the Purcell effect, which is studied from the point of view of a single spin. Therefore, we are able to underline spin-bath effects. With this point of view, it is also easy to show the convergence of quantum models (models 1 and 2) toward the semi-classical model (model 3). The second situation is the free induction decay. This situation is very important because it corresponds to the case where spins are emitting photons, and thus a measurable signal.

In the rest of this chapter, all the quantities are expressed in normalized units.

2.7.1 The Purcell effect of a spin ensemble

In this section, we study the Purcell relaxation of an excited spin ensemble (see section 1.5.2 for details on a single spin).

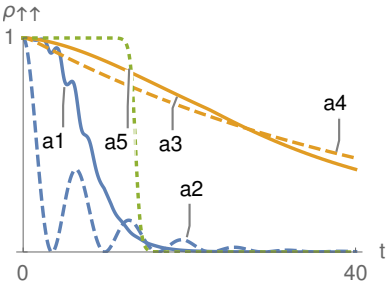

Figure 2.5: (Model 1) Blue: strong coupling, orange: weak coupling, solid lines: ensemble of 20 spins, dashed lines: 1 spin. Green dotted line: weak coupling with 20 spins at resonance.

Because of the large number of parameters, we propose a summary of the main results, completed by some particular examples of interest. For this study, we are interested in the trajectory of a single spin at resonance, and more particularly to the component $\hat{\rho}_{\uparrow\uparrow}(t)$ of its density matrix. This variable allows us to compare the results with the ones obtained with a single spin coupled to the cavity. However, single spin states are generally not defined in numerical simulations and specific procedures are required in order to trace out other degrees of freedom (section 2.5).

For the sake of simplicity, the ensemble of parameters (physical parameters, distribution data,...) used for calculations are included in table 2.1. Each curve enclosed in figures 2.5, 2.6, 2.7, 2.8, 2.9 has a label of the form "*letter* + *number*" (like "a1" or "f3") which refer to a line of table 2.1. All the parameters and data are contained in this table.

Model 1 (discretized ensemble): (see figure 2.5)

- Bad cavity (weak coupling): exponential decay (curves a3 and a4)
- Good cavity (strong coupling): Rabi oscillations (curves a1 and a2).
- The cooperativity C plays an important role: for a small cooperativity in the strong coupling regime (i.e. $\Omega \to 0, g \gg \kappa$), the relaxation approximates a step function (curve a5), and for large Ω the effect becomes smoother and closer to an exponential (curve a3).

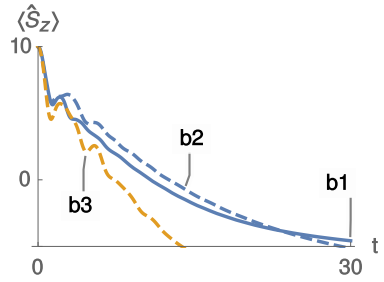

Figure 2.6: (Model 1 v.s. Model 2) Solid line: discretized distribution ($\Delta_D = 5$), blue dashed line: continuous ensemble with $\Omega = 2.5$ and orange dashed line with $\Omega = 0$.

Model 2 v.s. Model 1 (continuous and discretized ensembles): (see figure 2.6)

The two models have similar behaviors, except that:

- The spin-spin entanglement is underestimated in model 2, then Ω does not influence the Purcell relaxation. However, it has an effect on the global magnetization (curves b2, b3).
- Qualitative agreement for the average magnetization when distributions are similar (curves b1,b2,b3).
- The two models are equivalent when $\Omega \to 0$.

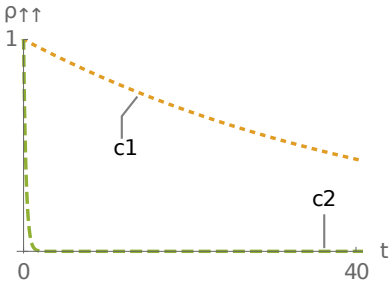

Figure 2.7: (Model 3) c1: weak coupling regime, c2: strong coupling regime.

Model 3 (semi-classical): (see figure 2.7)

The decay is always exponential, due to the introduction of a T_1 effect in the Bloch equation. Without photons in the cavity, the evolution of the spins is free and no Rabi-oscillation can be observed.

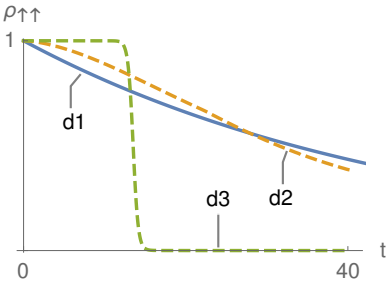

Figure 2.8: (Model 1 v.s. Model 3) solid line: Semi-classical model, dashed line: quantum model. Orange curve: low cooperativity, green: high cooperativity.

Quantum models v.s. Semi-classical model: (see figures 2.8 and 2.9)

- Good agreement in the low cooperativity limit (curves d1/d2, and f2/f5)
- Otherwise, trajectories are different because the semi-classical model does not take into account Rabi-oscilations and non Markovian effects (curves d1/d3, and f1/f3/f4).
- Models 2 and 3 are equivalent for $N_D = 1$ and $\kappa \gg g$.

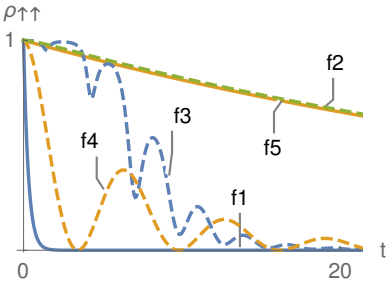

Figure 2.9: (Model 2 v.s. Model 3) solid lines: semi-classical model, dashed lines: quantum continuous ensembles with different N_D and different coupling regimes.

Summary

The inhomogeneous ensemble has an important impact on the relaxation of a single spin. *In the strong coupling regime we observe an important modification of non-Markovian effect* (curves a1,a4,f3) and one can use the model 1 for the study of realistic non-Markovian systems. On the other side, we have explicitly shown that *quantum models converge toward the semi-classical theory in the low cooperativity limit* (curves d1,d2,f5,f2). *Finally, one can underline the ability of the model 2 to reproduce dynamics similar to the ones of model 1.* However, during a simple Purcell relaxation, the model 2 describes only the entanglement of spins with the same offset. It results that non-Markovian effects can be underestimated. By playing with Ω and N_D, we can define an effective model, which reproduces qualitatively the model 1 (curves b1 and b2). Additionally, the model 2 requires generally a smaller Hilbert space dimension than the model 1 (for example, $\dim\mathcal{H}$=396 for the curve b1 and $\dim\mathcal{H}$=144 for the curves b2 and b3). Then, the model 2 seems promising for the study of systems in the intermediate regime ($C \approx 1$).

The results presented here follow qualitatively other results obtained with spin bath theory. Two approaches are usually employed in this field. The first one uses the cumulant expansion approximation [6, 178, 180], therefore, there is no fundamental difference with the semi-classical model. The second one is more general and uses path integrals for computing correlation functions [111, 147]. In all these references, the systems are slightly different: spins interact with each other through a Heisenberg coupling, while in this manuscript, they interact only through the electromagnetic field. Therefore, we do not expect to reproduce exactly the same results. However, we recover the initial coherence, followed by a quick relaxation of the spin ensemble.

As far as we know, this study is one of the first analyses in which the Purcell effect for an inhomogeneous ensemble is computed without a semi-classical approximation, in all parameter regimes.

Label	Type	model	ρ_0	g	κ	$n_{photon}(t=0)$
a1,b1,e3	Quantum	1	$\{5,\{5,10,5\}\}$	0.5	0.3	0.00001
a2	Quantum	1	$\{0,\{1\}\}$	0.5	0.3	0.00001
a3,d2	Quantum	1	$\{5,\{5,10,5\}\}$	0.125	3	0.00001
a4	Quantum	1	$\{0,\{1\}\}$	0.125	3	0.00001
a5	Quantum	1	$\{0,\{20\}\}$	0.125	3	0.00001
b2	Quantum	2	$\{2.5,20/8,8\}$	0.5	0.3	0.00001
b3	Quantum	2	$\{0,20/8,8\}$	0.5	0.3	0.00001
c1	Classical	3	$\{5,\{5,10,5\}\}$	0.125	3	0.00001
c2	Classical	3	Lorentzian, 801 bins	0.5	0.3	0
d1	Classical	3	$\{5,\{5,10,5\}\}$	0.125	3	0
d3	Quantum	1	$\{0,\{20\}\}$	0.125	3	0.00001
f1	Classical	3	$\{0,\{1\}\}$	0.5	0.3	0
f2	Classical	3	$\{0,\{1\}\}$	0.125	3	0
f3	Quantum	2	$\{1,1,8\}$	0.5	0.3	0.00001
f4	Quantum	2	$\{1,1,1\}$	0.5	0.3	0.00001
f3	Quantum	2	$\{1,1,1\}$	0.125	3	0.00001

Table 2.1 – List of parameters for labeled curves in figures 2.5,2.6,2.7,2.8,2.9. The initial state of the cavity for the quantum models is given by a coherent state of small amplitude (n_{photon}), but different from 0, in order to define correctly matrices M and r (used by the low rank algorithm).

2.7.2 Free Induction Decay

We are now interested in the coherence loss of a spin ensemble prepared in the Bloch sphere equator. This effect comes from the inhomogneous broadening and it is usually observed in NMR with a quick decrease of the magnetization. This evolution is qualified as: "Free Induction Decay". In NMR, the offset distribution determines entirely the evolution of the average magnetization (which is given by the Fourier transform of the distribution). When the spin ensemble is coupled to a cavity, the coherence with the radiation field is long enough for inducing a radiation damping effect, or super-radiance effect [75, 69]. For a spin ensemble prepared in the $-y$ direction, and if the Purcell relaxation is neglected during the decay, one can deduce from the semi-classical model the following evolution operator (see section 4.1.2 for further details):

$$\hat{U}_{SC}^{(n)}(t) = \exp\left(-ig\left(\int_0^t X(t')dt'\right)\hat{\sigma}_x^{(n)} + i\frac{\Delta_{(n)}}{2}\hat{\sigma}_z^{(n)}\right).$$

The field back action to the spin ensemble is thus a unitary transformation. However this back action takes the form of a T_1 relaxation in the case of the Purcell effect. Therefore, we expect that the process is composed of both a unitary and a relaxation transformation. The question is then to determine the proportion of unitary/non-unitary transformations. In order to answer this question, we consider the Bloch vector norm $R(t)$ of a single spin at resonance (The initial radius is set to 1). This is a direct measure of the degree of non-unitarity. Additionally, the angle $\phi = \arccos(\langle\hat{\sigma}_y(t)\rangle/R(t))$ gives the closest angle of rotation associated with a unitary transformation. Other quantities of interest are, the average magnetization $\langle\hat{S}_x\rangle$, $\langle\hat{S}_z\rangle$ and the mean value of the quadrature $\langle\hat{X}\rangle$, which is the simplest measurable quantity in experiments.

First we consider only the models 2 and 3. In the study of the Purcell effect, the T_2 relaxation does not play a role, but here it is necessary to specify its value. Following [31](p. 149) we used $T_2 = \Gamma_p/2$. The graphs showing the model comparison for three different situations are given in figure 2.12. All simulation parameters are presented in table 2.2.

As we can see, in the *low cooperativity regime, the classical and the quantum model predict exactly the same evolution of observable mean values*, thus the two models are not distinguishable from the experimental point of view. *Interestingly, despite the agreement between mean values, we have clearly different mechanisms of transformations*. The emission of photons follows the spin relaxation for the quantum model, while the semi-classical model uses mostly unitary transformations. For the strong coupling/high cooperativity regime, the semi-classical model is qualitatively similar to the quantum one, but it clearly underestimates the amplitude of Rabi-oscillations [119] and the steady-state is different. *By increasing the number of coherent spins (increase of N_D), we recover another semi-classical limit: the large spin limit*. This takes the form of a better agreement between R and ϕ, which means that single spin transformations are more unitary. The convergence is presented in figure 2.11.

We propose the following interpretation: classically ($J \to \infty$), the phenomenon is unitary, but here, we consider spins 1/2 with a state space of small dimension. Then, the non-unitary dynamics can be interpreted as a kind of "projection" of the unitary dynamics to a space of smaller dimension. The projection process is induced by cavity losses, which produce a statistical superposition of states. The convergence is observed numerically, and further analytic studies should clarify this point.

Finally, a FID produced with the model 1 is considered. Due to the low distribution sampling, the relevance of the simulation can be very contrasted: It fails to describe accurately the decay in the low cooperativity regime. But, in the high cooperativity

regime, the echo is dominated by Rabi-oscillations [119], as the ones in subfigures (B) and (C) of 2.12. In this case, the agreement quantum theory/semi-classical theory is comparable to the agreement observed with the model 2. As an example, figure 2.10 shows Rabi-oscillations predicted by the models 1 and 3. The parameters used in the simulations are $\rho_0 = \{5, \{5, 10, 5\}\}$, $g = 0.5$, $\kappa = 0.1$ and $n_{photon}(t = 0) = 0.00001$.

Label	Type	model	ρ_0	g	κ	$n_{photon}(t = 0)$
A	Quantum	2	$\{1, 1, 1\}$	0.05	2	0.00001
A	Classical	3	$\{1, 1, 1\}$	0.05	2	0
B	Quantum	2	$\{1, 1, 1\}$	3	0.3	0.00001
B	Classical	3	$\{1, 1, 1\}$	3	0.3	0
C	Quantum	2	$\{1, 1, 6\}$	3	0.3	0.00001
C	Classical	3	$\{1, 1, 6\}$	3	0.3	0

Table 2.2 – List of parameters for the curves in figure 2.12. The initial number of photons for the quantum models is chosen small but different from 0, in order to define correctly the matrices M and r used by the low rank algorithm.. Notice that the distribution used in semi-classical computations is a discretized Gaussian with 401 bins.

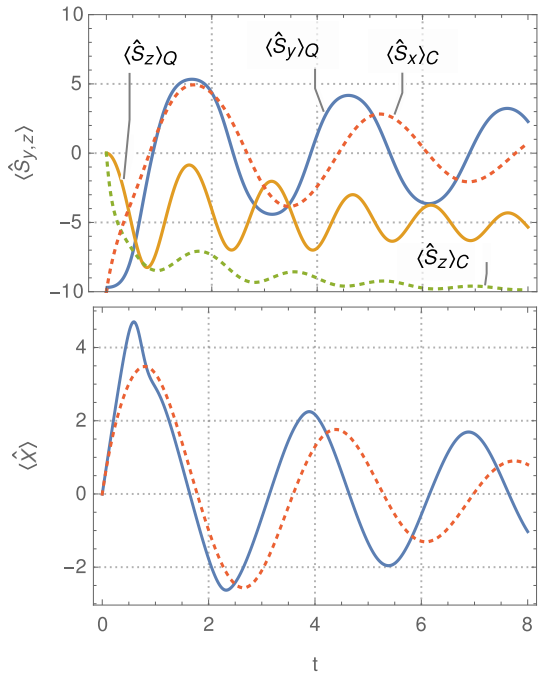

Figure 2.10 – Free induction decay (dominated by Rabi-oscillations) predicted by the models 1 and 3. Solid lines are associated to the model 1 and dashed line to the model 3.

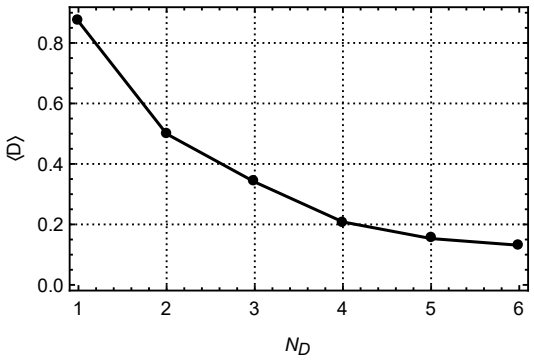

Figure 2.11 – Convergence of the quantum dynamics toward the classical dynamics. The measure $\langle D \rangle$ is defined by: $\langle D \rangle = \left(\frac{1}{T} \int_0^T |R_Q - R_C|^2 + |\phi_Q - \phi_C|^2 dt \right)^{1/2}$

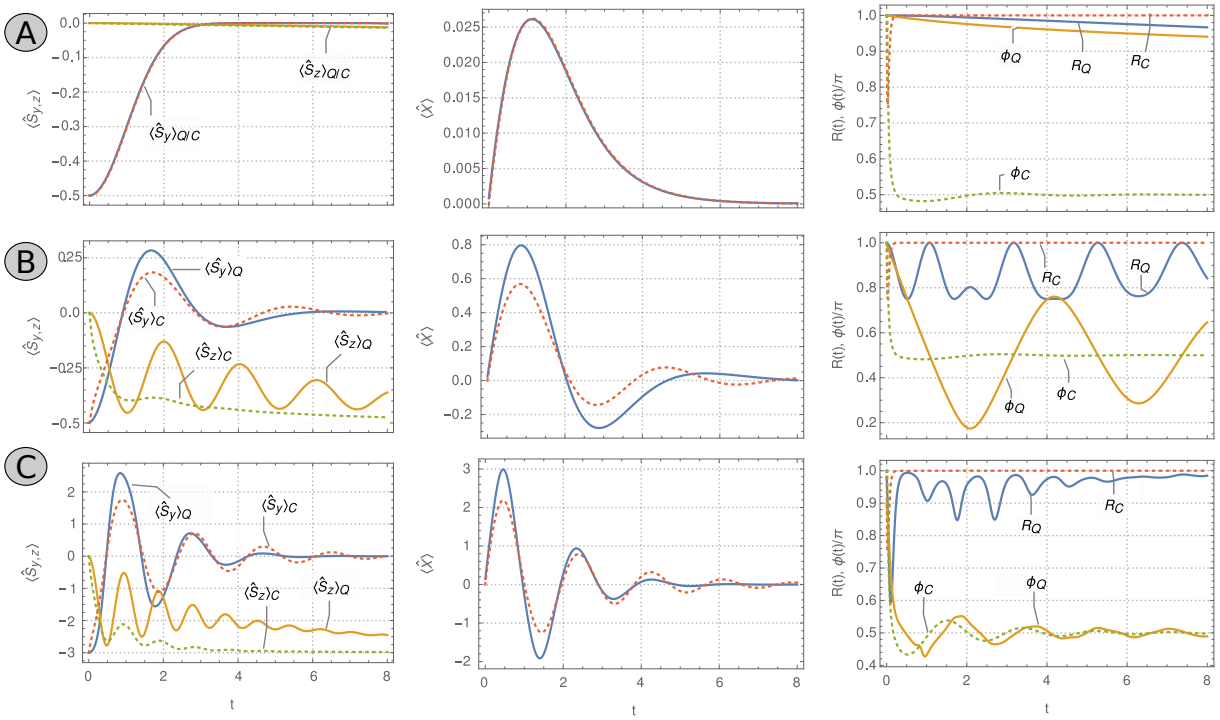

Figure 2.12 – Comparison between the models 2 and 3 for a free induction decay. Solid lines are associated to the model 2 and dashed line to the model 3. (**A**) Low cooperativity regime, (**B**) strong cooperativity regime with $N_D = 1$, (**C**) strong cooperativity regime with $N_D = 6$.

2.8 Conclusion

Simulating the full-master equation which characterizes a spin ensemble coupled to a cavity is a difficult task and several strategies have been used for that purpose. Two quantum models have been proposed, and their dynamics have been integrated with a low-rank algorithm.

The first model is based on a discretization of the spin distribution while the second uses a continuum of non-interacting spins. The two models describe the collective effects and the Purcell relaxation at the quantum level. Moreover, they both converge toward the semi-classical model (third model) in the weak coupling regime.

In order to compare the models and to provide a better understanding of dynamic effects, we performed simulations of the Purcell relaxation and the Free Induction Decay. This allowed us to emphasis that continuous spin ensemble (model 2) can underestimate non-Markovian effects during relaxation and discretized distributions (model 1) can suffer from a bad sampling effects in FID simulations. Finally, the role of the spin back action during a FID is discussed. Under the semi-classical approximation, this is a purely unitary effect (relaxation on the Bloch sphere) while it is non-unitary in quantum models (like the Purcell relaxation). The models converge to each other in the high spin limit ($J \to \infty$), and this reinforces the analogy radiation damping/super-radiance. Therefore, the relaxation can be viewed as the projection of a unitary transformation on a space of lower dimension.

In order to highlight the connections between the different regimes and the domains of applications of the three approaches, a summary is proposed in figure 2.13.

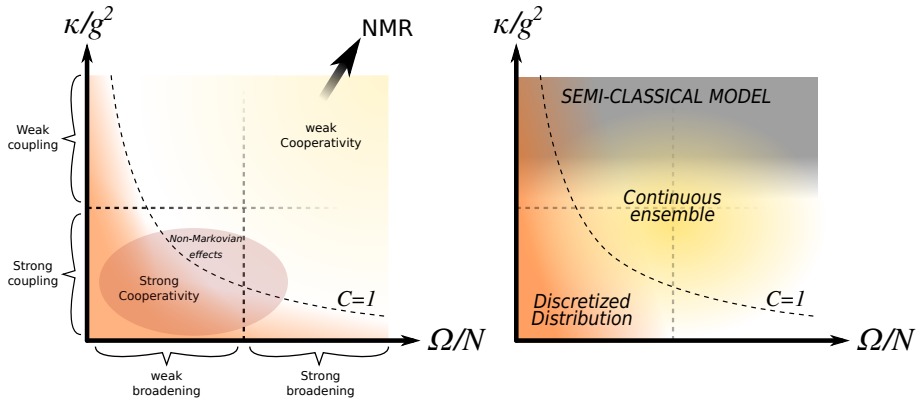

Figure 2.13 – *Left* - Different regimes: weak/strong coupling or equivalently bad/good cavity, and the weak/strong broadening. *Right* - Domains of application of the three models studied in this chapter.

The preliminary steps of the optimal control of an inhomogeneous spin ensemble coupled to a cavity have been solved in this chapter (numerical integration, characterization of the main physical effects). The next chapter focuses on the application of optimal control theory to this system.

Chapter 3

Control of an inhomogeneous spin ensemble

In chapter 1, we have introduced the model system and we have made the connection to the standard NMR dynamics. In chapter 2 we have shown how efficient simulations of the system can be performed in the different regimes. We focus in this chapter on the control of the spin ensemble. After a short introduction to state-of-the-art pulses (section 3.1), a general method is presented for the calculation of control fields. The purpose is to reformulate the control problem to get a simple description of the dynamics (sections 3.2). In a second step, generalized non-linear functions are used to compute approximate solutions of the master equation (section 3.3). The next step is the pulse design with numerical optimal control techniques to enhance the process fidelity in regimes where previous approximations fail. Several pulses are computed in the strong coupling and the weak coupling regimes (section 3.4). Finally, several situations are studied numerically, and a short presentation of the experimental realization of bump pulses is made (section 3.5).

3.1 State of the art pulses

State-of-the-art pulses correspond to the well-known square pulses used in NMR [21, 101], characterized by the function $\beta(t) = Ae^{i\omega t}\mathbb{I}_{[t_1,t_2]}(t)$. The exponential is used to account for the rotating frame, A is the amplitude, and t_1, t_2 are respectively the initial and the final times of the pulse. In NMR, these pulses are widely used and they are the basic building blocks of composite pulses [101, 35]. In cavity-QED, the efficiency of square pulses are very limited, due to the cavity transfer function. The shape of the pulse influences the spin dynamics as well as its duration and its energy. The deformation of the pulse is illustrated in figure 3.1. If we assume the pulse short enough so that a Dirac pulse is realized, then, according to equation (1.45), the field amplitude evolves as:

$$X(t) = Ae^{-\kappa t/2} \tag{3.1}$$

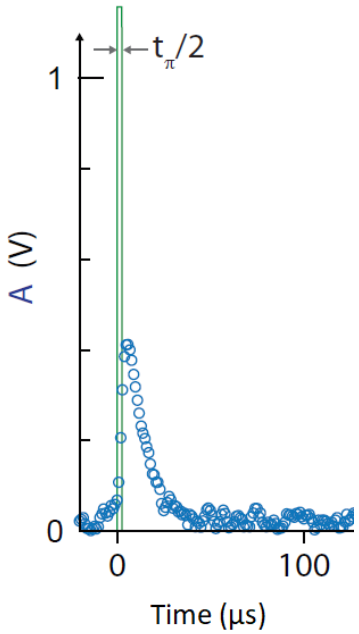

Figure 3.1: An example of square pulse used in recent experiments [21]. The green curve is the pulse input inside the resonator. The blue dots give the amplitude of the measured electromagnetic field.

Therefore, spins experience a pulse with an exponential form, and its duration is fixed by the cavity damping rate. In the next paragraphs, it is shown how the cavity effect can be removed, and how pulses can be efficiently shaped.

3.2 General method

3.2.1 Solution of the Schrödinger equation

In section 1.3.2, the dynamics of a driven quantum electromagnetic field in a non-perfect cavity is solved. The Lindblad equation is integrated using Lie-group methods and simple expressions are given in terms of coherent states. The coupling with a spin ensemble brings more complexity and numerical calculations are generally required[29]. Moreover, in standard NMR, without cavity, it is generally impossible to integrate analytically the Schrödinger equation for an arbitrary control field. Under some assumptions, we can recover state-of-the-art NMR control problem, and approximated solutions can be computed analytically.

Here, we propose an original procedure to tackle the problem. The goal is to provide a simple form of the evolution operator $\hat{U}$. The idea is to separate the evolution operator into products of simple operations. *This approach allows us to introduce the semi-classical dynamics in the evolution operator. Hence, in a second step, we can apply a "de-quantization procedure", similar to the Born-Oppenheimer approximation [159].*

[29] Notice that some attempts of analytic computations of the Lindblad equation have been made using path integrals [156] or group homomorphisms [58, 59]

General framework

The core of the computation lies on the intermediate representation theorem 13 (Appendix C), which is briefly recalled:

$$\hat{U}[\hat{A}+\hat{B}] = \hat{U}\left[\hat{A}\right].\hat{U}\left[\hat{U}[\hat{A}]^{-1}.\hat{B}.\hat{U}[\hat{A}]\right],$$

where the notation $\hat{U}[\hat{A}] = \mathbb{T}e^{\int_0^t \hat{A}(t')dt'}$ is used. This theorem tells us that one can decompose the time-ordered exponential of the sum of two Hamiltonians into the product of two time-ordered exponentials[30]. Notice that $\hat{B}$ is put in the interaction picture. The symmetry group of the electromagnetic field being abelian, one can expect simple commutation properties, and thus a simple final result.

[30] Another interesting point of view is the following: the operator $\hat{A}(t)$ describes a continuous gauge transformation and the theorem only expresses the gauge transformation of $\hat{B}(t)$ over time.

Decomposition of the evolution operator

In order to write complete, but "simple" equations, the spin-boson Hamiltonian is used in a first step[31]. The result for the Jaynes Cummings model is given in a second step, and multi-photon processes are briefly mentioned. Additionally, calculations are written for a single spin. The generalization to a spin ensemble is

[31] Since we do not diagonalize the Hamiltonian, it is faster to work with the spin-boson model. Indeed, commutation relations between Hamiltonian elements are shorter to write.

straightforward. The spin-boson Hamiltonian is:

$$\hat{H}_{SB} = \underbrace{\omega\hat{N} + i(\beta(t)\hat{a}^\dagger - \beta^*(t)\hat{a})}_{\hat{H}_F} + \underbrace{\frac{\omega_S}{2}\hat{\sigma}_x}_{\hat{H}_x} + \underbrace{g\hat{\sigma}_z}_{\hat{H}_z}(\hat{a}^\dagger + \hat{a}). \tag{3.2}$$

First, we extract the evolution of the electromagnetic field alone since its dynamics is perfectly known (proposition 1). A first use of the intermediate representation theorem on $\hat{U}(t) = \mathbb{T}e^{-i\int_0^t H(t')dt'}$ leads to:

$$\begin{aligned}\hat{U}(t) &= \hat{U}_F(t).\mathbb{T}\exp\left(-i\int_0^t \hat{U}_F^{-1}(t')\left[\hat{H}_z(\hat{a}^\dagger + \hat{a}) + \hat{H}_x\right]\hat{U}_F(t')dt'\right) \\ &= \hat{U}_F(t).\mathbb{T}\exp\left(-i\int_0^t \left[\hat{H}_z.\hat{U}_F^{-1}(t')(\hat{a}^\dagger + \hat{a})\hat{U}_F(t') + \hat{H}_x\right]dt'\right),\end{aligned} \tag{3.3}$$

where we use:

$$\hat{U}_F(t) = \mathbb{T}e^{-i\int_0^t \hat{H}_F(t')dt'}.$$

Using the non-Abelian Riemann Integral and a first order splitting, $\hat{U}_F$ is decomposed as[32]:

$$\hat{U}_F(t) = \lim_{N_k\to\infty} \mathbb{T}\prod_{k=1}^{N_k} e^{\gamma_k\hat{N}}.e^{\beta_k\hat{a}^\dagger - \beta_k^*\hat{a}}, \tag{3.4}$$

[32] Details are given in section 1.3.2.

with $\gamma_k = -i\omega\delta t_k$, $\beta_k = \beta(t_k).\delta t_k$ and $\sum_k^{N_k}\delta t_k = t$. The problem is then to determine:

$$\hat{U}_F^{-1}(t')(\hat{a}^\dagger + \hat{a})\hat{U}_F(t'). \tag{3.5}$$

For that purpose, we use the canonical commutation relation $[\hat{a}, \hat{a}^\dagger] = \hat{a}\hat{a}^\dagger - \hat{N} = \mathbb{I}$ and the decomposition of the displacement operator into a product of exponentials [131]

$$e^{\beta_k\hat{a}^\dagger - \beta_k^*\hat{a}} = e^{-|\beta_k|^2/2}.e^{\beta_k\hat{a}^\dagger}.e^{-\beta_k^*\hat{a}}$$

to determine the following commutation rules:

$$\begin{aligned} e^{-\beta_k^*\hat{a}}\hat{a}^\dagger &= \hat{a}^\dagger e^{-\beta_k^*\hat{a}} - \beta_k^* e^{-\beta_k^*\hat{a}} \\ e^{\beta_k\hat{a}^\dagger}\hat{a} &= \hat{a}e^{\beta_k\hat{a}^\dagger} - \beta_k e^{-\beta_k\hat{a}^\dagger} \\ e^{\gamma_k\hat{N}}\hat{a}^\dagger &= \hat{a}^\dagger e^{\gamma_k}e^{\gamma_k\hat{N}} \\ e^{\gamma_k\hat{N}}\hat{a} &= \hat{a}e^{-\gamma_k}e^{\gamma_k\hat{N}}. \end{aligned}$$

We have all the necessary building blocks for computing (3.5). We permute $(\hat{a}^\dagger + \hat{a})$ with $\hat{U}_F^{-1}$, and for a small time step, we have:

$$e^{-\gamma_k\hat{N}}.e^{-\beta_k\hat{a}^\dagger + \beta_k^*\hat{a}}(\hat{a}^\dagger + \hat{a}) = \left(\hat{a}^\dagger e^{-\gamma_k} + \hat{a}e^{\gamma_k} + \beta_k + \beta_k^*\right)e^{-\gamma_k\hat{N}}.e^{-\beta_k\hat{a}^\dagger + \beta_k^*\hat{a}}.$$

Then, after permuting the N_k terms and transforming the sums of γ_k and β_k in integrals, we obtain:

$$\hat{U}_F^{-1}(t')(\hat{a}^\dagger + \hat{a}.) = (\hat{a}^\dagger e^{i\omega t'} + \hat{a}e^{-i\omega t'} + \int_0^{t'} \left[\beta(t'')e^{i\omega(t'-t'')} + \beta^*(t'')e^{-i\omega(t'-t'')}\right] dt'')U_F^{-1}(t')' \tag{3.6}$$

We define $B(t') = \int_0^{t'} \left[\beta(t'')e^{i\omega(t'-t'')} + \beta^*(t'')e^{-i\omega(t'-t'')}\right] dt''$, and we insert equation (3.6) into (3.3). We arrive at:

$$\hat{U}(t) = \hat{U}_F(t).\mathbb{T}\exp\left(-i\int_0^t \left[\hat{H}_z.\left(\hat{a}^\dagger e^{i\omega t'} + \hat{a}e^{-i\omega t'} + B(t')\right) + \hat{H}_x\right] dt'\right)$$

To proceed further, we define the operator:

$$\hat{U}_S(t) = \mathbb{T}e^{-i\int_0^t B(t')H_z dt'}, \tag{3.7}$$

and the intermediate representation theorem is used again:

$$\hat{U}(t) = \hat{U}_F(t).\hat{U}_S(t) \times \mathbb{T}\exp\left(-i\int_0^t \left[\hat{H}_z.\left(\hat{a}^\dagger e^{i\omega t'} + \hat{a}e^{-i\omega t'}\right) + \hat{U}_S^{-1}(t')\hat{H}_x\hat{U}_S(t')\right] dt'\right) \tag{3.8}$$

The element $\hat{U}_S^{-1}(t')\hat{H}_x\hat{U}_z(t')$ can be simplified into:

$$\hat{U}_S^{-1}(t)\hat{H}_x\hat{U}_S(t) = \frac{\omega_S}{2}\left(e^{2ig\int_0^t B(t')dt'}\hat{\sigma}_+ + e^{-2ig\int_0^t B(t')dt'}\hat{\sigma}_-\right).$$

To summarize, equation (3.8) can be written in the form:

$$\hat{U}(t) = \hat{U}_F(t).\hat{U}_S(t).\hat{U}_E(t)$$

Each term of the product has a clear physical meaning: $\hat{U}_F(t)$ is, by construction, the evolution of the electromagnetic field alone, $\hat{U}_S(t)$ corresponds to the classical interaction of the spin with the electromagnetic field, and finally $\hat{U}_E(t)$ is a term that produces entanglement between the cavity and the spin. The procedure is illustrated in figure 3.2. Notice that similar formulas can be derived with the same procedure. For instance, $\hat{H}_x$ can be included together with $\hat{H}_z$ in $\hat{U}_S$, so that $\hat{U}_s = \mathbb{T}e^{-i\int_0^t (B(t')\hat{H}_z + \hat{H}_x)dt'}$.

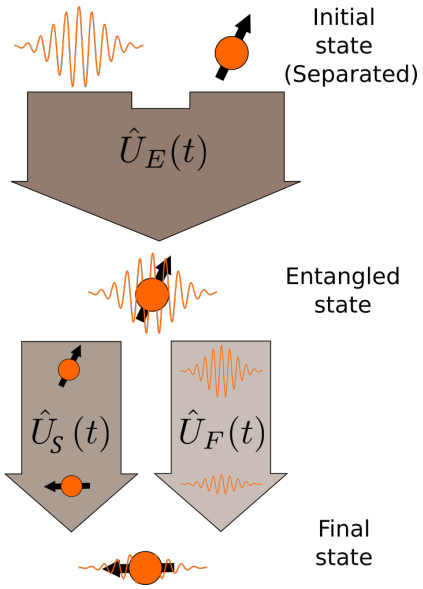

Figure 3.2: Evolution of a spin-boson system. First we consider a separated state. Then a first operator produces the entanglement of the system. Then two operators (which commute) change separately the state of the E.M. field and the state of the spin. In the limit where the coupling g is small, the entanglement can be neglected.

Case of the Jaynes-Cummings model

Calculations can be made in the Jaynes-Cummings model as well. However, due to the sum of two terms in the interaction Hamiltonian, calculations are longer. In this paragraph, we give the results for a single spin and a real control (in the quadrature Y).

Generalizations to a spin ensemble and to an arbitrary control are straightforward but quite long. More precisely, we use:

$$\hat{H}_{JC}(t) = \underbrace{\frac{\Delta}{2}\hat{\sigma}_z}_{\hat{H}_{spins}} + \underbrace{g(\hat{\sigma}_+\hat{a} + \hat{\sigma}_-\hat{a}^\dagger)}_{\hat{H}_i} + \underbrace{\frac{\omega_Y(t)}{2}(\hat{a}^\dagger + \hat{a})}_{\hat{H}_c}. \tag{3.9}$$

Without loss of generality, we have:

$$\begin{aligned}\hat{U}(t) =& \mathbb{T}e^{-i\int_{-\infty}^{t}\hat{H}_{JC}(t')dt'} \\ =& \underbrace{e^{-iB_Y(t)(\hat{a}^\dagger+\hat{a})/2}}_{\hat{U}_F} \\ &\times \underbrace{e^{-ig\mathsf{B}_Y(t)\hat{\sigma}_y/2}}_{\hat{U}_S} \\ &\times \underbrace{\mathbb{T}e^{-i\int_{-\infty}^{t}dt'\frac{\Delta}{2}(\cos(g\mathsf{B}_Y(t'))\hat{\sigma}_z - \sin(g\mathsf{B}_Y(t'))\hat{\sigma}_x) + \hat{H}_i}}_{\hat{U}_E},\end{aligned} \tag{3.10}$$

where the intermediate representation theorem has been used twice to determine the second equality. We also introduce: $B_Y(t) = \int_0^t \omega_Y(t')dt'$ and $\mathsf{B}_Y(t) = \int_0^t B_Y(t')dt'$.

Multi-photon process

This formalism can be extended straightforwardly to Hamiltonians with multi-photon interactions due to the commutation relations: $[e^{\beta_k\hat{a}^\dagger}, \hat{a}^m] = -m\beta_k e^{\beta_k\hat{a}^\dagger}$, and $[e^{\beta_k^*\hat{a}}, (\hat{a}^\dagger)^m] = -m\beta_k^* e^{\beta_k^*\hat{a}}$. Therefore, the control field experienced by the atoms is multiplied by the number of photons involved in the transition.

Adiabatic Elimination:

In the case of a control field with a total time shorter than the characteristic times of the spins, i.e. $t \ll 1/\Delta$ and $t \ll 1/g$, we have:

$$\hat{U}_E \simeq \mathbb{I}.$$

Moreover, the amplitude of B can be chosen so that it is of the order of $1/g$, which means that $\hat{U}_S(t)$ is of order zero. In this limit, we determine:

$$\hat{U}(t) = \hat{U}_F(t).\hat{U}_S(t)$$

Spins are driven without creation of entanglement (but with energy absorption). This behavior is the one expected in a semi-classical model : The electromagnetic field induces a change in the spin state but there is no measurable back action of the spin system.

3.2.2 Master equation

In this section, we consider the general system:

$$\frac{d\hat{\rho}(t)}{dt} = -i[\hat{H}(t), \hat{\rho}(t)] + \kappa \hat{D}[\hat{\rho}(t)]. \tag{3.11}$$

In this case, the analysis is more complicated because the intermediate representation theorem cannot be applied as easily as before. The operator which is "removed to the left" must be invertible (the operator $\hat{A}$ in theorem 13, appendix C). Here, the operator $\hat{D}$ is singular, and thus, we cannot separate the cavity dynamics as easily as in the unitary case. Fortunately, the analysis is still possible in Heisenberg's picture.

After determining the main Heisenberg equations of the system, and integrating the E.M. field operators, we determine (for a single spin):

$$\frac{d\hat{Q}_{X,Y}}{dt} = -\frac{\kappa}{2}\hat{Q}_{X,Y} + \omega_{X,Y} \mp 2g\hat{S}_{x,y}$$

$$\frac{d}{dt}\begin{pmatrix}\hat{S}_x\\ \hat{S}_y\\ \hat{S}_z\end{pmatrix} = \begin{pmatrix} g\int_0^t dt' e^{-\kappa(t-t')/2}(\omega_X(t') - 2g\hat{S}_y(t')) \\ g\int_0^t dt' e^{-\kappa(t-t')/2}(\omega_Y dt' + 2g\hat{S}_x(t')) \\ \Delta \end{pmatrix} \wedge \begin{pmatrix}\hat{S}_x\\ \hat{S}_y\\ \hat{S}_z\end{pmatrix}$$

where $\hat{Q}_{X,Y} = \hat{X}$ or $\hat{Y}$. The unitary case is recovered by setting $\kappa = 0$. From these equations, it is obvious that we can split pure control action (brown) and entanglement (orange) due to the linearity of the integral. Hence, by analogy with the unitary case, we write [33]: $\hat{U} = \hat{U}_F.\hat{U}_S.\hat{U}_E$ where $\hat{U}_F$ and $\hat{U}_E$ are two non-unitary operators. $\hat{U}_F$ is given by the evolution operator of the field without spin coupling (section 1.3.2), while $\hat{U}_E$ has a representation in terms of an infinite sum of commutators:

$$\hat{U}_E = e^{\log\hat{U} - \log\hat{U}_F - \log\hat{U}_S - [\log\hat{U}, \log\hat{U}_F + \log\hat{U}_S]/2 + \ldots}$$

(we do not enter into the details of the series convergence). The evolution of the spin keeps the same form as before [34], but the integral of the control is replaced by its equivalent in a damped cavity:

$$\frac{dB_{X,Y}}{dt} = -\frac{\kappa}{2}B_{X,Y} + \omega_{X,Y}, \tag{3.12}$$

or equivalently:

$$B_{X,Y} = \int_0^t dt' e^{-\kappa(t-t')/2}\omega_{X,Y}(t'). \tag{3.13}$$

To summarize, we have an evolution operator of the form [35]:

[33] *We keep the same notation as before, but here, the evolution operator acts on the density matrix such that* $\hat{\rho}(t) = \hat{U}(t)\hat{\rho}(0)$ *($\hat{U}$ is a "super-operator").*

[34] See equation (3.14) for the Jaynes-Cummings model, or (3.8) for the spin-boson model.

[35] For the Jaynes-Cummings model, with a single spin, and a control on the Y quadrature. $\hat{U}_E$ is deduced using the Baker–Campbell–Hausdorff formula.

$$\begin{aligned}\hat{U}(t) =& \mathbb{T} e^{-i\int_{-\infty}^{t}\hat{\mathcal{L}}(t')dt'} \\ =& \underbrace{\mathbb{T} e^{-i\int_{-\infty}^{t}\hat{\mathcal{L}}_F(t')dt'}}_{\hat{U}_F}\underbrace{e^{-ig\mathsf{B}_Y(t)[\hat{\sigma}_y,\cdot]/2}}_{\hat{U}_S} \\ &\times \underbrace{e^{\log\hat{U}-\log\hat{U}_F-\log\hat{U}_S-[\log\hat{U},\log\hat{U}_F+\log\hat{U}_S]/2+\ldots}}_{\hat{U}_E}.\end{aligned} \tag{3.14}$$

with $\hat{\mathcal{L}}_F$ defined by (1.24). We do not to compute explicitly $\hat{U}_E$ [36], but its main behaviors are highlighted. In the strong coupling regime, two effects fight against each other. The first one is the decoherence, which produces the Purcell effect and cancels the spin-photon entanglement, and the other one is the control which compensates cavity losses.

First of all, let us mention Ref. [154], where it is shown that the Purcell effect decreases with the photon number (with 10 photons, it generally decreases of $\simeq 50\%$, see figure 3.3). Therefore, with strong and short pulses, we could neglect the Purcell relaxation.

Regarding the entanglement spin-photon, we can derive only limiting cases. Indeed, the drive allows us to keep the coherence of the system for longer times, but the effect is limited. This point can be emphasized by computing the evolution of $\langle\hat{H}_i\rangle$. If we assume a third order cumulant expansion (section 1.6.1), we determine for a single spin at resonance:

$$\frac{d\langle\hat{H}_i\rangle}{dt} = \left(-\frac{\kappa}{2}+\omega_X(t)+\omega_Y(t)\right)\langle\hat{H}_i\rangle - ig\langle\hat{\sigma}_z\hat{N}\rangle, \tag{3.15}$$

and an integration with Green's functions gives:

$$\begin{aligned}\langle\hat{H}_i\rangle &= -ig\int_0^t e^{\Phi(t)-\Phi(t')}\langle\hat{\sigma}_z\hat{N}\rangle(t') \\ \Phi(t) &= B(t)+\frac{\kappa}{2}(\mathsf{B}(t)-t).\end{aligned} \tag{3.16}$$

The control modulates the horizon of coherence (given by Φ), but it does not change the fact that it is limited by $\kappa/2$. Hence, for long pulses, a loss of entanglement is expected. **Consequently, the adiabatic elimination (see page 67), has another time scale given by $\kappa/2$. For a pulse duration $T \ll \kappa/2$, the entanglement can be considered, but for $T \gg \kappa/2$, it can be neglected.**[37] This result can also be derived from an adiabatic elimination [13] (valid in the low coupling regime). This method is based on geometric singular perturbation theory and allows us to derive an effective Lindblad equation[38]:

$$\begin{aligned}\frac{d\hat{\rho}'}{dt} =& -ig[\langle\hat{a}\rangle\hat{\sigma}_+ + \langle\hat{a}^\dagger\rangle\hat{\sigma}_-,\hat{\rho}'] \\ &+\frac{4g^2}{\kappa}\left(\hat{\sigma}_-\hat{\rho}'\hat{\sigma}_+ - \frac{1}{2}\hat{\sigma}_+\hat{\sigma}_-\hat{\rho}' - \frac{1}{2}\hat{\rho}'\hat{\sigma}_+\hat{\sigma}_-\right).\end{aligned} \tag{3.17}$$

Generally, $4g^2/\kappa \gg T$, thus, only unitary transformations are conserved, and the entanglement is destroyed.

[36] There is no simple representation of the operator.

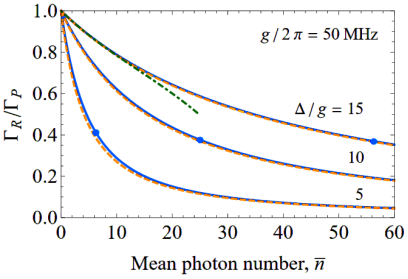

Figure 3.3: *figure extracted from [154].* The Purcell relaxation rate Γ_R normalized by the no-drive value Γ_P (equation (1.57)), as a function of the mean photon number $\bar{n}$ induced by the drive for several values of normalized detunings Δ/g: 15, 10, and 5. The dashed orange lines show $\Gamma(\bar{n})$, the blue solid gives an approximation with coherent state. The green dot-dashed line represents the truncated expansion of Γ_R (order 8). The blue dots on the lines indicate $\bar{n}_{crit}$.

[37] Under the approximation of a short pulse with zero photon in the cavity at its final time, one can derive the approximated expression: $\langle\hat{H}_i\rangle \simeq \int_0^T dt e^{-\kappa(T-t)/2}\langle\hat{\sigma}_z\hat{N}\rangle(t)$ with $\langle\hat{\sigma}_z\hat{N}\rangle(T) \simeq 0$.

[38] Notice the very similar result obtained in section 1.6. This can be viewed as a quantum version of the very bad cavity limit.

3.3 Control with non-linear generalized functions

3.3.1 Approximations induced by mollifiers

The new expression of the evolution operator $\hat{U}$ can be combined with non-linear generalized functions in order to derive simple formulas, and to recover basic control mechanisms in NMR. Generalized functions are very powerful tools and they generalize the notion of distribution, introduced by L. Schwartz [39]. The idea is to choose as a control field a function called *mollifier* (see definition 16, appendix B). These functions are regularized Dirac distributions: They have the same properties as distributions when they are applied to test functions (modulo a negligible rest). In the language of generalized functions, we say that a mollifier η is a representative of the Dirac distribution δ_0 and we write: $\eta \asymp \delta_0$. The strict equality is reached in the limit $\lim_{\varepsilon\to 0} \eta(t/\varepsilon)/\varepsilon = \delta_0(t)$. First, we investigate a control problem with $\kappa = 0$, and we choose[40]:

[39] An introduction is given in appendix B.

[40] For a definition of the function, see section 3.2.1 and more precisely equation (3.14).

$$\begin{aligned} \omega_Y(t) &= \frac{\alpha}{\varepsilon}\left(\frac{\kappa}{2} + \frac{d}{dt}\right)\eta\left(\frac{t - T/2}{\varepsilon}\right) \\ B_Y(t) &= \frac{\alpha}{\varepsilon}\eta\left(\frac{t - T/2}{\varepsilon}\right) \\ \mathsf{B}_Y(t) &= \frac{\alpha}{\varepsilon}\int_{-\infty}^{t}\eta\left(\frac{t' - T/2}{\varepsilon}\right)dt', \end{aligned} \tag{3.18}$$

where α is a flip angle. In a realistic experiment, one must choose a specific mollifier for the realization of the pulse, but for the moment we assume that η is a known mollifier of order q (q is the order where we stop the Taylor expansion of the functions, all orders above q are neglected). Explicit examples are presented later. In the next computations, we do not consider the limit $\varepsilon \to 0$, we keep it as a fixed parameter. Instead, we recover properties of Dirac distributions up to an order q of a Taylor expansion.

The goal is to determine a simple form of the evolution operator (3.14). First of all, ω_Y can be a function of compact support on the interval $[0, T]$, and η can be chosen such that $B_Y(T) = 0$. Under these assumptions we obtain some simplifications:

$$\hat{U}_F = \mathbb{I} \tag{3.19}$$

$$\hat{U}_S = e^{-ig\alpha\hat{\sigma}_y/2}. \tag{3.20}$$

If T is small enough, we can use the adiabatic approximation and write $\hat{U}_E = \mathbb{I}$, and we recover the well-known square pulses of NMR. **Therefore, under the adiabatic approximation, the use of adequate mollifiers allows us to reproduce any NMR pulse sequence**. If the entanglement is not negligible, we have to evaluate

$\cos(g\mathsf{B}_Y(t'))$ and $\sin(g\mathsf{B}_Y(t'))$. For that purpose we regularize the integral that defines B_Y :

$$\mathsf{B}_Y(t) = \lim_{h\to 0} \int \frac{\alpha}{\varepsilon}\eta\left(\frac{t'-T/2}{\varepsilon}\right)\phi_h(t-t')dt', \tag{3.21}$$

with

$$\lim_{h\to 0}\phi_h(t-t') = \mathbb{I}_{]-\infty,t]}(t'), \tag{3.22}$$

ϕ_h being a smooth function. It is possible to expand it in a Taylor series. Therefore:

$$\mathsf{B}_Y(t) = \lim_{h\to 0}\alpha\phi_h(t-T/2) + o(h^{q+1}), \tag{3.23}$$

and the powers of B_Y are:

$$\mathsf{B}_Y^n(t) = \lim_{h\to 0}\alpha\phi_h^n(t-T/2) + o(h^{q+1}). \tag{3.24}$$

As a result, we can define a regularized version of $f(\mathsf{B}_Y(t))$ for any analytic function f:

$$\begin{aligned} f(\mathsf{B}_Y(t)) &= \lim_{h\to 0} f\left(\alpha\langle\eta_h|\phi_h\rangle(t)\right) \\ &= \lim_{h\to 0} f(\alpha\phi_h(t-T/2)) + o(h^{q+1}) \\ &= \begin{cases} f(0)+o(h^{q+1}) & if \quad t<T/2 \\ f(\alpha/2)+o(h^{q+1}) & if \quad t=T/2 \\ f(\alpha)+o(h^{q+1}) & if \quad t>T/2 \end{cases} \end{aligned} \tag{3.25}$$

Plugging together (3.14), (3.18) and using the fact that (3.25) is approximately piecewise constant, we deduce:

$$\begin{aligned} \hat{U}_E(T) &\simeq e^{-i\frac{T}{2}\left(\frac{\Delta}{2}(\cos(g\alpha)\hat{\sigma}_z+\sin(g\alpha)\hat{\sigma}_x)+\hat{H}_i\right)}e^{-i\frac{T}{2}\left(\frac{\Delta}{2}\hat{\sigma}_z+\hat{H}_i\right)} \\ &\simeq e^{-iT\left(\frac{\Delta}{4}([1+\cos(g\alpha)]\hat{\sigma}_z+\sin(g\alpha)\hat{\sigma}_x)+\hat{H}_i\right)}. \end{aligned} \tag{3.26}$$

In the second line, we further assumed that the entanglement Hamiltonian is small enough so that we can use a Magnus expansion of order 1.

3.3.2 Examples: Bump and Gaussian pulses

Many different functions can be used to define η. Two examples of family are presented in this section. A family is parametrized by a mother function η_0. This function must approximate a Dirac distribution when its support is squeezed around 0 and its amplitude is rescaled proportionally. As mentioned previously, and explained in appendix B, another limit can be used in order to recover a Dirac distribution. For that purpose, a procedure (see section B.3.2) allows us to construct a sequence of mollifiers which approximates with a better accuracy a Dirac distribution as the order of convergence increases.

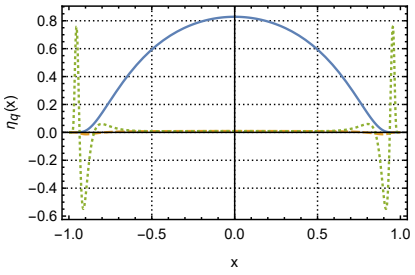

Figure 3.4: Bump pulse family. Blue solid line: order 0, Orange dashed line: order 2 and the green dotted line: order 4. Blue and orange curves have been divided by 100.

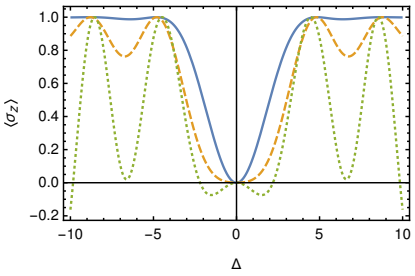

Figure 3.5: $\langle\uparrow|\hat{U}_x^\dagger(\Delta)\hat{\sigma}_z\hat{U}_x(\Delta)|\uparrow\rangle$ for the first elements of the bump family. Blue solid line: order 1, orange dashed line: order 3, green dotted line: order 4.

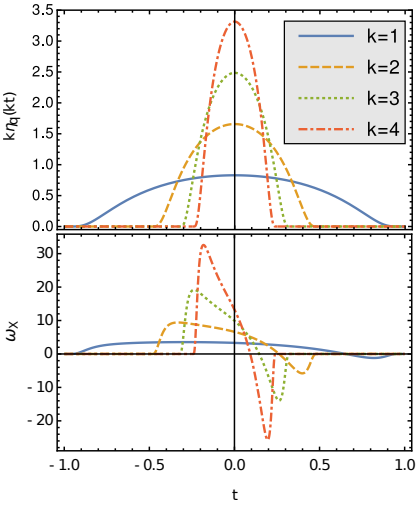

Figure 3.6: (top) Bump pulse of order 0 which defines the evolution of field quadratures. (bottom) control field to input inside the cavity in order to obtain the desired E.M. field. Curves are plotted for different pulse durations, which are defined by the scaling factor k. Computation of ω_X is made using $\kappa = 4$.

Bump pulses: We choose as a first example a family generated by the standard bump function:

$$\eta_0(x) = A_p e^{\frac{1}{x^p-1}} \mathbb{I}_{]-1,1[}(x). \tag{3.27}$$

The parameter $p \in 2\mathbb{N}$ can be chosen in order to make the pulse more or less flat around zero. In the rest of this paragraph, we use $p = 2$. The normalization factor A_p depends on p. For $p = 2$, it is expressed in terms of a Whittaker's function: $A_2 = \sqrt{\pi/e} W_{-1/2,1/2}(1) = 0.44399....$ Mollifiers of higher degrees are obtained by calculating:

$$\eta_q = \sum_{n=0}^{q} \alpha_n \partial_x^n \eta_0(x) = \eta_0(x) \sum_{n=0}^{q} \alpha_n P_n(x). \tag{3.28}$$

An explicit computation gives:

$$\begin{aligned} \alpha_0 &= 1 \\ \alpha_2 &= -0.07905681811965157 \\ \alpha_4 &= 0.004042404740618485, \end{aligned}$$

with $\alpha_{2n+1} = 0$ and,

$$\begin{aligned} P_0 &= 1 \\ P_2 &= \frac{-2+6x^4}{(-1+x^2)^4} \\ P_4 &= \frac{4(-3+6x^2+58x^4-132x^6+45x^8+30x^{10})}{(-1+x^2)^8}. \end{aligned}$$

The functions are plotted in figure 3.4. The pulse robustness can be visualized by plotting $\langle\uparrow|\hat{U}_x^\dagger(\Delta)\hat{\sigma}_z\hat{U}_x(\Delta)|\uparrow\rangle$ with $\hat{U}_x(\Delta) = \mathbb{T}e^{-i\int(\pi/2\eta(t')\hat{\sigma}_x+\Delta\hat{\sigma}_z)/2dt'}$. This shows the fidelity of an excitation pulse on a spin with offset Δ. This robustness profile is given in figure 3.5. Mollifiers are used to determine $B_{X,Y}$. The true control must be computed with (3.12). Examples of functions $\omega_{X,Y}$ are presented in figure 3.6.

As we can see in figure 3.4, bump pulses of order higher than 0 have localized peaks. This induces a very high control amplitude, which might not be feasible experimentally [41] Therefore, in standard applications, we use only the first pulse of the family.

Gaussian pulse: The second example is not of compact support but it is very interesting. For this family, the mother function is a Gaussian:

$$\eta_0(x) = \frac{1}{\sigma\sqrt{2\pi}} e^{-x^2/2\sigma^2}. \tag{3.29}$$

First order coefficients α_n and polynomials P_n are[42]:

[41] With high amplitudes, we can enter into a non-linear regime, and the theory developed so far is not valid anymore.

[42] Again, due to the function symmetry, odd orders have zero coefficients.

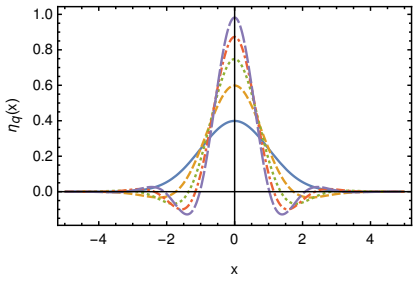

Figure 3.7: Family of mollifier generated by $\eta_0(x) = \frac{1}{\sqrt{2\pi}} e^{-x^2/2}$ ($\sigma = 1$). for orders 0,2,4,6,8.

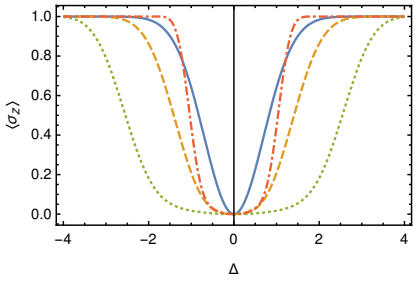

Figure 3.8: Excitation profile of Gaussian pulses. Blue solide line: order 0 and $\sigma = 1$, orange dashed line: order 2 and $\sigma = 1$, green dotted line: order 8 and $\sigma = 1$. red dashed-dotted line: order 8 and $\sigma = 2.4609375$. This value of sigma is chosen so that the maximum of the pulse corresponds to the maximum of a pulse of order 0 and $\sigma = 1$.

$$
\begin{aligned}
\alpha_0 &= 1 \\
\alpha_2 &= -\sigma^2/2 \\
\alpha_4 &= \sigma^4/8 \\
\alpha_6 &= -\sigma^6/48 \\
\alpha_8 &= -\sigma^8/384,
\end{aligned}
$$

$$
\begin{aligned}
P_0 &= 1 \\
P_2 &= \frac{(x-\sigma)(x+\sigma)}{\sigma^4} \\
P_4 &= \frac{x^4 - 6x^2\sigma^2 + 3\sigma^4}{\sigma^8} \\
P_6 &= -\frac{x^6 - 15x^4\sigma^2 + 45x^2\sigma^4 - 15\sigma^6}{\sigma^{12}} \\
P_8 &= \frac{x^8 - 28x^6\sigma^2 + 210x^4\sigma^4 - 420x^2\sigma^6 + 105\sigma^8}{\sigma^{16}}.
\end{aligned}
$$

First iterations up to the order 8 are plotted in figure 3.7. We clearly see the similitude with a sinc function multiplied by an apodization function. This shows the robustness of sine cardinal pulses. However, as we can see in figure 3.8, the excitation profile is smoother than the one of sinc pulses [43].

Short comparison between the two pulse families: In order to compare the pulses, we choose $\sigma = 1/2.08$, which corresponds to a width of the Gaussian pulse so that the maximum of amplitude is (approximately) the same as a bump function. Thus, we compare pulses of duration 2 (bump family) and 4 (Gaussian family). The time is chosen so that the effect of the Gaussian pulse outside the interval $[-2, 2]$ is negligible). Pulse energies are presented in table 3.1 (orders 0 to 8). We see that the two pulses are similar up to the order 2. Nevertheless, the amplitude of bump pulses diverges quickly as q increases [43]. If the need of robustness is not too important, bump pulses are more advantageous, because of their true compact support. Otherwise, Gaussian pulses seem more interesting. Concerning the robustness, they are close to optimal pulses [168]. Time and energy are of the same order as the ones found in the literature (e.g.[35, 43, 127, 168], to cite a few). *In terms of performance, they are not the best pulses, but they are simple, analytic, derivable, and they cancel on the boundaries of the time interval. These properties are exactly the ones required for the control of spins coupled to a cavity.*

q	Bump	Gaussian
0	0.675117	0.584841
2	1.34713	0.987314
4	1.34713	1.29515
6	3.75×10^{7}	1.55457
8	5.86×10^{13}	1.55561

Table 3.1: Pulse energies for different orders.

[43] This point is due to the compact support of the function.

3.3.3 Numerical results

In order to verify the validity of the approach, several integrations of the Linblad equation (1.49) have been performed. The control

field is defined by a bump pulse of order 0, and a flip angle $\pi/2$. We have considered a spin, initially in the state $|\uparrow\rangle$, at different offsets ($\Delta = 0, 2.5$) and different damping rates ($\kappa = 0, 10$). The coupling constant and the pulse duration have been set to $g = 0.5$ and $T = 0.5$. In a second step, the quantum fidelity $F_Q = Tr\left[\left(\sqrt{\hat{\rho}_1}.\hat{\rho}_2.\sqrt{\hat{\rho}_1}\right)^{1/2}\right]$ of the final state has been computed with respect to the approximated transformations defined by (3.20) and (3.26). Results are presented in table 3.2.

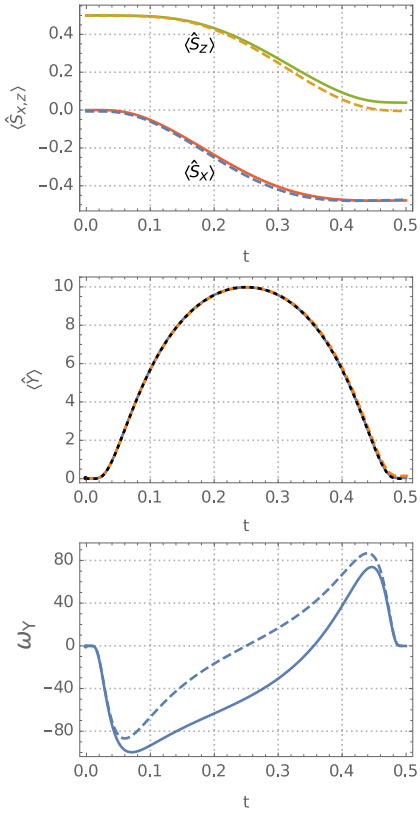

Figure 3.9: Evolution of the system controlled by a bump pulse of area $-\pi/2$, for a cavity without damping ($\kappa = 0$, dashed lines) and a damped cavity ($\kappa = 10$, solid lines). The gray dotted curve on the middle panel is the theoretical curve, given by a bump function (the curves are superimposed).

	$\Delta = 0$	$\Delta = 2.5$
$\kappa = 0$	$F_Q^1 = 0.9768$ $F_Q^2 = 0.9953$	$F_Q^1 = 0.9605$ $F_Q^2 = 0.9868$
$\kappa = 10$	$F_Q^1 = 0.9882$ $F_Q^2 = 0.9729$	$F_Q^1 = 0.9723$ $F_Q^2 = 0.9643$

Table 3.2 – Fidelity F_Q^1 and F_Q^2 between exact numerical integration and approximations defined respectively by (3.20) and (3.26).

An example of dynamics is plotted in figure 3.9. It shows that the field in the cavity is well described by a bump function and the final state is reached with a very good accuracy. The results are in very good agreement with the expected values.

3.4 Pulse design with numerical algorithms

In the last section, we have presented simple pulses which allow to manipulate spin states with a high fidelity. However, the approach works well only for short pulses and offsets near the resonance. In experiments, field inhomogeneity and non-negligible spin-field interaction reduce the pulse efficiency. Fortunately, robust controls can be designed to balance these dynamic effects. Robust pulse sequences are nowadays standard in magnetic resonance [67, 90, 91, 125] either for point to point transformations or universal rotations. This section is devoted to the adaptation of this latter pulse class. Two cases are distinguished:

- The good cavity (i.e. strong coupling) regime, where a full integration of the master equation is required in order to compute the pulse fidelity. In this case, the initial state is a density matrix $\hat{\rho}_{ini}$, and the goal of the control field is to reach a target state $\hat{\rho}_{target}$. This is a point to point transformation and the pulse properties are not necessarily conserved if the initial state changes.

- The bad cavity regime (i.e. weak coupling regime). In this case, thanks to semi-classical equations (1.60), we can follow the method used with mollifiers (equation (3.18)), and universal rotations can be optimized.

In order to keep the interesting properties of bump pulses (like the cancellation of the field on the boundaries of the time interval), pulses are optimized with smooth parametrized functions. The efficiency of the approach has been demonstrated several times [157, 168]. In general, it is sufficient to optimize only a small number of parameters ($\lesssim 10$).

3.4.1 Good cavity regime

*These results are at a preliminary stage. They are presented as "**a proof of principle**" of optimization in the good cavity regime. Some important points are detailed, and others are left to next studies.*

When the parameters g, κ, Ω and T have similar values, it is generally necessary to use optimized pulses to take into account the inhomogenity, the spin correlations and the entanglement with the cavity. Since the pulse is specific to a parameter set, a new optimization is required if the setup changes[44].

Several strategies can be used for optimization. Here we focus on pulses parametrized by the following analytic functions:

$$\begin{pmatrix} B_X(t) \\ B_Y(t) \end{pmatrix} = \frac{\pi}{2} A(t) \sum_{m=0}^{M} \begin{pmatrix} a_m \cos\left(\frac{2\pi m}{T} t\right) \\ b_m \cos\left(\frac{2\pi m}{T} t\right) \end{pmatrix}, \tag{3.30}$$

where $A(t)$ is a bump pulse (order 0) of parameter $p = 10$. In order to reduce as much as possible the computation time, the dependence of $B_{X,Y}$ is chosen linear with the parameters. The second point to clarify is the choice of the cost function. As emphasized in the previous paragraph, we can perform only a state-to-state transfer, but we still have the liberty to choose the cost to minimize. Three different possibilities have been studied:

1. $C = \|\vec{O}_{target} - \vec{O}(T)\|$, where $\vec{O} = (Tr[\hat{O}_1\hat{\rho}], ..., Tr[\hat{O}_k\hat{\rho}])$ is a vector of mean values of operators. In this case, the goal is to maximize the fidelity of some observables. In applications we choose $\vec{O} = (\langle\hat{S}_x\rangle, \langle\hat{S}_y\rangle, \langle\hat{S}_z\rangle, \langle\hat{X}\rangle, \langle\hat{Y}\rangle)$.

2. $C = \|\hat{\rho}_{S,target} - Tr_B[\hat{\rho}(t)]\|$ is the distance between two subsystem density matrices. Such a density matrix is computed with the partial trace Tr_B. A typical subsystem is a single spin at resonance. This cost is interesting in the context of non-Markovian dynamics.

3. $C = \|\hat{\rho}_{target} - \hat{\rho}(T)\|$. This is the most general case, where the target state is the density matrix of the full system.

The optimization task consists of determining the set of parameters $\{a_m, b_m\}_{m=0..M}$ which minimizes the cost C at the end of the pulse. Here, a simple simulated annealing algorithm (section A.2.2) has been used [45].

It should be emphasized that other cost functions can be chosen. For example, instead of the norm, we can use the distance square or the quantum fidelity. Notice that this latter option is

[44] The robustness against parameter variations can be relatively small. The area of robustness must be determined case by case, since it depends on the cost function used for the optimization. Moreover, all the parameters do not have the same sensitivity to parameters variations.

[45] Notice that if the number of parameters is small, an optimization "by hand", using contour plots, can be efficient, accurate, and faster than an optimization algorithm. Depending on the Hilbert space dimension, a numerical optimization algorithm can take several hours or several days to converge, while a good solution can be found in a few minutes/hours using plots of C.

	Pulse 1		Pulse 2	
m	a_m	b_m	a_m	b_m
0	-3.5	0	-2.932	3.163
1	0.6	0	2.273	-4.117
2	-4	0	11.630	3.064
3	-1.75	0	5.685	-3.924
4	0.15	0	0	0

Table 3.3: List of parameters to generate a pulse that maximizes the magnetization vector on the x coordinate (pulse 1), and another one that minimizes the distance with a density matrix given by an ideal rotation of angle $-\pi/2$ around the y-axis (pulse 2).

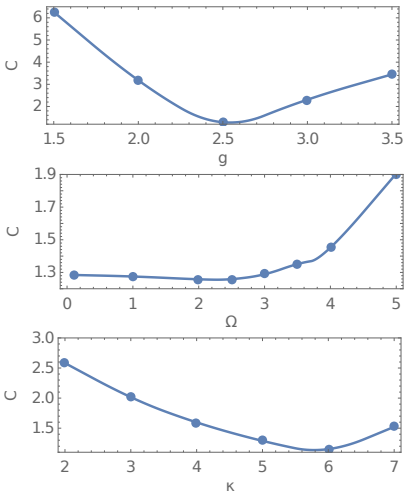

Figure 3.10: Variations of C around the point $\Omega = 3$, $g = 2.5$, $\kappa = 5$.

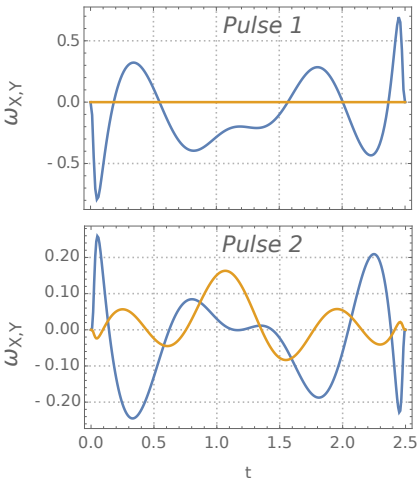

Figure 3.11: The two optimized pulses. Notice the similarity between the pulses, which are determined using different models.

computationally more demanding. For a simulated annealing algorithm, using the norm or the square norm is not very different since the algorithm is gradient-free.

Optimizing a distance between mean values or reduced density matrices is generally easier than considering the full-density matrix. In both cases, the target state is rather an equivalent class of density matrix and different solutions are possible to approach the target state. For example, in the non-Markovian picture, it is not difficult to reach a fidelity higher than 90 %. *However, cautions must be taken as the final bath state is not constrained.* The solutions we have determined in this context seem irrelevant for practical uses. Hence, we focus on the two other cases.

Regarding the definitions 1 and 3 of the cost function, they are generally not equivalent, even if the final results are qualitatively similar. For example, an excitation pulse has been optimized for a system defined by $\rho_0 = \{3,1,3\}$ (model 2), $g = 2.5$, $\kappa = 5$, and $T = 2.5$. The target state is $\vec{O}_{target} = (1.5,0,0,0,0)$. The pulse is plotted in figure 3.11, and its parameters are given in table 3.3. The fidelity of this first pulse is quite good, since we have $\vec{O}(T) = (1.15,0,0.25,1,0)$, while a simple bump pulse gives the final state $(0,0,-1.5,0.85,0)$ (The pulse has a negligible effect, due to the relaxation). The quantum fidelity is respectively $F_Q = 0.488$, and $F_Q = 0.2$. The first value is very low compared to the good approximation of the target state. On the opposite, for a good quantum fidelity ($\simeq 0.75$) does not mean that the magnetization is in the right state. Nevertheless, a very good fidelity ($\gtrsim 0.9$) always agree with the expected mean values of observable. This point is made clearer with the second example.

In order to provide an idea of the pulse robustness against variations of the parameters Ω, g, and κ, we computed variations of C around the values chosen for the optimization. They are plotted in figure 3.10. We observe that the pulse is not robust according to g and κ, but the robustness in Ω is quite good. Hence, this optimized pulse has similar properties as NMR broadband optimized pulses [90]. For a second case study, we considered a very simple system composed of two spins with $\Delta = \pm 3$ (model 1), $g = 2.5$, $\kappa = 5$ and $T = 2.5$. The optimization is performed for a state-to-state transfer of the full-density matrix. We start from $\hat{\rho} = |\downarrow,\downarrow,0\rangle\langle\downarrow,\downarrow,0|$, and the goal is to reach the target state $\hat{\rho} = |-x,-x,0\rangle\langle-x,-x,0|$, where $|x\rangle$ symbolizes the state of a spin aligned along the x direction. The pulse is plotted in figure 3.11, and its parameters are given in table 3.3.

In order to verify the pulse performance, the latter is compared to different pulses of reference (bump pulse of order 0, Gaussian pulse of order 4), and different systems (discretized ensemble, continuous ensemble). The quantum fidelity of each case is given in table 3.4.

As mentioned above, we observe a non-negligible disagreement between quantum-fidelity and observable mean values. This can be seen for the bump pulse which has a fidelity of 72% for a single spin, but a totally wrong magnetization vector. However a

System	1 spin	2 spins	$\rho_0 = \{2,1,1\}$	$\rho_0 = \{3,1,1\}$
	$(\Delta = 0)$	$(\Delta = \pm 3)$		
Color in Fig. 3.12	Blue	Orange	Green	Red
Bump order 0	0.724*	0.453	0.229	0.315
Gauss. order 4	0.526	0.457	0.216	0.190
optimal pulse	0.937	0.907	0.795	0.699

Table 3.4 – Quantum fidelity for a spin ensemble excitation performed by different pulses. The value with an * is quite good, however, contrary to other cases with a similar fidelity, the final magnetization vector is absolutely not the desired one (we have $\vec{S} = (-0.25, 0, -0.96)$ instead of $(-1, 0, 0)$).

very high fidelity ($> 90\%$) implies necessarily a good alignment of the magnetization. This fact is illustrated in figure 3.12, where the final magnetization vectors are plotted on the Bloch sphere. We observe that for all situations, the bump pulse fails to rotate contrary to the optimal pulse. Moreover, this result is in agreement with the robustness in Ω observed with the first pulse (see figure 3.10).

Gaussian and bump pulses are very robust in standard NMR, they are similar to sinc pulses or optimized pulses with the SRL algorithm [127]. However, they do not take into account the spin-field interaction, and their *quantum fidelity is low*. **Only an optimally designed pulse can produce the desired transformation with a high fidelity.**

With these two simple examples, we have demonstrated the importance of the optimization process in the strong coupling regime and we have shown that it is easily implemented in our algorithm using parametrized analytic functions. Several non equivalent approaches can be used, with a state defined by mean values of operators, or with a density matrix.

It should be emphasized that the fidelity after optimization is relatively low (around 0.9), compared to the value required for quantum computation tasks (> 0.999). Better solutions should be determined by increasing the number of parameters (a_m, b_m), and by increasing the region of optimization. However, these two solutions increase considerably the computation time. Despite our efforts to integrate the dynamics of the many-body quantum system in the most efficient way, the integration is a challenging issue and it can take several minutes (in the best cases). This is a considerable limiting factor for the optimization point of view because hundred or thousands integrations are required to solve the optimization task. A next step could be to extend the GRAPE algorithm (section A.2.1) to the integration scheme in order to obtain a fast computation of the gradient. Another important issue could be to perform computations using a GPU, since it allows an important speed up [177].

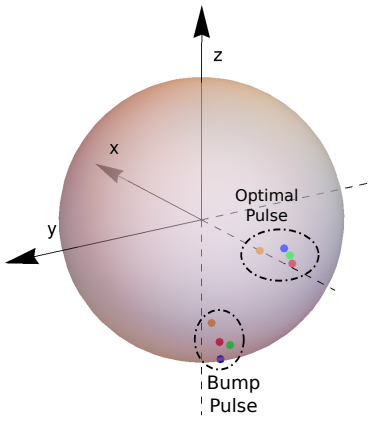

Figure 3.12: Position of the spin ensemble magnetization vectors after the bump pulse and the optimal pulse. The color associated to each system is given in table 3.4. Only optimized pulses allow to reach a magnetization close to the target state $(-1, 0, 0)$. In each case, the magnetization is normalized to 1. For the sake of clarity we do not show the points given by the Gaussian pulse. They are located near the points of the bump pulse.

p	10	
$\mathcal{A}_0$	95.64329	
n	a_n	b_n
0	2.48502	0
1	-0.61460	0.02222
2	-0.14640	-0.32631
3	0.24956	0.21203
4	-0.38051	-0.29431
5	-0.85098	0.29200
6	0.00534	-0.28452
7	-0.44574	-0.00924

Table 3.5: List of parameters for a Δ- robust $(\pi/2)_y$ universal rotation.

p	10	
$\mathcal{A}_0$	95.64329	
n	a_n	b_n
0	3.65529	0
1	-0.18629	0.30164
2	0.15696	0.95174
3	0.88614	-0.52373
4	-0.39488	0.43953
5	-0.36251	-0.26185
6	0.17478	0.27852
7	0.03328	0.00976

Table 3.6: List of parameters for a Δ- robust $(\pi)_y$ universal rotation.

p	2	
$\mathcal{A}_0$	35.37878	
n	a_n	b_n
0	1.45731	0
1	-1.90458	0
2	0.47185	0
3	-0.16459	0
4	0.69102	0

Table 3.7: List of parameters for g-robust $(\pi/2)_y$ universal rotation.

3.4.2 Bad cavity regime

In chapter 2, we have underlined the very good agreement between the quantum model and the semi-classical model. Therefore, we use the semi-classical approximation (1.60) for the design of robust pulses. Notice that the pulses are optimized under the assumption of a negligible relaxation. From (1.60), we deduce that the field to input in the cavity is determined by:

$$\omega_X = \frac{d}{dt}\langle\hat{X}\rangle + \frac{\kappa}{2}\langle\hat{X}\rangle + 2\sum_j g_{(j)}\langle\hat{S}_y^{(j)}\rangle \tag{3.31}$$

$$\omega_Y = \frac{d}{dt}\langle\hat{Y}\rangle + \frac{\kappa}{2}\langle\hat{Y}\rangle - 2\sum_j g_{(j)}\langle\hat{S}_X^{(j)}\rangle. \tag{3.32}$$

Therefore, the protocol is the following:

1. Using a standard pulse optimization algorithm, optimize a universal rotation where the control fields are the variables $B_X = \langle\hat{X}\rangle$ and $B_Y = \langle\hat{Y}\rangle$. This field has to be derivable at any time.
2. Integrate the Bloch equations with the control $B_{X,Y}$ and compute $\sum_j g_j\langle\hat{S}_{x,y}^{(j)}\rangle$ (the cavity is not taken into account in this integration). This step can be neglected in the low cooperativity regime.
3. Compute the control $\omega_{X,Y}$ to input in the cavity with (3.32).

For the design of $B_{X,Y}$, we still use parametrized functions. The parameterization (3.30) can be used as well, but we rather consider a slightly different parameterization. Since we do not take into account the relaxation, we can restrict our search in a subspace close to the time-minimum solution that is known to be a regular pulse [167, 90, 91]. A regular pulse is a pulse of constant amplitude (ideally the highest amplitude allowed by the system) and a time-dependent phase. In order to adapt a regular pulse to a cavity system, the pulse must be smoothed at the boundaries of the time interval. More precisely, we use the following parametrization:

$$\begin{aligned} B_X(t) &= \mathcal{A}_0 A_p(t)\cos(\phi(t)) \\ B_Y(t) &= \mathcal{A}_0 A_p(t)\sin(\phi(t)) \\ \phi(t) &= \frac{a_0}{2} + \sum_{n=1}^{N_F} a_n \cos\left(\frac{2\pi n}{T}t\right) + b_n \sin\left(\frac{2\pi n}{T}t\right), \end{aligned} \tag{3.33}$$

where $\mathcal{A}_0$ is a normalization factor setting the pulse energy, A_p is a bump function of parameter p, and $\{a_n, b_n\}_{n=0..N_F+1}$ is the set of $2(N_F+1)$ parameters to optimize. Optimizations are performed with a modified GRAPE algorithm (section A.2.1). The algorithm

uses $SU(2)$ evolution operators to maximize the following figure of merit:

$$\mathcal{F} = \frac{1}{2N}\sum_{k=1}^{N} \Re\left(\mathrm{Tr}\left[U_{target}^{\dagger} U(T,\Delta_k)\right]\right). \tag{3.34}$$

Numerical computations have been performed for two different situations. The first case consists of a uniform offset distribution[46] in the interval $\Delta \in [-30, 30]$ and a constant coupling strength $g = g_0 = 1$. Normalized units are used at this stage of the process, and experimental values are taken into account in the next steps. This change of unit is straightforward if we set the time in second and the amplitude in Hz. Then reducing the pulse duration requires to multiply the pulse amplitude by the same factor. In the second case, the spins are assumed to be at the resonance but the coupling strength is distributed uniformly according to the relation $g = g_0(1+\alpha)$, $\alpha \in [-0.3, 0.3]$. In the two cases, the control duration is set to $T = 1$.

Different pulse shapes are plotted in figure 3.13. The values of the pulse parameters are presented in tables 3.5 to 3.8. A robust pulse against both offset and coupling strength inhomogeneities can also be designed along the same lines but at the price of a longer control time or a larger pulse energy.

p	2
$\mathcal{A}_0$	70.75757

n	a_n	b_n
0	1.05923	0
1	-1.06434	0
2	0.19778	0
3	-0.98585	0
4	-0.68062	0
5	-0.68062	0

Table 3.8: List of parameters for g robust $(\pi)_y$ universal rotation.

[46] It is not necessary to use the experimental distribution of offsets during the first protocol step.

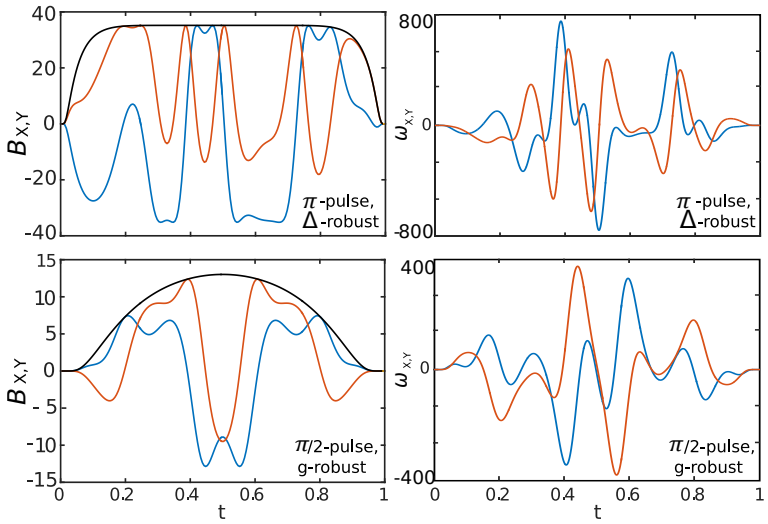

Figure 3.13 – Two examples of optimized robust pulses.*(Top)*, π-rotation robust with respect to g. *(Bottom)*, rotations of $\pi/2$ and robust in Δ. *(Left panels)*, X, Y and $(X^2+Y^2)^{1/2}$ are displayed respectively in red, blue and black solid lines. *(Right panels)*, plot of the corresponding control fields ω_X and $\omega_Y(\kappa = 4)$.

Discussion about the second step of the protocol: The second step of the protocol can be neglected in the low cooperativity regime, but it is essential in the regime of strong-cooperativity and bad cavity limit (non-linear effects are not negligible but they are small enough for a semi-classical treatment). However, caution must be taken. First the Purcell effect must remain negligible.

Otherwise, canceling the field does not preserve the dynamics. Second, the spin distribution has to be known with a high precision. Otherwise, the pulse loses its robustness (an error of 10% on the offset distribution width leads to an error of $\sim 10\%$ on the spin state and an error of 30% on the width induces an error of $\sim 50\%$ on the final state).

Discussion about the very bad cavity limit: In this limit, radiation damping equations (1.61) provide a good description of the experiment. The optimal control of a spin ensemble under radiation damping has been studied and the optimal synthesis is known [184]. Standard results of NMR radiation damping can be used for the pulse design.

3.5 Applications

3.5.1 T_1 inversion recovery

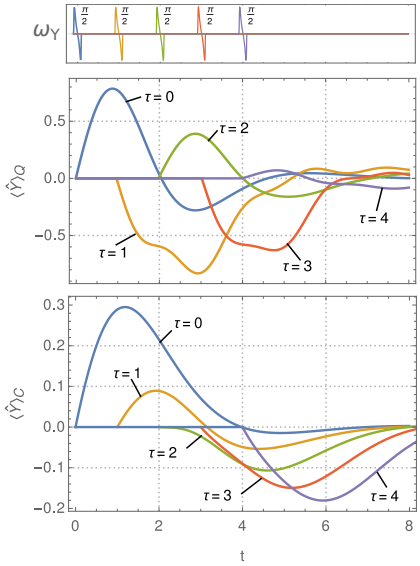

Figure 3.14: Superposition of FID produced by several inversion recovery sequences. $\pi/2$ pulses are produced at times $0, 1, 2, 3, 4$. Upper panel: Sequence of $\pi/2$ pulses, middle panel: model 2, lower panel: model 3. Notice that in the graph, the pulse duration is chosen arbitrarily (They are in fact instantaneous).

As a first example of concrete application, we investigate the response of the system under an inversion recovery sequence. The sequence is given by a first π-pulse, in order to excite the spin ensemble. Then, a $\pi/2$-pulse is applied after a time τ. This pulse produces a measurable FID with an amplitude scaled by the T_1 relaxation. In this paragraph, we propose to revisit such pulse sequences in the strong coupling regime. For that purpose, we used the relation (3.20) to include the control in the numerical integration. Calculations have been performed using a continuous spin ensemble (model 2) defined by $\rho_0 = \{1, 1, 1\}$. Other parameters are: $g = 0.5$, $\kappa = 1$ and $n_{photon}(t = 0) = 0.00001$. Figure 3.14 shows the superposition of FID produced after a $\pi/2$ pulse for $\tau = 0, 1, 2, 3, 4$. Calculations have also been performed with the semi-classical model. As expected, predictions are totally different. The quantum model takes into account Rabi-oscillations during the Purcell relaxation, contrary to the semi-classical model. Few minutes are required for the calculation of figure 3.14. We thus hope that the continuous ensembles are good for describing experimental results.

3.5.2 Spin echo in the bad cavity regime

As a second illustrative example, we consider a spin echo sequence performed on a system with a bad cavity. A spin echo is a revival of the (mean) magnetization. Such effects can be produced using an appropriate control sequence. The sequence generally consists of an excitation pulse (rotation of $\pi/2$) followed by an inversion pulse (rotation of π) after a time T_e. The excitation pulse aligns the spins along the x (or y) direction (depending on the control), and the inversion changes the precession sense of the spins. The π-pulse leads to a refocusing of the inhomogeneous ensemble after a second time lapse T_e. The reader interested in

more technical details about spin echo experiments could refer to [101, 35, 43].

Spin echoes produced by different pulses are studied in detail in the next chapter, devoted to SNR maximization. Here, a simple illustration is made by comparing Δ-robust pulses and square pulses, in a regime where the spin back action is not negligible (cooperativity $C = 27$). We chose $N = 2917$ spins, distributed according to a distribution $\rho_{Purcell}$ (equation (1.72)) of width $\Omega_p = 310$ kHz. The coupling constant is $g = 4240$ Hz, and the damping rate is given by $\kappa = 157$kHz. As illustrated in figure 3.15, robust pulses allow an efficient control of the spin ensemble and the echo can be easily measured on the X and Y quadratures. On the other side, square pulses cannot prepare a spin echo correctly.

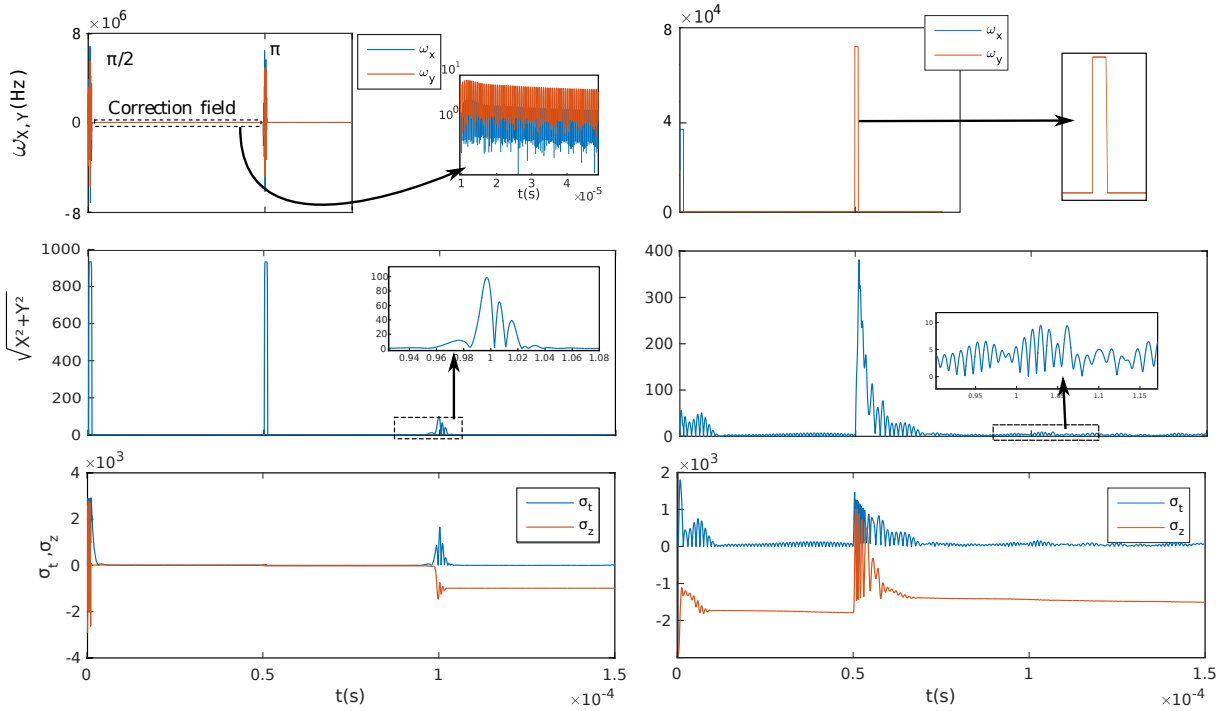

Figure 3.15: Numerical comparison between Δ-robust (left) and the square pulses (right) for a spin echo experiment. The top panels display the control fields. We point out the very simple structure of the square pulses, while a correction field is applied between the $\pi/2$ and the π rotations in the first case. This correction originates from the back action of the spins onto the cavity. Panels in the middle show the evolution the electromagnetic field. On these curves we can see the spin echo that occurs around the time $t = 10^{-4}$ s. With robust pulses, the shape of the echo is well preserved and its maximum is very high, contrary to the other case, where the echo is deformed and has many small bumps. Lower panels present the evolution of the spin magnetization ($\sigma_t = \sqrt{\sigma_x^2 + \sigma_y^2}$). With these curves it is easy to see the relaxation mechanism which occurs when σ is high and not corrected by the control field.

3.5.3 Experimental realization of bump pulses

Bump pulses have been applied experimentally at the Quantronics group (CEA of Saclay). Figure 3.16 shows the pulse produced by the experimental setup. The latter is not perfect, but it is accurate enough to improve state-of-the-art experiments. Figure also shows the FID produced by the pulse. This is the first time that a FID is recorded by this kind of experiment. As we can see, the decay of the FID is slower than the one predicted by the theory. For the moment, the origin of this small disagreement is not fully understood. Is it an inaccuracy of the model, of the pulse shaping, or something more fundamental? However, the agreement with spin-echo simulations is very good.

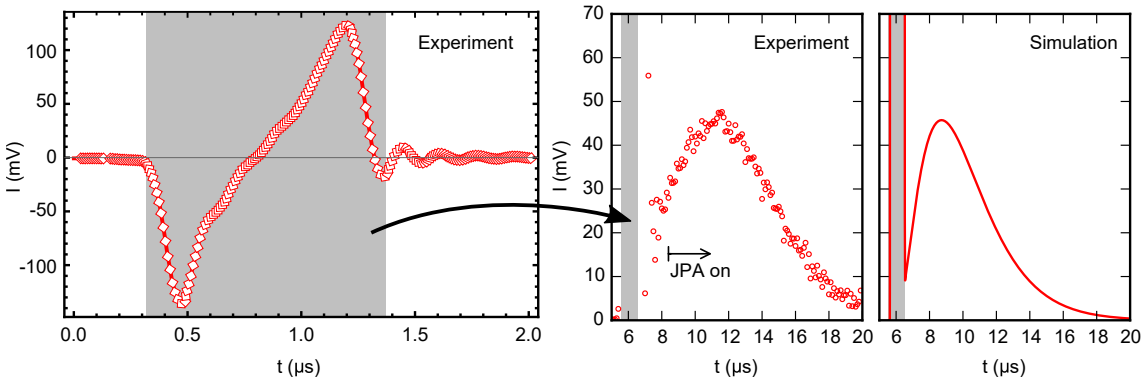

Figure 3.16 – Experimental implementation of a bump pulse. The left panel shows a $\pi/2$- pulse input by the inductor wire in the cavity. The middle and right panels show the experimental and theoretical FID induced by the pulse. The gray areas represent the pulse. Notice that the scale of the pulse and the FID is different, because the JP-Amplifier is switched on during the FID measurement.

Experimental results are going to be published in [133].

3.6 Conclusion

The evolution of the system has been written in a form which highlights the understanding of control mechanisms. The new form of $\hat{U}$ consists of a product of three operators $\hat{U}_F, \hat{U}_S, \hat{U}_E$. Each of them has a specific meaning. $\hat{U}_E$ is the evolution of the electromagnetic field without interaction with the spins, as presented in section 1.3.2. $\hat{U}_S$ is the evolution of the spin ensemble in the semi-classical model, with the electromagnetic field replaced by its mean value. Finally, $\hat{U}_E$ describes the entanglement between the spins and the cavity.

This new expression of $\hat{U}$ has allowed us to use non-linear generalized functions to derive simple approximated expressions, and to generalize square pulses. A particularly interesting pulse family is the one of bump pulses. They are smooth functions of compact support, and they realize approximated Dirac pulses. Bump pulses have been studied analytically, numerically and implemented experimentally at the Quantronics group. Contrary to square pulses, bump pulses take into account the cavity response and the spins are controlled efficiently.

Following the control strategies given by generalized functions, new broadband optimal pulses have been computed using numerical algorithms. As bump pulses, optimized pulses are smooth functions of compact support and they depend on a few parameters. Moreover, they can be designed in the bad or the good cavity regimes. Optimizations

in the good cavity regime can be considered as a proof of principle. A complete work of characterization is still missing (time/energy physical limits, control mechanisms...). These tasks are not easy to complete, because of the long computation time. On the other side, pulses constructed in the low coupling regime are well understood and standard $\pi, \pi/2$ universal rotations robust against g, and Δ variations have been derived. These pulses are similar to the ones already derived in NMR, but they take into account cavity constraints.

Finally, two different applications have been proposed. The first one is the measurement of the FID. New pulses allow its measurement, while it is impossible with state-of-the-art pulses. Numerical simulations show that the result of a T_1-inversion recovery sequence could differ if it is calculated with a full-quantum model or the semi-classical model. Then, the control sequence can be useful to characterize an experiment in the good cavity regime. The second example of application is a spin-echo sequence in the high cooperaitivity regime, but with a bad cavity. In this case, we show that the new method allows us to prepare an echo, contrary to the state-of-the-art approach.

The spin echo sequence is the main building block of current experiments, and optimal control theory can push the process to its physical limit in terms of sensitivity. Next chapter focuses on this point through the maximization of the SNR.

Chapter 4

Maximization of the Signal to Noise Ratio

The previous chapters are devoted to general methods, and only a few examples are detailed. This chapter focuses on a very specific problem. A current experimental challenge in cavity QED is to maximize the Signal-to-Noise-Ratio (SNR) of spin echos [35, 162, 146, 98]. One of the original contributions of this work is to show under which conditions the SNR can be maximized. Additionally, a straightforward application of new pulses introduced in section 3 allows to reach the SNR physical limit. In this chapter, the SNR maximization problem is tackled analytically for spin-echo and CPMG sequences [35]. Simple analytic formulas are derived and maximization conditions are found in section 4.1. The results are more general than the one presented in [19]. In a second step, the problem is investigated numerically in order to test the efficiency of pulses. This is the purpose of section 4.2.

4.1 Analytic approach

Experiments are made in a bad cavity regime [21, 132], where the semi-classical model is valid. Therefore, in this chapter, we restrict our analysis to the semi-classical equations.

The theory presented in this chapter is constructed in successive steps, which are used at different stages. For example, maximization rules derived for CPMG sequences depend on spin echo maximization rules, which depend on the dynamics of the system. Each result can be considered independently but only a sequential development from equations of the dynamics allows a good understanding of the physics. Therefore, in order to make the structure of this chapter as clear as possible, we start with a summary:

1. A spin echo is entirely described by a real number $\mathcal{S}$. This number is simply the integral over time of the electromagnetic field. We show that this quantity is a solution of the transcendent equation: $\mathcal{S} = \mathcal{S}_0 \cos^2(g\mathcal{S})$ where g is the coupling constant of the spins and $\mathcal{S}_0$ is a simple function of the system parameters. In the limit $g \to 0$ we obtain the relation : $\mathcal{S} = \mathcal{S}_0$.

2. The SNR of a spin echo is proportional to the quantity: $SNR_{1\ echo} \propto \frac{\mathcal{S}^2\kappa^2}{16\pi\rho_0^2(0)}\Lambda[\rho_0]$, where κ is the damping rate of the cavity, ρ_0 is the offset distribution and Λ is a measure that depends only on κ. From this relation, we show that the SNR is maximized when the spin ensemble is perfectly excited on the transverse plane. We also show the existence of a non-trivial maximum of the SNR according to the

parameters of the setup. Thus, the setup design has an important impact on the SNR and an improvement of several orders of magnitude is expected in some cases.

3. A CPMG sequence allows a great enhancement of the SNR, which can be expressed by: $SNR_{CPMG} = (SNR_{1\ echo} - \langle \delta SNR \rangle)/(e^{T_r/T_2} - 1)$ where $\langle \delta SNR \rangle$ is the mean value of the (small) deviations of the SNR at each iteration, T_r is the repetition time and T_2 is the transverse relaxation time. We show that reducing the ratio T_r/T_2 is always more advantageous than reducing $\langle \delta SNR \rangle$.

4.1.1 Main definitions

The system

The system is governed by the semi-classical equation (1.6). Since spin-spin quantum correlations are negligible, we can express the spin ensemble with a continuous ensemble over g and Δ via the probability distributions $\rho_1(g)$ and $\rho_0(\Delta)$ [1]:

$$|\Psi(t)\rangle = \sqrt{\rho_1(g)\rho_0(\Delta)}|\psi(g,\Delta,t)\rangle. \tag{4.1}$$

Consequently, the mean value of $\hat{\sigma}_\mu = \sum_{n=1}^{N} \hat{\sigma}_\mu^n$ is given by:

$$\langle \hat{\sigma}_\mu \rangle = N \int d\Delta.dg.\rho_1(g).\rho_0(\Delta).\langle \psi(g,\Delta,t)|\hat{\sigma}_\mu|\psi(g,\Delta,t)\rangle. \tag{4.2}$$

Spin echo

In this section, we are mostly interested in the echo [101, 35, 43]. Therefore, we assume an excitation along y and we assume that the time T_e between the excitation and the inversion pulses is long enough so that it can be taken as infinity. The origin of the time axis is chosen at the center of the echo, i.e. when all spins are in phase. Under these conditions, the initial state of the spin ensemble is:

$$|\psi(g,\Delta,-T)\rangle = e^{i\Delta.T\hat{\sigma}_z/2}.e^{-i\pi\hat{\sigma}_x/2}|\uparrow\rangle, \tag{4.3}$$

where the limit $T \to \infty$ will be taken later. This equation is true only if the initial state is perfectly prepared. To study realistic situations, we prefer:

$$|\psi(g,\Delta,-T)\rangle = e^{i\Delta.T\hat{\sigma}_z/2}.e^{-i\phi(g,\Delta)\hat{\sigma}_x/2}|\uparrow\rangle, \tag{4.4}$$

where $\phi(g,\Delta)$ is an angle that characterizes an imperfect excitation.

In experiments, measurements are possible only via the electromagnetic field. Therefore, we focus on the quadratures X and Y (in the weak coupling regime, field quadratures are entirely determined by their mean values and we drop the notation $\langle . \rangle$ for simplicity). Because of the initial state (4.3), $\langle \hat{\sigma}_x \rangle = 0$ for any time t, and we consider only X [2]. From (1.60), and using Green functions we determine:

$$X(t) = -\int_{-\infty}^{t} dt' e^{-\kappa(t-t')/2} \langle g\hat{\sigma}_y \rangle(t'). \tag{4.5}$$

[1] The formalism is the same as the one presented in section 2.4.1. However, we do not use quantized field here, because the electromagnetic field is a classical quantity.

[2] This fact is due to the symmetry of the system. the magnetization of negative offsets cancels the magnetization of positive offsets on the x axis.

However, for an SNR analysis, it is the integral of the echo, $\mathcal{S}$, which is interesting:

$$\mathcal{S} = \int X(t)dt. \tag{4.6}$$

This useful quantity characterizes the entire dynamics, and more specifically it gives the field back action to a spin during an echo.

CPMG sequence

A CPMG (Carr-Purcell-Meiboom-Gill) experiment [43, 35] starts exactly as a spin echo experiment but additional π-pulses are used in order to produce multiple spin refocusings. Concretely, a π-pulse is applied after each echo with a delay T_e. The resulting sequence is of the form: $\pi - T_e - echo - T_e - \pi - T_e - echo - T_e - \pi$.... Such a sequence takes the form of a product of evolution operators. In the case of M echos, we have:

$$\hat{U} = \mathbb{T}\left[\prod_{k=0}^{M} \hat{U}_{echo,k}.e^{-i\Delta T_e\hat{\sigma}_z/2}.\hat{U}_\pi.e^{-i\Delta T_e\hat{\sigma}_z/2}\right], \tag{4.7}$$

where $\mathbb{T}$ denotes time ordering and $\hat{U}_{echo,k}$ is a possible evolution induced by the back action of the E.M. field during the echo. $\hat{U}_\pi$ is the evolution operator during a π pulse. It has a duration T_c, and under the short pulse approximation, it is reduced to $\hat{U}_\pi \simeq e^{-i\pi\hat{\sigma}_y/2}$. The expression of $\hat{U}_{echo,k}$ will be specified later. During a CPMG sequence, relaxation mechanisms are generally important and unitary transformations are not sufficient for a good description of experiments. In most of experiments, the T_1 relaxation is negligible during pulses. In this case, only the T_2 relaxation is measurable between two consecutive echoes, with a decrease of the Bloch vector amplitude by a factor e^{-T_r/T_2}. Therefore, $\langle\hat{\sigma}_y\rangle_{k+1}/\langle\hat{\sigma}_y\rangle_k = e^{-T_r/T_2}$. Notice the introduction of the repetition time T_r, which is the period between each sequence iteration. By definition, it is given by the sum of the control duration T_c and twice the time which separates the echo and the pulses: $T_r = T_c + 2T_e$.

Signal-to-noise-ratio

The signal to noise ratio is by definition the ratio between the signal power and the noise power [35, 162]. In the context of quantum measurements, the same definition is used, except that the noise has a lower bound given by quantum fluctuations:

$$SNR = \frac{\int X^2(t)dt}{(\Delta X)^2}. \tag{4.8}$$

Two definitions are used in the literature for the SNR: the ratio of powers, or the ratio signal/standard deviation. ***In this manuscript, the first definition is chosen to avoid square roots in calculations. Analytic expressions and numerical results can be converted to the other notation by calculating their square root.*** During a signal-amplification process, the noise can be amplified as well, but this additional step is not considered in this paper. We assume that we work around the quantum noise limit $(\Delta X)^2 \simeq 1/4$. This assumption remains realistic for experiments at ultra-low temperature [19, 60]. For practical reasons, the following notation is introduced:

$$\mathcal{S}^{(2)} = \|X\|_{L^2}^2 = \int X^2(t)dt. \tag{4.9}$$

The sensitivity can be further enhanced using CPMG sequences. Multiple refocusing increases the integration time but the noise remains constant. Thus, the accumulation of echoes increases the signal contribution. Assuming that echoes do not overlap leads to the following SNR:

$$SNR_{CPMG} = \sum_{k=0}^{M} SNR_k, \tag{4.10}$$

where SNR_k is the signal to noise ratio of the echo number k. Notice that the SNR decreases as a function of k, due to the relaxation.

4.1.2 Dynamics during a spin echo

In this paragraph, we derive the time evolution of several physical quantities. We proceed in two steps. First, we focus on the easiest case: when the spin back action is negligible, and the results of [19] are recovered. This is also a good introduction for the second part, where a more general case is considered. The last paragraph shows a comparison between analytic formulas and realistic simulations of the full system.

Echo in the linear regime

The linear regime is obtained when the field back action is negligible ($g.X(t) \simeq 0$). From the semi-classical equations and (4.3), we determine:

$$\langle g\hat{\sigma}_y \rangle(t) = g_0 N \int d\Delta \rho_0(\Delta) \cos(\Delta t), \tag{4.11}$$

where we introduce the mean value of g : $g_0 = \int g.\rho_1(g).dg$. It is then possible to compute the time evolution of the E.M. field. The core of the following computation setps are basic applications of the Fubini theorem [141] and the Fourier-transform. First we determine:

$$X(t) = -g_0 N \int d\Delta \rho_0(\Delta) \left(\frac{e^{i\Delta t}}{\kappa - 2i\Delta} + \frac{e^{-i\Delta t}}{\kappa + 2i\Delta} \right). \tag{4.12}$$

A second time integration is performed. After inserting (4.12) into (4.6) and using the definition of the Dirac distribution:

$$\delta_0(\Delta) = \frac{1}{2\pi} \int e^{i\Delta t} dt, \tag{4.13}$$

we obtain:

$$\mathcal{S} = -2\pi g_0 N \int d\Delta \rho_0(\Delta) \left(\frac{\delta_0(\Delta)}{\kappa - 2i\Delta} + \frac{\delta_0(\Delta)}{\kappa + 2i\Delta} \right). \tag{4.14}$$

Therefore,

$$\mathcal{S} = \mathcal{S}_0 \equiv -\frac{4\pi g_0 N}{\kappa} \rho_0(0). \tag{4.15}$$

To proceed further, a spin distribution must be specified. Several cases are investigated.

ρ_0 is a Lorentzian distribution:

$$\rho_0(\Delta) = \frac{\Omega}{2\pi}\frac{1}{\Delta^2 + \Omega^2/4}, \tag{4.16}$$

since $\rho_0(0) = 2/\pi\Omega$, we have:

$$\mathcal{S}_{Lorentz} = -\frac{8g_0N}{\Omega\kappa}. \tag{4.17}$$

Notice the very simple result. Nevertheless, this result holds only in an ideal case. In practice, the spins are not perfectly excited. What happens in this latter case?

Imperfect excitation: An effective distribution of offsets and an effective number of spins are defined from equation (4.4):

$$\rho_{eff}(\Delta) = \frac{\rho_0(\Delta)\sin(\phi(g_0,\Delta)}{\int d\Delta\rho_0\sin(\phi(g_0,\Delta)} \tag{4.18}$$

$$N_{eff} = N\int d\Delta\rho_0(\Delta)\sin(\phi(g_0,\Delta)). \tag{4.19}$$

Here, for the sake of simplicity, we assume that all the spins have the same coupling constant g_0. The angle ϕ is generally close to $\pi/2$, then, a first order expansion of the sine function is possible: $\sin(\phi(g_0,\Delta) = 1-\epsilon(\Delta)$. It follows that $N_{eff} = N(1-\langle\rho|\epsilon\rangle)$ and the integrated echo is given by:

$$\mathcal{S}_{eff} = \mathcal{S}_0(1-\epsilon(0)). \tag{4.20}$$

This result confirms the intuition: imperfect excitations decrease the signal.

Echo in the non-linear regime

The linear regime is very restrictive because when the spins emit photons to produce a measurable signal, they should relax to their ground state. Subsequently, we consider the field back action to the spin dynamics. The method is similar to the previous one, the first step is to provide the time evolution of the mean magnetization:

$$\langle g\hat{\sigma}_y\rangle(t) = N\int dg.d\Delta.\rho_1(g).\rho_0(\Delta).g.\cos(\Delta t).f(g,\Delta,t), \tag{4.21}$$

where the function f will be specified later. Then, the integrated echo is given by:

$$\mathcal{S} = -N\int dg.g\int dt_1\int_{-\infty}^{t_1} dt_2.e^{-\kappa(t_1-t_2)/2}\int d\Delta.\rho_1.\rho_0.f.\cos(\Delta t_2). \tag{4.22}$$

The second step is to introduce the Fourier transform of f and to permute integrals over Δ,ω with the integral over time:

$$\begin{aligned}\mathcal{S} &= -2\pi N\int dg.d\Delta.d\omega.g.\rho_1.\rho_0.\tilde{f}(g,\Delta,\omega)\times\left(\frac{\delta_0(\Delta-\omega)}{\kappa-2i(\Delta-\omega)}+\frac{\delta_0((\Delta+\omega)}{\kappa+2i(\Delta+\omega)}\right)\\ &= -\frac{2\pi N}{\kappa}\int dg.d\Delta.g.\rho_1.\rho_0\left(\tilde{f}(g,\Delta,\Delta)+\tilde{f}(g,\Delta,-\Delta)\right)\end{aligned}$$

This result is exact, nevertheless, $\tilde{f}$ is an unknown function and a numerical integration is required without new assumptions. In order to proceed further, we use the following approximated solution:

Proposition 4 (FT of $f(g,\Delta,t)$): *If the transition between the initial and final values of f is shorter than other characteristic times, the Fourier transform of $f(g,\Delta,t)$ is given by:*

$$\tilde{f}(\omega) = \frac{1}{2}(1+\cos(g\mathcal{S}))\delta_0(\omega). \tag{4.23}$$

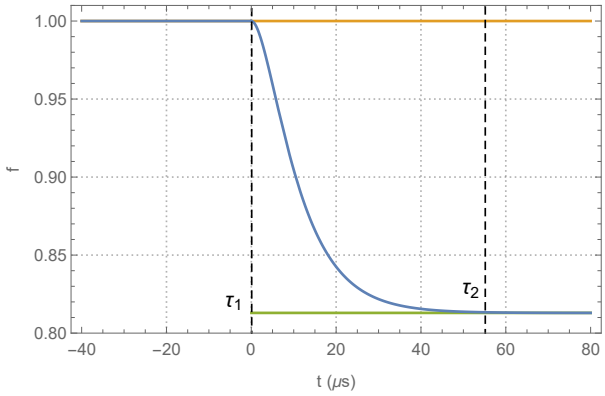

Figure 4.1 – Example of function f (blue curve) for $g = g_0 = 2664$ rad/s, $\kappa = 774.7 \times 10^3$ rad/s $\Omega = 10^7$ rad/s. The orange horizontal line is the first term of (4.27) and the green horizontal line is the second. A transition is observed between the times τ_1 and τ_2 (represented by vertical dashed lines).

Proof. In order to determine f, we must determine $\langle\psi|\hat{\sigma}_y|\psi\rangle$. The simplest correction of the order zero (linear regime, i.e. no back-back action of the electromagnetic field) is a first order expansion of the Magnus operator[22] around $t = 0$:

$$\mathbb{T}e^{-i/2\int_{-T}^{t}dt'(gX(t')\hat{\sigma}_x+\Delta\hat{\sigma}_z)} \simeq e^{-i/2\int_{-T}^{t}dt'gX(t')\hat{\sigma}_x}e^{-i\Delta/2(t+T)\hat{\sigma}_z}. \tag{4.24}$$

Then, the use of the initial condition (4.3) allows us to write:

$$\langle\psi|\hat{\sigma}_y|\psi\rangle \simeq \cos(g\mathcal{S}(t))\cos(\Delta t), \tag{4.25}$$

where we introduce the partially integrated echo:

$$\mathcal{S}(t) = \int_{-T}^{t} X(t')dt' \simeq \int_{-\infty}^{t} X(t')dt'. \tag{4.26}$$

We can compute the FT of $f = \cos(g\mathcal{S}(t))$. For that purpose, we express the function with the following expansion:

$$f(g,\Delta,t) = 1 + \epsilon(g,\Delta)\mathbb{I}_{[\tau_1,\infty[}(t) + h(g,\Delta,t), \tag{4.27}$$

where $\epsilon(g,\Delta) = f(g,\Delta,\infty) - 1$ describes the steady state of f and h is a function with a (approximate) compact support on $[\tau_1,\tau_2]$. It describes the transition of f during the echo. An example of curve is presented in figure 4.1. The FT of the first term is trivial and gives a Dirac distribution. One must proceed carefully for the two other terms.
Computation of $FT[\epsilon\mathbb{I}_{[\tau_1,\infty[}]$: The Fourier transform of a constant can be computed with the following regularization:

$$\begin{aligned} FT[\mathbb{I}_{[\tau_1,\infty[}](\omega) &= \frac{1}{2\pi}\int_{\tau_1}^{\infty} e^{-i\omega t}dt \\ &= \frac{1}{2\pi}\lim_{\varepsilon\to 0}\int_{\tau_1}^{\infty} e^{-t(\varepsilon+i\omega)}dt \ ; \ \varepsilon > 0, \end{aligned}$$

which is a complex valued distribution:

$$FT[\mathbb{I}_{[\tau_1,\infty[}](\omega) = \lim_{\varepsilon\to 0} \frac{e^{-\tau_1(\varepsilon+i\omega)}}{2\pi}\frac{\varepsilon - i\omega}{\varepsilon^2+\omega^2}. \tag{4.28}$$

We recognize that the real part is a Lorentzian with an area of $1/2$, and in the limit $\varepsilon \to 0$ it gives a Dirac distribution of weight $1/2$. The imaginary part gives a principal value distribution:

$$FT[\mathbb{I}_{[\tau_1,\infty[}](\omega) = e^{-i\omega\tau_1}\left[\frac{1}{2}\delta_0(\omega) - \frac{i}{2\pi}\mathfrak{p}\left(\frac{1}{\omega}\right)\right]. \tag{4.29}$$

It is possible to compute the action of the principal value on a test function ϕ:

$$\begin{aligned}&\frac{-i}{2\pi}\langle\phi(\omega)|e^{-i\omega\tau_1}\mathfrak{p}(1/\omega)\rangle = \\ &\quad\frac{-i}{2\pi}\lim_{\varepsilon\to 0}\left(\int_{-\infty}^{-\varepsilon} d\omega\frac{\phi(\omega)}{\omega}e^{-i\omega\tau_1} + \int_{\varepsilon}^{\infty} d\omega\frac{\phi(\omega)}{\omega}e^{-i\omega\tau_1}\right).\end{aligned}$$

The next step consists of splitting the test function into odd and even functions: $\phi = \phi_- + \phi_+$. We start with the even one:

$$\frac{-i}{2\pi}\langle\phi_+(\omega)|e^{-i\omega\tau_1}\mathfrak{p}(1/\omega)\rangle = \frac{2\tau_1}{2\pi}\int_0^{\infty} d\omega\phi_+(\omega)\frac{\sin(\omega\tau_1)}{\omega\tau_1}.$$

In general, τ_1 is small (see figure 4.1), then we can take the limit $\tau_1 \to 0$ and it cancels the integral. For the odd function, we have:

$$\frac{-i}{2\pi}\langle\phi_-(\omega)|e^{i\omega\tau_1}\mathfrak{p}(1/\omega)\rangle = \frac{-2i\tau_1}{2\pi}\lim_{\varepsilon\to 0}\int_{\varepsilon}^{\infty} d\omega\phi_-(\omega)\frac{\cos(\omega\tau_1)}{\omega\tau_1}.$$

The problem of the singularity is solved with integration by parts. By using the following identities:

$$\begin{aligned}\frac{d}{d\omega}\frac{(n-1)\cos(\omega\tau_1)}{\omega^n\tau_1} &= -n(n-1)\frac{\cos(\omega\tau_1)}{\omega^{n+1}\tau_1} - (n-1)\frac{\sin(\omega\tau_1)}{\omega^n}\\ \sum_{n=1}^{\infty}\frac{n-1}{\omega^n} &= \frac{1}{(\omega-1)^2}\\ \sum_{n=1}^{\infty}\frac{n(n-1)}{\omega^{n+1}} &= \frac{2}{(\omega-1)^3},\end{aligned}$$

we determine:

$$\begin{aligned}&\frac{-i}{2\pi}\langle\phi_-(\omega)|e^{i\omega\tau_1}\mathfrak{p}(1/\omega)\rangle\\ &\quad= \frac{-2i\tau_1}{2\pi}\left[\lim_{\varepsilon\to 0} -\Phi_-(\varepsilon)\frac{\cos(\varepsilon\tau_1)}{\tau_1}\left(\frac{2}{(\varepsilon-1)^3} + \frac{\varepsilon+1}{\varepsilon^2}\right) + \int_0^{\infty} d\omega\phi_-(\omega)\frac{\sin(\omega\tau_1)}{(\omega-1)^2}\right],\end{aligned}$$

where we introduce, Φ_-, the integral of ϕ_-. The integral involving the sine function can be evaluated with the residue theorem and it vanishes when $\tau_1 \to 0$. Moreover,

the term with the cosine vanishes, due to $\Phi_-(\varepsilon)$. The latter converges toward 0 faster than $1/\varepsilon^2$ diverges. To summarize:

$$\begin{aligned}&\frac{-i}{2\pi}\langle\phi_-(\omega)|e^{-i\omega\tau_1}\mathfrak{p}(1/\omega)\rangle\\&\quad=\frac{1}{\pi}\int_0^\infty d\omega\sin(\omega\tau_1)\left(\frac{\phi_+(\omega)}{\omega}-i\frac{\tau_1\phi_-(\omega)}{(\omega-1)^2}\right)\simeq 0 \text{ when } \tau_1\to 0.\end{aligned} \tag{4.30}$$

Computation of $FT[h](\omega)$: Here we provide few arguments to justify the fact that this function is negligible. By using the Plancherel theorem we determine:

$$2\pi\parallel h\parallel_{L^2}=\parallel\tilde{h}\parallel_{L^2}. \tag{4.31}$$

Here, the norm is bounded by the norm of the rectangle, which includes h (see figure 4.1):

$$\parallel h\parallel_{L^2}\leq|\epsilon|/\sqrt{\tau_2-\tau_1}. \tag{4.32}$$

Then, with a simple geometric argument, we can relate the norm to the maximum value. The Fourier transform gives $(\tau_2-\tau_1)\to 1/(\tau_2-\tau_1)$, then:

$$\max(|\tilde{h}|)\lesssim\frac{|\epsilon|}{2\pi}\sqrt{\tau_2-\tau_1}\ll|\epsilon|. \tag{4.33}$$

Approximate expression of $\tilde{f}$: with equation (4.25) we deduce that at first order: $1+\varepsilon=\cos(g\mathcal{S})$. Moreover, in the case $\max(|\tilde{h}|)\to 0$ and $\tau_1\to 0$ we can write:

$$\tilde{f}(\omega)=\frac{1}{2}(1+\cos(g\mathcal{S}))\delta_0(\omega). \tag{4.34}$$

□

As illustrated in figure 4.2, the approximations give us a simple mechanism of the relaxation process occurring in the non-linear regime.

It is now possible to write an approximated solution in the non-linear regime. In the case of a single value of $g=g_0$:

$$\mathcal{S}_{g_0}=\mathcal{S}_0\cos^2(g_0\mathcal{S}_{g_0}/2). \tag{4.35}$$

Notice that even if this equation looks simple, it is a transcendent equation, and no analytic solution exists.

In the rest of this section, we focus mostly on a negligible g distribution. However, if g is not negligible, then equation (4.35)can be modified accordingly by integrating over ρ_1:

$$\mathcal{S}_{\langle g\rangle}=-\frac{4\pi N}{\kappa}\rho_0(0)\int dg\rho_1(g).g.\cos^2(g\mathcal{S}_{\langle g\rangle}/2) \tag{4.36}$$

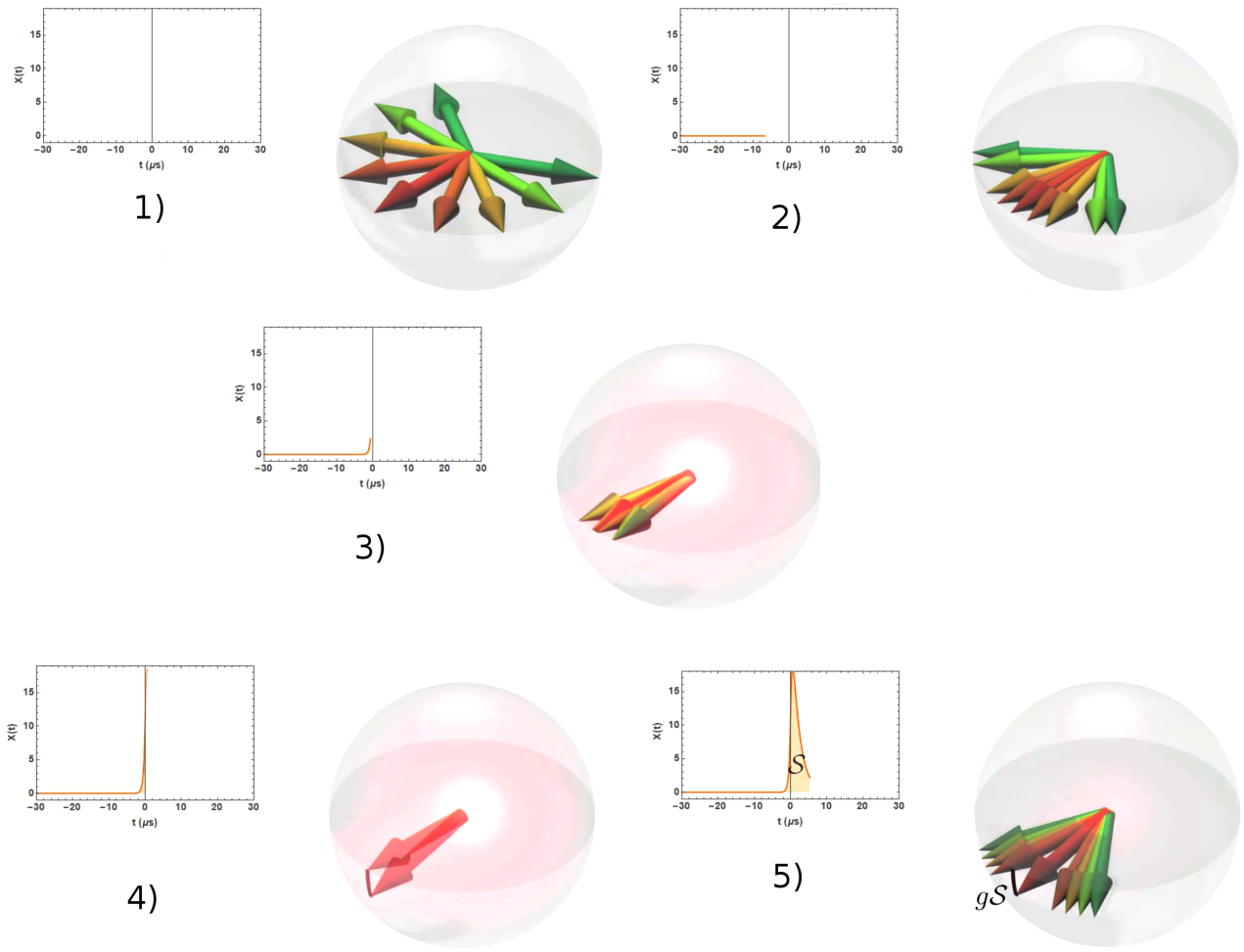

Figure 4.2 – Dynamics during a spin echo. 1) first, each spin is dephased and the average magnetization is zero. In absence of external driving, the electromagnetic field is in its ground state. 2) the spin ensemble starts to refocus. 3) Spins are closed to be in phase, and they start to emit photons, nevertheless, the field is not strong enough for having a visible effect on the dynamics. 4) At the maximum of the echo, the emission of photons is important and emitted photons can interact again with the spins. This produces a spin relaxation. 5) Spins dephase. At the end of the echo, they have rotated of an angle proportional to the area of the electromagnetic field produced during the echo.

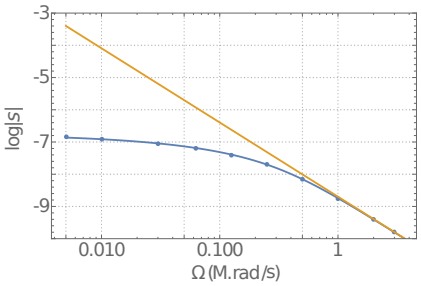

Figure 4.3: Integrated echo as a function of the distribution bandwidth. Exact values from numerical simulations are given by blue dots. The zero and first order analytic expressions (equations (4.15) and (4.35)) are represented respectively by the orange and the blue solid lines.

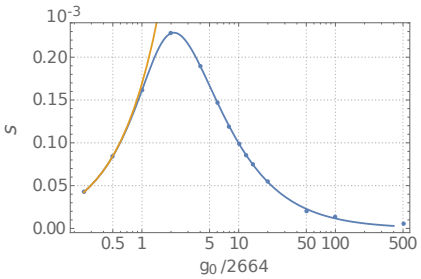

Figure 4.4: Integrated echo as a function of the coupling constant. Exact values from numerical simulations are given by blue dots. The zero and first order analytic expressions (equations (4.15) and (4.35)) are represented respectively by the orange and the blue solid lines. At $g_0/2664 > 401$, the approximation breaks down because $g_0 S > \pi$, nevertheless, it occurs in a regime where the semi-classical approximation is not valid anymore.

Numerical analysis

Formulas (4.15) and (4.35) have been checked numerically in several situations. First, the example of a spin ensemble with a Lorentzian distribution is studied. We choose $g = g_0 = 2664$ rads^{-1}, and $\kappa = 0.986 \times 10^6\ s^{-1}$, and $\mathcal{N} = 13500$. The dynamics of the system are integrated numerically with equations (1.60) from the initial state (4.3). Notice that $\rho_0(0)$ is evaluated numerically, because of the discretization of the distribution. The comparison with "exact" values and the zero/first order analytic formulas is shown in figure 4.3. A similar analysis is made as a function of g_0. In this case, we have $\Omega = \kappa$. The related results are plotted in figure 4.4. The two figures show a very good agreement with the first order expansion, thus this approximation is accurate on the entire validity domain of the semi-classical model.

4.1.3 Maximizing the SNR

SNR of a single echo

At this point, all the tools are gathered for the computation of (4.9). The main steps are the same as the ones followed during the computation of $\mathcal{S}$, but calculations are restricted to the zero and first order expansions. In the previous section, analytic expressions of $\tilde{f}$ are provided: $\tilde{f}(g,\omega) = \alpha(g).\delta_0(\omega)$ with:

$$\alpha(g) = \begin{cases} 1 & \text{for the order } 0 \\ \cos^2(g\mathcal{S}/2)) & \text{for the order } 1 \end{cases} \tag{4.37}$$

The next steps of the calculations are the same as before. First, X^2 is determined by introducing $\tilde{f}$, and this allows us to simplify the expression, due to the presence of two Dirac distributions. The second step is to integrate again over time and to permute integrals. Finally, we arrive at the following expression:

$$\mathcal{S}^{(2)} = \pi N^2 \left(\int dg \rho_1(g).g.\alpha(g) \right)^2 \times \int \frac{d\Delta}{\kappa^2/4 + \Delta^2} \left(\rho_0(\Delta)^2 + \rho_0(\Delta)\rho_0(-\Delta) \right).$$

The integral over g can be replaced as soon as $\mathcal{S}$ is computed (see equation (4.36)). It follows:

$$\mathcal{S}^{(2)} = \frac{\mathcal{S}^2\kappa^2}{16\pi\rho_0(0)^2} \int \frac{d\Delta}{\kappa^2/4 + \Delta^2} \left(\rho_0(\Delta)^2 + \rho_0(\Delta)\rho_0(-\Delta) \right). \tag{4.38}$$

For the sake of conciseness, the measure Λ and the even part of ρ_0 are introduced. They are respectively defined by: $d\Lambda = d\Delta/(\kappa^2/4 + \Delta^2)$ and $\rho_0^+(\Delta) = (\rho(\Delta) + \rho(-\Delta))/2$. Finally,

$$\boxed{\mathcal{S}^{(2)} = \frac{\mathcal{S}^2\kappa^2}{16\pi\rho_0^2(0)} \Lambda(2\rho_0\rho_0^+).} \tag{4.39}$$

This general result can be specified by choosing examples of offset distributions.

Lorentzian distribution:

$$\rho_0(\Delta) = \frac{\Omega}{2\pi}\frac{1}{\Delta^2 + \Omega^2/4}, \tag{4.40}$$

gives:

$$\mathcal{S}^{(2)}_{Lorentz} = \frac{\mathcal{S}^2\kappa\Omega(\kappa+2\Omega)}{16\pi(\kappa+\Omega)^2}. \tag{4.41}$$

Perturbation of the excitation profile: Here, the effective distribution (4.18) is applied and a single value of g is assumed:

$$\mathcal{S}^{(2)}_{eff} = \pi N^2 g_0^2 \Lambda\left((\rho_0^2(1-\epsilon)^2\right). \tag{4.42}$$

From equation (4.39), a gradient method allows to determine the maximum. Results are presented in table 4.1 The introduction of the first order expansion has significant consequences. For some offset distributions, the optimum can change and take non-trivial values. If one has a uniform distribution, this effect can be seen only with g_0, but it is extended to Ω and κ with a Lorentzian distribution. A numerical calculation is required to evaluate the set of optimum parameters. For example, figure 4.5 highlights the different cases of (g^*, Ω^*) presented in table 4.1. A specific example is given in table 4.2.

What do we learn from these results? *First of all, it is better to excite perfectly the ensemble of spins (i.e. with $\epsilon = 0$). This statement is obvious in the linear regime but it is still true in the nonlinear one. This goal can be reached with robust optimal pulses (chapter 3). These pulses allow us to prepare the initial state correctly, and thus, they maximize N_{eff} and minimize ϵ. The second point is that the maximum is given by non-trivial values of g, Ω and κ. Depending on the experimental constraints, an optimal solution can be computed in few seconds with equation (4.39).*

	maximum
N	∞
g_0	∞ order 0 g^* order 1
Ω	0 order 0 Ω^* order 1
κ	0 order 0 κ^* order 1
$\epsilon(\Delta)$	0

Table 4.1: Position of the maximum of $\mathcal{S}^{(2)}$ for each parameter. All results are obtained by considering $\rho_1(g) = \delta_{g_0}(g)$.

N	13500
g_0	2664 rads^{-1}
Ω^*	0.197 Mrads^{-1}
κ	$0.974\times10^6 s^{-1}$
$\epsilon(\Delta)$	0

Table 4.2: Examples of values that give an optimum Ω^* in the case of a Lorentzian distribution.

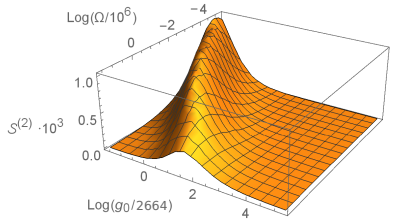

Figure 4.5: $\mathcal{S}^{(2)}$ as a function of g_0 and Ω for a Lorentzian distribution. Numerical values necessary for their calculations are the same as the ones used since the beginning of this chapter (see section 3.5.2).

SNR of CPMG sequences

The previous analysis of a single echo allows us to go further, and to explore the case of CPMG sequences. Here, we are interested in the SNR defined by equation (4.10). From section 4.1.3, it is known that echoes are correlated and this influences the SNR: this introduces fluctuations of the successive SNR. The relaxation effect due to the non-linear dynamics can be hidden into an effective distribution of spins, which changes after successive echos. Equation (4.42) shows that $\mathcal{S}^{(2)}$ can be split into an unperturbed and a perturbation parts. Then, for the echo number k of the CPMG sequence we have:

$$\mathcal{S}^{(2)}_k = \mathcal{S}^{(2)} - \delta\mathcal{S}^{(2)}_k. \tag{4.43}$$

Another important point is the number of echoes that can be produced:

$$M_r \equiv 5T_2 \bmod T_r \approx 5T_2/T_r. \tag{4.44}$$

Therefore, after inserting (4.43), (4.44), (4.8) into (4.10), and under the assumption that variations of $\delta\mathcal{S}_k^{(2)}$ remains around their average ($\delta\mathcal{S}_k^{(2)} \simeq \langle\delta\mathcal{S}^{(2)}\rangle$), we determine:

$$SNR_{CPMG} \simeq \frac{\mathcal{S}^{(2)} - \langle\delta\mathcal{S}^{(2)}\rangle}{(\Delta X)^2}\frac{1}{e^{T_r/T_2}-1}. \tag{4.45}$$

Notice that a necessary condition for $SNR_{CPMG} > SNR$ is that $T_r/T_2 < \ln(2)/2$. From this equation we see that two quantities play a role in the maximization: The repetition time T_r and the average perturbation of the echo $\langle\delta\mathcal{S}^{(2)}\rangle$. They both have to be minimized and they both have positive lower bounds (given by the smallest echo duration and the perturbation induced by the relaxation during the echo). They are minimized by an appropriate choice of control sequence. The ideal case is the one with short robust pulses against g and Δ inhomogeneities.

Given an experimental setup, numerical tests are required in order to find the best pulse (see the next section). *However, we can go further in the analytic analysis and give a qualitative rule for the optimization: It is more advantageous to minimize the ratio T_r/T_2 than $\langle\delta\mathcal{S}^{(2)}\rangle$.* In other words, it is better to use short pulses with quite a good robustness than a robust pulse, but with a long duration (and consequently a long T_r). For the analysis, we define $\alpha = SNR_{CPMG}/\mathcal{S}^{(2)}$, $\beta = \langle\delta\mathcal{S}^{(2)}\rangle/\mathcal{S}^{(2)}$ and $\gamma = T_r/T_2$. From (4.45) a gradient in direction α can be computed. Here we are only interested in the ratio $(\partial\alpha/\partial\gamma)/(\partial\alpha/\partial\beta)$, and more particularly when the latter is larger than 1. This gives:

$$(1-\beta)\frac{e^{\gamma}}{e^{\gamma}-1} > 1. \tag{4.46}$$

The parameters γ and β are generally extremely small, therefore:

$$\gamma - \ln(\gamma) > \beta. \tag{4.47}$$

Because $\gamma \ll 1$, we have $\gamma - \ln(\gamma) \gg 1$. Therefore, this inequality is always true for experimentally interesting values of β and γ. With (4.47) we see easily that the gradient in γ is always larger than the gradient in β. Then, a small decrease of γ has a more important effect than an enhancement in β. To conclude, during a CPMG sequence, instead of trying to produce the most perfect control, it is better to choose a pulse less efficient, but with the smallest possible duration.

4.2 Numerical experiments

This section focuses on the numerical verification of the theory presented in the last section. We recover the main results using numerical examples and we compare the pulses presented in chapter 3.

We investigate an example in the low cooperativity regime reproducing recent experiments in ESR [21, 132]. In these experiments, the offset distribution is well described by $\rho_{purcell}$ (section 1.7). This distribution depends on the repetition rate of the experiment that we choose equal to 10 Hz. Additionally, we consider 940 spins in the distribution. Relaxation times are taken to be $T_1 = 3$ s, $T_2 = 1.7$ ms and $T_1^p \simeq 100$ ms for $\Delta = 0$. We also set $g_0 = 2664$ rad/s and $\kappa = 9.8 \times 10^5\ s^{-1}$. Then, with such parameters, the effective spin distribution is approximately Lorentzian of full width at half maximum (FWHM) $\Omega_p/2\pi = 1$ MHz, and the cooperativity is $C = 0.01$.

We first investigate the robustness of the excitation process against offset and coupling strength inhomogeneities for the bump, square and g-robust pulses. The g-robust control sequence is defined in section 3.4.2. The square pulses correspond to very short square pulses in ω_X and ω_Y (section 3.1). Note that the square pulses are highly deformed by the response function of the cavity. They are considered below as a reference of the control process. The spins are initially assumed to be along the z-axis with a polarization given by the Purcell effect and interacting with a cavity with zero photon. As could be expected, we observe in figure 4.6 that the efficiency of bump fields is preserved for a wide range of offset frequencies, while a very good fidelity against variation of the g- parameter is achieved on resonance for the g- robust pulse. Bump and g- robust solutions lead to a more robust control protocol than the standard square pulses.

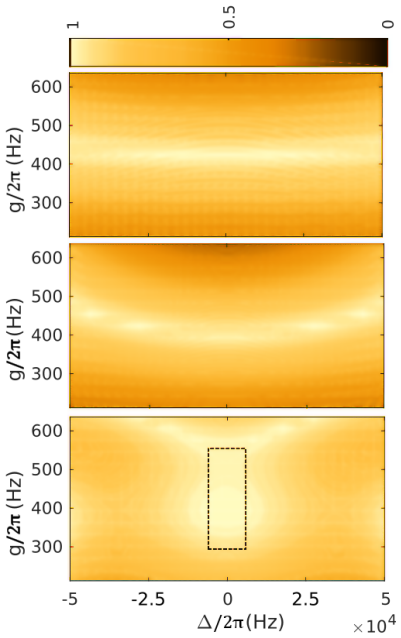

Figure 4.6: Robustness of a $\pi/2$-excitation process against coupling strength g and offset Δ inhomogeneities of a bump pulse (top), a square pulse (middle) and a g- robust pulse (bottom). The rectangle in dashed lines indicates the spins used in the optimization. In order to provide a fair comparison, we fix the maximum value of X during the pulse. The pulse duration is set to satisfy this constraint: $t_{\text{square}} = 1\ \mu$s, $t_{\text{bump}} = 2t_k = 3.9\ \mu$s and $t_{\text{g-robust}} = 19.5\ \mu$s.

As a second point of comparison, we study the performance of g- robust, bump and square pulses in the maximization of the SNR. For each control sequence, we consider two cases, one corresponding to a constant $g = g_0$ distribution and the second to inhomogeneities of the form $g = g_0(1 + \alpha)$, with $\alpha \in [-0.3, 0.3]$. We also simulate ideal rotations on the spin system in order to estimate the maximum echo signal that can be reached with the spin distribution. The numerical results are displayed in figure 4.7, which shows the echo signal observed with the different pulses. For sake of comparison, the duration of the bump pulses is the same as the one of g- robust fields (better results could be obtained with shorter bump pulses). An echo with a higher amplitude and a shorter time is achieved with the optimal solutions. We observe that the area of the different echos in figure 4.7 is roughly the same for the different excitations. However, due to the shorter echo, the SNR is indeed increased with the optimal pulses.

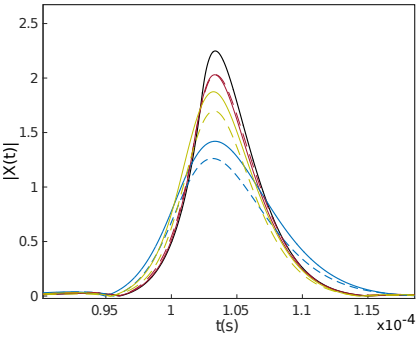

Figure 4.7: (Color online) Comparison of the echo signal in X for square pulses (in blue), for bump pulses (in green) and for g- robust pulses (in red). The physical limit with ideal spin rotations is displayed in black. The solid and dashed lines depict respectively the echo signal without and with g- inhomogeneities. The pulse duration is set to 1 μs.

As a second example, we consider a CPMG sequence with a period T_r after the excitation process. We assume a perfect initial $\pi/2$- excitation of the spin ensemble and the different relaxation effects are accounted for. The time T_r has been fixed to its minimum value for each pulse sequence (such that echos and π-pulses are not overlapping). Table 4.3 gives the normalized SNR for one echo and for the whole CPMG sequence. We observe in table 4.3 that g-robust pulses give a better SNR than the bump pulses. A noticeable enhancement is also obtained with respect to

π- pulse	$\min(t_f)$ (s)	M_r	$\frac{\text{SNR}_1}{\text{SNR}_1^{max}}$	$\frac{\text{SNR}_{M_r}}{\text{SNR}_{Mr}^{max}}$
Phys. limit	1.3×10^{-5}	321	1	1
Bump	3.69×10^{-5}	240	0.822	0.915
g- robust	3.8×10^{-5}	231	0.935	0.943
Square	6.1×10^{-5}	160	0.568	0.164

Table 4.3 – Parameters of the different CPMG sequences. The physical limit corresponds to ideal π- rotations for each spin of the ensemble. M_r indicates the maximum number of echos which can be observed. The number of spins N_{min} for a SNR of 1 is computed for the first 100 echos of the sequence.

the square pulses. The results achieved with the two optimal solutions are in addition very close to the physical limit of an ideal spin echo sequence. The improvement is even more striking for a CPMG sequence. Due to its short duration, which allows a larger number of repetitions, the bump pulse gives in this case the best result.

These numerical tests for a realistic system are in good agreement with analytic formulas. Moreover, we recover the fact that short pulses produce a better SNR during a CPMG sequence. Notice that the system simulated here has a low cooperativity and it is well described by the linear approximation (negligible relaxation during the echo).

4.3 Conclusion

The SNR of a spin-echo has been studied in the semi-classical regime. Simple formulas have been derived in order to predict the value of the SNR, even when the collective effects are not negligible. The choice of the system parameters have an important impact and a non-trivial maximum exists. We have shown that the SNR is always maximized when the spin ensemble is perfectly excited. This goal can be reached with the pulses presented in the previous chapter. Optimized pulses have a better efficiency in a single spin echo experiment because they allow us to prepare the spins in a state close to the ideal state. Nevertheless, shorter, but less robust pulses are better in CPMG sequences because their lack of robustness is compensated by a higher number of repetitions, and thus, a larger signal.

Numerical experiments have been performed using relevant experimental values in ESR. This has demonstrated the superiority of the new pulses in terms of SNR and sensitivity with respect to the standard square pulses. Moreover, the numerical results have shown that a good compromise is provided by the

bump pulses, which combine simplicity, efficiency and robustness against offset inhomogeneities. Their short duration is also a key factor for the enhancement of the SNR by CPMG sequences.

The application of optimized pulses to the SNR maximization is another example of the efficiency of this approach. The new pulses have a broad area of applications, they can be used for quantum computations (as logic gates). They also push the sensitivity of the experimental setup to its physical limit.

Part II

Parameters measurement and selectivity in NMR

Chapter 5

Selective $SO(3)$ transformations by optimal control

5.1 Introduction

During the last decade, many different studies have been devoted to $SO(3)$ and $SU(2)$ transformations and to the design of robust transformations against offset parameters [101, 45, 26]. These transformations have applications extending from magnetic resonance to quantum information science [67, 32, 8, 50, 45]. This difficult problem is nowadays well understood, and various solutions can be found in the literature [91, 26, 27, 7, 104, 167]. On the other hand, performing efficient selective transformations (or more precisely: band-selective transformations) remains a challenge of practical and fundamental interest [35, 127, 174, 175, 109]. The selectivity problem has been studied for several years, but very few in the optimal control framework [169].

A selectivity problem can be seen as a robustness problem [91, 167], but with the additional constraint that offsets outside the interval of robustness are left unchanged. Among this class of problem we can underline the following one: *What is the control field that generates in minimum time a given transformation* $\hat{U} \in SO(3)$ *for* $\Delta = 0$ *and* $\hat{\mathbb{I}}$ *for* $\Delta \neq 0$*?* Simple arguments using Fourier-transforms suggest that the control field spectrum should approximate a Dirac distribution. Optimal control theory (OCT) [25, 88, 166, 125], and more particularly the Pontryagin Maximum Principle (PMP) has been applied to many quantum computing and spin dynamic problems [99, 98, 7, 61] to derive the global optimum of the control problem. The goal of this chapter is therefore to apply the PMP in order to derive optimal selective SO(3) transformations.

Ultra-selective transformations could have applications in ESR and cavity QED experiments (Part I of this manuscript). Such pulses could allow us to excite only the spin near the resonance, leading thus to an excitation close to the single spin limit. Considering a time constraint can ensure us to perform the maximum of repetitions per measurement cycle. Then, the time minimization is a guarantee of SNR maximization.

In this chapter, we consider this control problem with the study of simple time minimum selective pulses. We restrict the study to the usual NMR framework in order to ignore the cavity constraints. The use of geometric and numerical optimal-control theory allows us to derive simple control mechanisms and to emphasize the physical limit of the process. In particular, we show the central role of singular control fields in time minimum solutions. We find using both analytical and numerical arguments that in the ultra-selective case, the optimal solution is a singular constant pulse. We also present two cases of locally robust pulses on a given offset interval. Depending on the robustness interval, the optimal control is either a singular trajectory or a regular trajectory.

Additionally, several bounds of the process are derived in each case.

We restrict the study to the design of $SO(3)$ transformations (rotation matrices). The study of time optimal state-to-state transfers is addressed in another study [169].

This chapter is organized as follows: We first introduce some definitions about the control of $SO(3)$ transformations. Then, we review some basics of OCT applied to $SO(3)$-ensembles (section 5.3). In the first case under study, we consider the symmetric selective transformation around the resonance. The last section (5.5) is devoted to the study of two examples of locally robust selective pulses.

5.2 Notations

- $\mathcal{C}_\Delta$: set of offsets considered in the discretized problem.
- Δ, Δ_n: an offset parameter.
- Δ_0: smallest offset that produces the transformation identity for a constant pulse of amplitude u_0.
- Δ_e: smallest offset that produces the transformation identity for a constant pulse of amplitude u_e.
- $\hat{e}_x, \hat{e}_y, \hat{e}_z$: generators of the $\mathfrak{so}(3)$ algebra.
- F: cost function to minimize, defined by the average distance to a set of target states.
- H_p: Pontryagin's Hamiltonian.
- l_n^a: component of a local Hamiltonian lift.
- $l^a = \sum_n l_n^a$: component of the global Hamiltonian lift.
- $\vec{l}_n = (l_n^x, l_n^y, l_n^z)$: vector form of the local Hamiltonian lift.
- $\vec{l} = (l^x, l^y, l^z)$: vector form of the Global Hamiltonian lift.
- l^0: drift part of Pontryagin's Hamiltonian.
- $\vec{m} = \vec{l}_1 - \vec{l}_{-1}$: difference between the local Hamiltonian lifts of the offset $n = -1$ and $n = 1$.
- $\hat{P}_n, \langle \hat{P}_n |$: Adjoint state of the system n.
- $\hat{U}_n, |\hat{U}_n\rangle$: state of the system n.
- u: an arbitrary (constant) control amplitude.
- u_0: maximum bound of the control amplitude.
- u_e: amplitude of the energy-minimum pulse.
- $\omega_x(t), \omega_y(t)$: control fields in directions x and y.

5.3 $SO(3)$ transformations and the PMP

5.3.1 Definitions and general properties

We consider $SO(3)$ transformations generated by the Bloch equations [101, 104]:

$$\begin{aligned}\frac{d\hat{U}_n}{dt} &= \begin{pmatrix} 0 & \Delta_n & -\omega_y(t) \\ -\Delta_n & 0 & \omega_x(t) \\ \omega_y(t) & -\omega_x(t) & 0 \end{pmatrix} \hat{U}_n \\ &= \left(\omega_x \hat{\epsilon}_x + \omega_y \hat{\epsilon}_y + \Delta_n \hat{\epsilon}_z\right) \hat{U}_n,\end{aligned} \tag{5.1}$$

with the initial condition $\hat{U}_n(0) = \hat{\mathbb{I}}$. The parameter Δ_n is the offset and ω_x, ω_y are two time-dependent controls. $\epsilon_x, \epsilon_y, \epsilon_z$ are generators of the $\mathfrak{so}(3)$ algebra [72, 45]. They verify the commutation relations $[\hat{\epsilon}_x, \hat{\epsilon}_y] = -\hat{\epsilon}_z$, $[\hat{\epsilon}_y, \hat{\epsilon}_z] = -\hat{\epsilon}_x$, and $[\hat{\epsilon}_z, \hat{\epsilon}_x] = -\hat{\epsilon}_y$. They play the same role as Pauli matrices for the group $SU(2)$. They are defined such that $(\hat{\epsilon}_c)_{ab}$ are the matrix elements of the Levi-civita symbol ϵ_{abc}. These matrices are related to the wedge product with the relation: $-\vec{A} \wedge \vec{B} = \left(\sum_a \vec{A}_a \hat{\epsilon}_a\right) \vec{B}$.

From the physical point of view, the coupling constant is set to $g = 1$. B_1 inhomogeneity is not taken into account in this problem.

In order to state the Maximum Principle (theorem 2, appendix A), it is necessary to choose only a finite number of systems. Hence, we fix N offsets Δ_n and we consider the transformations generated over the set $\mathcal{C}_\Delta = \{\Delta_n\}_{n=1...N}$. Moreover, we define an inner product in the space of evolution operators:

Definition 2 (Frobenius inner product): $\langle a|b\rangle : \mathbb{R}^{n\times m} \times \mathbb{R}^{n\times m} \to \mathbb{R}$, *such that:*

$$\langle \hat{A}|\hat{B}\rangle = Tr\left[\hat{A}^T \hat{B}\right]. \tag{5.2}$$

In particular, this defines an inner product on both $SO(3)$ and $\mathfrak{so}(3)$ [79].

This allows us to introduce the following cost function:

Definition 3 (Cost function):

$$F[T, \omega] = \sum_{n=1}^{N} \frac{F_n}{N} = \sum_{n=1}^{N} \frac{1}{3N} \|\hat{U}_n[T, \omega] - \hat{U}_{n,target}\|^2, \tag{5.3}$$

where the Frobenius norm $\|\hat{A}\|^2 = \langle \hat{A}|\hat{A}\rangle$ is used.

This cost function gives the mean (square) difference between the transformations induced by a control and the desired target states $\{\hat{U}_{n,target}\}_{n=1..N}$. Notice that the target state can be different for each offset. The time-optimization task consists of determining $\min_{\omega,T}[F]$.

Definition 4 (Spectrum): *By analogy with the usual Fourier Transform formalism, we call "spectrum" or "excitation profile" the distribution of transformations $\hat{U}(\Delta, T)$. The finite set $\{\hat{U}_n(T)\}_{n=1..N}$ is a discretization of the continuous spectrum.*

5.3.2 The PMP applied to an inhomogeneous ensemble of uncoupled spins

In this section, we introduce Hamilton's formalism on the system [167, 61]. This is a straightforward application of the PMP (theorem 2, appendix A):

Definition 5 (PMP of a spin ensemble): *The PMP of an ensemble of uncoupled spins is given by:*

$$H_p = \sum_{n=1}^{n} \langle \hat{P}_n | d_t \hat{U}_n \rangle + p^0 f^0 \tag{5.4}$$

$$\frac{\delta H_p}{\delta \vec{\omega}(t)} = 0 \text{ or } \|\vec{\omega}\| = u_0, \tag{5.5}$$

where $p^0 f^0$ describes additional degrees of freedom that encode the cost to minimize.

In this chapter, we consider a time minimization. Then, we use $p^0 f^0 = -1$ [25, 166, 88] This term describes a cost function that is different from F. The fidelity of the final state with the target state does not appear explicitly in the PMP . Additionally, the norm of the control field $\|\vec{\omega}\|$ is assumed to belong to the interval $[0, u_0]$. The introduction of this bound is motivated by physical constraints: we cannot produce a magnetic field of arbitrary high amplitude.

By inserting Bloch equation (5.1) into the Pontryagin Hamiltonian (5.4), and by applying the second constraint (5.5), specific equations can be derived for both singular ($\delta H_P / \delta \vec{\omega}(t) = 0$) and regular trajectories ($\|\vec{\omega}\| = u_0$). For the sake of simplicity, it is convenient to introduce the local Hamiltonian lift $l_n^a = \langle \hat{P}_n | \hat{e}_a \hat{U}_n \rangle$ and the global Hamiltonian lift $l^a = \sum_n l_n^a$.

First, let us focus on the regular case. The maximization of Pontryagin's Hamiltonian leads to:

$$\begin{aligned} H_p &= \omega_x l^x + \omega_y l^y + \sum_{n=1}^{N} \Delta_n l_n^z \\ \omega_a &= u_0 \frac{l^a}{\sqrt{(l^x)^2 + (l^y)^2}}. \end{aligned} \tag{5.6}$$

Additionally, by using Hamilton's equations:

$$d_t \hat{U}_n(t) = \frac{\delta H_p}{\delta \hat{P}_n(t)} \;\; ; \;\; d_t \hat{P}_n(t) = -\frac{\delta H_p}{\delta \hat{U}_n(t)}, \tag{5.7}$$

it is possible to determine a differential equation for the time evolution of the Hamiltonian lift:

$$\begin{aligned} \frac{d}{dt} \hat{P}_n(t) &= -\hat{P}_n(t) \left(\omega_x \hat{e}_x + \omega_y \hat{e}_y + \Delta_n \hat{e}_z \right) \\ &\equiv -\hat{P}_n(t) \hat{H}(t), \end{aligned} \tag{5.8}$$

where the Hamiltonian operator $\hat{H}$ is introduced by analogy with quantum mechanics.

Now, we compute $d_t l_n^a$:

$$\begin{aligned}\frac{dl_n^a}{dt} &= \langle d_t\hat{P}_n|\hat{e}_a|\hat{U}_n\rangle + \langle\hat{P}_n|\hat{e}_a|d_t\hat{U}_n\rangle \\ &= -\langle\hat{P}_n|\hat{H}\hat{e}_a|\hat{U}_n\rangle + \langle\hat{P}_n|\hat{e}_a\hat{H}|\hat{U}_n\rangle \\ &= -\langle\hat{P}_n|[\hat{H},\hat{e}_a]|\hat{U}_n\rangle \\ &= -\left(\omega_x\langle\hat{P}_n|[\hat{e}_x,\hat{e}_a]|\hat{U}_n\rangle + \omega_y\langle\hat{P}_n|[\hat{e}_y,\hat{e}_a]|\hat{U}_n\rangle + \Delta\langle\hat{P}_n|[\hat{e}_z,\hat{e}_a]|\hat{U}_n\rangle\right).\end{aligned}$$

From the commutation relations of $\hat{e}$ matrices, we deduce:

$$\boxed{\frac{d\vec{l}_n}{dt} = -(\omega_x\hat{e}_x + \omega_y\hat{e}_y + \Delta\hat{e}_z)\vec{l}_n,} \tag{5.9}$$

with $\vec{l}_n = (l_n^x, l_n^y, l_n^z)$. If l^x and l^y are simultaneously different from zero on a time interval, the Hamiltonian lift belongs to this set, it is entirely determined by the $3N$ initial conditions of (5.9). In practice, it would be sufficient to determine a smaller number of initial conditions, by determining additional constant of motions [167]. If the dimension is reduced to only one control (in the x direction for example), regular controls are bang-bang, such that:

$$\omega_x = u_0.\text{sign}\,(l^x) \quad , \quad \omega_y \equiv 0. \tag{5.10}$$

However, any regular control can be expressed as: $\omega_x = u_0\cos\theta(t)$ and $\omega_y = u_0\sin\theta(t)$, where θ is a function to determine. This parametrization is compatible with the single input case (bang-bang controls) if θ is restricted to the values 0 or π.

Singular trajectories occur when $l^x = l^y = 0$ on a time interval. This corresponds to a singularity of equation (5.6). In this case, other computation methods are required to determine the optimal field. The procedure is different for one or two-dimensional control fields. The general method is described in section A.1.1. A direct application of the method allows us to determine the following equation for the single input case:

$$\boxed{\omega_x = -\frac{\{\{l^x,l^0\},l^0\}}{\{\{l^x,l^0\},l^x\}} = \frac{\sum_n(\Delta_n)^2 l_n^x}{\sum_n \Delta_n l_n^z},} \tag{5.11}$$

where $\{A,B\} = \sum_{i=1}^n \frac{\delta A}{\delta q_i(t)}\frac{\delta B}{\delta p^i(t)} - \frac{\delta B}{\delta q_i(t)}\frac{\delta A}{\delta p^i(t)}$ is the Poisson bracket and $l^0 = \sum_{n=1}^N \Delta_n l_n^z$. Furthermore, for two-dimensional controls, singular trajectories are given by:

$$\boxed{\begin{aligned}\omega_x &= -\frac{\{l^y,l^0\}}{\{l^y,l^x\}} = \frac{\sum_n \Delta_n l_n^x}{l^z} \\ \omega_y &= -\frac{\{l^x,l^0\}}{\{l^x,l^y\}} = \frac{\sum_n \Delta_n l_n^y}{l^z}.\end{aligned}} \tag{5.12}$$

To summarize, the controls that are candidates for optimality belong to the following categories:

- Regular controls: they have a constant amplitude and a time-dependent phase
- Singular controls: they verify (5.11).
- Regular-Singular controls: The control switches between regular and singular arcs. A jump from a regular arc to a singular one can happen during a phase switching.

The optimization task consists of first determining in which category belongs the optimal solution, and in a second step to compute explicitly the structure of the field.

5.4 Ultra-selective pulse

5.4.1 Analytic approach

First, we consider an ensemble $\mathcal{C}_\Delta = \{-\Delta, 0, \Delta\}$, and the goal is to find the shortest corresponding selective pulse. More precisely, the aim is to find a control field that produces a rotation of angle ϕ at resonance, and the identity transformation for the shortest offset $|\Delta|$. The situation is summarized in the graph 5.1.

In order to derive analytic results, we restrict, in a first step, the control to the x-axis. More general situations are considered in a second step. This restriction has the advantage to produce symmetric transformations. Then, we consider only two offsets at frequencies 0 and $\Delta > 0$.

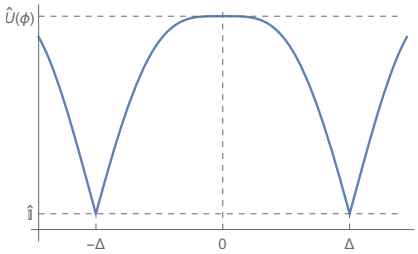

Figure 5.1: Spectrum of an ultra-selective pulse.

Structure of singular trajectories

We start the presentation with the analysis of singular trajectories.

Proposition 5 (time singular 1D-control): *Let $\mathcal{C}_\Delta = \{0, \Delta\}$ be the offset ensemble. Assume $\omega_y = 0\ \forall t$. Then, singular controls are constants.*

Proof. A direct calculation using equations (A.8), (A.9) and (A.10) gives us:

$$\begin{aligned} l^x = 0 &\Rightarrow l_0^x = -l_1^x \\ d_t l^x = 0 &\Rightarrow l_1^y = 0 \\ d_t^2 l^x = 0 &\Rightarrow \omega_x = \Delta \frac{l_1^x}{l_1^z}. \end{aligned} \tag{5.13}$$

The Hamiltonian $H_p = \Delta l_1^z$ is a constant of motion, thus, l_1^z is also a constant. It remains to compute $l_0^x(t) = \langle \hat{P}_0(t) | \hat{e}_x | \hat{U}_0(t) \rangle$. Since at resonance, the Bloch equation is reduced to $d_t \hat{U}_0 = \omega_x(t) \hat{e}_x \hat{U}_0$, the matrix $\hat{e}_x$ commutes with the evolution operator at any time, and therefore, $l_0^x(t) = \langle \hat{P}_0(t) | \hat{U}_0(t) \hat{e}_x \rangle = \langle \hat{P}_0(0) | \hat{e}_x \rangle$ is a constant of motion. □

It is interesting to make a comment concerning the energy minimum solution. We can deduce from the PMP (by using an appropriate choice of $p_0 f_0$) that singular trajectories of the energy-minimum problem are also constant pulses. Then, the set of singular trajectories is the same for both time and energy minimum cases. This point can be deduced from the PMP, but it is even more straightforward to use the Cauchy-Schwartz inequality:

$$\left| \int_0^{T_e} f(t) g(t) dt \right| \leq \left(\int_0^{T_e} |f(t)|^2 dt \right)^{1/2} \left(\int_0^{T_e} |g(t)|^2 dt \right)^{1/2},$$

where T_e is the time of the energy-minimum pulse, a fixed parameter. If we set $f = \omega_x$, and $g = 1$. Then,

$$|\phi| \leq T_e \left(\int_0^{T_e} |\omega_x(t)|^2 dt \right)^{1/2}, \tag{5.14}$$

with equality only if $\omega_x(t)$ is constant.

Now, we analyze the trajectories produced by these singular controls in order to relate the time, the offset constraint, and the control amplitude. We assume that the control is positive with amplitude $u_e \leq u_0$. For a constant control, the evolution operator is given by a simple matrix exponential:

$$\begin{aligned}
\hat{U}(T_e) =& e^{T_e(u_e\hat{\epsilon}_x + \Delta\hat{\epsilon}_z)} \\
=& e^{T_e\sqrt{u_e^2+\Delta^2}(n_x\epsilon_x + n_z\hat{\epsilon}_z)} \\
=& \cos\left(T_e\sqrt{u_e^2+\Delta^2}\right)\hat{\mathbb{I}} + \frac{\sin\left(T_e\sqrt{u_e^2+\Delta^2}\right)}{\sqrt{u_e^2+\Delta^2}}(u_e\hat{\epsilon}_x + \Delta\hat{\epsilon}_z) \\
&+ \left(\cos\left(T_e\sqrt{u_e^2+\Delta^2}\right) - 1\right)\frac{u_e\Delta}{u_e^2+\Delta^2}\hat{\epsilon}_y,
\end{aligned} \tag{5.15}$$

where (n_x, n_z) is a unitary vector (figure 5.2). The condition for producing a rotation of angle ϕ at resonance is the following:

$$T_e u_e = \phi. \tag{5.16}$$

By using the rotation angle of the transformation: $T_e\sqrt{u_e^2+\Delta^2}$, it is direct to calculate the smallest offset $\Delta = \Delta_e$ that produces a 2π-rotation:

$$\Delta_e = \frac{1}{T_e}\sqrt{4\pi^2 - \phi^2}. \tag{5.17}$$

If the control amplitude is such that $u_e = u_0$, we denote respectively by T_0 and Δ_0 the associated control duration and the smallest offset. In this case, the singular control is also regular and it is time optimal for the offset Δ_0.

Proposition 6 (optimal control for Δ_0): *Let $\mathcal{C}_\Delta = \{0, \Delta_0\}$ be the offset ensemble. Assume a rotation of angle ϕ around x at resonance. Then, the time optimal control is a bang pulse of amplitude u_0 and duration T_0.*

Proof. The control is time optimum at resonance, but, is it possible to find a control that produces the same final state in the same time T_0 for an offset $\Delta < \Delta_0$? Without assumptions on the control (regular, singular, one or two-dimensional), we have:

$$\int_0^{T_0} \omega_x(t)dt \leq u_0 T_0 \equiv \phi, \tag{5.18}$$

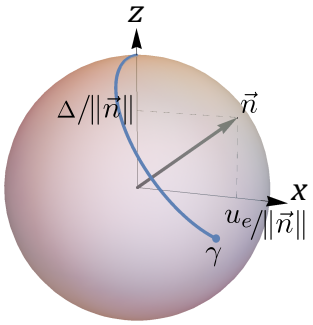

Figure 5.2: The rotation axis $\vec{n}$ and the rotation angle $\gamma = T_e\sqrt{u_e^2+\Delta^2}$ defined by equation (5.15).

The *equivalent class* is determined by the ensemble of control that produces the same spectrum. This point is described in the paragraph on 2D-controls.

Then, the constant pulse is the only control that produces the desired transformation at resonance, thus it is not possible to find an offset smaller than Δ_0. □

This proposition is trivial, but it helps understanding the underlying mechanisms.

We have highlighted a very simple situation, where the optimal trajectory is both singular and regular. However, we still have to determine the time-optimal solution for $\Delta < \Delta_0$. For that purpose we have to consider regular and singular-regular trajectories. The case $\Delta > \Delta_0$ is not investigated because it concerns only large values of offsets. They are interesting for the design of robust pulses but not for ultra-selective pulses. However, in this latter case, it is not difficult to see that the optimal trajectory contains necessary regular arcs.

Structure of regular pulses

This section focuses on regular trajectories. The Hamiltonian lift is integrated in order to determine the switching times, and the structure of the pulse is determined by a recurrence formula. Additionally, we study the case of a switching to a singular arc. Using the Hamiltonian lift and its time derivative (5.9),we compute:

$$\frac{d}{dt}\begin{pmatrix} l^x \\ l^y \\ l^z \end{pmatrix} = \begin{pmatrix} -\Delta l_1^y \\ \Delta l_1^x - \omega_x l^z \\ \omega_x l^y \end{pmatrix}. \tag{5.19}$$

Therefore, a regular control depends only on $l_1^x(t), l_1^y(t)$, and $l_1^z(t)$ (we recall the definition: $\omega_x = u_0 \text{sign}(l^x) = u_0 l^x/|l^x|$). We deduce that regular pulses of the sets $\mathcal{C}_\Delta = \{0, \Delta\}$ and $\{\Delta\}$ are the same, i.e. the ensemble of regular control for two offsets, with one at resonance is identical to the ensemble of a single offset. The time optimal synthesis of this problem is studied in detail in [26] using the Hopf fibration.

Here we propose a simple analysis based on the solution of (5.19). By using (5.9), it is straightforward to determine $l_1^y(t)$ between two switchings:

$$l_1^y(t_s^i + t) = l_1^y(t_s^i)\cos(\Omega t) + \frac{l_1^x(t_s^i)\Delta - l_1^z(t_s^i)u}{\Omega}\sin(\Omega t), \tag{5.20}$$

where t_s^i is the time of the switching number i, $u = \pm u_0$ and $\Omega = \sqrt{u_0^2 + \Delta^2}$. Then, a second time integration allows us to determine $l^x(t)$ as a function of the state of $\vec{l}_1$, at the last switching:

$$l^x(t_s^i + t) = -\frac{\Delta}{\Omega}\left[l_1^y(t_s^i)\sin(\Omega t) + \frac{l_1^x(t_s^i)\Delta - l_1^z(t_s^i)u}{\Omega}(1 - \cos(\Omega t)) \right].$$

In order to simplify equations, we introduce the constant:

$$A = \frac{l_1^x(t_s^i)\Delta - l_1^z(t_s^i)u}{l_1^y(t_s^i)\Omega}, \tag{5.21}$$

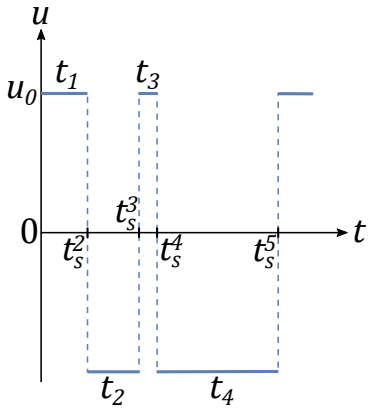

Figure 5.3: Structure of a regular control field (single input case) with several switchings.

and we deduce the general form of the control as a function of system states at the switching number i:

$$\omega_x(t_s^i + t) = u_0 \text{sign}(-\Delta l_1^y(t_s^i)\,[\sin(\Omega t) + A(1 - \cos(\Omega t))]).$$

An example of regular control is plotted in figure 5.3. It remains to determine the duration of the bang: $t_i = t_s^{i+1} - t_s^i$. This is achieved by solving $l^x(t_s^i + t) = 0$. This last equation can be expanded into:

$$\sin(\Omega t) + A(1 - \cos(\Omega t)) = 0 \;\;,\;\; l_1^y(t_s^i) \neq 0,\; A \neq 0. \tag{5.22}$$

The cases $l_1^y(t_s^i) = 0$ or $A = 0$ *correspond to singular trajectories*, according to equation (5.13). Therefore, the duration of the bang is given by:

$$t_i = \min_{k>0, t>0} \left[t = \frac{2}{\Omega}\left(k\pi - \arctan\left(\frac{1}{A}\right)\right)\right]. \tag{5.23}$$

The structure of the control as a function of A, Ωt, and $\text{sign}(\Delta l_1^y(t_s^i))$ is plotted in figure 5.4.

We deduce that the control is entirely determined by $l^x(t = 0)$, $l_1^y(t = 0)$, *and* $A(t = 0)$. *We also have* $t_i \in [0, T_0]$.

The sequence of t_i can be determined easily with a numerical computation. Several examples of sequences are plotted in figure 5.5. We can see that the sequence is periodic and alternates between two different values.

Proposition 7 (Switching regular-singular): *Let* $\mathcal{C}_\Delta = \{0, \Delta\}$ *be the offset ensemble. Assume* $\omega_y = 0\ \forall t$, *and a bang-bang regular arc at the beginning of the dynamics. Then, the regular arc cannot switch to a singular arc.*

Proof. The proof is made in two steps. First we determine the time t such that $l_1^y(t_s^i + t) = 0$. From equation (5.20), we deduce:

$$\cos(\Omega t) + A\sin(\Omega t) = 0, \tag{5.24}$$

and

$$t = \frac{1}{\Omega}\left(k\pi - \arctan\left(\frac{1}{A}\right)\right). \tag{5.25}$$

Equations (5.23) (definition of t_i) and (5.25) do not have joint solutions, then l_1^y and l^x cannot be simultaneously equal to zero. Thus, the conditions to obtain a bang-singular arc cannot be fulfilled. □

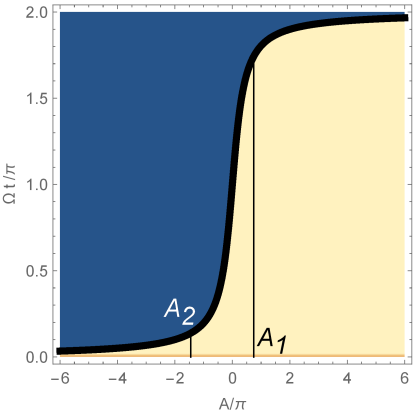

Figure 5.4: Structure of a regular control. If $\text{sign}(\Delta l_1^y(t_s^i)) > 0$, the blue area corresponds to $+u_0$ and the light yellow area corresponds to $-u_0$. Otherwise, if $\text{sign}(\Delta l_1^y(t_s^i)) < 0$, the sign of the control is switched. The black line of the equation: $2k - 2\arctan(1/A)/\pi$ determines the switching area. The graph must be read as follows. At time t_s^i, the control admits a certain value $A(\Omega t = 0)$ (for example A_1). Then, the system evolves in a straight vertical line as Ωt increases. When it crosses the intersection between the blue and the yellow area, it returns to the position $\Omega t = 0$, with potentially new values of A and l_1^y (for example A_2).

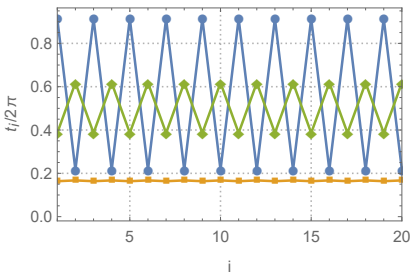

Figure 5.5: Examples of sequence of t_i for 3 different initial conditions chosen randomly (equation (5.19)).

Distinction between singular and regular trajectories

Now that the two classes of admissible controls are well characterized, the goal is to determine the optimal solution. Without computing exactly a regular pulse (by determining the sequence of times t_i), it is possible to analyze analytically the differences

between the two cases and to reduce considerably the number of solutions.

Proposition 8 (non-optimality): *Let us consider $\mathcal{C}_\Delta = \{0, \Delta\}$, and a single control ω_x of duration $T_e > T_0$ to produce a rotation of angle ϕ around x at resonance. Then,*

1. *If the control is bang-bang with one, two or three switchings, there is no offset $\Delta < \Delta_e$, which produces the identity.*
2. *In the limit of an infinite number of switchings, such that for all small intervals $[t_1, t_2]$, $\int_{t_1}^{t_2} \omega_x(t)dt = \frac{\phi}{T}(t_2 - t_1) + o((t_2 - t_1)^2)$, regular controls have the same behavior as a constant pulse of amplitude u_e and duration T_e.*

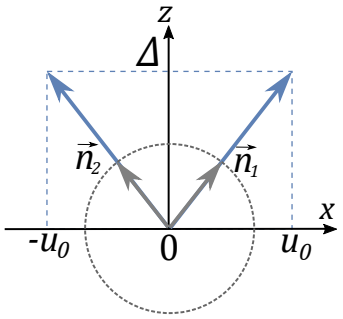

Figure 5.6: The two possible rotation axes involved in a regular control.

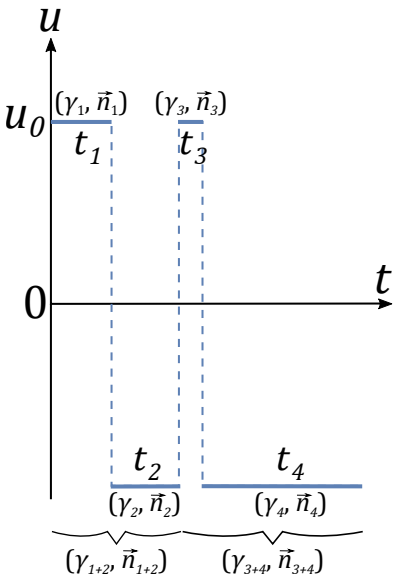

Figure 5.7: Example of regular control with 3 switchings. Each bang is characterized by an angle γ_i and a vector $\vec{n}_i$. The product of consecutive bangs gives effective angles $\gamma_{i+j+..}$ and effective vectors $\vec{n}_{i+j+...}$. In this example, $t_+ = t_1 + t_3$ and $t_- = t_2 + t_4$.

Proof. The proof uses proposition 14 (see appendix C). We consider a bang-bang pulse of duration T_e with one or more switchings. Each bang is associated to a rotation angle $\gamma_i = t_i\sqrt{u_0^2 + \Delta^2}$ around an axis $\vec{n}_i$ (see figure 5.6). We also introduce the notation $\gamma_{i+j+k+...}$ and $\vec{n}_{i+j+k+...}$ to denote effective rotation angles and rotation axes produced by the composition of several pulses $i, j, k, ...$ We also need the cumulative duration of positive and negative pulses, denoted t_+ and t_- (see figure 5.7). Due to the problem constraints, we have $t_+ + t_- = T_e$ and $t_+ - t_- = T_0$.

1) First, let us focus on the case with one switching. Here, we do not take into account the control sign during the first bang. Following the proposition 14, we deduce that a $\gamma_{1+2} = 2m\pi$ only if $\frac{\gamma_1 - \gamma_2}{2} = k\pi$ and $\frac{\gamma_1 + \gamma_2}{2} = n\pi$. This result uses the fact that an identity operator is parametrized by a unit quaternion of scalar part ± 1. This condition can also be found by computing explicitly the solutions of $Tr[\hat{U}_2\hat{U}_1] = 3$ (figure 5.8). These are the only solutions because $\vec{n}_1$ and $\vec{n}_2$ are not collinear (see figure 5.6). Therefore:

$$(t_1 - t_2)\sqrt{u_0^2 + \Delta^2} = 2k\pi \ , \ k \geq 1 \tag{5.26}$$

$$(t_1 + t_2)\sqrt{u_0^2 + \Delta^2} = 2n\pi \ , \ n \geq 1. \tag{5.27}$$

Additionally, we have the constraint: $t_1 - t_2 = T_0$. Then, inserting this equation into (5.26) gives:

$$T_0\sqrt{u_0^2 + \Delta^2} = 2k\pi \tag{5.28}$$

The smallest offset that verifies this condition is Δ_0 (by definition). Consequently, there is no offset $\Delta < \Delta_e < \Delta_0$ that produces the identity with a bang-bang pulse (1 switching) of duration T_e.

2) The case with two switchings is more involved. Indeed the first two bang pulses can produce a rotation about an axis

collinear to the last rotation axis. More precisely, we have to consider the following solutions:

$$\vec{n}_{1+2} \neq \pm\vec{n}_3 \tag{5.29}$$
$$\vec{n}_{1+2} = \pm\vec{n}_3. \tag{5.30}$$

In the first case, we must have:

$$\begin{cases} \gamma_{1+2} + \gamma_3 &= 2k\pi \\ \gamma_{1+2} - \gamma_3 &= 2n\pi \end{cases} \Rightarrow \begin{cases} \gamma_{1+2} &= 2k'\pi \\ \gamma_3 &= 2n'\pi \end{cases} \tag{5.31}$$

The condition $\gamma_{1+2} = 2k\pi$ is similar to the case with one switching. Then we can sum (5.26) and $\gamma_3 = 2n'\pi$ in order to obtain:

$$\begin{aligned} (t_1 - t_2 + t_3)\sqrt{u_0^2 + \Delta^2} &= 2(k' + n')\pi \\ \Rightarrow T_0\sqrt{u_0^2 + \Delta^2} &= 2l\pi. \end{aligned} \tag{5.32}$$

The smallest offset is obtained for $l = 1$, and it is Δ_0.
It remains the case with collinear rotation axes. An explicit computation of the product of evolution operators gives:

$$\begin{aligned} Tr[\hat{U}_{1+2+3}] = &\frac{1}{4}\left(8\cos(2\theta)\sin^2\left(\frac{\gamma_2}{2}\right)\sin^2\left(\frac{\gamma_1+\gamma_3}{2}\right)\right. \\ &- 8\cos(\theta)\sin(\gamma_2)\sin(\gamma_1+\gamma_3) \\ &+ 3\cos(\gamma_1 - \gamma_2 + \gamma_3) + 3\cos(\gamma_1 + \gamma_2 + \gamma_3) \\ &\left.+2\cos(\gamma_1+\gamma_3) + 2\cos(\gamma_2) + 2\right) \end{aligned}$$

A necessary condition to obtain $Tr[\hat{U}_{1+2+3}] = 3$ is: $\gamma_2 = 2k\pi$.
The same result can be deduced as well by computing the real part of the product of 3 unit quaternions:

$$\begin{aligned} Re[\mathbf{q}_{1+2+3}] = &\cos(\gamma_1)\left(\cos(\gamma_2)\cos(\gamma_3) - \sin\left(\frac{\gamma_2}{2}\right)\sin\left(\frac{\gamma_3}{2}\right)\cos(\theta)\right) \\ &- \sin\left(\frac{\gamma_1}{2}\right)\left(\sin\left(\frac{\gamma_2}{2}\right)\cos(\gamma_3)\cos(\theta) + \cos(\gamma_2)\sin\left(\frac{\gamma_3}{2}\right)\right) \end{aligned}$$

The composition rules of the two other angles give: $\gamma_1 + \gamma_3 = 2n\pi$. We can now use $T_0 = t_+ - t_-$ to determine:

$$\begin{aligned} (t_\pm - t_\mp)\sqrt{u_0^2 + \Delta^2} &= \pm 2(l - m)\pi \\ \Rightarrow T_0\sqrt{u_0^2 + \Delta^2} &= 2n\pi \\ \Rightarrow \min\Delta &= \Delta_0 \end{aligned} \tag{5.33}$$

3) With three switchings, the control is decomposed into 4 parts. However, it is more interesting to split it in two, and to study rotations 1+2 and 3+4 as single blocks. The conditions to produce the identity are:

$$\vec{n}_{1+2} \neq \pm\vec{n}_{3+4} \Rightarrow \begin{cases} \gamma_{1+2} = 2k\pi \\ \gamma_{3+4} = 2n\pi \end{cases} \tag{5.34}$$

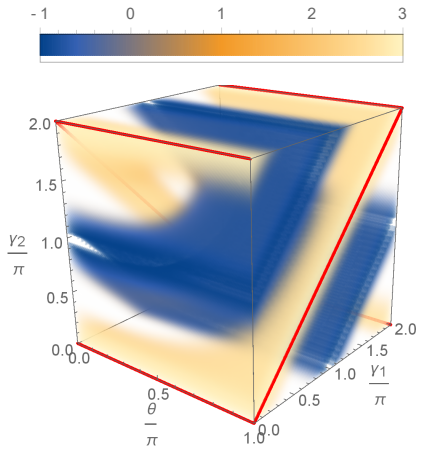

Figure 5.8: Density plot of $Tr[\hat{U}_{1+2}] = Tr[\hat{U}_2\hat{U}_1]$ as a function of the rotation angles γ_1, γ_2 and the angle θ between the two rotation angles. The identity $\hat{U}_{1+2} = \hat{\mathbb{I}}$ is obtained only if the trace is equal to 3. We observe that solutions exist only if $\theta = k\pi$ or γ_1 and γ_2 are multiples of 2π. These solutions are plotted in red lines.

$$\vec{n}_{1+2} = \pm\vec{n}_{3+4} \Rightarrow \gamma_{1+2} + \gamma_{3+4} = 2m\pi. \tag{5.35}$$

For the first case, we proceed as in equation (5.32), and we prove that it is not possible. Therefore, as for 2 switchings, only the case with collinear axis is not trivial. From proposition 14, we deduce that two products of (two) rotations produce an effective rotation around the same axis, only if the angles are respectively equal (modulo $2k\pi$ and a sign, but here, all angles are defined positive). Therefore:

$$\gamma_1 = \gamma_3 \; ; \; \gamma_2 = \gamma_4 \tag{5.36}$$

$$\Rightarrow \gamma_{1+2} = \gamma_{3+4} = \pi. \tag{5.37}$$

This is possible only if:

$$\gamma_1 + \gamma_2 = (2k+1)\pi \tag{5.38}$$
$$\gamma_1 - \gamma_2 = (2n+1)\pi, \tag{5.39}$$

and we deduce that:

$$(t_+ - t_-)\sqrt{u_0^2 + \Delta^2} = 2m\pi. \tag{5.40}$$

And we recover the same result as the other cases.
4) Finally, we consider the second claim. This is a basic result of average Hamiltonian theory. We assume M subdivisions of $[0, T_e]$. Because of our hypothesis, we have $\mathbb{T}e^{\int_{\sigma_i} dt(\omega_x(t)\hat{e}_x + \Delta\hat{e}_z} = e^{T_e\omega_x\hat{e}_x/M + o(T_e^2/M^2)}e^{T_e\Delta\hat{e}_z/M + o(T_e^2/M^2)}$. In the limit $M \to \infty$ we can use the Trotter formula (theorem 12, appendix C), which gives: $\hat{U}(T_e) = e^{T_e(u_e\hat{e}_x + \Delta\hat{e}_z)}$.

□

We could continue the calculations presented in the proof for 4,5,6,... switchings, but the number of possibilities diverges. However, we conjecture that we always obtain the condition: $(t_+ - t_-)\sqrt{u_0^2 + \Delta^2} = 2n\pi$, which is not optimal. However, if the product of two "small" rotations about respectively $\vec{n}_1$ and $\vec{n}_2$ gives " a small rotation" about the vector defined by Δ_e and u_e, we can approximate a singular pulse by a regular one.

Following the same computation steps as above, we can show that singular-bang trajectories (or inversely) cannot be optimal.[47].

Before the statement of a general conjecture, we investigate analytically the case of a 2-dimensional control field.

5.4.2 The two input case

For the moment, the study has been restricted to the single input case, but in this section, the results are extended to a system controlled by (ω_x, ω_y).

The goal of the following paragraphs is to connect 1D and 2D

[47] For that purpose, we consider a pulse of duration T_e, made of a regular arc of duration t_1 and a singular arc of duration t_2. The constraint at resonance gives: $u_0 t_1 + u_e t_2 = \phi = T_e u_e \Rightarrow T_e = t_2 + t_1 u_0/u_1$. For $|u_e| < u_0$, rotations axes $\vec{n}_1$ and $\vec{n}_2$ are different, and a necessary condition to produce a 2π rotation is $\gamma_1 + \gamma_2 = 2\pi$. We define $\Omega(\Delta) = \sqrt{u_e^2 + \Delta^2}$ and we deduce: $\gamma_1 = t_1\Omega(\Delta)\sqrt{\frac{u_0^2+\Delta^2}{u_e^2+\Delta^2}} = t_1\Omega(\Delta)f$, and $\gamma_2 = t_2\Omega(\Delta)$. By definition, we have $T_e\Omega(\Delta_e) = 2\pi$, which is equal to $\gamma_1 + \gamma_2 = \Omega(\Delta_e)(t_2 + t_1 u_0/u_e)$. We compare f and u_0/u_e by computing their ratio: $\sqrt{\frac{u_0^2}{u_e^2}\frac{u_e^2+\Delta^2}{u_0^2+\Delta^2}} = \sqrt{\frac{1+u_0^2 X}{1+u_e^2 X}} > 1$, with $X = \Delta/(u_0^2 u_e^2)$. Therefore, $\frac{\Omega(\Delta)}{\Omega(\Delta_e)} = \frac{T_e}{t_2+t_1 f} > 1 \Rightarrow \Delta > \Delta_e$. The smallest offset that can produce an identity transformation with a regular-singular pulse is larger than Δ_e. Thus, these pulses are not optimal.

control fields, and to extend some of the previous results to the two input case. First, the scaling property of Fourier Transforms is extended to time-ordered exponentials and we use this property to connect 2D-regular controls to 1D singular controls.

First of all, let us rewrite the evolution operator of a regular control, defined by its amplitude u and its phase generator θ.

$$\begin{aligned}\hat{U}(u_0,\theta,T,\Delta) &= \mathbb{T}\exp\left(\int_0^T u_0(\cos(\theta(t))\hat{e}_x+\sin(\theta(t))\hat{e}_y)+\Delta\hat{e}_z dt\right)\\ &= \mathbb{T}\exp\left(\int_0^T u_0 e^{-\theta(t)\hat{e}_z}\hat{e}_x e^{\theta(t)\hat{e}_z}+\Delta\hat{e}_z dt\right)\\ &= e^{-\theta(T)\hat{e}_z}\mathbb{T}\exp\left(\int_0^T u_0\hat{e}_x+(\Delta+d_t\theta(t))\hat{e}_z dt\right),\end{aligned} \tag{5.41}$$

where the last equation is determined from theorem 13 (appendix C). Then, a 2D regular control can be seen as a constant pulse, with a time-dependent offset. We recover the single input case with a change of frame. In the new frame, the offset is given by u_0 and the control is $\Delta + d_t\theta$. However, the "new control variable" is unbounded [48]. By using the same arguments as the ones in the proof of proposition 8, we can assume that the constant pulse is optimal in the two input case. This intuition is reinforced by the next results. With equation (5.41), it is clear that the transformation can be rescaled in time and amplitude in order to produce the same transformation for a different offset, like usual constant pulses:

$$\begin{aligned}&\hat{U}(u_0,\theta,T,\Delta)=\hat{U}(u_e,\theta',T',\Delta/a)\Rightarrow\\ &e^{-\theta(T)\hat{e}_z}\mathbb{T}\exp\left(\int_0^T u_0\hat{e}_x+(\Delta+d_t\theta(t))\hat{e}_z dt\right)\\ &\quad= e^{-\theta'(T')\hat{e}_z}\mathbb{T}\exp\left(\int_0^{T'} u_e\hat{e}_x+(\Delta/a+d_t\theta'(t))\hat{e}_z dt\right),\end{aligned} \tag{5.42}$$

with the change of variable $v = t/a$, we obtain:

$$e^{-\theta'(T')\hat{e}_z}\mathbb{T}\exp\left(\int_0^{T'/a} au_e\hat{e}_x+(\Delta+d_v\theta'(av))\hat{e}_z dv\right). \tag{5.43}$$

Thus, we naturally relate: $u_0 = au_e$, $T = T'/a$, and $\theta'(at) = \theta(t)$. **A completely symmetric transformation is obtained if $d_t\theta$ is a negligible function or a function equal to zero almost everywhere.** [37, 141, 152]

Fast oscillating functions are good approximations of zero functions if their oscillations are in average close to zero for any sufficiently large integration domains [33]. Hence, we generalize proposition 8, 2) for the two input case.

Furthermore, we can compute the singular controls in the two-input case:

[48] Notice that a new Pontryagin Hamiltonian can be written using the Hamiltonian in the rotated frame $\hat{H}_n = u_0\hat{e}_x + (\Delta_n + \phi(t))\hat{e}_z$, where $\phi(t) = d_t\theta(t)$ is a new control variable. Since this control is unbounded, the optimal trajectory is a singular control of this new problem. Straightforward computations give: $l^z = 0$, $l^y = 0$ and $\phi = -\frac{\sum_n \Delta_n l_n^x}{l^x}$. This is another parametrization for regular trajectories of (ω_x, ω_y).

Proposition 9 (time singular control n°2): *Let $\mathcal{C}_\Delta = \{0, \Delta\}$ or $\mathcal{C}_\Delta = \{-\Delta, \Delta\}$ be the ensemble of offsets. Singular controls of the two-input case are given by the following parametrization:*

$$\omega_x(t) = u\cos(\phi_0 t + \phi_1) \tag{5.44}$$
$$\omega_y(t) = u\sin(\phi_0 t + \phi_1), \tag{5.45}$$

where u, ϕ_0, and ϕ_1 are real constants.

Proof. Case $\mathcal{C}_\Delta = \{0, \Delta\}$: From condition (5.12) and equation (5.9), we can determine:

$$\omega_x = \Delta\frac{l_1^x}{l^z} = \Delta\frac{l_0^x}{l^z} \tag{5.46}$$
$$\omega_y = \Delta\frac{l_1^y}{l^z} = \Delta\frac{l_0^y}{l^z} \tag{5.47}$$
$$l^z = Cst. \tag{5.48}$$

Then, by calculating explicitly $d_t\vec{l}_0$ we can compute the general form of ω_x and ω_y.
Case $\mathcal{C}_\Delta = \{-\Delta, \Delta\}$: The proof is similar. Using (5.9), we can compute $d_t\vec{l}$ and $d_t\vec{m} = d_t(\vec{l}_1 - \vec{l}_{-1})$. Then we show that $\omega_x \propto m_x$, $\omega_y \propto m_y$, and we can determine them using sine and cosine functions. □

From equation (5.41), it is straightforward to show that $\phi_0 = \phi_1 = 0$ and $u = u_e$ in order to produce a symmetric transformation. Therefore, we can expect that the constant pulse is also time optimal in these conditions. However, we do not have a proof of this statement, a proof can be established only by solving the complete problem, defined with $\mathcal{C} = \{-\Delta, 0, \Delta\}$. This is far more difficult. As a matter of fact, singular controls associated with the full problem are solutions of:

$$\omega_x = \frac{\Delta}{l_z}m_x \tag{5.49}$$
$$\omega_y = \frac{\Delta}{l_z}m_y \tag{5.50}$$
$$\frac{d}{dt}\begin{pmatrix} m_x \\ m_y \\ m_z \end{pmatrix} = -\begin{pmatrix} \Delta l_0^y - \omega_y m_z \\ \Delta l_0^x + \omega_x m_z \\ 0 \end{pmatrix} \tag{5.51}$$
$$\frac{d}{dt}\begin{pmatrix} l_0^x \\ l_0^y \\ l_0^z \end{pmatrix} = -\begin{pmatrix} -\omega_y l_0^z \\ \omega_x l_0^z \\ \omega_x l_0^y - \omega_y l_0^x \end{pmatrix}. \tag{5.52}$$

We do not have a general solution of this system, however, we can verify that constant pulses are solutions of the system.

Summary and conjecture

Single input case:

1. Regular controls with a small number of switchings cannot be optimal.
2. In the continuum limit, they can reproduce the behavior of a singular (constant) pulse.
3. A regular arc cannot switch to a singular arc.

Two-input case:

1. A 2D-regular pulse can be expressed with a single input system. A symmetric solution of the new problem is given by constant pulses.
2. 2D-singular pulses of $\mathcal{C}_\Delta = \{0, \Delta\}$ or $\mathcal{C}_\Delta = \{-\Delta, \Delta\}$ with symmetric spectrum are given by constant pulses.

Therefore, we conjecture that the time optimal solution is a constant pulse.

5.4.3 Numerical Analysis

In order to verify the conjecture, numerical investigations are performed. The goal is to solve the problem by "brute force" optimizations. We do not present numerical simulations for all the different cases investigated so far, but we focus on the most general problem defined with two controls (ω_x, ω_y), and $\mathcal{C} = \{-\Delta, 0, \Delta\}$.

Two algorithms have been used, a shooting algorithm, based on the integration of (5.9) (section A.2.3), and the well-known GRAPE algorithm (section A.2.1). We restricted the shooting algorithm to regular controls, but the GRAPE can design both regular and singular extremals.

As a concrete example we choose $\Delta = \pi/4$ and $u = 1$ to produce a rotation of π around the axis x. In this case, the pulse duration is a free parameter to determine. The control given by the shooting algorithm is plotted in figure 5.9, and the comparison with the best singular control is given in table 5.1.

The fast oscillating control phase (observed in figure 5.9) is in average constant. This is in agreement with the formula (5.41) and the proposition 8.

In order to understand the relation between the pulse duration and the offset selectivity, several optimizations at fixed final time have been performed for different offset values. Results are presented in figures 5.10a and 5.10b. We see that the curve of equation $T(\Delta) = \frac{1}{\Delta}\sqrt{4\pi^2 - \phi^2}$ defines the global minimum of F, and that the selectivity cannot be pushed below this curve. In order to verify the generality of these results, we proceed to several optimizations for different rotation angles and different pulse durations (offsets are fixed). These results are plotted in figure 5.11.

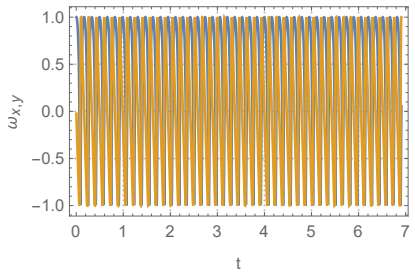

Figure 5.9: Control field determined by the shooting algorithm. ω_x : blue, ω_y : orange.

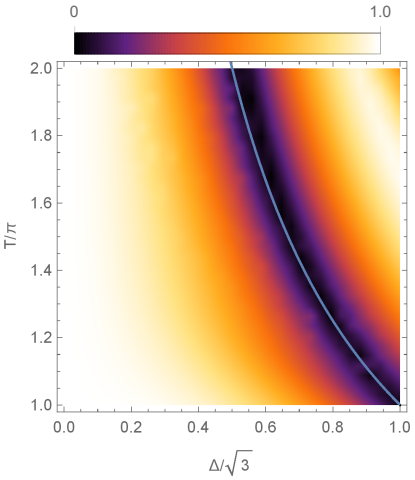

(a) Shooting Algorithm

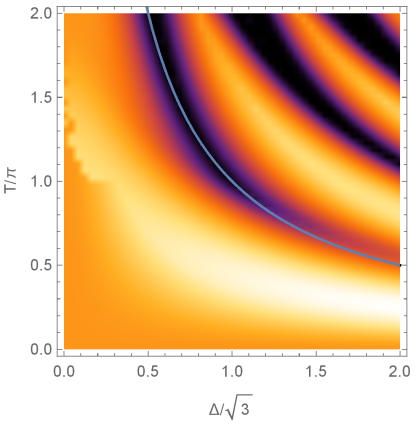

(b) GRAPE

Figure 5.10: Optimal control landscape of F as a function of the pulse duration T and the offset Δ, for selective π-rotation around x. The blue curve has the equation: $T(\Delta) = \frac{1}{\Delta}\sqrt{4\pi^2 - \phi^2}$. In the two figures, the cost is normalized and the contrast is adjusted to help the reading.

	Optimized pulse	Square pulse
F	0.035	0
T	6.9097	6.9282
u	1	0.4534
$\int_0^T \omega_x(t)dt$	3.1934	π
$\frac{1}{T}\int_0^T \omega_x(t)dt$	0.4622	0.4534
$\int_0^T \omega_y(t)dt$	-0.0926	0

Table 5.1 – Main features of an optimized pulse and a square pulse for the offset $\Delta = \pi/4$.

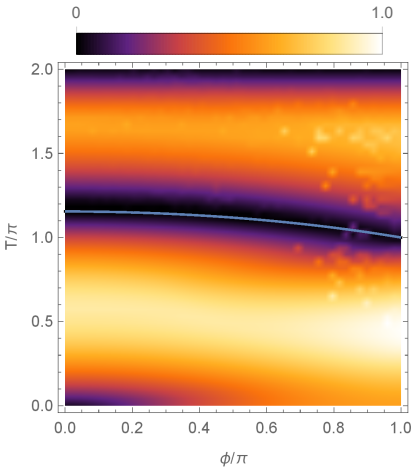

Figure 5.11: Optimal control landscape of F as a function of the pulse duration T and the angle of rotation ϕ. We set $u_0 = 1$ and $\Delta_0 = \sqrt{3}$. The blue solid line has for equation $T = \frac{1}{\sqrt{3}}\sqrt{4\pi^2 - \phi^2}$.

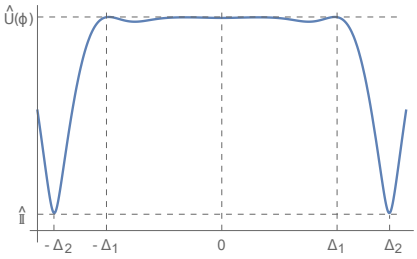

Figure 5.12: Spectrum of a locally robust selective pulse.

All these results are in agreement with the previous analytical results, and they confirm our conjecture.

5.5 Selective pulse with local robustness

In this section, two other situations are presented. In each case, a small area of robustness is considered. This area is defined by two neighborhood offsets with the same transformation. Since the problem complexity increases quickly with N, we focus on numerical calculations.

5.5.1 Case 1

In this section, we are interested in a standard situation, with a pulse robust on a small interval. In order to keep tractable computations, we choose the following ensemble of offsets:

$$\mathcal{C}_\Delta = \{-\Delta_2, -\Delta_1, \Delta_1, \Delta_2\}.$$

An example of spectrum is plotted in figure 5.12. As in the previous section, the goal is to produce a rotation of ϕ for the first offset and the identity for the second. Using [26], we know that for $\Delta_1 < \pi/2$, the time optimal control to achieve a rotation is given by a regular control, with eventually several switchings. A maximum bound for the number of switchings has been calculated and the structure of the control depends on three numbers to determine (see [26] for more details). The optimal control is one-dimensional, then, for symmetry reasons, we consider only positive offsets. In this chapter, we assume that the optimal pulse has at most one switching. Hence, the control is determined by two numbers: t_1, the time before the switching, and t_2, the time after the switching. We also define $T = t_1 + t_2$. The phase of the control is chosen positive at the origin. The proposition 14 gives

the following conditions to produce the identity.

$$(t_1 - t_2)\sqrt{u_0^2 + \Delta_2^2} = 2k\pi \tag{5.53}$$

$$(t_1 + t_2)\sqrt{u_0^2 + \Delta_2^2} = 2n\pi. \tag{5.54}$$

Choosing Δ_1 gives t_1 and t_2, and the ratio k/n and Δ_2. For the same reasons that constant pulses are optimal ultra-selective pulses, these bang-bang pulses should be optimal in this new situation.

The behavior of these locally robust controls have been investigated numerically. A similar graph as the one of figure 5.10b is produced. For that purpose, we used $\Delta_1 = 0.5$, $u_0 = 1$ and $\phi = \pi$ (rotation around x). The second offset $\Delta_2 = \Delta$ and the pulse duration T vary and the best control is determined in each situation. The result is shown in figure 5.13. The minimum time to generate the ϕ rotation is $T^* = 5.9$, and we see that no field is found under this limit. Therefore, the case $n = 1$ is not possible and only interesting solutions are found for $n > 1$.

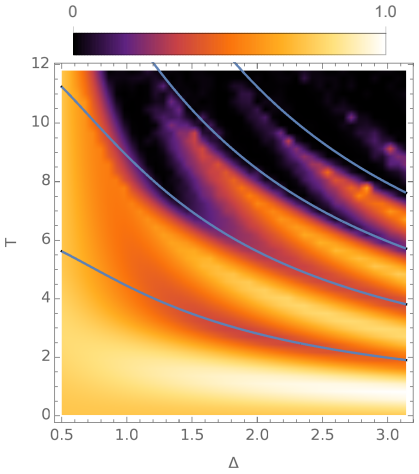

Figure 5.13: Optimal control landscape of F as a function of the pulse duration T and the offset of fidelity Δ, for a locally-broadband selective rotation of π around x. Blue curves are given by equation (5.54) for different values of k.

5.5.2 Case 2

The second example consists of a selective pulse robust for the identity. For that purpose, we consider an ensemble

$$\mathcal{C}_\Delta = \{-\Delta_2, -\Delta_1, 0, \Delta_1, \Delta_2\},$$

and we consider a rotation of angle ϕ around x at resonance. The other offsets correspond to the identity (figure 5.14). There is a trivial solution for $\Delta = \sqrt{(2k\pi)^2 - \phi^2}/T$, so we impose that $T|\Delta_2| \in [\sqrt{(2\pi)^2 - \phi^2}, \sqrt{(4\pi)^2 - \phi^2}]$. The time optimal pulse solution of the case 1 is not trivial, then we directly use a numerical approach. We chose a maximum control bound $u_0 = 1$, and we set $\Delta_1 = \sqrt{3}$, and $\phi = \pi$. Then, we performed several optimizations with GRAPE for different pulse durations T and different offsets Δ_2. The minimum of Fidelity as a function of these two parameters is plotted in figure 5.15. We see that above the curve of equation:

$$T = \phi\left(1 + \frac{\Delta_1}{\Delta_2 - \Delta_1}\right), \tag{5.55}$$

the algorithm always finds a very good solution. Therefore, we can consider that equation (5.55) defines a time optimal upper bound. We derived it with a heuristic approach from equation (5.41). As a matter of fact, the pulse duration must be scaled inversely to the offset scale. In this case, the offset of reference is Δ_1 and we consider a second offset Δ_2, which is free to move on the offset axis according to the scaling factor $\frac{\Delta_2 - \Delta_1}{\Delta_1}$. Hence, we deduce that the time to perform the full transformation is approximately the minimum time to transform Δ_1 plus the time induced by the scaling.

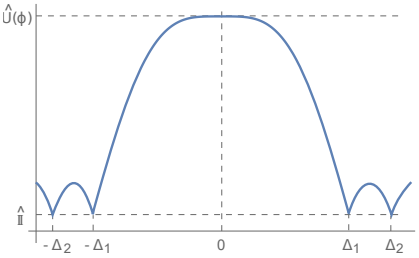

Figure 5.14: Spectrum of a locally robust selective pulse.

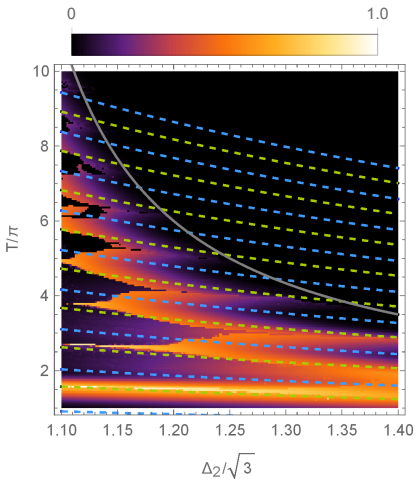

Figure 5.15: Optimal control landscape of F as a function of the pulse duration T and the offset Δ_2, for a locally-broadband selective rotation of π around x. Blue dashed curves are given by equation (5.54) for different values of k. Green dashed curves are given by equation (5.57). The gray curve is given by equation (5.55).

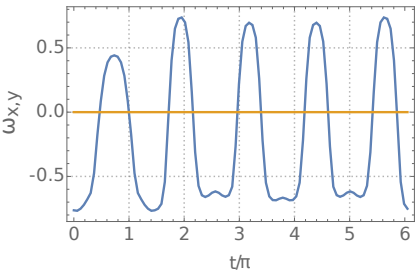

Figure 5.16: Optimal control field computed for $\Delta_2 = 1.13\sqrt{3}$ and $T = 5.34\pi$. The blue solid line is ω_x, the orange solid line is ω_y. For this control, $F = 5 \times 10^{-13}$.

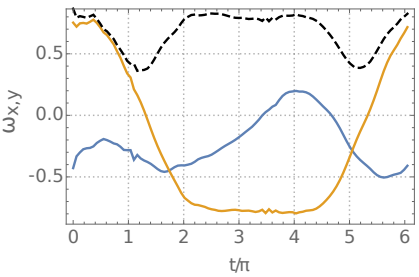

Figure 5.17: Optimal control field computed for $\Delta_2 = 1.23\sqrt{3}$ and $T = 5.34\pi$. The blue solid line is ω_x, the orange solid line is ω_y and the black dashed line is the norm. For this control $F = 9.9 \times 10^{-4}$.

However, good solutions can be found below the curve of equation (5.55). The landscape has a complex structure with areas of extremely small costs ($< 10^{-13}$) surrounded by areas of extremely large costs (around 1, the maximum of F). Additionally, the transition between such areas is generally not smooth. Areas of good and bad fidelity can be described qualitatively by two functions. The first one is the usual law of square pulses:

$$T = \frac{1}{\Delta_2}\sqrt{4k^2\pi^2 - \phi^2}. \tag{5.56}$$

The second one is given by the function that defines the control phase switching in the optimal control of a single offset (see proposition 6 in [61]):

$$T = -\frac{(4n \pm 1)\pi}{\Delta_2}. \tag{5.57}$$

These two equations give respectively low and high values of F near $\Delta_2 \simeq \Delta_1$, and near (5.55). However, we observe a switching around half the distance of these two extremities.

This switching is not fully understood yet, but we can conjecture that this latter is related to a switching between singular and regular solutions. Two examples of control (of same duration $T = 5.34\pi$), taken on both sides of the "bad cost area", are plotted in figures 5.16 and 5.17. The optimal trajectory seems to be singular in 5.16, and regular in 5.17. The difference between the curves shows the variety of the solutions.

5.6 Discussion & conclusion

In this chapter, we studied several cases of selective pulses with geometrical and numerical tools of OCT.

For the first case, we have computed singular and regular trajectories for the time minimization problem. Singular arcs correspond to constant pulses. A study based on analytical and numerical computations has shown that regular pulses cannot produce a more selective transformation than a constant pulse. This point can be understood heuristically with a simple geometric argument: a rotation produced by a $SO(3)$-transformation can be seen as a trajectory on a sphere, where each rotation produces a small arc [96, 18, 44]. The product of two rotations defines a spherical triangle on this sphere. Therefore, due to the triangle inequality, the effective rotation angle must be equal or smaller than the sum of the two rotation angles ($\gamma \leq \alpha + \beta$, see figure 5.18). In the selectivity problem, the goal is to produce the identity, or equivalently, a 2π-rotation, as quickly as possible. Regular controls produce exactly the opposite effect, because, the successive product of rotations is an effective rotation, with an angle smaller than the sum of the primitive angles. Thus they cannot be time-optimal.

These results must be compared with another recent study of optimal selective state-to-state transfer in magnetic resonance [169]. The system used in this study is slightly different: Two spins are assumed to be initially at the north pole of the Bloch sphere, and the goal is to steer a spin of offset $-\Delta$ towards the equator (or the south pole), while bringing back the other spin, with offset $+\Delta$, to the initial state. For this system, the optimal solution is a concatenation of two regular arcs, separated by a singular arc. Moreover, with this system, singular controls are zero. This drastic change of structure is explained by the smaller number of variables required to parametrize a vector than a rotation matrix. The system is less constrained, and there exist faster trajectories than the constant pulse solution.

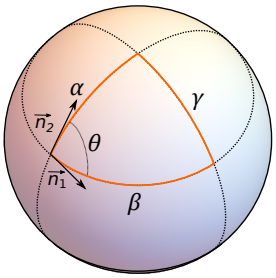

Figure 5.18: Spherical triangle produced by two rotations about $\vec{n}_1$ and $\vec{n}_2$, with respective angles α and β. γ is the effective angle of rotation.

The second part of this work is devoted to two other selectivity problems with additional robustness constraints. This constraint is introduced with additional offsets in $\mathcal{C}_\Delta$, which must produce either a rotation of ϕ or the identity. The introduction of a local robustness leads to a new control strategy. As a matter of fact, one needs to cancel the phase accumulation at the new offset frequencies. Thus, regular controls are particularly efficient for that purpose. Numerical calculations, and analytic results, show that regular controls are the optimal solutions in several situations. Nevertheless, we have also found cases where the optimal solution seems singular. The simultaneous presence of regular and singular solutions for the same system (but with different parameters) is a point to explore in future works.

Nevertheless, we found similar structures in the landscape of optimal solutions (figures 5.10b, 5.13, 5.15). The minimum time solution can be predicted with simple equations.

This study opens the way to a series of control problems. An interesting issue is to extend this analysis to a case with relaxation effects. In experiments, these effects can be neglected when the control duration is very short, but if one uses very long pulses (in order to produce a very selective excitation), the relaxation could not be negligible. The simultaneous control of two spins with relaxation has been studied recently [24] and singular trajectories have been analyzed in detail for the contrast problem. The selectivity problem can be viewed as a slightly modified contrast problem, and new non-trivial solutions could exist. The selectivity problem can also be tackled from the fingerprinting point of view. This is the topic of the next chapter.

Chapter 6

Optimal database design for Fingerprinting experiments

6.1 Introduction

The fingerprinting method is a well-known technique generally used for determining the identity of a person. The basic concept is illustrated in Fig. 6.1. The overall process can be decomposed into three different steps: *(i)* a fingerprint recording of an ensemble of subjects, *(ii)* the creation of a database (also called dictionary) where fingerprint images are associated with person identities, and *(iii)* a recognition process where a numerical search algorithm finds the closest database element to the fingerprint of an unknown subject. Assuming that fingerprints are different for each person, a mapping between fingerprints and persons can be defined, making possible the identification protocol. This idea can be generalized to any system, which has unique properties that can be revealed by a measurement process. This approach can be applied in a static setting, but also in a dynamical one where the system is subjected to an external control field. In this latter case, each element of the database corresponds to the time evolution of some observables under the action of the field, thus increasing the complexity of the fingerprints and the precision of the estimation. This idea has been recently adapted to Magnetic Resonance Imaging (MRI) for the identification of tissue parameters [110]. This initial investigation led to an impressive number of studies in this domain (see e.g. [130, 12] to cite a few). A crucial issue in this fingerprinting process is the design of the excitation field. A simple approach using a time-dependent random field was proposed in [110] in order to limit the correlations between the different fingerprints. However, this approach does not incorporate information about the system dynamics and the recognition process and is therefore not expected to reach its precision limit. To overcome this fundamental difficulty, we propose in this paper to combine a standard fingerprinting process with recently developed optimal control techniques in quantum control [63, 67, 87]. This Optimal Fingerprinting Process (OFP) allows us to maximize the efficiency of the identification and to minimize the errors made in the pa-

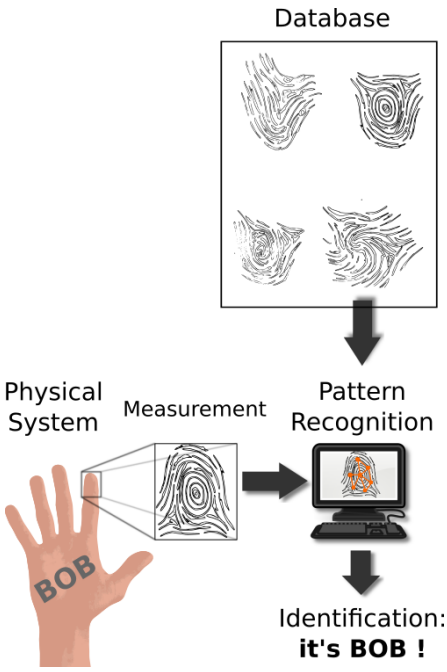

Figure 6.1: The fingerprinting principle: A physical system is identified by using a pattern recognition between a fingerprint measurement and the elements of a database.

rameter estimation. As an illustrative example, this method will be used to identify the relaxation parameters of a spin- 1/2 particle. In this case, the estimation is made from a series of free-induction decay signals induced by impulsive excitations of different intensities. Note also that the measurements we consider are classical as they result from a continuous measurement of a large number of quantum systems. Nevertheless, the same type of processes [107, 183] could be carried out with quantum measurements in quantum metrology [66, 65]. Closely related but different concepts using external fields to estimate the parameters of quantum systems have also been developed in the past few years [63, 64, 149, 150, 149, 103, 102]. The combination of optimization and fingerprinting techniques has been explored in recent works in MRI [12, 113].

The chapter is organized as follows. Section 6.3 describes the theoretical framework of the method. The technique is studied numerically in Sec. 6.4.1 to estimate its efficiency on spin system. The stability of the estimation in presence of noise is discussed and analyzed. Finally, the optimal fingerprinting process is demonstrated experimentally in Sec. 6.5 on a spin 1/2 particle by using techniques of Nuclear Magnetic Resonance.

6.2 Notations

- *Dictionary* and *Database* are two synonyms words in this document. They refer to a collection of entities (functions, images, words..) associated to distinct physical systems. In the context of OFP, dictionary has a specific meaning : it is a set of N possible measurements.
- $\mathcal{S} = \{S_n\}$ is the set of system physical parameters.
- $\mathcal{L}^2$ is a space of real square Lebesgue integrable functions.
- σ_n is the partition number n of $\mathcal{L}^2$.
- $\{f_n\}_{n=1..N} \subset \mathcal{L}^2$ is the dictionary.
- N : size of the dictionary.
- f_n is a function (an element) of the dictionary.
- $D[f, g]$ is the square distance between normalized functions f and g.
- $(\cdot, \cdot)$ is the scalar product on $\mathcal{L}^2$.
- $\langle \cdot | \cdot \rangle$ denotes other scalar products, generally in Hilbert spaces.
- $\alpha_n[g] \in \mathbb{R}$ is the scaling factor of g relatively to f_n.
- $g \sim_n \tilde{g}$: g and $\tilde{g}$ belong to the same equivalent class.
- $\mathcal{C}_n^\alpha$: an equivalent class α for D.

- g a function of $\mathcal{C}_n^\alpha$ such that $(g, g) = 1$.
- C : Figure of merit.
- A_n is the connection of the dynamical manifold associated to the system n.
- u, ω are the control fields (ω is used in the Bloch equation).
- $\hat{U}_n(0,t)$: evolution operator from 0 to t for the system n.
- $\hat{U}_n^k$: evolution operator from the pulse $k-1$ to the pulse k for the system number n.

6.3 Theoretical framework

The optimization problem related to a fingerprinting experiment is not standard. Instead of bringing an initial state to a final one in minimum time or energy, we aim at generating a database (dictionary) that maximizes the efficiency of the recognition process. Therefore, the target is not an element of a vector space, but rather an unknown set of vectors, connected by dynamical properties[49]. This optimization is not trivial at all, and the figure of merit to maximize depends strongly of the measurement protocol. In order to obtain a well-defined problem, it is necessary to define rigorously the recognition process. Then, optimization procedures are investigated.

[49] As explained below, initial and final states are not fixed, they are free to move in the entire space. The relevant quantity is the distance between the vectors.

6.3.1 The recognition process

We consider three different sets:

- a space of real square integrable functions g, with $g : [0,T] \mapsto \mathbb{R}^d$. This space is the set of all the possible measurements and d is the number of components of g.
- a set $\mathcal{S}$ of N elements $\vec{S}_n$. Each S_n is a p-tuple of values of the p physical parameters to estimate, $S_n = (S_1(n), \cdots, S_p(n))$.
- a set of N time-dependent functions f_n : $\{f_n\}_{n=1,\cdots,N}$, f_n : $[0,T] \mapsto \mathbb{R}^d$. This set is the dictionary used in a fingerprinting process.

The space of possible measurements is partitioned into N different subsets, $\{\sigma_n\}_{n=1,\cdots,N}$. A function f_n of the dictionary is associated with each element σ_n (figure 6.2). Ideally, the partitioning satisfies the constraints:

1) $f_n \in \sigma_n$ and $\forall k \neq n$, $f_n \notin \sigma_k$,

2) $\forall g \in \sigma_n$, $D[f_n, g] < D[f_k, g]$. If $D[f_n, g] = D[f_k, g]$, then g belongs to the joined boundary between σ_n and σ_k.

The functional D is defined by:

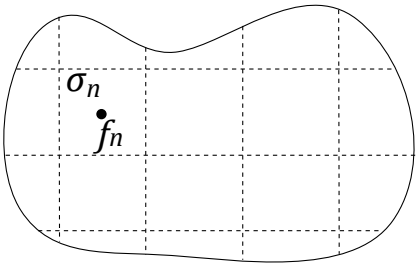

Figure 6.2: Partitioning of the space of possible measurements.

$$D[f_n, g] = \left\| \frac{f_n}{\|f_n\|} - \frac{g}{\|g\|} \right\|^2 \tag{6.1}$$

D is the square of the distance between two normalized functions. The first function, f_n, belongs to the dictionary, and g, is the result of a measurement. $\|f\|$ refers to the norm of f, defined by $\|f\| = \sqrt{(f,f)}$, $(\cdot,\cdot)$ being the scalar product. In the continuous case, the scalar product of two functions $f(t)$ and $g(t)$ can be defined as $(f(t), g(t)) = \int_0^T f(t)g(t)dt$.

Definition 6 (recognition process): *The recognition process consists of associating a function g to an element σ_n of the partition. To each σ_n is attached a set of values of the physical parameters S_n. A bijection can thus be defined between a partition and a specific physical system.*

The recognition process can be mathematically defined as follows:

$$f_m = \arg \left[\min_{n=1,\cdots,N} (D[f_n, g]) \right]. \tag{6.2}$$

Equation (6.2) means that the function f_m associated with g is the one minimizing $D[f_n, g]$ over all the possible functions f_n. Note that the functional D can also be written as:

$$D[f_n, g] = 2\left(1 - \frac{(f_n, g)}{\|f_n\|.\|g\|}\right). \tag{6.3}$$

6.3.2 Figure of merit

Definitions and theorems

It is worth noting that normalized functions are used in the definition of the functional D. This point is due to the fact that the measurement process is defined up to a scaling factor. The amplitude of the signal depends on many unknown parameters, such as the number of spins or the spectrometer sensitivity. The comparison theory/experiment is always performed in normalized units. From a mathematical point of view, this means that we do not consider a function but a class of functions. This paragraph is aimed at giving a rigorous framework to this issue. The main result is the simplification of the figure of merit from a functional to a real function of one real variable. This geometric description gives also an upper bound on the values of the figure of merit. We first define the equivalence classes of the functional D.

Definition 7 (Equivalence class): *Two functions g and g' are said to be equivalent and denoted $g \sim_n g'$ if and only if $D[f_n, g] = D[f_n, g']$. The equivalence class is given by $\mathcal{C}_n^\alpha = \{g,\ D[f_n, g] = 2(1 - \cos\alpha_n)\}$, where α_n is the angle between g and f_n, with $(g, f_n) = \|g\|\|f_n\|\cos\alpha_n$ (see Eq. (6.3)).*

Note that the use of equivalence classes transforms the functional $D[f_n, g]$ defined over an infinite dimensional space into a simple function $D(\alpha_n)$ over $\mathbb{R}$ and the only relevant parameter is the angle α_n. The use of equivalence classes allows us to rewrite D as a simple function of α_n:

$$D[f_n, g] = 2(1 - \cos(\alpha_n)). \tag{6.4}$$

The main difficulty from the optimization point of view is to define the concept of a *good dictionary*. In particular, the size of the dictionary is arbitrary and depends on the discretization used for the physical parameters. Since the parameters take their values in a continuous set, it is possible to consider a dictionary of arbitrarily large size. Furthermore, the dictionary must be independent on experimental imperfections because it is computed before the measurement process. **We solve this problem with the following proposition: The best dictionary is the one that optimizes the recognition process. We introduce the following figure of merit C_N to measure the quality of the dictionary.**

Definition 8 (figure of merit OFP): *The figure of merit C_N for a dictionary of N elements is given by the mean value of all the possible square distances between the functions f_n and f_k:*

$$C_N = \frac{1}{2N^2} \sum_{n,k=1}^{N} D[f_n, f_k]. \tag{6.5}$$

As shown below, the normalization factor $2N^2$ is chosen so that the upper bound of C_N is 1. Some properties of C_N can be established. Equivalent classes allow us to formulate the problem into a simple geometric picture. The normalized functions $\vec{f}_n = f_n / \|f_n\|$ can be viewed as points belonging to a $(N-1)$- sphere S^{N-1} of radius 1, and consequently the dictionary is a $(N-1)$-simplex. The distance between two vertices $\vec{f}_n$ and $\vec{f}_k$ is given by $\sqrt{D[\vec{f}_n, \vec{f}_k]}$. We are interested in the shape of the simplex that maximizes C_N (i.e which maximizes the sum of the lengths of the edges). Examples of optimal solutions are plotted in figure 6.3. For $N = 2$, it is obvious that the maximum is reached when $\vec{f}_1 = -\vec{f}_2$. For the case $N = 3$, it can be shown that the highest value of C_3 is obtained for an equilateral triangle where each angle α_{nk}, with $(\vec{f}_n, \vec{f}_k) = \cos(\alpha_{nk})$, is equal to $2\pi/3$, $\forall n, k$. For higher values of N, we get a regular simplex [50]:

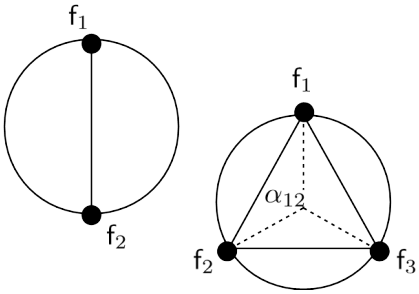

Figure 6.3: Geometric representation of the optimal solution for $N = 2$ and $N = 3$.

Theorem 1 (Optimal simplex): *The optimal simplex is given by the set of functions $\{\vec{f}_n\}_{n=1,\cdots,N}$ corresponding to a $(N-1)$- regular simplex of radius 1. The upper bound of C_N is equal to 1.*

Proof. We consider $\vec{f}_n$ as a vector going from the center O to a

[50] Theorem 1 does not take into account dynamical constraints imposed by the physical system. In practice, this optimal configuration might not be reached.

point of the hypersphere of radius 1. We have:

$$\sum_{n,k=1}^{N} \|\vec{f}_n - \vec{f}_k\|^2 = 2N^2 - 2 \sum_{n,k=1}^{N} (\vec{f}_n, \vec{f}_k).$$

Since

$$\| \sum_{n=1}^{N} \vec{f}_n \|^2 = \sum_{n,k=1}^{N} (\vec{f}_n, \vec{f}_k),$$

we deduce that

$$\sum_{n,k=1}^{N} \|\vec{f}_n - \vec{f}_k\|^2 = 2N^2 - 2\| \sum_{n=1}^{N} \vec{f}_n \|^2.$$

This expression shows that the maximum value of $\sum_{n,k} \|\vec{f}_n - \vec{f}_k\|^2$ is $2N^2$, i.e. the inverse of the normalization factor of C_N. We obtain that $C_N \leq 1$. The maximum value is reached for $\sum_{n=1}^{N} \vec{f}_n = 0$. This is the equation of the simplex barycenter, which is equal to zero for a regular simplex [77]. □

It is possible to generalize the figure of merit to optimize by adding weighting coefficients μ_{nk} such as:

$$C_N = \frac{1}{2N^2} \sum_{n,k=1}^{N} \mu_{nk} D[f_n, f_k]. \tag{6.6}$$

But in this case, the optimal simplex is not regular anymore and edge lengths are determined by the coefficients.

Discussion about the figure of merit

The definition of the functionals D and C are quite subjective, and other definitions are possible. Many different possibilities have been investigated. In this section, we come back to the different criteria and the different definitions of D and C we investigated. Comparisons are presented in table 6.1.

Figures of merit can be classified according to the two following criteria:

- The figures of merit, which take into account the experimental scaling factor, and the ones which do not.
- The ones based on the distance between functions, and the ones based on their scalar product [51].

[51] Of course, the definition of D can be changed to agree with the definition of C.

In order to explain the choice made in this work, we summarize the investigations:

- The introduction of a scaling factor during the optimization is a crucial point. When the latter is considered, the gradient $\delta C/\delta u$ is very complicated, and it is almost impossible to derive analytic expressions. Despite this rise of complexity, the scaling factor is necessary. Otherwise, **the choice**

of the normalization becomes arbitrary and a control field could appear extremely good with a specific choice of normalization and absolutely disastrous with another choice. Indeed, saying that "a dictionary is good" is very "*vague*", since many different configurations can satisfy the optimal conditions. Fixing the scaling factor reduces the number of possibilities and allows us to perform well-defined optimizations.

- A curve recognition could be used with two different procedures : *(1)* by minimizing a distance, or *(2)* by maximizing the scalar product. Due to the well-known relation : $|a-b|^2 = |a|^2 + |b|^2 - 2\langle a, b\rangle$, the two approaches are similar, but the distance contains more information. We have noticed that in general, the scalar product leads to non-interesting solution. For example, suppose that the functions are not normalized during the optimization. Then, we can show that the simplest solution for the algorithm is to put the norm of the functions to zero. This solution is then trivial.... and useless. Now, if functions are normalized, the amplitude cannot go to zero, but we observe that the algorithm becomes unstable and depends strongly on the initial condition. The control landscape looks also more complex, and in practice it has been almost impossible to compute optimized fields with a real advantage over random fields.

6.3.3 Continuum limit

A better accuracy of the fingerprinting process can be obtained by increasing the size of the dictionary. However, this procedure has a limit in terms of computational time, in particular to find the global optimum of the problem since the complexity of the control landscape increases rapidly with N [52]. These numerical difficulties inherent to OFP can be avoided by using curve fitting in the post-measurement lookup stage. The fit is made with a minimization of $D[f,g]$ based on a descent gradient algorithm with respect to the physical parameters to identify. In this case, the control field is fixed and a discrete derivative is used to compute the gradient $\{\partial_{\lambda_k} D[f(\{\lambda_k\}), g]\}_{k=1..p}$. Numerical simulations reveal that this approach converges after 50 or 100 iterations. Note that this concept is close to the Levenberg-Marquardt Method [116], which is included in most of curve fitting codes.

An experimental example is displayed in Fig. 6.4, where we observe the fluctuations of the signal around a mean value. The experimental setup is modeled by considering a simulated noise added to the response of the system:

$$g(t) = \bar{g} + \epsilon\mathcal{N}(t), \tag{6.7}$$

where $\bar{g}$ is the mean value of g over many measurements, ϵ the standard deviation and $\mathcal{N}$, a Gaussian noise centered in 0 with a variance of 1.

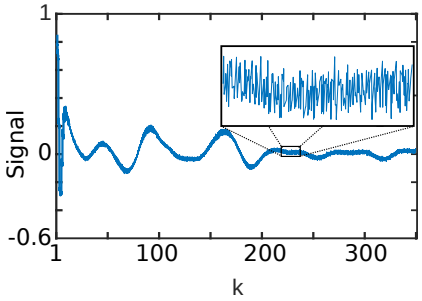

Figure 6.4: Time evolution of the experimental signal during a sequence of 350 δ- pulses. The signal is expressed in arbitrary units. The insert is a zoom showing the fluctuations of the signal. The parameter k refers to the number of the pulse in the control process.

[52] For example, if a precision of 1 ms (or 1 Hz) in the measurement is needed, around 10^8 dictionary elements must be computed in order to cover a sufficiently large parameter area. For sequences of 500 pulses, this represents more than 10 Tb of memory, and 1400 hours of CPU computation time.

	$\sum \|\|f_n - f_k\|\|^2$	$\sum(\mathfrak{f}_n, \mathfrak{f}_k)$	$\sum \left\| f_n - \frac{(f_n,f_k)}{\|\|f_n\|\|.\|\|f_k\|\|} f_k \right\|^2$	$\sum D[f_n, f_k]$
$+$	intuitive, allows analytic solution of the control field	intuitive definition	take into account the scaling factor	take into account the scaling factor, easy to work with
$-$	sensitive to the choice of scaling factor	defines a bad dictionary from the experimental point of view	same problem as the scalar product, too sensitive to the initial field during the numerical optimization	
$\sum \|\|f_n - f_k\|\|^2$	-			
$\sum(\mathfrak{f}_n, \mathfrak{f}_k)$		-	Equivalent systems	
$\sum \left\| f_n - \frac{(f_n,f_k)}{\|\|f_n\|\|.\|\|f_k\|\|} f_k \right\|^2$		Equivalent systems	-	Same symmetry group and classes of equivalence
$\sum D[f_n, f_k]$			Same symmetry group and classes of equivalence	-

Table 6.1: List of advantages/drawbacks and the connections to the different definitions of C.

Note that performing an optimization on a dictionary of small size, and using the continuum limit does not preserve the optimality of the control field. However, in practice, only a local extremum of C is reached by the numerical algorithm. The only important point is to improve in average the result of the recognition process.

6.3.4 Measurable functions for linear systems

Functions f_n can be any time-dependent function that characterizes the output signal. They have the following properties:

$$\begin{array}{ccccc} \mathcal{S} \times \mathcal{L}^2(\mathbb{R}^k, dt) & \longrightarrow & \{f_n\}_{n=1..N} & \longrightarrow & \mathbb{R} \\ S_n \times u & \longrightarrow & f_n[u] & \longrightarrow & C[u] \end{array}$$

In this manuscript, we focus on systems whose dynamics are defined by a linear differential equation, like the Bloch or the Schrödinger equation. More precisely, the evolution is assumed to be of the form:

$$\frac{d\hat{U}_n(t)}{dt} = \left(A_n^0 + u(t)A^1\right)\hat{U}_n(t) \; ; \; A^0, A^1 \in \mathfrak{g} \tag{6.8}$$

where $\mathfrak{g}$ is a Lie-algebra to specify. In order to use a gradient ascent algorithm (section A.2.1), functions f_n are defined as dif-

ferentiable maps of $\hat{U}_n(t)$ into $\mathbb{R}^d$. An example is given by:

$$f_n(t) = \begin{pmatrix} Tr[\hat{P}_1\hat{U}_n(0,t)] \\ Tr[\hat{P}_2\hat{U}_n(0,t)] \\ \cdots \\ Tr[\hat{P}_i\hat{U}_n(0,t)] \\ \cdots \\ Tr[\hat{P}_d\hat{U}_n(0,t)] \end{pmatrix} = \sum_{i=1}^{d} Tr[\hat{P}_i\hat{U}_n(0,t)]|P_i\rangle \qquad (6.9)$$

where $\hat{P}_i$ is a projector, which specifies dynamical boundary conditions. More complicated maps could be considered. For example, if we measure the mean value of an observable, we can define:

$$f_n(t) = \sum_{i=1}^{d} \left(\int_{\{m\}} Tr[\hat{P}_i\hat{U}_{n,m}(0,t)]d\rho(m) \right) |P_i\rangle \qquad (6.10)$$

where the label m refers to a subsystem belonging to the global system n: $S_n = \cup_m S_m$ and ρ is a probability measure. For example, in NMR, measurements are expressed as a mean value of the magnetization produced by several spins with different offsets. Concrete examples are given in section 6.4.

6.3.5 Summary of the optimization procedure

Optimization and measurement processes are summarized graphically in figure 6.6.

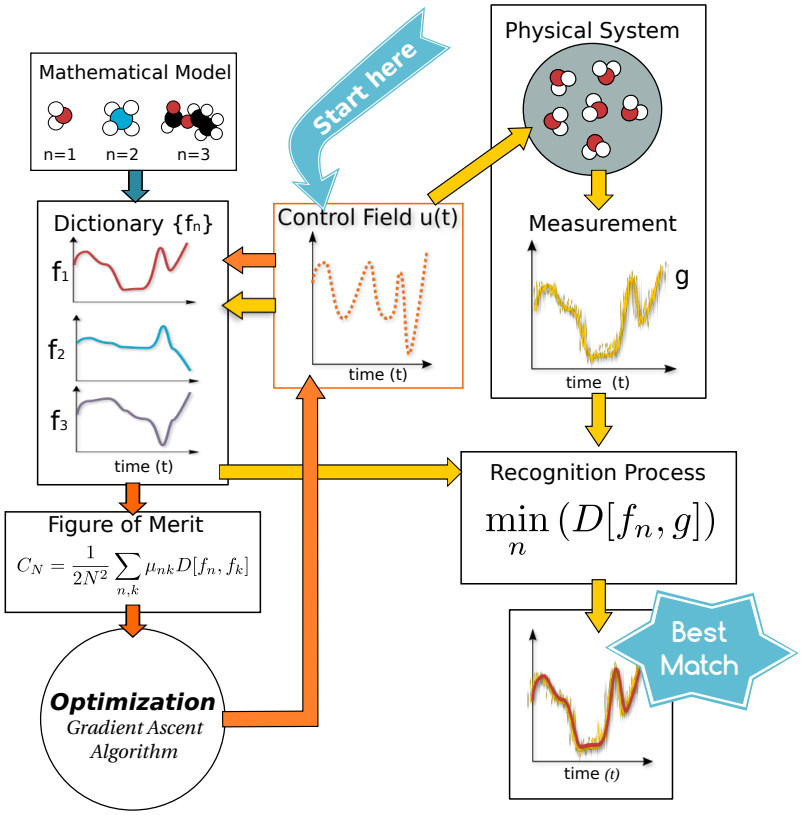

Figure 6.5: The OFP is composed of two different loops. The first loop (yellow arrows) is the standard fingerprinting process. A control field $u(t)$ is designed at the starting point of the loop. This field is applied to a physical system, which returns a specific response $g(t)$. On the other side, the response is computed numerically for an ensemble of physical systems with different values of the parameters. These simulations define a *dictionary* of functions $f_n(t)$. The recognition process allows us to find the best match between elements of the dictionary f_n and the result of the measurement g. The second loop (orange arrows) describes the dictionary optimization. The optimization is performed for an ensemble of N systems with different values of the parameters. An optimal control algorithm is used to maximize numerically the figure of merit.

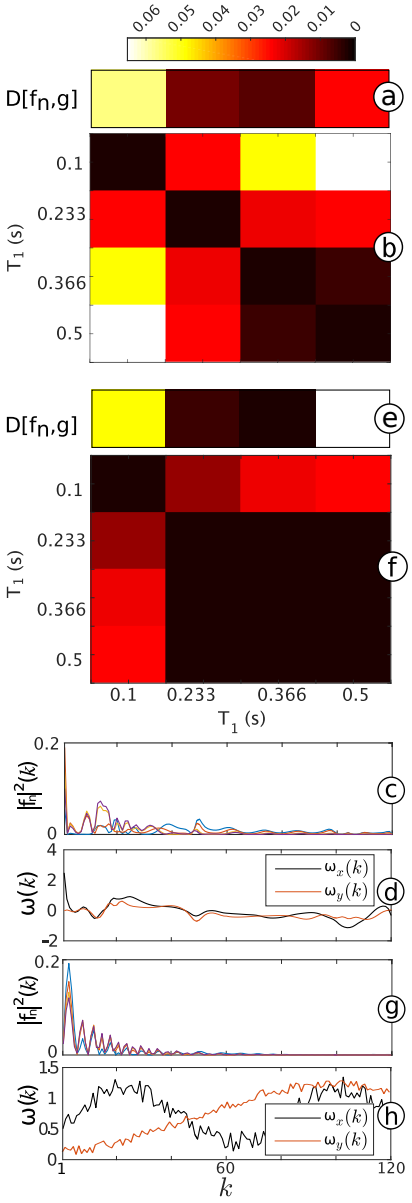

Figure 6.6: The dictionary is composed of 4 elements regularly distributed in the interval $T_1 \in [0.1, 0.5]$ s. Giving an optimal (d) and a random (h) control fields (the black and the red (dark gray) lines represent respectively ω_x and ω_y), we can compute the associate square modulus of dictionary functions (c) and (g). The dictionary functions are dimensionless. The efficiency can be checked with the recognition maps $(T_1(m), T_1(n)) \mapsto D[f_m, f_n]$ in (b) and (f). The panels (a) and (e) show the distance between the elements of the dictionary and the system to identify ($T_1 = 0.3$ s). The parameter k refers to the number of pulses in the control process.

6.4 Application to spin systems

In order to apply OFP on spin systems for NMR experiments, we consider the Bloch equation with relaxation (1.54). The ensemble of parameters to determine is given by $(T_1, T_2, \Delta\omega, \bar{\omega})$ where $\Delta\omega$ is the full width at half maximum (FWHM) of the B_0 offset distribution and $\bar{\omega}$ is the center of the distribution. We assume that the effect of the B_1 distribution is negligible (the coupling constant is set to $g = 1$ for each spin and its dimension is absorbed in the definition of the control.). Functions of the dictionary are chosen to be the transverse magnetization:

$$f_n(t) = \begin{pmatrix} \bar{M}_x(t) \\ \bar{M}_y(t) \end{pmatrix} = \begin{pmatrix} \int \rho(\Delta, \Delta\omega_n, \bar{\omega}_n) \langle x|U_n(\Delta, t)|z\rangle d\Delta \\ \int \rho(\Delta, \Delta\omega_n, \bar{\omega}_n) \langle y|U_n(\Delta, t)|z\rangle d\Delta \end{pmatrix} \tag{6.11}$$

At $t = 0$, each spin is assumed to be in the state $|z\rangle$ (north pole of the Bloch sphere).

The control field is a sequence of Dirac pulses (with respect to T_1 and T_2):

$$\omega_\mu(t) = \sum_{k=1}^{N_p} \omega_{\mu,k} \delta(t - kT), \qquad \mu = x, y, \tag{6.12}$$

where $\omega_{\mu,k}$ is the amplitude of the k-th pulse, N_p the number of pulses and T the time between each pulse. This approximation leads to a straightforward time discretization of the system dynamics. The measured signal corresponds to the average magnetization just after each δ- pulse, $(\bar{M}_x^{(n)}(t = kT), \bar{M}_y^{(n)}(kT))$ with $k = 1, \cdots, N_p$. Under these assumptions, an analytic expression of the gradient is determined. Using its expression in GRAPE (section A.2.1) provides an important speed up of the overall process.

By inserting equation (6.11) into the figure of merit (definition 8) and using functional derivatives (theorem 15), The gradient is expressed as follows:

$$\frac{\delta\langle\mu|\hat{U}_n|z\rangle}{\delta\omega_{\mu,i}} = -\frac{2}{N^2} \sum_{n=1}^{N} \sum_{l>i} \mathbf{A}_n . \frac{\delta f_n^l}{\delta\omega_{\mu,i}} . f_n^l + \left(\sum_{k=1}^{N} \mathbf{B}_{nk} f_k^l \right) \frac{\delta f_n^l}{\delta\omega_{\mu,i}} \tag{6.13}$$

with

$$\mathbf{A}_n = \sum_{k=1}^{N} \frac{(f_n, f_k)}{\|f_k\| . \|f_n\|^3} \quad ; \quad \mathbf{B}_{nk} = \frac{1}{\|f_k\| . \|f_n\|}$$

and

$$\frac{\delta f_n^l}{\delta\omega_{\mu,i}} = \langle\mu| \left(\prod_{k=i+1}^{l} \hat{U}^k \right) A^\mu \left(\prod_{k=1}^{i} \hat{U}^k \right) |z\rangle$$

6.4.1 Numerical example

We first analyze the ideal situation of a homogeneous ensemble of spin- 1/2 particles irradiated on resonance. For this first example the distribution of offset is assumed to be negligible. We

assume that $T_2 = 0.2$ s is perfectly known, the goal being to estimate the value of $T_1 = 0.3$ s. To simplify the presentation of the results, we consider a simple database associated with four values of T_1: 0.1, 0.233, 0.366 and 0.5 s. Following the general procedure of OFP, we compute the optimal field for this dictionary in the case where all the coefficients μ_{mn} are set to 1. The time T is set to 10 ms. The efficiency of the optimal solution is benchmarked against a time-dependant random field as shown in Fig. 6.6, which displays the recognition map $(T_1(m), T_1(n)) \mapsto D[f_m, f_n]$ for the two databases and the time evolution of the different elements of the dictionary. The contrast of Fig. 6.6 gives a first quantitative measure of the precision of the recognition process. In this example, C_N is equal to 0.06 for the optimal fields and 0.03 under the random fields. The minimum values of the recognition maps are respectively 0.019 and 0.001.

A first estimation of the value of T_1 can be made directly with the colorbars of Fig. 6.6 and leads to $T_1 \simeq 0.366$ s. Better accuracy of the fingerprinting process can be obtained using the continuum limit (section 6.3.3). In the continuum limit, the minimization in the set $\{D[f_n, g]\}$ is replaced by a gradient descent algorithm that minimizes the distance $D[f(T_1), g]$. The gradient $\partial D[f(T_1), g]/\partial T_1$ is estimated numerically using finite differences. For the ideal system, we obtain $T_1 = 0.3$ s both for the optimal and the random fields.

In order to verify the robustness of the method against the experimental noise, recognition process in the continuum limit has been made on a theoretical signal with an additive noise of amplitude ϵ. Since the radius of the Bloch ball is normalized to 1, ϵ can be interpreted as a percent deviation. Using optimal and random fields of Fig. 6.6, we optimize the parameter T_1 for different responses $g(t)$. The algorithm converges towards different values of T_1 for each response of the system. Figure 6.7 displays the mean value and the width of the T_1- distribution (denoted by $\Delta T_1^{\mathrm{OPT}}$ and $\Delta T_1^{\mathrm{RAND}}$ for the optimal and random fields respectively) as a function of ϵ. For each value of ϵ, we consider 30 measurements $g(t)$ and the widths are determined by assuming a Gaussian distribution. This width can be interpreted as the accuracy of the corresponding estimation process. We observe in Fig. 6.7 that the gain can be very large with the optimization procedure, a factor of the order of 100 for $\epsilon = 0.001$ is obtained. The random field fails to predict T_1 accurately, even for low noise amplitude. In a standard experiment, the amplitude of the noise is generally of the order of 1% of the maximum of the signal. This corresponds here to $\epsilon = 0.01$.

We also study the efficiency of OFP with respect to the Inversion Recovery approach (IR), which is a standard way to estimate the relaxation time T_1 [101]. IR is based on the successive application of a π- pulse followed by a series of $\pi/2$- pulses at different times to measure the transverse magnetization. A fair comparison between the two estimation techniques is difficult and heavily depends on the features of the experimental set-up. For the IR, we

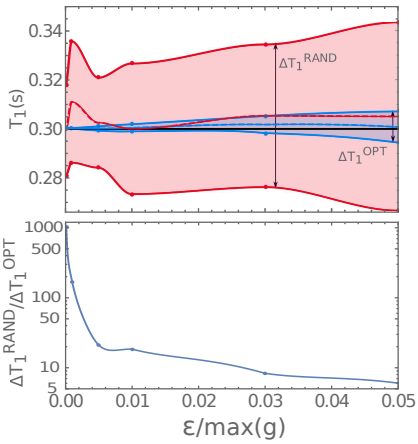

Figure 6.7: (top) Width of the distribution of the estimated T_1 values by the fingerprinting process (blue - optimal,red - random) as a function of the noise amplitude ϵ, which is dimensionless. The dashed lines depict the mean values of the two distributions. The horizontal solid line is the value of the T_1 parameter. (bottom) Plot of the ratio $\Delta T_1^{\mathrm{RAND}}/\Delta T_1^{\mathrm{OPT}}$ of the width of the two distributions as a function of ϵ.

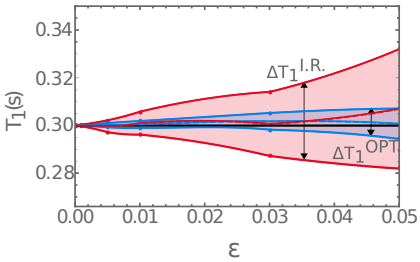

Figure 6.8: Width of the distribution of the estimated T_1 values by OFP (dark gray or blue) and IR (light gray or red) as a function of the noise amplitude ϵ, which is dimensionless. The dashed lines depict the mean values of the two distributions. The horizontal solid line is the value of the T_1 parameter.

consider a single-shot measurement process during a relaxation towards the thermal equilibrium state in which the longitudinal relaxation can be measured in an arbitrary short time with a noise added to the response of the system. Note that the waiting time between each acquisition is not included in this ideal approach, which overestimates the efficiency of a realistic IR. The response of the system is described as follows:

$$g(t_m) = M_z(t_m) + \varepsilon \mathcal{N}(t_m).$$

The time evolution of the longitudinal magnetization is given by a perfect inversion dynamics $M_z(t) = 1 - 2\exp[-t/T_1]$ with 120 times t_m separated by 10 ms. The same noise and the same number of measurement points are therefore used for OFP and IR, which ensures a fair comparison. The results are displayed in Fig. 6.8 and show that OFP has a better accuracy than IR. For a T_1 value of 300 ms and a noise amplitude $\varepsilon = 0.05$, OFP achieves a precision of the order of ± 0.05 ms, whereas the precision of IR is larger than 2 ms. A gain of a factor of 4 in estimating T_1 is obtained. Since there is no steady state in OFP, this factor is expected to increase for longer pulse sequences.

6.4.2 "The microscope"

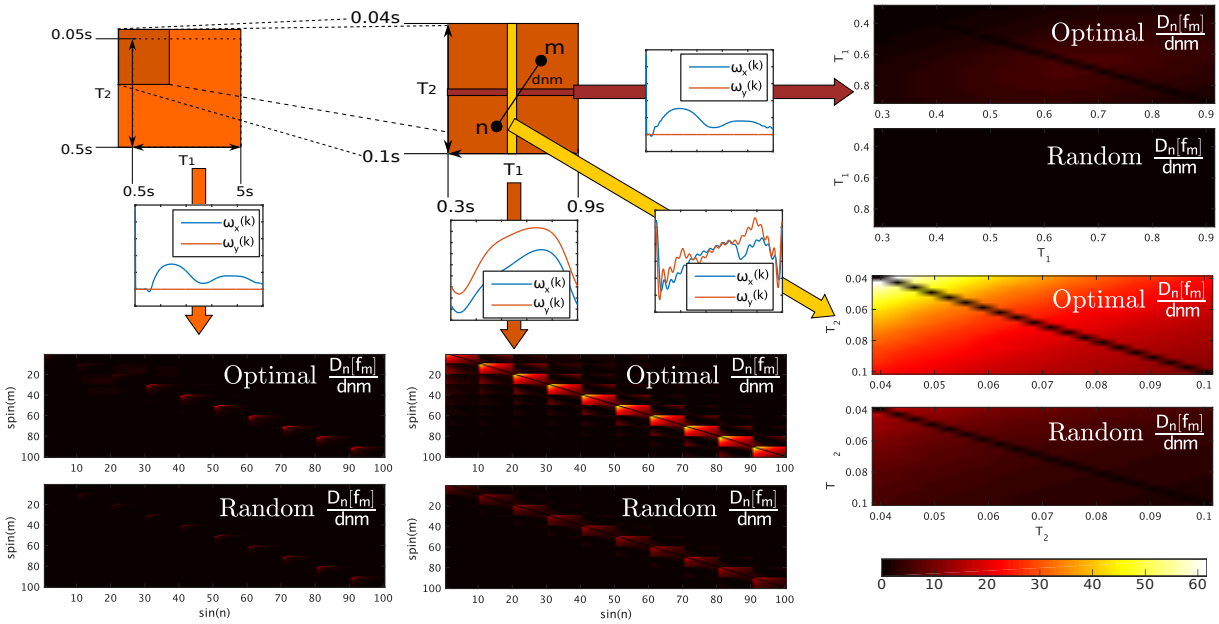

Figure 6.9: The figure shows the "*microscope*" property of the optimization. Each square and rectangle (■■■■) symbolizes a different set of spin relaxation times T_1, T_2. An optimal control field $u = (u_x, u_y)$ is computed for each case in order to maximize the average distance between dictionary functions. In order to emphasize the superiority of the optimization, the recognition map $D[f_n, f_k]$ is plotted for each field and for a reference random field (the shape of this random field is not shown). The higher the contrast in a recognition map plot, the higher is the field efficiency. For each set, the optimal case provides higher contrast, showing the usefulness of the optimization.

Several optimizations over several dictionaries can be made in order to increase the efficiency of the fingerprinting process. It is possible to start the measurement protocol by using a dictionary

of a few elements spread in a large area of the parameter space. After the evaluation of the parameters, a new optimization can be performed with a new dictionary centered on the last measured values. This process can be iterated until a given accuracy threshold. The microscope property is illustrated in figure 6.9.

6.5 Experimental Results

As a proof of principle, the simultaneous estimation of the relaxation time T_2 and the distribution parameters of the offset inhomogeneities have been studied experimentally. We investigate this situation rather than the measurement of T_1 because it leads to non-trivial results. The offset distribution $\rho(\omega)$ is assumed to be Lorentzian:

$$\rho(\Delta) \propto \left(1 + \frac{4(\Delta - \bar{\omega})^2}{\Delta\omega^2}\right)^{-1}, \tag{6.14}$$

where $\Delta\omega$ is the full width at half maximum (FWHM) and $\bar{\omega}$ the center of the distribution. The parameter T_1 was previously estimated to be 87 ms by inversion recovery [101]. The estimation of the parameter T_2 is a challenging issue because T_2 and $\Delta\omega$ are both responsible for the decay of the measured transverse magnetization. An effective transverse relaxation time T_2^* defined by the relation

$$\frac{1}{T_2^*} = \frac{1}{T_2} + \frac{\Delta\omega}{2} \tag{6.15}$$

is usually introduced in magnetic resonance to account for the two physical effects [101]: the transverse relaxation and the spin dephasing.

A specific optimal pulse sequence sensitive to T_2 for a spin ensemble with an average value of $\Delta\omega = 20$ rad.s^{-1} was designed. Note that only one control field along the x- direction is used to improve the convergence of the algorithm. Experiments were performed at room temperature on a Bruker Avance 600 MHz spectrometer. We have used the ^{1}H spins of H_2O with D_2O (99.9%) as a solvent in a Shigemi tube. $CuSO_4$ is added as a T_1-shortening agent. The control field is a sequence of $N_p = 500$ δ-pulses separated by a time $T = 10$ ms. The control field and the time evolution of the transverse magnetization are plotted in figures 6.10 and 6.11.

A reasonable match is found between the theoretical and the experimental results, which can be compared with the experimental error made in the measurement of the Bloch vector, as shown in Fig 6.11. Independent measurement based on a spin echo sequence leads to $T_2 = 60.5 \pm 0.5$ ms and $\Delta\omega = 28.5$ rad.s^{-1}. If we assume that the value of $\Delta\omega$ is known then OFP gives $T_2 = 60.4 \pm 3.6$ ms and $\bar{\omega} = 0.1 \pm 0.6$ rad.s^{-1}. In the general case, due to the correlations between $\Delta\omega$ and T_2, it was not possible to estimate the two parameters precisely.

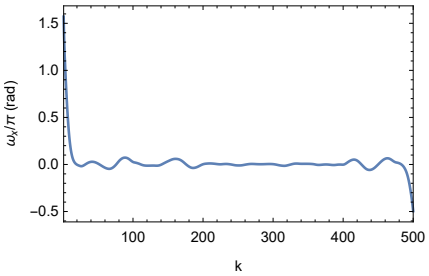

Figure 6.10: Optimized control field along the x- direction ($\omega_y = 0$) to estimate the parameter T_2.

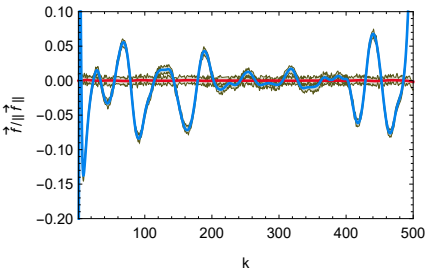

Figure 6.11: Time evolution of the simulated trajectories $M_x(t)$ and $M_y(t)$. The experimental data correspond to the gray areas around the numerical solutions, which give an estimation of the accuracy of the measurement.

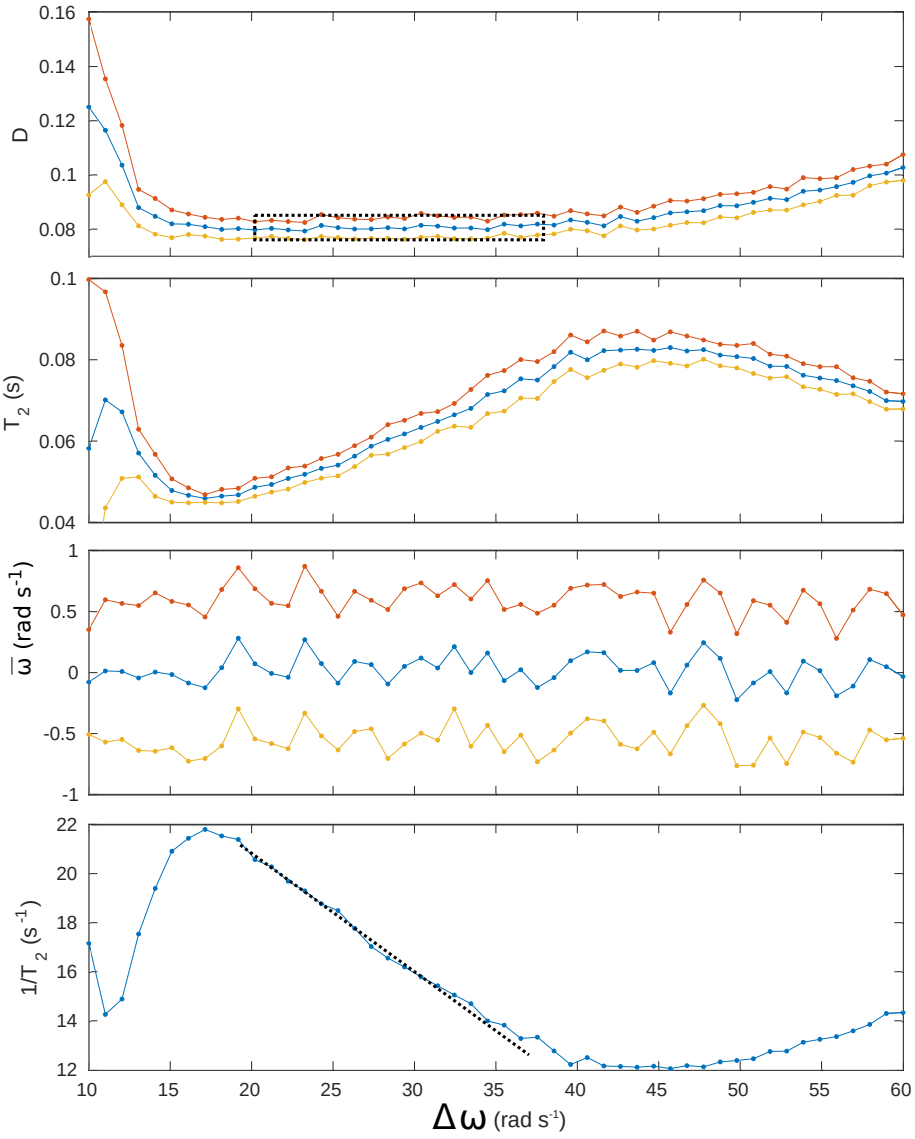

Figure 6.12 – (Top) Minimum distance D (defined in Eq. (6.3), D is dimensionless) between the simulated and the experimental curves as a function of $\Delta\omega$. The dashed rectangle indicates the interval where D is minimum. (Middle) Evolution of T_2 and $\bar{\omega}$ as a function of $\Delta\omega$. In the different panels, the blue and the red/yellow curves represent respectively the mean value of the signal and the upper/lower bounds of uncertainty. (Bottom) Plot of $1/T_2$ as a function of $\Delta\omega$. In the interval $[20, 38]$ rad.s^{-1}, the parameter T_2^* is constant as shown by the dotted line.

As displayed in figure 6.12, we observe that the figure of merit D is almost the same for $\Delta\omega \in [20, 38]$ rad.s^{-1}. On this interval, the value of T_2^* is constant and in agreement with the experiment. Additional information would be required to estimate T_2 independently of $\Delta\omega$. From a computational point of view, it seems difficult to include different values of the bandwidth in the definition of the dictionary for improving the accuracy of the estimation. The same analysis was performed with several random sequences and we were not able to recover the right values of T_2 or T_2^*, showing thus the efficiency of OFP.

6.6 Conclusion

We have introduced in this work the principles of OFP with an application to spin dynamics. The optimization procedure provides a method to approach the physical limits of the protocol in terms of sensitivity. **FP has several advantages over the conventional methods. It allows a quantitative estimation of multiple parameters at the same time (e.g. the times T_1 and T_2), while only information about a single parameter is traditionally achieved. This advantage must be tempered if several parameters are correlated. This aspect has been illustrated in Sec. 6.5 with the offset terms and the T_2 relaxation time. The repeated acquisitions of data for the standard techniques are replaced by a single-shot measurement process in FP, which can drastically reduce the overall time of the experiment [110]. Finally, FP is expected to be less sensitive to experimental imperfections and to the presence of noise. All these aspects are improved by the optimization procedure proposed in this chapter. As shown in Sec. 6.4.1, the better stability of OFP against noise perturbation is illustrated in a model example.**

This analysis paves the way for further investigations in MRI and realistic in vivo experiments [16, 40, 99] in which the standard version of the fingerprinting process with random pulses has been applied with success [110]. The concept of OFP could also be transferred to other domains such as quantum optics and atomic and molecular physics. An example is given by the control of molecular alignment and orientation in which pulse shaping techniques have been applied with success [158]. The measure of the alignment could be used to estimate molecular parameters such as, e.g., the collisional relaxation rates [136, 172, 171]. Another aspect could be to explore the applicability of this approach in a dynamical feedback framework where the control field would be adjusted in real time according to the results of the measurements. Finally, it seems promising to combine this technique with other methods of data analysis such as Bayesian estimation [151] or Fisher information [12].

Chapter 7

Conclusion

This manuscript is organized as follows: The first part focuses on the optimal control of an inhomogeneous spin ensemble coupled to a cavity, while the second part is dedicated to two selectivity problems, the design of selective transformations in minimum time, and the optimal database design for fingerprinting experiments.

Part 1 In the first chapter, the theory of a spin ensemble coupled to a cavity has been introduced. In order to describe the similarities and the differences between cavity-QED and NMR, different models have been derived from non-relativistic Dirac equation. We have emphasized that in the two cases, equations of dynamics obey the same structure and they can be represented in terms of a Bloch equation. Then, collective effects and relaxation processes have been highlighted. Finally, the bad cavity limit has allowed us to derive semi-classical equations in terms of operator mean values. With the semi-classical model, an analogy is established between the NMR radiation damping and the super-radiance effect.

The second chapter is devoted to the numerical integration of quantum systems. Such a problem is challenging to solve, because the spin ensemble is composed of a large number of spins. Several numerical strategies have been proposed using specific numerical algorithms (split-Euler scheme or a low rank approximation) and an appropriate representation of the quantum system: Either a discretized ensemble or a continuous ensemble. To derive the representation of the spin ensemble, two approximations are made. In the first case, the spin distribution is discretized with the smallest possible sampling, and in the second case, we assume that the correlation between spins with different offsets is negligible such that we can represent the ensemble with a continuum. The main advantage of these approaches is to describe accurately the Purcell relaxation and collective effects by using quantum mechanics. Models are studied numerically with two physical examples: a Purcell relaxation and a FID. Additionally, we have demonstrated numerically that the discretized and the continuous model converge toward the semi-classical model in the weak-coupling regime, and in the large J-limit.

The third chapter focuses on the control of a spin ensemble coupled to a cavity. The first part of this chapter shows how the evolution operator can be rewritten in order to provide an intuitive understanding of the dynamics, and how the semi-classical regime can be derived. Based on this analysis, we have derived a systematic procedure for the design of control fields. With this approach, most of NMR state-of-the-art control sequences can be directly implemented in a cavity-QED setup. As a first application, non-linear generalized functions are used to derive simple and approximated control protocols. This idea allows us to generalize standard square pulses by a smooth function of compact support. In a second step, numerical algorithms are used to optimize pulses in the strong or the weak coupling (bad/good cavity) regimes. These optimal pulses are

required if the pulse duration is of the same order of magnitude as other characteristic times of the system. Few examples of applications are given such as a T_1-inversion recovery in the strong coupling regime, and a spin echo. Additionally, the theory is illustrated by an experimental measurement of the FID, using the new bump pulse.

Chapter 4 focuses on a very specific application: The maximization of the SNR during spin echo/CPMG experiments. Such experiments are performed in the weak coupling regime, so that the bad cavity limit can be used. In this limit, the dynamics are integrated analytically, and simple formulas for the SNR are derived. Then, we have demonstrated the existence of a non-trivial maximum according to the system parameters, and that robust optimal pulses allow us to maximize the SNR of a single spin echo. We also show that, short pulses (such as bump pulses) are the most efficient pulses for CPMG sequences.

Perspectives of this work are both experimental and theoretical. For the moment, only bump pulses have been implemented experimentally, and it is still a challenge to implement optimal pulses with a sufficient efficiency. Optimal pulses require a fine modulation of the intra-cavity field, at the limit of setup capacity. Moreover, some questions are still opened, such as the origin of the small disagreement observed between the theory and FID records. From the theoretical point of view, the bad cavity regime is well understood but the opposite regime remains to be explored. Optimal control in this regime is still at its beginning. To proceed further in this direction, it is necessary to work on a specific experiment. This could help us to choose a specific model (should we use a continuous distribution? What is the best quantum representation?), and a specific cost function for the optimization. This opens the door to the control of non-Markovian quantum systems, with a relatively simple and realistic system.

Part 2 Chapter 5 presents the problem of optimal selective transformations with time or energy constraints. The idea is to determine the pulse which produces offset-selective transformations in minimum time or minimum energy. For that purpose, the PMP is applied to an ensemble composed of two or three offsets. Two different classes of trajectories (control fields) are distinguished in optimal control theory: Regular and singular trajectories. In the case of two offsets (0 and Δ), we have shown that singular pulses are constant and that regular controls with fewer than four bangs cannot be optimal. We have also demonstrated that regular controls converge toward a singular control in a specific limit. Then we have conjectured that regular control fields cannot be optimal, and this point is in agreement with the numerical calculations. Other cases are also investigated, with more offsets and more complicate excitation profiles (including local areas of robustness). In these other cases, the optimal trajectory is not singular anymore, and new structures occur in the control landscape. For instance, if one considers a control with a fixed duration, "jumps", i.e. transitions between different control strategies can appear as a function of offset parameters. This is due to periodicity conditions of the evolution operator.

Perspectives of this work are mostly turned toward more complicated systems (more complicated excitation profiles, higher number of offsets,...). Additionally, an interesting link between the selectivity problem and the robustness problem might exist. It will also be interesting to establish a connection between optimal trajectories found in the time-optimal selective state to state transfers [169], and time optimal selective universal rotation.

Finally, in chapter six, another selectivity problem is studied by considering fingerprinting experiments. A rigorous mathematical description of the recognition and the optimization processes is made. For an ensemble of different spins (each of them has different parameters, e.g. T_1 or T_2 relaxation times) and a specific control field, a database

composed of magnetization trajectories can be generated numerically, in order to analyze in a second step, a spin system. With a specific optimization procedure, we are able to find a control field which maximizes the distance between the trajectories, and thus, minimizes the error of the recognition process in presence of noise. The advantages of optimal database design over random control sequences and other standard measurement methods are demonstrated numerically and experimentally. Additionally, an experiment allows us to highlight the physical limit of the recognition process with correlated parameters (such as the T_2 relaxation time and the B_0 distribution).

Several directions can be taken in further works. The most important might be to implement Bayesian-optimization tools in the recognition process. It is also interesting to extend the method to systems with radiation damping. Indeed, the non-linear effects can reduce considerably the measurement accuracy. Another problem of interest is to generalize the method to interacting systems or with several T_1, T_2 parameters (per sample).

As a general perspective, we can mention the work that can be continued at the experimental level. Many results derived in this thesis are theoretical, and they are all closely related to experiments. Few experiments have already been done: experimental realizations of bump pulses and the proof of principle of fingerprinting optimizations, but many other experiments can be performed, like the control of spins in the good cavity regime or other fingerprinting experiments combined with NMR spectrum analysis.

Part III

Appendices

Appendix A

Optimal control theory

A.1 Geometric approach

Optimal control theory was officially born during the cold war, between the United States and the URSS. At that time, the motivation of both sides was to determine how aircrafts and rockets could reach a target in minimum time and energy consumption. These challenges were new and difficult because new fast planes were subjected to many non-linear effects. At the beginning, mathematicians of both sides were working in secret on these topics and they both introduced, from their own side, similar ideas. Then, it is difficult to say who is the "*true father*" of the theory, but something is sure, an important step forward was made when their works were gathered together. [129]. However the background of this theory is far older since it uses principles of variational calculus proposed by Lagrange, Euler, Bernoulli and Hamilton [68, 73, 74]. Optimal control theory can be seen as a sophisticated theory to determine the extremum of a function. Generally, a simple gradient analysis is sufficient to determine such extrema, but in the case of a system driven by a time-dependent function, the analysis is more involved and advanced mathematical tools are required.

The problems encountered in optimal control are similar to the ones of classical mechanics. For example, one could search for trajectories, which minimize the action. The solutions of this problem satisfy the well-known Euler-Lagrange equation. Another example is the one of the fastest trajectory, which connects two points in a homogeneous gravitational field. The solution was proposed by Newton, Leibniz, L'Hospital and the two Bernoulli brothers [15] and solutions are brachistochrone functions (figure A.1). Another issue is to determine constrained trajectories which minimize (or maximize) a function. Depending on the context (minimization or maximization), we call this function *the cost* or *the figure of merit*. In standard mechanical problems, constraints are given by the environment (for example, it is given by the gravitational field), but in more elaborate situations, constraints can be modified and chosen in order to reach the goal more efficiently (usually, we use the electromagnetic field).

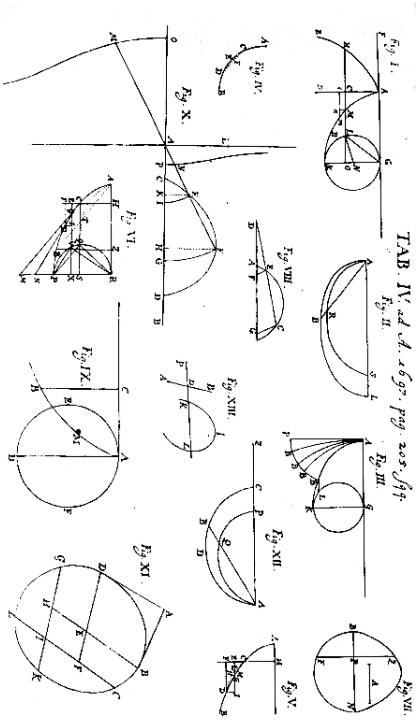

Figure A.1: Extract of Bernoulli's book (1696), which shows different brachistochrone curves. In order to solve this problem, physicists and mathematicians had to elaborate the foundation of the current optimal control theory. These curves are the solution of the following problem formulated by Bernoulli: *"Given two points A and B in a vertical plane, what is the curve traced out by a point acted on only by gravity, which starts at A and reaches B in the shortest time."*

Then, it is not surprising that optimal control theory follows the path traced by physicists with the variational calculus. As in usual mechanics, different (and equivalent) formalisms can be adopted. Each of them provides a different point of view and sometimes, it can be interesting to switch from one formalism to another to solve a specific case study. In modern optimal control theory, we generally distinguish two approaches. The first one is based on Pontryagin principle. This approach can be seen as a classical Hamiltonian formulation of the control problem. As in classical mechanics, this formalism is based on constants of motion. Then, low dimensional problems can be solved by using simple geometric tools [25]. The second approach is based on Hamilton-Jacobi equation [166]. In that case, the cost function is the solution of an equation similar to the Schrödinger equation and its analysis is closer to the formalism of Quantum mechanics. This second approach is particularly interesting for control in noisy environment, and for that purpose, path integrals are powerful tools [182, 165].

Generally, an optimal control problem is defined by the following data:

- A system to control. The latter is defined by a state $x(t)$, an element of a vector space, and the state is the solution of a first order differential equation [53] of the form:

  $$\frac{d}{dt}x(t) = f(x(t), u(t), t), \tag{A.1}$$

  where u is the control and f is a function which characterizes the dynamics. Of course, an initial state $x(0)$ must be specified to define a solution of this equation.

- A cost function (figure of merit) to minimize (maximize) F. The cost can be any function, which depends on the dynamics, but generally we use a cost of the form:

  $$F = h(x(t_f), t_f) + \int_0^{t_f} f_0(x(t), u(t), t)dt. \tag{A.2}$$

  The function h is called the terminal cost. The second part of the cost function depends on the trajectory followed to reach the target state. In physical applications, h defines the target state and f_0 is generally the time of the process or the energy of the control field.

[53] The system can be nonlinear

For example, in most of quantum mechanics applications, we use $h = \langle\psi_f|\psi_0\rangle$, or $h = \|\psi_f - \psi_0\|$, or any function that allows us to describe a notion of distance between two vectors of the Hilbert space. This part of the cost function is maybe the most important one in the numerical approach, and it is crucial to control a spin ensemble because we are not sure we can reach the target state exactly. On another side, we usually use $f_0 = 1$ for a time minimization, because $\int_0^{t_f} 1.dt = t_f$ is the simplest cost function that

describes the control duration. For an energy minimization, we use $f_0 \propto \|u\|^2$.

A.1.1 Hamiltonian formalism

In order to solve the optimal control problem, we follow the path of other generalizations of Hamilton formalism. For example, when Einstein introduced the notion of space-time, we had to generalize Hamilton formalism to 4-dimensional physical problems [142, 143]. In relativity, the time becomes a generalized coordinate and a momentum is assigned to this latter. In optimal control theory, we proceed in the same spirit: the control and the cost function are introduced as new generalized coordinates [54]. Then, we consider a vector of the configuration space $q = \{x, u, f^0\}$ and its associated momentum p (we also use the name *adjoint vector*)[41]. In order to solve the dynamics, we introduce a function of q and p, called Pontryagin's Hamiltonian:

$$H_p = \langle p | d_t q \rangle - L(q, d_t q), \tag{A.3}$$

where $\langle .|. \rangle$ is the scalar product defined on the extended vector space of generalized coordinates. The Pontryagin's Hamiltonian lives in a phase space with a symplectic structure given by Hamilton's equations:

$$\begin{aligned} \frac{\delta H_p}{\delta q_a(t)} &= -\frac{d}{dt} p^a(t) \\ \frac{\delta H_p}{\delta p^a(t)} &= \frac{d}{dt} q_a(t), \end{aligned} \tag{A.4}$$

where a is the dimension indice in the configuration space, and covariant/contravariant tensor notations are used [170, 143]. However, as most of Hamiltonian systems, additional constrains are required. Frequently, there is no constraint on the derivative of the control (there is no constraint of the form $d_t u = ...$), then, we introduce the *first class constraint* [55]:

$$p_u^a = \frac{\delta L}{\delta d_t u_a(t)} = 0 \ \forall t \tag{A.5}$$

$$\Rightarrow \frac{\delta H_p}{\delta u_a(t)} = 0. \tag{A.6}$$

Imposing $p_u^a = 0$ ensures that no artificial constraint is created on the control. Then, we talk about *the weak Pontryagin Principle*. By weak, we mean that no constraint is taken into account by the control, it is free to take any arbitrary real value (only the cost function and the dynamics of the system constrain the control in the optimization procedure). However, in many applications, the control field might be bounded such as $\|u\| \leq u_0$. Therefore, it is clear that the minimum of the cost function might not be a

[54] The time is not necessarily introduced *explicitly* as a new generalized coordinate since the cost takes into account this degree of freedom. For example, if $F = \int_0^t dt$, then it is exactly the time coordinate.

[55] Here, we introduce heuristically this constraint, which is nothing else than Pontryagin principle, and we see that it comes naturally with our definition, using simple arguments. However, a rigorous mathematics proof can be established [25]

smooth extremum, it is rather determined by the boundary of the control set [56]. In this new situation, the first class constraint must be extended and we talk about the *Pontryagin Maximum Principle* (PMP). The PMP was introduced heuristically by Pontryagin in the 50'. Nowadays, it has been proved with several approaches (see for example [49])[57]:

Theorem 2 (Pontryagin Maximum Principle): *Let us consider the system*

$$d_t x = f(x(t), u(t), t),$$

where $f : \mathbb{R} \times \mathbb{R}^n \times \mathbb{R}^m \to \mathbb{R}^n$ *is a continuous function and the control* u *is a measurable bounded mapping* $u : [0, t_f] \to U \subset \mathbb{R}^m$. *$U$ is the ensemble of admissible controls, which connect an initial point* $x(0)$ *to a target state* $x(t_f)$. *The cost associated to a control* u *on* $[0, t]$ *is defined by:*

$$F(u, t) = h(x(t), t) + \int_0^t f_0(x(t'), u(t'), t')dt',$$

where $f^0 : \mathbb{R} \times \mathbb{R}^n \times \mathbb{R}^m \to \mathbb{R}$ *and* $h : \mathbb{R} \times \mathbb{R}^n \to \mathbb{R}$ *are continuous functions and* $x(.)$ *is the trajectory of the system associated to the control* u.
The optimal control problem is to find u^* *such as* $F(u^*, t_f) = \min_u F(u, t_f)$ *and* x *starts from an initial state* $x(0)$ *and goes to a desired target state* $x(t_f)$. *The final time* t_f *can be fixed or not.*
- if u *is optimal on* $[0, t_f]$*; then there exists a map* $p : [0, t_f] \to \mathbb{R}^n$ *absolutely continuous called adjoint vector, and a real constant* $p^0 \leq 0$, *and a function:*

$$H_p(x, p, p^0, u, t) = \langle p(t), f(x(t), u(t), t) | + \rangle p^0 f_0(x(t), u(t), t),$$

which verifies Hamilton's equations (A.4). *Moreover, we have the following maximization condition almost everywhere on* $[0, t_f]$*:*

$$H_p(x, p, p^0, u^*, t) = \max_u H_p(x, p, p^0, u, t).$$

- If the final time is not fixed, we have the condition:

$$\max_u H_p(x(t_f), p(t_f), p^0, u, t_f) = -p^0 \frac{\partial h}{\partial t}(x(t_f), t_f)$$

- If the initial and target states are two manifolds $M(t)$ *of* $\mathbb{R}^n$ *with tangent spaces in* $x(0)$ *and* $x(t_f)$, *then the adjoint vector can be constructed in order to verify the transversality conditions (or just one of the two):*

$$p(0) \perp T_{x(0)} M(0),$$

and

$$p(t_f) = p^0 \frac{\partial h}{\partial t} \perp T_{x(t_f)} M(t_f).$$

[56] For example, the function $F = -u^2$ such as $u \in [-1, 1]$ has a minimum on the interval boundaries and not in $d_u F = 0$

[57] This is the usual presentation of the PMP, as can be found in [166]. The presentation is a little bit different than the one presented so far. More precisely, there is no mention of an adjoint vector for the control.

Definition 9 (regular, singular, abnormal):

- *if the control verifies* $\frac{\delta H_p}{\delta u_a(t)} = 0$ *on an interval* $I \in [0, t_f]$*, the control and its associated trajectory are called* ***singular****.*
- *if the control verifies* $\|u\| = u_0$ *on an interval* $I \in [0, t_f]$*, the control and its associated trajectory are called* ***regular****.*
- *if* $p^0 = 0$ *the system is* ***abnormal****, otherwise, it is* ***normal****.*

If the system is abnormal, the Pontryagin Hamiltonian does not depend on the cost function f_0. Then, the optimal trajectory is intrinsic to the system. For time optimal trajectories, abnormal and normal trajectories are the same.

As we can see, the PMP gives necessary conditions on the control to be optimal. These conditions also exist in the original formulation of the problem, but here, the Hamiltonian structure allows us to classify the trajectories and it gives us powerful tools to search which trajectory(ies) is(are) optimal.

For example, if we are interested in time optimality of an autonomous system, the Hamiltonian is a constant of motion, and one can choose the transversality condition such as:

$$\forall t \in [0, t_f] \ , \ \max_u H_p(x(t), p(t), p^0, u) = 0. \tag{A.7}$$

Moreover, if the system is linear, we can compute regular controls. In this case, the Hamiltonian can be written in the form: $H_p = \sum_a u_i . l^i + l^0$, where l^i and l^0 are functions that depend explicitly on the system state and its adjoint state, but they do not depend explicitly on the control. Equations for 1D or 2D control fields are different. We start with the single input case ($H_p = u.l^1 + l^0$). We can use the fact that l^1 and all its derivatives are equal to zero on an interval. The computation of the derivatives can be done with the Poisson Brackets[58]:

$$0 = l^1 \tag{A.8}$$

$$0 = d_t l^1 = \{l^1, l^0\} \tag{A.9}$$

$$0 = d_t^2 l^1 = \{\{l^1, l^0\}, l^0\} + u\{\{l^1, l^0\}, l^1\}. \tag{A.10}$$

Generally, an explicit computation of the Poisson Bracket allows us to determine easily the set of singular trajectories. Notice that these results can be generalized for arbitrary even dimension [25].

For the two-dimensional input case (or odd dimension), we use the fact that $l^0 = 0$ (because $d\delta H_P / \delta u(t) = 0$) and the Poisson brackets to determine:

$$\{l^j, l^0\} + \sum_{i=0}^{n-1} \{l^j, l^i\} u_i = 0. \tag{A.11}$$

By using the conditions listed above, we can compute regular, singular or regular-singular trajectories and then, we can evaluate the ones which are optimal. This task is generally very difficult and numerical algorithms are generally used.

[58] $\{A, B\} = \sum_{i=1}^{n} \frac{\delta A}{\delta q_i(t)} \frac{\delta B}{\delta p^i(t)} - \frac{\delta B}{\delta q_i(t)} \frac{\delta A}{\delta p^i(t)}$

A.1.2 Hamilton-Jacobi formalism

This section is devoted to a short presentation of the Hamilton-Jacobi formalism. Since this formalism has not been used to solve concrete problems in my thesis, I do not enter into the details, but I would like to say a few words about this formalism because there is a nice interpretation in terms of a quantum mechanical system. More precisely, solving an optimal control problem with this formalism can be seen as solving a quantum mechanical problem in the first quantization framework [41]. First of all, in the Hamilton-Jacobi formalism, it is necessary to define the *Hamilton function*[144]:

$$S\left(x(t),u(t),t,x(t'),u(t'),t'\right)=\int_t^{t'} f_0\left(x(s),u(s),d_s x(s),d_s u(s),s\right)ds.$$

This quantity is very similar to the action $S[x]$. However, they are different in the sense that the action is a function of the full trajectory x and the Hamilton function is a function of generalized coordinates at the boundaries of the time interval. By using Hamilton or Euler-Lagrange equations, we can show that the dynamics can be rewritten into the form:

$$\frac{\partial S}{\partial t}+H_p\left(t,x,u,\frac{\partial S}{\partial t}\right)=0. \tag{A.12}$$

This equation is called the *Hamilton-Jacobi equation*. When the Hamilton function describes a wave packet, S is the wave function of a quantum system and the function H_p is rewritten into the form of a linear differential operator. Therefore, the Hamilton function of the extended system $\{x,u,t\}$ can be considered as the "*quantum state of the control problem*". A powerful method to solve such problems is to use path integrals. Such integrals, and more precisely the numerical algorithms used for their computation have been used for control problems in a noisy environment and robotics [182, 165].

As an example of Hamilton-Jacobi equation, the case of a classical free particle is considered. The action is [59]:

$$S[x]=\int dt\frac{1}{2}m(d_t x)^2. \tag{A.13}$$

Equations of motions are trivially integrated in this case and we determine:

$$d_t x=\frac{x'-x}{t'-t}. \tag{A.14}$$

Then, the Hamilton function is given by:

$$S(x,t,x',t')=\int_t^{t'}\frac{1}{2}m\left(\frac{x'-x}{t'-t}\right)ds=\frac{m(x'-x)^2}{2(t'-t)}. \tag{A.15}$$

An advantage of the Hamilton-Jacobi formalism is the following: if the minimization problem is solved locally on a small time interval, it is a necessary condition for optimality.

[59] Notice that the system considered here *is not* a quantum free particle. A quantum free particle has a different action: it is the action of a complex field. However, the action of the classical particle is recovered in the path-integral formalism.

A.2 Numerical approach

Optimal control problems are generally very difficult to solve and numerical computations are required most of the time. We can distinguish two main categories of algorithm [166]: *direct* and *indirect* methods. Indirect methods are called "shooting methods" and they are based on the evaluation of the dynamics for the state and the adjoint state of the system for an ensemble of initial values of the adjoint state. Direct methods are minimization algorithms for non-linear functions. Scientific computation programs such as *Matlab* or *Mathematica* have different native solvers: gradient algorithm, simplex algorithm, genetic algorithm or simulated-annealing algorithms.

Indirect methods are extremely precise and current algorithm allows us to reach the global extremum in many cases [23], but the method is generally very slow and an important preliminary work is required. On the other side, direct methods are faster in terms of code writing and computation time. However, with such algorithms, the control field must be discretized as a piecewise constant function or as a parametrized functions (Fourier series, Legendre polynomials...).

From these "main" families, we can also distinguish several variants, with their specific behaviors. For example, in quantum control a well-known algorithm is GRAPE, which is a specific gradient-based algorithm [145, 112, 46]. This section contains few elements about the numerical algorithms used in this thesis.

A.2.1 Gradient Ascent algorithm

Gradient algorithms are powerful algorithms to determine the local extremum of a function. They are based on a simple iterative procedure, which brings an initial guessed solution to its nearest maximum (or minimum). The structure of the algorithm is simple:

Definition 10 (Gradient algorithm):

1. *Choose an arbitrary control field u (or at least a 'quite good' guess).*
2. *Compute the figure of merit $F[u]$ to maximize*
3. *Compute the gradient $\frac{\delta F[u]}{\delta u(\tau)}$.*
4. *Increment the control field with the gradient : $u(\tau) \leftarrow u(\tau) + \epsilon \frac{\delta F[u]}{\delta u(\tau)}$, where ϵ is an arbitrary small real positive number.*
5. *Iterate steps 2,3,4 until F reaches a stationary value*

If the figure of merit (or the cost) must be minimized, ϵ is chosen negative. The step 2) is not necessary if the number of iterations is fixed.

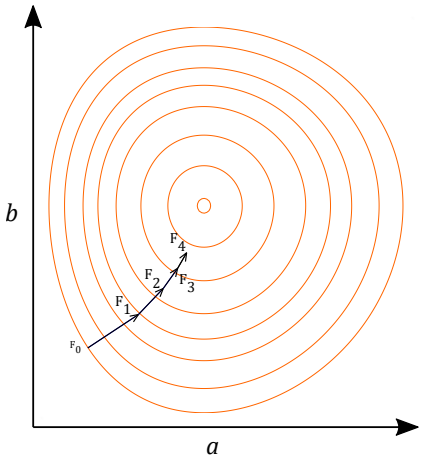

Figure A.2: An example of trajectory followed by a gradient ascent algorithm. Orange lines are isolines of the figure of merit F in the control landscape of the control. Here, for the sake of simplicity, we assume that the control depends on two parameters (a and b). The goal is to determine the two parameters, which maximize F. First, the user chooses an initial ensemble of values for the control. This gives a figure of merit F_0. Then, by evaluating successively the gradient of F, the algorithm changes successively the control parameters until it reaches the values, which maximize F. These iterations ($F_0, F_1, F_2, ...$) give a trajectory in the landscape of F.

[60] Here, the scalar product is assumed to be real. This is the case if x is the magnetization vector or a matrix in $SO(3)$. But if it is a $SU(2)$ element, one must use the real part or the absolute value of the scalar product.

[61] See theorem 15 (appendix C) for further details

[62] See propositions 15 and 16 (appendix C) for further details

Here, the algorithm is presented in a continuous form (the gradient is a function defined at any time), but in practice, it is discretized. A simple illustration of the algorithm is presented in figure A.2.

In this algorithm, the evaluation of the gradient is generally very demanding. If it is evaluated in finite difference ($dF = F[u + \Delta u] - F[u]$), it requires two integrations of the dynamics. However, in specific examples, this computation can be made more efficiently. This is the goal of the GRAPE algorithm. The latter is designed for systems of the form:

$$\frac{dx}{dt} = A(u,t).x,$$

where $A \in GL(\mathbb{C})$ and x can be a vector or a Lie group matrix. The goal is to generate in time t_f the transformation $x_i \to x_f$ with the control field u. The figure of merit [60] is defined with $F = \langle x_f | x(t_f) \rangle$. The computation of the gradient is straightforward using the derivative of a time ordered exponential [61]:

$$\frac{\delta F[u]}{\delta u(\tau)} = \underbrace{\langle x_f | \mathbb{T} e^{\int_\tau^{t_f} A dt}}_{\langle p(\tau)|} \frac{\delta A}{\delta u(\tau)} \underbrace{\mathbb{T} e^{\int_0^\tau A dt} | x_0 \rangle}_{|x(\tau)\rangle}. \tag{A.16}$$

By using a split operator algorithm, time ordered exponential at different times can be computed with a very good approximation (or exactly in some cases). Then it is possible to evaluate $|x(\tau)\rangle$ and $\langle p(\tau)|$ after a single time propagation, and the gradient can be computed without introducing addition errors than the one induced by the time propagation. In practice, the way we code the gradient depends strongly on the system. Generally, we parametrize the pulse with a finite unknown variables to determine (amplitude of the small piece-wise constant pulse or parameters of analytic functions). Then, we do not consider the gradient with respect to $u(t)$ but the gradient with respect to the different parameters. For that purpose, we use the relation[62]:

$$\frac{\partial F}{\partial \lambda} = \langle x_f | \int_0^{t_f} \frac{\delta |x(t_f)\rangle}{\delta u(\tau)} \frac{\delta u(\tau)}{\delta \lambda} d\tau. \tag{A.17}$$

The term $\frac{\delta u(\tau)}{\delta \lambda}$ can be computed analytically and an explicit relation can be used in numerical codes. On another side, the integral over time is computed numerically. Since the quantity $\langle x_f | \frac{\delta}{\delta u(\tau)} | x(t_f) \rangle$ is known, the integral is evaluated with a trapezoidal method (with low numerical cost).

If the operator A is such that $A = A_0 + uA_1$, and the control is piece-wise constant, of amplitudes u_k on the interval k, the gradient can be simplified as follows:

$$\frac{\partial F}{\partial u_k} = \Delta t_k \langle p(t_k) | A_1 | x(t_k) \rangle. \tag{A.18}$$

This expression for the gradient is the one used in most of the GRAPE algorithms [145].

A.2.2 Simulated-Annealing algorithm

Gradient ascent algorithms are efficient only for a smooth variation of the figure of merit. Sometimes, it is not the case and one has to consider other algorithms. Among every optimization algorithm, which are gradient independent, the one I used the most is based on the simulated-annealing method [5]. This algorithm is generally the fastest for global optimization on bounded domains, and for a small number of parameters, the convergence is better than gradient algorithms[63].

[63] the option `"simualted annealing"` of *Mathematica*'s `Nminize` function is particularly well optimized and easy to use. In many applications, it was better and faster than other similar algorithms in *Matlab*.

The name comes from a formal analogy between a minimization problem and the physical process of driving metal to its minimal energy state by successive heating and cooling cycles (annealing). Technically, the program uses a Markov chain to determine a local minimum (or maximum) of a function. Then the code is similar to the metropolis algorithm or a path integral algorithm for computing the ground state of a quantum system [140].

Definition 11 (Simulated-Annealing algorithm):

1. *First choose a guessed field* u_0
2. *Choose an initial value for the temperature parameter* T *(this parameter is here for the convergence of the algorithm. This step can be assimilated to the heating of the metal in metallurgy).*
3. *While,* T *is large enough:*

   - While, the number of accepted transition is below a threshold level:

   - Apply a random perturbation $u_{n+1} = u_n + \delta u$.

   - If $F[u_{n+1}] < F[u_n]$*, keep the new state, or accept it with a probability* $P \propto e^{f(F[u_{n+1}]-F[u_n],T)}$

   - Set $T = T - \delta T$.

f is a function to specify. Generally we use: $f = -\frac{F[u_{n+1}]-F[u_n]}{T}$.

The ability of the algorithm to converge toward the global minimum depends on the initial values of u and T. The function f also plays an important role. However, generally, preselected parameters are sufficient and they do not have to be changed.

In order to illustrate the algorithm and its ability to explore the control landscape, the function $F(u) = 2 + u\sin(u+1)/2$ has been maximized numerically on the interval $u \in [0, 8]$. On this interval, F has two maxima, in 1.25 and 7. The global maximum is $F(7) = 5.45$. The initial value of u is chosen to 1, then the algorithm must find a maximum which is not the nearest one from the initial position. The evolution of u and F as a function of the iteration number is plotted in figures A.3 and A.4.

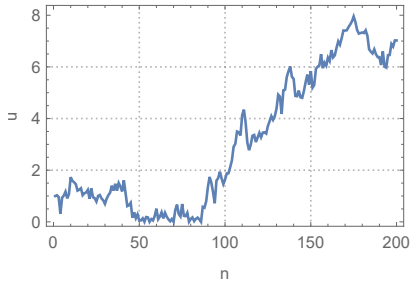

Figure A.3: Evolution of the parameter u as a function of the iteration number n for the maximization of $F(u) = 2 + u\sin(u+1)/2$ on the interval $[0, 8]$.

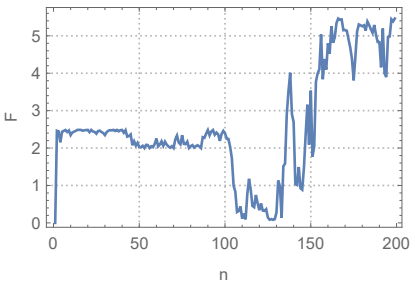

Figure A.4: Evolution of Figure of merit F as a function of the iteration number n for the maximization of $F(u) = 2 + u\sin(u+1)/2$ on the interval $[0, 8]$.

A.2.3 Shooting algorithms

There exist many variants of shooting algorithms, then only a brief presentation is made. First of all, it must be emphasized that very good codes exist: COTCOT [1] and Hampath [2]. They are not explained here. Instead, a simple code is presented, which can be used to determine optimal regular controls in spin dynamics.

For ensembles of N spins, the Pontryagin Hamiltonian [64] can be written in the form $H_p = u_x l^x + u_y l^y + l^0$, where (l^x, l^y, l^0) is the Hamiltonian lift. We have $l^{x,y} = \sum_{n=1}^{N} l_n^{x,y} = \sum_{n=1}^{N} \langle P_n(t)|\epsilon_{x,y}|M_n(t)\rangle$ and $l^0 = \sum_{n=1}^{N} \Delta_n l_n^z = \sum_{n=1}^{N} \Delta_n \langle P_n(t)|\epsilon_z|M_n(t)\rangle$. By using Hamilton's equation, we determine that the Bloch equation (with a negative sign) governs the dynamics of (l_n^x, l_n^y, l_n^z):

$$\frac{d\vec{l}_n}{dt} = \vec{l}_n \wedge \vec{u} + \Delta_n \vec{l}_n \wedge \vec{e}_z.$$

In this case, the maximization condition gives the following regular controls:

$$u_a = u_0 \frac{l^a}{\sqrt{\sum_{b=1}^{2} \sum_n (l_n^b)^2}}.$$

Then, regular controls are entirely parametrized by $3N$ parameters[65] $\{(l_n^x(0), l_n^y(0), l_n^z(0))\}$. It is possible to determine regular control which minimizes F with the following algorithm[66]:

Definition 12 (Shooting algorithm): *With a simulated annealing algorithm, minimize the function $F[\{(l_n^x(0), l_n^y(0), l_n^z(0))\}]$. The function F is computed as follows:*

1. *Integrate the Hamiltonian lifts $\vec{l}_n$ with the Bloch equation from $t = t_0$ to a time $t = t_{max}$ large enough.*
2. *Compute the control $u(t)$ with the Hamiltonian lift.*
3. *Determine $M(t)$ with the Bloch equation.*
4. *Compute $F = \min_t \left(\langle M_{target}|M(t)\rangle\right)$.*

Here, a simulated annealing algorithm is preferred for the last step, because the control landscape is generally not continuous (especially around extrema), or some areas are flat. Therefore, gradient algorithms are not well suited for solving the problem.

[64] See the chapter 5 for more information.

[65] This number can be lowered by determining additional constants of motion

[66] It has been interesting to use *Mathematica* for integrating the differential equations. Indeed, the routine `NDSolve` adapts the integration step automatically (this ensures a very good precision), but more important, it returns an interpolated function. Then, the solution is a true function of time, and it avoids the propagation of errors due to successive integrations on a fixed time grid!

Appendix B

Product of Dirac distributions and non-linear generalized functions

A full chapter is devoted to the theory of generalized functions [70, 38, 39], which is an extension of the well-known Schwartz's theory of distributions. Compared to optimal control theory, generalized functions are less important in this manuscript, however, they are used several times and they play a central role in the integration of differential equations.

Despite the popularity of distributions, generalized functions are rather unknown in physics. This is quite surprising because it allows well defined algebraic computations with distributions, and it proves rigorously many different calculations made in Quantum Field Theory. In this framework, products of distributions are well defined and it is not anymore "*the ugly and heretic things written by physicists*".

First, the subject is introduced with some basics of distribution theory. Then, the problem is tackled with the integration of the Dirac distribution over a simplex. These first calculations are performed within the simple measure theory and the resulting theorem allows a well-defined computation of time ordered exponential when the connection is a Dirac distribution. The second part of this chapter extends the results by introducing the Colombeau algebra. Finally, interesting examples in physics are studied.

B.1 Preliminaries

The following materials are extracted from Laurent Schwartz original book [152].

Definition 13 (test functions of compact support):

- (D_K) *is the sub-space of test function* (D) *with a support included in the compact* K *of* $\mathbb{R}^n$.
- (C_K) *is the vector space of continuous functions on* $\mathbb{R}^n$*, equal to zero except on the ensemble* K *of* $\mathbb{R}^n$.

Theorem 3 (Distribution defined by a measure): *If a distribution* T *is defined by a measure* μ*, it is necessary and sufficient that it it is continuous on each* (D_K) *equipped with the topology induced by* (C_K)*. Then,* μ *is well defined and unique.*

Theorem 4 (Positive distribution): *A distribution* ≥ 0 *is a measure* ≥ 0.

Theorem 5 (Theorem of approximation (p75)): *The vector space (D) of test function considered as subspace of the vector space (D') of distributions is dense in (D').*

A direct consequence of this theorem is the following: **any distribution is a limit of infinitely derivable functions with compact support**.

Definition 14 (vague convergence): *We say that μ_n converges vaguely toward μ if for every function $f \in (C_K)$, $\int f d\mu_n \to \int f d\mu$.*

According to Schwartz, the product of distribution is not always well-defined because the product of two summable functions is not always finite. Then, Schwartz provided the product of distribution as follows:

Theorem 6 (product of distributions): *Let $T \in (D')$ and $\Psi \in (D)$. Then:*

$$\langle \Psi T | \phi \rangle = \langle T | \Psi \phi \rangle,$$

and $\Psi T \in (D')$.

Problems come with the product of singular distributions such as δ^2. The main goal of generalized functions is to extend product rule to any distribution.

We start our discussion by an example. We usually define the Dirac distribution acting on a function $f \in (D)$ by:

$$\delta_a(f.\mathbb{I}_A) = \begin{cases} f(a) \text{ if } a \in A \\ 0 \text{ otherwise} \end{cases}, \tag{B.1}$$

with $a \in \mathbb{R}$ and A an ensemble in $\mathcal{B}$. Now, we consider the product measure $\delta_a(f.\mathbb{I}_A) \otimes \delta_a(f.\mathbb{I}_B)$ defined on the $\sigma-$algebra $\mathcal{B} \times \mathcal{B}$. Due to Fubini's theorem, we have:

$$\begin{aligned} \delta_a(f.\mathbb{I}_A) \otimes \delta_a(f.\mathbb{I}_B) &= \int_A \left(\int_B f(y) d\delta_a(y) \right) f(y) d\delta_a(x) \\ &= \begin{cases} f(a)^2 & \text{if } B = [0, x] \subset A \\ 0 & \text{if } B = [0, x[\subset A, a \in A \end{cases}. \end{aligned} \tag{B.2}$$

Then, we understand that the boundary of integration is crucial. This "pathological" example is encountered in various fields, such as PDE or quantum field theories. In physical systems, the Dirac distribution generally comes as a limit of a very localized subsystem, like a single particle in classical electrodynamics. In quantum mechanics, saying that a particle is on the boundary of a volume means that the particle can be found inside or outside the volume with specific probabilities.

Therefore, as it is illustrated in figures B.1 and B.2 we are motivated to include behaviors on the boundary in the definition:

$$\delta_a(f.\mathbb{I}_A) = \begin{cases} f(a) & \text{if } a \in A/\partial A \\ \frac{f(a)}{2} & \text{if } a \in \partial A \\ 0 & \text{otherwise} \end{cases}. \tag{B.3}$$

This definition seems to solve the problem of the boundary, but this result holds only in dimension one. Caution must be taken with higher dimensions. How can we generalize this definition to the product of Dirac distributions and its integration on hypervolumes? The next section is aimed at providing a precise answer to this question for integration over a n-simplex.

B.2 A first approach: limit of a product of functions

Schwartz's theorem for products of distribution works only with few cases, but according to theorems 3 and 4 one can define a distribution, which is the limit of a product of measure. The result is always well-defined as soon as integrals are converging. The purpose of this section is to introduce a new definition of the Dirac distribution as a limit of functions. This solves the problem highlighted in the last paragraph.

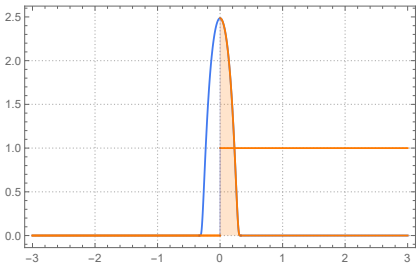

Figure B.1: Example of a function ϕ_n (blue) centered in 0 such as $\lim_{n\to\infty}\phi_n = \delta_0$, which acts on an indicator function. In this case we have the integral: $\int \phi_n \mathbb{I}_A dx = 1/2$

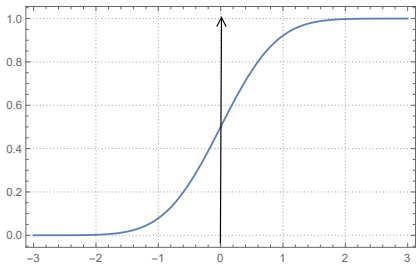

Figure B.2: Inverse point of view of B.1: an indicator function is approximated by a smooth function. Additionally, $\int \phi_n d\delta_0 = 1/2$

Definition 15 ($n-$product of Dirac distributions): *Let us consider a sequence of function $\phi_a^k \in (C_K)$ such as:*

- $\phi_k^i : B \to \mathbb{R}^+$ *such as* $B = [a_i - k, a_i + k]$. *Moreover, the function is symmetric around a_i.*
- $\int \phi_k^i(x_i)dx_i = 1$.

A $n-$ product of Dirac distributions is the measure:

$$\delta_{a_1}(x_1)\cdot\delta_{a_2}(x_2)\cdot\ldots\cdot\delta_{a_n}(x_n)[f] = \lim_{\{k_n\}\to 0}\langle\prod_{i=1}^{n}\phi_{a_n}^{k_n}|f\rangle \equiv \delta_a^n(f),$$

where $a = \{a_1, a2, ..., a_n\} \in \mathbb{R}^n$.

Notice that the limit is kept outside the integral. Indeed, the sequence of function ϕ_k being unbounded, the dominated convergence theorem does not hold and the integral does not commute with the limit.

Theorem 7 (result of a $n-$product of Dirac distributions): *Let $f : \mathbb{R}^n \to \mathbb{R}$ be a test function in (D), and Δ^n a $n-$simplex,then:*

$$\delta_a^n(f\mathbb{I}_{\Delta^n}) = f(a)\delta_a^n(\mathbb{I}_{\Delta^n}),$$

with $\delta_a^n(\mathbb{I}_{\Delta^n}) = 1/(2^m d!)$, m being the dimension of the face and d is the dimension of the wedge in which belongs the point a.

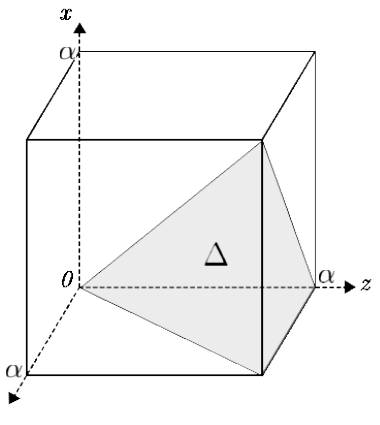

Figure B.3: Part of the volume that defines the integration domain Δ^n

Proof of theorem 7: We consider a point $a = \{a_1, a_2, ..., a_n\} \in \mathbb{R}^n$ and a hypercube $A^n = [0, \alpha]^n$ such as $a \in A^n$. We also define the integration domain $\Delta^n = \{(x_1, x_2, ..., x_n)|x_1 < x_2 < ... < x_n < \alpha\}$.

Lemma:

$$\int_{\Delta^n} d\lambda^n = \frac{\alpha^n}{n!} \tag{B.4}$$

Proof. We use Fubini and the fact that $\int_0^x (y^k/k)dy = x^{k+1}/(k(k+1))$, and by recursion from $k = 0$ to $k = n$ we compute the integral. □

Now let us consider the integral:

$$\int_{\Delta\sigma} \phi_k(x) d\lambda^n(x) = \int_0^{\alpha} \phi_k^n(x_{\sigma(n)}) \int_0^{x_{\sigma(n)}} \phi_k^{n-1}(x_{\sigma(n-1)}) \dots \int_0^{x_{\sigma(2)}} \phi_k^1(x_{\sigma(1)}) d\lambda^n(x)' \tag{B.5}$$

with $\sigma : \{i\}_{i=1..n} \to \{i\}_{i=1..n}$ a switching of indices, and $\Delta\sigma$ the domain after switching. Because all functions ϕ_k^i are identical, the theorem of Fubini allows to switch integrals, then the result of the integral is invariant under permutations of x_i. For the sake of simplicity, we use the notation $\phi_k = \prod_i \phi_k^i$ during the rest of this proof.

Because we are interested in the limit when the support converges toward a single point, only few cases are necessary to be distinguished in order to give a proof:

1) $B \subset \Delta$

$$\int_{\Delta} \phi_k d\lambda^n = \int_{\mathbb{R}^n} \phi_k d\lambda^n = 1. \tag{B.6}$$

2) $B \nsubseteq \Delta$

$$\int_{\Delta} \phi_k d\lambda^n = \int_{\mathbb{R}^n} 0.\phi_k d\lambda^n = 0. \tag{B.7}$$

3) $a \in \partial\Delta$ **and** $B \subset A^n$ In that case, we can separate the integral into two parts. A first one with the domain of ϕ_k^i included inside the boundary, and a second one transverse to the surface. Let us assume that there exists $d < n$ functions ϕ_k^i for which the support crosses $\partial\Delta$. By permutation invariance we have :

$$\int_{\Delta\sigma} \phi_k d\lambda^n = \int_{\delta/\delta\Delta} \phi_k \left[\int_{\Delta} \phi_k d\lambda^{n-d} \right] d\lambda^d = \int_{\delta/\partial\Delta\sigma} \phi_k d\lambda^d \quad \forall\sigma. \tag{B.8}$$

Again, by using the permutation invariance property, we can calculate the rest of the integral. For that purpose, it is necessary to note that a switching σ, changes the integration support ($\Delta^n \to \Delta^n_\sigma$). Its volume is still the same, but its position in A^d is different. Consequently, we have the equality:

$$\sum_{\sigma} \int_{\Delta^n_\sigma} \phi_k d\lambda^d = \int_{A^d} \phi_k d\lambda^d = 1. \tag{B.9}$$

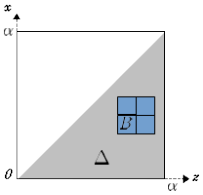

Figure B.4: The support of ϕ_k is included in Δ^n.The center of B corresponds to the point a.

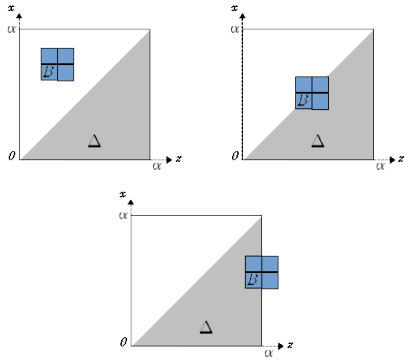

Figure B.5: (*left*) The support of ϕ_k is outside Δ^n, (*right*) it can be on the boundary of Δ or even partially include in the hypercube A^n (*bottom*).

By using the Lemma on the volume of the simplex, we deduce that the number of permutations corresponds to the ratio between the volume of the cube and the volume of the simplex. Finally, we deduce :

$$\int_{\Delta^n} \phi_k d\lambda^n = \frac{1}{d!} \tag{B.10}$$

4) $a \in \partial\Delta$ **et** $a \in \partial A^n$

Like previously, with reasoning on volumes, one can determine the value of the integral when a part of B is not integrated. For that purpose, we look at the ratio between the full volume of B and the volume of the integrated part. Of course, this reasoning is possible only because ϕ_k^i are symmetric functions around a. Under these conditions we obtain:

$$\int_{\Delta^n} \phi_k d\lambda^n = \frac{1}{2^m} \ , \ m < n. \tag{B.11}$$

Now we can define a measure μ_k associated to the density $\phi_k \mathbb{I}_{\Delta^n}$ such as:

$$\forall C \in \mathcal{B}(\mathbb{R}^n) \quad \mu_k(C) = \int \mathbb{I}_C . \mathbb{I}_{\Delta^n} \phi_k d\lambda^n.$$

Theorem 8 (weak convergence): *Let $\mu_n \in \mathcal{M}_b$ such as $A = sup_n \mu_n(1) < +\infty$. Then, there exists a sub-sequence (μ_{n_k}) and $\mu_n \in \mathcal{M}_b$ such as (μ_{n_k}) converges weakly toward μ.*

[67]

[67] We note $\mathcal{M}_b$ the ensemble of bounded measure on $\mathcal{B}(\mathbb{R}^n)$

Proposition 10 (values of μ): $\forall a \in \mathbb{R}^n$, $\exists k_0 \mid \forall k < k_0$, $\mu_k(C)$ *takes the values* 0; 1; $1/(d!2^m)$. *This proposition derives directly of ϕ_k properties when $k \to 0$, $B \to \{a\}$.*

Because $\mu_k(1) \leq 1$, there exists a sequence of measure μ_k, which converges toward a measure noted δ_a^n. This measure at the limit takes the values computed previously when it acts on a set $\mathcal{B}(\mathbb{R}^n)$. Then, we have $\forall f \in C_K$, μ_k that converges vaguely toward δ_a^n.

Proposition 11 (distribution δ_a^n): *et $\forall f \in C_K$, then*

$$\delta_a^n(f) = f(a).\delta_a^n(1)$$

Proof.

$$\forall \varepsilon > 0, \ \exists k_0 \mid \forall x \in B(a,k) \ , \ |f(x) - f(a)| < \varepsilon.$$

Now, we consider the limit when $k \to 0$

$$\begin{aligned} |\mu_k(f) - f(a).\mu_k(1)| &= \left| \int_\Delta f.d\mu_k - \int_\Delta f(a)d\mu_k \right| \\ &\leq \int_\Delta |f - f(a)|d\mu_k \\ &\leq \int_\Delta \varepsilon d\mu_k. \end{aligned}$$

because the measure $\mu_k(S)$ is bounded,we have the equality :

$$|\mu_k(f) - f(a).\mu_k(1)| \leq \varepsilon.$$

□

This finishes the proof for the first part of theorem 7.

Conclusion Product of Dirac distributions as presented here is well defined by a limit of measure. The resulting distribution is generally different from the measure product of 1-dimensional Dirac distribution. However, this theory is limited to a product defined with a tensor product, and we cannot define rigorously product of the kind $\delta_a(x).\delta_b(x)$, where the integration is performed on the same variable for the two distributions. When we apply this product on a test function, we see easily that properties of distributions are not conserved. Hence, we need to consider more general objects than distributions. These objects are called *"generalized functions"*

B.3 Colombeau Algebra and non-linear generalized functions

B.3.1 Definitions and basic theorems

In order to introduce generalized function, let us start with a small calculation of $\langle \delta_a^2 | f \rangle$. If we define Dirac distributions as a limit of positive function ϕ_k^i, we can apply the mean value theorem [68]:

$$\lim_{k\to 0} \int_{B(a,k)} dx.\phi_k^1(x)\phi_k^2(x)f(x) = \lim_{k\to 0} f(c_k \in B) \int_{B(a,k)} dx.\phi_k^1(x)\phi_k^2(x). \tag{B.12}$$

In the limit $k \to 0$, $f(c_k) \to f(a)$ but obviously, the integral on the right-hand side diverges. Moreover, it looks like a sequence of functions which defines a Dirac distribution. Then, this integral might not be a number, but rather a distribution.

The product $\langle \delta_a^2 | f \rangle$ can be adjusted to become a convolution, and convolutions have a well-defined algebra. Then, it is the starting point for defining a well-defined algebraic structure on the space of generalized functions. The second point is to introduce some regularizations of singular distributions, which are recov-

[68] previously we imposed that functions ϕ_k^i are all identical. Here we can weaken this condition and allows different sequences of functions

ered in a limit. For that purpose, we introduce functions called mollifier:

Definition 16 (mollifier): *A mollifier η is an element of a set $\mathcal{A}_\infty$ of real functions such that $\eta \in (S)$ or (D) and $FT[\eta] = 1$ in a neighborhood of 0.*

Theorem 9 (moments of a mollifier):

$$\int \eta(x)dx = 1$$

$$\int x^n \eta(x)dx = 0.$$

Sometimes, it is not necessary to impose zero momentum at any order, it is enough to impose null momentum up to an order q. We will come back to this point latter. An example of mollifier and its Fourier transform are plotted in figures B.6 and B.7.

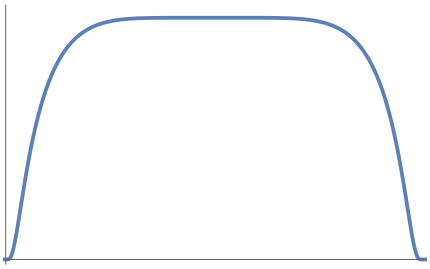

Figure B.6: An example of Fourier transform of a mollifier, which is a function of compact support locally constant to 1.

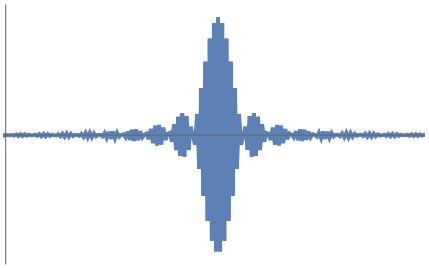

Figure B.7: The mollifier, after inverse Fourier transform.

Proof. This is a straightforward calculation. From the definition we obtain:

$$\int x^n \eta(x)dx = \frac{1}{2\pi} \int x^n \tilde{\eta}(\omega) e^{i\omega x} d\omega dx, \tag{B.13}$$

if $n = 1$, we see the introduction of the Fourier representation of a Dirac distribution. Then we have:

$$\int x^n \eta(x)dx = \tilde{\eta}(0) \equiv 1, \tag{B.14}$$

otherwise, we use the identity that involves the n-th derivative of δ: $FT^{-1}(x^n) = i^n \delta_0^{(n)}$.

$$\begin{aligned} \int x^n \eta(x)dx = i^n \int x^n \eta(\omega) \delta_0^{(n)}(\omega)\omega = i^n \int \tilde{\eta}(\omega)^{(n)} \delta(\omega)d\omega \\ = i\tilde{\eta}^{(n)}(0) = 0 \end{aligned} \tag{B.15}$$

Because $\tilde{\eta}$ is equal to 1 on a neighborhood of 0.

□

Now, we consider the ensemble:

$$\mathcal{E} = \left\{ f_\varepsilon \mid f_\varepsilon(x) = \frac{1}{\varepsilon} \eta\left(\frac{-x}{\varepsilon}\right) * f(x) \ , \ f \in (D) \right\}. \tag{B.16}$$

Functions in $\mathcal{E}$ can be expanded in Taylor series as follows:

$$\begin{aligned} f_\varepsilon(x) &= \int dy \frac{1}{\varepsilon}\eta\left(\frac{y-x}{\varepsilon}\right) f(y) = \int dz.\eta\,(z)\, f(x+\varepsilon z) \\ &= f(x)\int \eta(z) + \sum_{n=1}^{\infty} \frac{\varepsilon^n f^{(n)}(x)}{n!} \int dz.z^n \eta(z) \end{aligned} \quad . \tag{B.17}$$

And from theorem 9 we deduce:

$$f_\varepsilon(x) = f(x) \tag{B.18}$$

If the definition of mollifers is weakened such that every moment vanishes up to an order q (finite) we have the relation:

$$f_\varepsilon(x) = f(x) + o(\epsilon^{q+1}). \tag{B.19}$$

Equations (B.18) and (B.19) show that a mollifier behaves like a Dirac distribution according to the convolution product. More precisely, $f_\varepsilon(x) = f(x)$ + *a negligible function of order* q. The interesting point is that every algebraic operation allowed with the convolutions algebra and the multiplications of equivalent classes[69] stay equivalent up to an order q. Let us call $\mathcal{N}$ the ensemble of negligible functions. It is possible to prove that $\mathcal{E}$ and $\mathcal{N}$ are differentiable algebras, and we define:

[69] Here, equivalent classes are defined with a function modulo other negligible functions of order q

Definition 17 (Colombeau algebra):

$$(\mathcal{G}) = \frac{\mathcal{E}}{\mathcal{N}}.$$

Elements $g \in (\mathcal{G})$ is an equivalence class $D(g_\varepsilon)$ of function g_ε modulo a negligible function. Functions g_ε are called representatives of g. The multiplication of g and h in $(\mathcal{G})$, denoted by $g \odot h$ is defined by: $g \odot h = D[g_\varepsilon \cdot h_\epsilon]$ ("$\cdot$" is the point-wise product).
Elements of $(\mathcal{G})$ are called: generalized functions.

Notice that it results the following inclusion relation:

$$(C_K) \subset (D') \subset (\mathcal{G}). \tag{B.20}$$

The Colombeau algebra is bigger than the space of Distribution so we might find examples of generalized functions, which are not distributions of Schwartz's theory. More precisely, the connection with distribution is made as follows:

Definition 18 (association of generalized functions): *Two generalized functions g and h in $(\mathcal{G})$ of respective representative g_ε and h_ε are said to be associated, and one write $g \sim h$ if and only if:*

$$\lim_{\varepsilon\to 0} \int dx\,(g_\varepsilon(x) - h_\varepsilon(x))\,\phi(x) = 0\,,\ \forall \phi(x) \in (D).$$

Theorem 10 (Colombeau local structure theorem): *Any distribution is locally a moderate (i.e. multipliable) generalized function*

It is important to notice the following relations:

$$g \sim h \Rightarrow D(g_\varepsilon) \sim D(h_\varepsilon) \tag{B.21}$$

$$\forall d_1, d_2 \in (D') \Rightarrow D[d_1] \odot D[d_2] \notin (D'), \text{(generally)}. \tag{B.22}$$

It is obvious that n-product of Dirac distributions, as introduced in the previous section (definition 15), makes sense in Colombeau's framework. The advantage of this framework is the regularization properties, based on convolution and equivalence classes. Notice that the notion of equivalence class generalized functions is weaker than in distribution theory (which are defined modulo functions null almost everywhere for Lebesgue measure).

More precisely, the connection between notations is the following:

$n-$product of δ	Colombeau formalism
$\delta_a(f)$	$\lim_{\varepsilon\to 0}[\eta_\epsilon * f](a) = \lim_{\varepsilon\to 0}\int \frac{dy}{\varepsilon}\eta(\frac{y-a}{\varepsilon})f(y)$
$\delta_{a_1}\cdot\ldots\cdot\delta_{a_n}[f]$	$\lim_{\varepsilon\to 0}\int \frac{dy^n}{\varepsilon}\prod_{k=1}^n \eta(\frac{y_k-a_k}{\varepsilon})f(y)$

B.3.2 Construction of mollifiers

We propose here an iterative procedure to compute mollifiers of order q. For each order, an analytic formula is derived. The latter is a polynomial that depends on a "mother" function (an input of the procedure), and its derivatives. Coefficients might be evaluated numerically but it is generally very fast (few milliseconds). The procedure is nothing else that the proof of the existence of such functions. It is a standard result in non-linear generalized function theory. More details can be found in [37].

Definition 19 (Space of mollifier): *The space of mollifier $\mathcal{A}_q$ of order q is a subset of the space of C^∞ function of compact support (D_K) on K such as:*

$$\mathcal{A}_q = \left\{\eta \in (D_K) \mid \int \eta(x)dx = 1 \right. \\ \left. \text{and } \int x^n\eta(x)dx = 0\ \forall 1 \le n \le q\right\} \tag{B.23}$$

Proposition 12 (Non-void set): *The set $\mathcal{A}_q$ is non-void for $q = 1, 2...$*

Proof. Let us choose a function $\eta_0 \in (D_K)$ such as $\int \eta(x)dx = 1$. Since there exists functions that satisfy this property, it proves

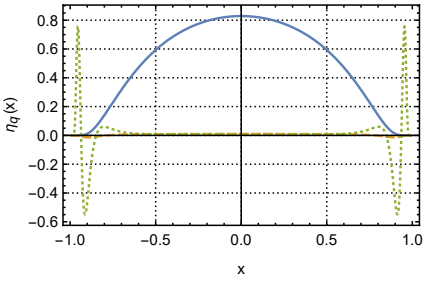

Figure B.8: Family of mollifier defined by $\eta_0(x) = e^{(x^2-1)^{-1}}\mathbb{I}_{]-1,1[}(x)$. Blue solid line: order 0, Orange dashed line: order 2 and the green dotted line: order 4. Blue and orange curves have been multiplied by 100.

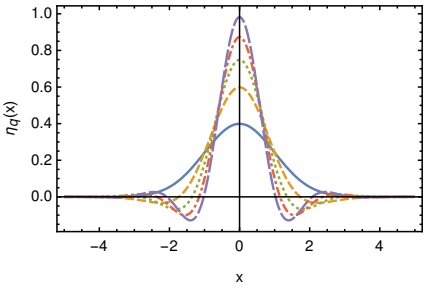

Figure B.9: Family of mollifier generated by $\eta_0(x) = \frac{1}{\sqrt{2\pi}}e^{-x^2/2}$ ($\sigma = 1$). for orders 0,2,4,6,8.

the proposition for $q = 0$. Now let us construct a function with $\eta_1 = \eta_0 + \alpha_1 \partial_x \eta_0$. The goal is to find α_1 so that $\eta_1 \in \mathcal{A}_1$.

$$\int x \partial_x \eta(x) dx = -\int \eta(x) dx = -1.$$

Therefore, it suffices that

$$\alpha_1 = \int x \eta_0(x) dx.$$

At order two, we define $\eta_2 = \eta_1 + \alpha_2 \partial_x^2 \eta(x)$. And we compute:

$$\begin{aligned}\int x^2 \eta(x) dx &= \int x^2 \eta_1(x) dx + \alpha_2 \int x^2 \partial_x^2 \eta_0(x) dx \\ &= \int x^2 \eta_1(x) dx + 2\alpha_2,\end{aligned}$$

therefore, we choose:

$$\alpha_1 = -\frac{1}{2} \int x^2 \eta_1(x) dx.$$

It is straightforward to show that $\int \eta_2(x) dx = 1$ and $\int x \eta_2(x) dx = 0$. So we have $\eta_2 \in \mathcal{A}_2$. By induction, we construct mollifiers of higher degree with the relation:

$$\eta_q = \eta_{q-1} + \alpha_q \partial_x^q \eta_0 \tag{B.24}$$

$$\alpha_q = -\frac{1}{n!} \int x^q \eta_{q-1}(x) dx, \tag{B.25}$$

and we have $\eta_q \in \mathcal{A}_q$. □

Definition 20 (family of mollifiers): *A family of mollifiers is the ensemble of mollifiers η_q generated from the mother function η_0 and its derivatives.*

Two examples of family are presented in figures B.8 and B.9.

B.4 Applications

B.4.1 proof of the "operator splitting" in ordered exponentials

We would like to prove that the solution of the Schrödinger equation:

$$\frac{d\hat{U}(t)}{dt} = -i \left(\hat{H}_0 + \hat{\delta}(t - T) H_1 \right) \hat{U}(t) \tag{B.26}$$

can be expressed in the form

$$\hat{U}(t) = e^{-i\hat{H}_1} e^{-i\hat{H}_0 T}. \tag{B.27}$$

When $t \in [0, T[$, the Hamiltonian does not depend on time, $\hat{U}$ is simply given by:

$$\hat{U}(t \in [0, T[) = e^{-i\hat{H}_0 t}. \tag{B.28}$$

For the computation at time T we use the intermediate representation theorem.

$$\hat{U}(T) = \lim_{\epsilon \to 0} \hat{U}_1(T+\epsilon) \times \mathbb{T} e^{-i \int_0^{T+\epsilon} \hat{U}_1^{-1}(t) \hat{H}_0 \hat{U}_1(t) dt}, \tag{B.29}$$

where we used the notation:

$$\hat{U}_1(t) = \mathbb{T} e^{-i \int_0^t \hat{H}_1 \delta(t'-T) dt'}. \tag{B.30}$$

Knowing that $\forall K(t)$:

$$\begin{aligned} \mathbb{T} e^{\int_0^a K(t)\delta(t-T)dt} =& \mathbb{I}_H + \sum_{n=1}^{+\infty} (-i)^n \int_0^a K(t_n) \int_0^{t_n} K(t_{n-1}) ... \int_0^{t_1} K(t_1) \\ & \times \delta(t_1 - T) dt_1 .. \delta(t_{n-1} - T) dt_{n_1} \delta(t_n - T) dt_n \end{aligned} \tag{B.31}$$

with theorem 7, we deduce:[70]

$$\mathbb{T} e^{\int_0^a K(t)\delta(t-T)dt} = \mathbb{I}_H + \sum_{n=1}^{+\infty} \frac{(-iK(T))^n}{n!} = e^{-iK(T)}.$$

Then, it is easy to see that :

$$\hat{U}_1(t) = e^{-i\hat{H}_1 \mathbb{I}_{[T,+\infty[}(t)}. \tag{B.32}$$

Inserting (B.32) into (B.29) gives:

$$\begin{aligned} \hat{U}(T) &= \lim_{\epsilon \to 0} e^{-i\hat{H}_1} e^{-ie^{i\hat{H}_1} \hat{H}_0 e^{-i\hat{H}_1} \epsilon} e^{-i\hat{H}_0 T} \\ &= e^{-i\hat{H}_1} e^{-i\hat{H}_0 T} \end{aligned}. \tag{B.33}$$

[70] One can ask about the meaning of using theorem 7 on this computation. The answer invokes the physical meaning of the Hamiltonian. Here, a δ-pulse is an idealization of an extremely short and powerful pulse. Then we understood the system as a limit, exactly like the one used in the new definition of the Dirac distribution.

B.4.2 Elimination of fast damping quantities in differential equations

We consider a system of the form:

$$\frac{dX(t)}{dt} = -\kappa X(t) + A(t) \tag{B.34}$$

$$\frac{dY(t)}{dt} = f(X, Y, t). \tag{B.35}$$

The use of green functions allows us to write an expression of X in integral from:

$$X(t) = \int_{-\infty}^{t} e^{-\kappa(t-t')} A(t') dt'. \tag{B.36}$$

Now, if κ is very large with respect to all other characteristic times of the system, one could approximate the exponential by half of a Dirac distribution. Indeed:

$$\lim_{\kappa\to\infty} \frac{2}{\kappa} e^{-\kappa|t|} = \delta_0(t). \tag{B.37}$$

Thus, the integration over the half of the time domain gives:

$$X(t) = \frac{1}{\kappa} A(t), \tag{B.38}$$

and the dynamics of Y is given by the differential equation:

$$\frac{dY(t)}{dt} = f(X, A(t)/\kappa, t). \tag{B.39}$$

B.4.3 Scalar product of two Dirac distributions

An equality which is commonly used in quantum field theory is the following:

$$\langle \delta_x | \delta_{x'} \rangle = \delta_0(x - x'), \tag{B.40}$$

which is a nonsense from the point of view of Schwartz's theory. Nevertheless, despite the ugly notation, this equality makes sense with generalized functions. The proof is a simple calculation, which involves two representatives of a Dirac distribution:

$$\begin{aligned} \langle \delta_x | \delta_{x'} \rangle &= \int dy \frac{1}{\varepsilon\varepsilon'} \eta\left(\frac{y-x}{\varepsilon}\right) \eta\left(\frac{y-x'}{\varepsilon'}\right) \\ &= \int dz \frac{1}{\varepsilon'} \eta(z) \eta\left(\frac{\varepsilon z + x - x'}{\varepsilon'}\right) \end{aligned}, \tag{B.41}$$

η functions are smooth functions, which can be expanded in Taylor series:

$$\begin{aligned} \langle \delta_x | \delta_{x'} \rangle &= \frac{1}{\varepsilon'} \eta\left(\frac{x-x'}{\varepsilon'}\right) \int \eta(z) dz + \sum_{n=1}^{\infty} \frac{(\varepsilon/\varepsilon')^n}{n!} \eta^{(n)}\left(\frac{x-x'}{\varepsilon'}\right) \int dz . z^n \eta(z) \\ &= \frac{1}{\varepsilon'} \eta\left(\frac{x-x'}{\varepsilon'}\right) + o((\varepsilon/\varepsilon')^q) \end{aligned}. \tag{B.42}$$

So it is immediate that $\langle \delta_x | \delta_{x'} \rangle$ is a function of x and x', and that it is a representative of δ in $(\mathcal{G})$.

Appendix C

Lie groups and geometry

The theory of fiber bundle, differential geometry and Lie-groups is essential in quantum control. These theories allow us to formulate control problems with beautiful geometric objects, and it helps us to have an intuition of system properties. In this manuscript, many tools and theorems from these theories are used, but it would be too long to give a detailed description of them. Therefore, this chapter is only devoted to some interesting and useful results [89, 139, 45, 143, 96, 18, 44].

C.1 Matrix and vector representations

Theorem 11 (Vector representation of density matrices): *Let ρ be a $N \times N$ density matrix and A, B two operators. Then :*

$$A\rho B \sim (A \otimes B^T)\tilde{\rho},$$

where B^T is the transpose of B and $\tilde{\rho}$ is the vector representation of ρ :

$$\rho = \begin{pmatrix} \rho_{11} & \rho_{12} \\ \rho_{21} & \rho_{22} \end{pmatrix} \rightarrow \tilde{\rho} = (\rho_{11}, \rho_{12}, \rho_{21}, \rho_{22})^T.$$

Proof. By using the Einstein tensor notation:

$$(A\rho B)_\mu^{\ \vartheta} = A_\mu^{\ \nu} \rho_\nu^{\ \sigma} B_\sigma^{\ \vartheta} = A_\mu^{\ \nu} B_\sigma^{\ \vartheta} \rho_\nu^{\ \sigma}.$$

We would like to write it in the form : $C_\mu^{\ \tau} \tilde{\rho}_\tau$ with $\tilde{\rho}_{(\nu-1)N+\sigma} = \rho_\nu^{\ \sigma}$.
Note that $(A \otimes B)_{\mu\ \sigma}^{\ \nu\ \vartheta} = A_\mu^{\ \nu} B_\sigma^{\ \vartheta}$, and it follows :

$$(A \otimes B^T)_\mu^{\ \tau} \tilde{\rho}_\tau = \sum_{\nu,\sigma,\vartheta} A_\mu^{\ \nu} B^\vartheta{}_\sigma \tilde{\rho}_{(\nu-1)N+\sigma} = A_\mu^{\ \nu} B_\sigma^{\ \vartheta} \rho_\nu^{\ \sigma} \delta_{\vartheta\vartheta}.$$

□

C.2 Lie Groups

Definition 21 (Lie Groupe & Algebra homomorphism):
1) *Let two Lie groups $\mathcal{G}$, $\mathcal{H}$ and a map $\phi : \mathcal{G} \to \mathcal{H}$. ϕ is a Lie homomorphism if it is a $\mathcal{C}^\infty$ map of manifolds and a group homomorphism.*
2) *Let $\mathfrak{g}$ and $\mathfrak{h}$ the respective Lie Algebra of $\mathcal{G}$ and $\mathcal{H}$. A map $\phi : \mathfrak{g} \to \mathfrak{h}$ is said to be a Lie Algebra homomorphism if :*

- *$d\phi$ is linear.*
- *$d\phi([X,Y]) = [d\phi(X), d\phi(Y)]$ for all $X, Y \in \mathfrak{g}$.*

Proposition 13 (Commutative diagram): *We have the following Commutative diagram :*

$$\begin{array}{ccc} & \overset{\phi}{\longrightarrow} & \\ \mathcal{G} & & \mathcal{H} \\ \exp\uparrow & & \uparrow\exp \\ \mathfrak{g} & & \mathfrak{h} \\ & \underset{d\phi}{\longrightarrow} & \end{array}.$$

Proof. 1) $g = e^{X.t}$ with t a scalar and $\phi(g) = e^{d\phi(X)t}$.
for $t \to 0$ we have $g = \mathbb{I}_{\mathcal{G}}$ and $\phi(G) = Id_{\mathcal{H}}$.
2) Because of the Baker–Campbell–Hausdorff formula:$e^X e^Y = e^{X+Y+[X,Y]/2+\dots}$ we have:

$$\phi(e^X)\phi(e^Y) = e^{d\phi(x)}e^{d\phi(Y)} = e^{d\phi(X+Y+[X,Y]/2+\dots)} = \phi(e^X e^Y)$$

□

Proposition 14 (Product of rotations): *Let α and β two rotation angles around the respective axes $\vec{n}_1$ and $\vec{n}_2$. The composition of the two rotations gives an effective angle of rotation γ around an axis $\vec{n}_3$. They are given by:*

$$\cos\left(\frac{\gamma}{2}\right) = \cos\left(\frac{\alpha-\beta}{2}\right)\sin^2\left(\frac{\theta}{2}\right) + \cos\left(\frac{\alpha+\beta}{2}\right)\cos^2\left(\frac{\theta}{2}\right) \tag{C.1}$$

$$\vec{n}_3 = \frac{(\cos(\alpha/2)\sin(\beta/2)\vec{n}_2 + \cos(\beta/2)\sin(\alpha/2)\vec{n}_1 - \sin(\alpha/2)\sin(\beta/2)\vec{n}_1 \wedge \vec{n}_2)}{\sin(\gamma/2)} \tag{C.2}$$

where $\vec{n}_1.\vec{n}_2 = \cos(\theta)$

Proof. We give a detailed proof only for the computation of the rotation angle. The proof for the rotation axis follows the same idea [96, 18, 44]. For the sake of simplicity, we use the quaternion representation of rotations. A rotation of angle α around an axis $\vec{n}$ is described by the quaternion $\mathbf{q} = \cos(\alpha/2) - \sin(\alpha/2)(n_x\mathbf{i} + n_y\mathbf{j} + n_z\mathbf{z})$. It is enough to focus on the real part of the quaternion for determining the angle of rotation. A straightforward computation gives:

$$Re[\mathbf{q_1}\mathbf{q_2}] = \cos\left(\frac{\alpha}{2}\right)\cos\left(\frac{\beta}{2}\right) - \sin\left(\frac{\alpha}{2}\right)\sin\left(\frac{\beta}{2}\right)\vec{n}_1.\vec{n}_2.$$

Since $\vec{n}_1$ and $\vec{n}_2$ are two unit vectors, we can introduce the angle between the two vectors. Moreover, after introducing $Re[\mathbf{q_1 q_2}] = \cos(\gamma/2)$, we obtain:

$$\cos\left(\frac{\gamma}{2}\right) = \cos\left(\frac{\alpha}{2}\right)\cos\left(\frac{\beta}{2}\right) - \sin\left(\frac{\alpha}{2}\right)\sin\left(\frac{\beta}{2}\right)\cos(\theta),$$

and after few trigonometric computations we arrive at:

$$\cos\left(\frac{\gamma}{2}\right) = \cos\left(\frac{\alpha-\beta}{2}\right)\sin^2\left(\frac{\theta}{2}\right) + \cos\left(\frac{\alpha+\beta}{2}\right)\cos^2\left(\frac{\theta}{2}\right).$$

□

C.3 Path ordered exponential, gauge change and derivations

Theorem 12 (Trotter Formula): *For any operator $\hat{A}_j$ in a Banach space:*

$$\exp\left(\sum_j \hat{A}_j\right) = \lim_{N\to\infty}\left(\prod_j \exp\left(\hat{A}_j/N\right)\right)^N.$$

Proof. see [161]. □

Theorem 13 (intermediate representation): *Let $A(t)$ and $B(t)$ two inversible elements of a Lie algebra. Then:*

$$\mathbb{T}e^{\int_0^t(\hat{A}(t')+\hat{B}(t'))dt'} = \mathbb{T}e^{\int_0^t \hat{A}(t')dt'}.\mathbb{T}e^{\int_0^t\left[\mathbb{T}e^{-\int_0^{t'}\hat{A}(t'')dt''}.\hat{B}(t').\mathbb{T}e^{\int_0^{t'}\hat{A}(t'')dt''}\right]dt'}.$$

Proof. Let us denote $\hat{U}[\hat{A}] = \mathbb{T}e^{\int_0^t \hat{A}(t')dt'}$. By definition, we have:

$$d_t\hat{U}[\hat{A}+\hat{B}] = (\hat{A}+\hat{B}).\hat{U}[\hat{A}+\hat{B}]$$
$$d_t\hat{U}[\hat{A}] = (\hat{A}).\hat{U}[\hat{A}],$$

but,

$$d_t\hat{U}[\hat{A}]^{-1} = -(d_t\hat{U}[\hat{A}])\hat{U}[\hat{A}]^{-2} = -\hat{A}\hat{U}[\hat{A}]^{-1},$$

so

$$\hat{A} = -(d_t\hat{U}[\hat{A}]).\hat{U}[\hat{A}] = -\hat{U}[\hat{A}]d_t\hat{U}[\hat{A}]^{-1}$$

then

$$d_t\hat{U}[\hat{A}+\hat{B}] = (-\hat{U}[\hat{A}]d_t\hat{U}[\hat{A}]^{-1} + \hat{B})\hat{U}[\hat{A}+\hat{B}]$$
$$\hat{U}[\hat{A}]^{-1}d_t\hat{U}[\hat{A}+\hat{B}] = (d_t\hat{U}[\hat{A}]^{-1} + \hat{U}[\hat{A}]^{-1}\hat{B})\hat{U}[\hat{A}+\hat{B}]$$
$$\hat{U}[\hat{A}]^{-1}d_t\hat{U}[\hat{A}+\hat{B}] + (d_t\hat{U}[\hat{A}])\hat{U}[\hat{A}+\hat{B}] = \hat{U}[\hat{A}]^{-1}\hat{B}\hat{U}[\hat{A}+\hat{B}]$$
$$d_t(\hat{U}[\hat{A}]^{-1}\hat{U}[\hat{A}+\hat{B}]) = (\hat{U}[\hat{A}]^{-1}\hat{B}\hat{U}[\hat{A}])(\hat{U}[\hat{A}]^{-1}\hat{U}[\hat{A}+\hat{B}]),$$

with gives by definition:

$$\hat{U}[\hat{A}]^{-1}\hat{U}[\hat{A}+\hat{B}] = \hat{U}[\hat{U}[\hat{A}]^{-1}\hat{B}\hat{U}[\hat{A}]].$$

□

Theorem 14 (Gauge transformation): *Let $g : \mathbb{R} \to \mathcal{G}$ be a smooth function over time in value of a Lie group $\mathcal{G}$. And $A : \mathbb{R} \to \mathfrak{g}$ a function of the Lie Algebra $\mathfrak{g} = Lie(\mathcal{G})$. Then,*

$$\mathbb{T}e^{\int_0^t dt' g^{-1}(t')A(t')g(t') - g^{-1}(t')d_t g(t')} = g^{-1}(t)\mathbb{T}e^{\int_0^t dt' A(t')}g(0)$$

Proof. See [89]. It can also be seen as a variant of the intermediate representation theorem (13). □

Theorem 15 (Functional derivative of a path ordered exponential): *Let $A = A_a^i(x)\tau_i dx^a$ be a connection one form in a group $\mathcal{G}$ on a manifold ($\{\tau_i\}$ are generators of the Lie algebra and x^a are coordinates in the manifold), and γ be a path in the manifold. Let $\hat{U}[\gamma] = \mathbb{P}e^{\int_\gamma A}$ be the path ordered exponential along γ. Then,*

$$\frac{\delta}{\delta A_a^i(x)}\hat{U}[\gamma] = \int_\gamma ds\delta(x-\gamma(s))\frac{d\gamma^a}{dt}\hat{U}[\gamma_2]\tau_i\hat{U}[\gamma_1],$$

with $\gamma = \gamma_2 \circ \gamma_1$, with a cut at the point s. If the system is restricted to a path, the exponential can be rewritten in terms of a time ordered exponential $\hat{U}(0,t)$. In that case, the integral over γ is canceled by the Dirac distribution and we have:

$$\frac{\delta}{\delta A_a^i(\tau)}\hat{U}(0,t) = \frac{d\gamma^a(\tau)}{d\tau}\hat{U}(\tau,t)\tau_i\hat{U}(0,\tau).$$

Proof. This is a long, but straightforward calculation. Note: *It is important to use functional derivatives and not usual derivatives, otherwise, the proof does not work.* □

Proposition 15 (Partial derivative of a time ordered exponential): *Suppose that the connection A is a differentiable function of a parameter λ. Then*

$$\frac{\partial\hat{U}}{\partial\lambda} = \lim_{\varepsilon\to 0}\frac{\hat{U}(\lambda+\varepsilon)-\hat{U}(\lambda)}{\varepsilon} \tag{C.3}$$

$$\frac{\partial\hat{U}}{\partial\lambda} = \sum_{m=0}^{\infty}\int_{\Delta^m}\sum_{l=1}^{m}\left(\prod_{k=l+1}^{m}A(t_k)dt_k\right)\frac{\partial A(t_l)}{\partial\lambda}dt_l\left(\prod_{k=0}^{l-1}A(t_k)dt_k\right). \tag{C.4}$$

This expression could be simplified by introducing the Magnus expression : $\hat{U} = e^{\Omega(t,\lambda)}$ where Ω is the Magnus operator[22]. It follows :

$$\frac{\partial\hat{U}}{\partial\lambda} = \int_0^1 e^{(1-x).\Omega(t,\lambda)}\frac{\partial\Omega(t,\lambda)}{\partial\lambda}e^{x.\Omega(t,\lambda)}dx \tag{C.5}$$

Proof.

$$\frac{\partial \hat{U}}{\partial \lambda} = \frac{\partial}{\partial \lambda} e^{\Omega} = \sum_{m=0}^{\infty} \frac{1}{(m+1)!} \sum_{k=0}^{m} \Omega^k \frac{\partial \Omega}{\partial \lambda} \Omega^{m-k}.$$

By using the identity [22]:

$$\sum_{n=0}^{\infty} \sum_{k=0}^{n} f_{n,k} = \sum_{k=0}^{\infty} \sum_{n=k}^{\infty} f_{n,k} = \sum_{k=0}^{\infty} \sum_{n=0}^{\infty} f_{n+k,k},$$

the partial derivative becomes

$$\frac{\partial \hat{U}}{\partial \lambda} = \sum_{k=0}^{\infty} \sum_{m=0}^{\infty} \frac{1}{(m+k+1)!} \Omega^k \frac{\partial \Omega}{\partial \lambda} \Omega^m. \tag{C.6}$$

Now the equation is multiplied and divided by $m!k!$ and with the use of the Beta function:

$$B(m+1, k+1) = \frac{m!k!}{(m+k+1)!} = \int_0^1 x^n (1-x)^k dx,$$

an integral is introduced in equation (C.6):

$$\frac{\partial \hat{U}}{\partial \lambda} = \int_0^t \sum_{m,k} \frac{1}{m!k!} \Omega^k (1-x)^k \frac{\partial \Omega}{\partial \lambda} \Omega^m x^m . dx$$

Sums are arranged into exponential and it finishes the proof. □

If the parameter used to differentiate a time ordered exponential is constant over time, we can connect partial and functional derivatives:

Proposition 16 (From functional to partial derivatives): *Suppose that* $\hat{U} = e^{(A_n^0 + u_i . A^1)(t_1 - t_0)}$ *where* $u(t) = u_i$ *on* $[t_0, t_1]$. *Then:*

$$\frac{\partial \hat{U}}{\partial u_i} = \frac{1}{t_1 - t_0} \int_{t_0}^{t_1} \frac{\delta \hat{U}}{\delta u(\tau)} d\tau.$$

Bibliography

[1] "cotcot: conditions of order two, conjugate times." [Online]. Available: http://apo.enseeiht.fr/cotcot/

[2] "HamPath : http://www.hampath.org/." [Online]. Available: http://www.hampath.org/

[3] *Pattern Recognition and Machine Learning | Christopher Bishop | Springer*. [Online]. Available: http://www.springer.com/us/book/9780387310732

[4] *Advances in Atomic, Molecular, and Optical Physics*. Academic Press, Oct. 2008, google-Books-ID: Thnwk4EDVCMC.

[5] E. Aarts, J. Korst, and W. Michiels, "Simulated Annealing," in *Search Methodologies*. Springer, Boston, MA, 2005, pp. 187–210. [Online]. Available: https://link.springer.com/chapter/10.1007/0-387-28356-0_7

[6] K. A. Al-Hassanieh, V. V. Dobrovitski, E. Dagotto, and B. N. Harmon, "Numerical Modeling of the Central Spin Problem Using the Spin-Coherent-State P Representation," *Physical Review Letters*, vol. 97, no. 3, p. 037204, Jul. 2006. [Online]. Available: https://link.aps.org/doi/10.1103/PhysRevLett.97.037204

[7] F. Albertini and D. D'Alessandro, "Minimum Time Optimal Synthesis for a Control System on SU(2)," *arXiv:1407.7491 [quant-ph]*, Jul. 2014, arXiv: 1407.7491. [Online]. Available: http://arxiv.org/abs/1407.7491

[8] C. Altafini and F. Ticozzi, "Modeling and Control of Quantum Systems: An Introduction," *IEEE Transactions on Automatic Control*, vol. 57, no. 8, pp. 1898–1917, Aug. 2012, arXiv: 1210.7127. [Online]. Available: http://arxiv.org/abs/1210.7127

[9] Q. Ansel, S. Probst, P. Bertet, S. J. Glaser, and D. Sugny, "Optimal control of an inhomogeneous spin ensemble coupled to a cavity," *Physical Review A*, vol. 98, no. 2, p. 023425, Aug. 2018. [Online]. Available: https://link.aps.org/doi/10.1103/PhysRevA.98.023425

[10] A. Ashtekar, J. Lewandowski, D. Marolf, J. Mourão, and T. Thiemann, "Quantization of diffeomorphism invariant theories of connections with local degrees of freedom," *Journal of Mathematical Physics*, vol. 36, no. 11, pp. 6456–6493, Nov. 1995. [Online]. Available: https://aip.scitation.org/doi/10.1063/1.531252

[11] A. Ashtekar and C. Rovelli, "A Loop Representation for the Quantum Maxwell Field," *Classical and Quantum Gravity*, vol. 9, no. 5, pp. 1121–1150, May 1992, arXiv: hep-th/9202063. [Online]. Available: http://arxiv.org/abs/hep-th/9202063

[12] J. Assländer, S. J. Glaser, and J. Hennig, "Pseudo Steady-State Free Precession for MR-Fingerprinting," *Magnetic Resonance in Medicine*, vol. 77, no. 3, pp. 1151–1161, 2016. [Online]. Available: https://onlinelibrary.wiley.com/doi/abs/10.1002/mrm.26202

[13] R. Azouit, A. Sarlette, and P. Rouchon, "Adiabatic elimination for open quantum systems with effective Lindblad master equations," *arXiv:1603.04630 [quant-ph]*, Mar. 2016, arXiv: 1603.04630. [Online]. Available: http://arxiv.org/abs/1603.04630

[14] A. D. Bandrauk and H. Shen, "Exponential split operator methods for solving coupled time dependent Schrodinger equations," *The Journal of Chemical Physics*, vol. 99, no. 2, pp. 1185–1193, Jul. 1993. [Online]. Available: https://aip.scitation.org/doi/abs/10.1063/1.465362

[15] J. Bernoulli, *Supplementum defectus geometria cartesianae circa inventionem locorum*, 1696. [Online]. Available: https://www.sophiararebooks.com/pages/books/2899/leibniz-lhospital-tschirnhaus-newton-johann-bernoulli-jakob/1-johann-supplementum-defectus-geometria-cartesianae-circa-inventionem-locorum-2-leibniz/?soldItem=true

[16] M. A. Bernstein, K. F. King, and X. J. Zhou, *Handbook of MRI Pulse Sequences*. Elsevier, Sep. 2004, google-Books-ID: d6PLHcyejEIC.

[17] P. Bertet and K. Moelmer, "Method and Device for Very High Sensitivity Electron Spin Resonance Spectroscopy," US Patent US20 180 045 795A1, Feb., 2018. [Online]. Available: https://patents.google.com/patent/US20180045795A1/en

[18] L. C. Biedenharn, *Angular Momentum in Quantum Physics: Theory and Application*. Addison-Wesley Publishing Company, Advanced Book Program, Jan. 1981, google-Books-ID: 8HWQwdXqcXAC.

[19] A. Bienfait, J. J. Pla, Y. Kubo, M. Stern, X. Zhou, C. C. Lo, C. D. Weis, T. Schenkel, M. L. W. Thewalt, D. Vion, D. Esteve, B. Julsgaard, K. Mølmer, J. J. L. Morton, and P. Bertet, "Reaching the quantum limit of sensitivity in electron spin resonance," *Nature Nanotechnology*, vol. 11, no. 3, pp. 253–257, Mar. 2016. [Online]. Available: https://www.nature.com/articles/nnano.2015.282

[20] A. Bienfait, J. J. Pla, Y. Kubo, X. Zhou, M. Stern, C. C. Lo, C. D. Weis, T. Schenkel, D. Vion, D. Esteve, J. J. L. Morton, and P. Bertet, "Controlling spin relaxation with a cavity," *Nature*, vol. 531, no. 7592, pp. 74–77, Mar. 2016. [Online]. Available: https://www.nature.com/articles/nature16944

[21] A. Bienfait, "Magnetic resonance with quantum microwaves," Ph.D. dissertation, 2016. [Online]. Available: https://tel.archives-ouvertes.fr/tel-01496176/

[22] S. Blanes, F. Casas, J. A. Oteo, and J. Ros, "The Magnus expansion and some of its applications," *Physics Reports*, vol. 470, no. 5-6, pp. 151–238, Jan. 2009, arXiv: 0810.5488. [Online]. Available: http://arxiv.org/abs/0810.5488

[23] B. Bonnard and O. Cots, "Geometric numerical methods and results in the contrast imaging problem in nuclear magnetic resonance," *Mathematical Models and Methods in Applied Sciences*, vol. 24, no. 01, pp. 187–212, Apr. 2013. [Online]. Available: https://www.worldscientific.com/doi/abs/10.1142/S0218202513500504

[24] B. Bonnard, O. Cots, J. Rouot, and T. Verron, "Time minimal saturation of a pair of spins and application in Magnetic Resonance Imaging," Apr. 2018. [Online]. Available: https://hal.archives-ouvertes.fr/hal-01764022

[25] B. Bonnard and D. Sugny, *Optimal Control with Applications in Space and Quantum Dynamics*. American Institute of Mathematical Sciences, 2012, google-Books-ID: cw2EMAEACAAJ.

[26] U. Boscain and Y. Chitour, "Time Optimal Synthesis for Left–Invariant Control Systems on SO(3)," *arXiv:math/0502483*, Feb. 2005, arXiv: math/0502483. [Online]. Available: http://arxiv.org/abs/math/0502483

[27] U. Boscain and P. Mason, "Time Minimal Trajectories for a Spin 1/2 Particle in a Magnetic Field," *Journal of Mathematical Physics*, vol. 47, no. 6, p. 062101, Jun. 2006, arXiv: quant-ph/0512074. [Online]. Available: http://arxiv.org/abs/quant-ph/0512074

[28] S. J. Bosman, M. F. Gely, V. Singh, A. Bruno, D. Bothner, and G. A. Steele, "Multi-mode ultra-strong coupling in circuit quantum electrodynamics," *npj Quantum Information*, vol. 3, no. 1, Dec. 2017, arXiv: 1704.06208. [Online]. Available: http://arxiv.org/abs/1704.06208

[29] S. Boutin, C. K. Andersen, J. Venkatraman, A. J. Ferris, and A. Blais, "Resonator reset in circuit QED by optimal control for large open quantum systems," *Physical Review A*, vol. 96, no. 4, p. 042315, Oct. 2017. [Online]. Available: https://link.aps.org/doi/10.1103/PhysRevA.96.042315

[30] H.-P. Breuer, E.-M. Laine, J. Piilo, and B. Vacchini, "Non-Markovian dynamics in open quantum systems," *Reviews of Modern Physics*, vol. 88, no. 2, Apr. 2016, arXiv: 1505.01385. [Online]. Available: http://arxiv.org/abs/1505.01385

[31] H.-P. Breuer and F. Petruccione, *The Theory of Open Quantum Systems*. Oxford: Oxford University Press, Mar. 2007.

[32] C. Brif, R. Chakrabarti, and H. Rabitz, "Control of quantum phenomena: Past, present, and future," *New Journal of Physics*, vol. 12, no. 7, p. 075008, Jul. 2010, arXiv: 0912.5121. [Online]. Available: http://arxiv.org/abs/0912.5121

[33] A. Brinkmann, "Introduction to average Hamiltonian theory. I. Basics - Brinkmann - 2016 - Concepts in Magnetic Resonance Part A - Wiley Online Library," 2018. [Online]. Available: https://onlinelibrary.wiley.com/doi/abs/10.1002/cmr.a.21414

[34] C. L. Bris and P. Rouchon, "Low rank approximation for the numerical simulation of high dimensional Lindblad and Riccati equations," *Physical Review A*, vol. 87, no. 2, Feb. 2013, arXiv: 1207.4580. [Online]. Available: http://arxiv.org/abs/1207.4580

[35] R. W. Brown, Y.-C. N. Cheng, E. M. Haacke, M. R. Thompson, and R. Venkatesan, *Magnetic Resonance Imaging: Physical Principles and Sequence Design*. John Wiley & Sons, May 2014, google-Books-ID: rQGCAwAAQBAJ.

[36] C. M. Caves, "Quantum limits on noise in linear amplifiers," *Physical Review D*, vol. 26, no. 8, pp. 1817–1839, Oct. 1982. [Online]. Available: https://link.aps.org/doi/10.1103/PhysRevD.26.1817

[37] J. F. Colombeau, *Elementary Introduction to New Generalized Functions*. Elsevier, Aug. 2011, google-Books-ID: HjF4UVHjmg0C.

[38] ——, "Topics on nonlinear generalized functions," *arXiv:1105.4457 [math]*, May 2011, arXiv: 1105.4457. [Online]. Available: http://arxiv.org/abs/1105.4457

[39] ——, "Nonlinear Generalized Functions: their origin, some developments and recent advances," *arXiv:1401.4755 [math]*, Jan. 2014, arXiv: 1401.4755. [Online]. Available: http://arxiv.org/abs/1401.4755

[40] S. Conolly, D. Nishimura, and A. Macovski, "Optimal control solutions to the magnetic resonance selective excitation problem," *IEEE transactions on medical imaging*, vol. 5, no. 2, pp. 106–115, 1986.

[41] M. Contreras, R. Pellicer, and M. Villena, "Dynamic optimization and its relation to classical and quantum constrained systems," *Physica A: Statistical Mechanics and its Applications*, vol. 479, pp. 12–25, Aug. 2017, arXiv: 1607.01317. [Online]. Available: http://arxiv.org/abs/1607.01317

[42] R. Coquereaux, *Espaces fibres et Connexions*, Centre de Physique Theorique Luminy - Marseille, 2002. [Online]. Available: http://www.cpt.univ-mrs.fr/~coque/EspacesFibresCoquereaux.pdf

[43] M. D. Corps and M. Decorps, *Imagerie de résonance magnétique : Bases physiques et méthodes*. Les Ulis; Paris: EDP Sciences, Jun. 2011.

[44] C. Counsell, M. Levitt, and R. Ernst, "Analytical theory of composite pulses," *Journal of Magnetic Resonance (1969)*, vol. 63, no. 1, pp. 133–141, Jun. 1985. [Online]. Available: https://www.sciencedirect.com/science/article/pii/002223648590160X

[45] D. D'Alessandro, *Introduction to Quantum Control and Dynamics*, 1st ed. Boca Raton: Chapman and Hall/CRC, Aug. 2007.

[46] P. de Fouquieres, S. G. Schirmer, S. J. Glaser, and I. Kuprov, "Second order gradient ascent pulse engineering," *Journal of Magnetic Resonance*, vol. 212, no. 2, pp. 412–417, Oct. 2011, arXiv: 1102.4096. [Online]. Available: http://arxiv.org/abs/1102.4096

[47] R. H. Dicke, "Coherence in Spontaneous Radiation Processes," *Physical Review*, vol. 93, no. 1, pp. 99–110, Jan. 1954. [Online]. Available: https://link.aps.org/doi/10.1103/PhysRev.93.99

[48] P. Dirac, "On the Theory of Quantum Mechanics," *Proceeding of the Royal Society A*, vol. 112, 1926. [Online]. Available: https://ethw.org/w/images/0/06/P2_Proc._R._Soc._Lond._A-1926-Dirac-661-77.pdf

[49] A. Dmitruk and N. Osmolovskii, "On the proof of Pontryagin's maximum principle by means of needle variations," *arXiv:1412.2363 [math]*, Dec. 2014, arXiv: 1412.2363. [Online]. Available: http://arxiv.org/abs/1412.2363

[50] D. Dong and I. R. Petersen, "Quantum control theory and applications: a survey," *IET Control Theory & Applications*, vol. 4, no. 12, pp. 2651–2671, Dec. 2010. [Online]. Available: http://digital-library.theiet.org/content/journals/10.1049/iet-cta.2009.0508

[51] F. Engelke, "Virtual photons in magnetic resonance," *Concepts in Magnetic Resonance Part A*, vol. 36A, no. 5, pp. 266–339, Sep. 2010. [Online]. Available: https://onlinelibrary.wiley.com/doi/abs/10.1002/cmr.a.20166

[52] R. R. Ernst, G. Bodenhausen, and A. Wokaun, *Principles of Nuclear Magnetic Resonance in One and Two Dimensions*. Oxford: Clarendon Press, Sep. 1990.

[53] H. Ezawa and Y. Murayama, *Quantum Control and Measurement*. Elsevier, Jun. 1993, google-Books-ID: nYjCjNJ3dSQC.

[54] R. P. Feynman, "Simulating Physics with Computers," *International Journal of Theoretical Physics*, vol. 21, pp. 467–488, 1982. [Online]. Available: https://people.eecs.berkeley.edu/~christos/classics/Feynman.pdf

[55] R. P. Feynman and A. R. Hibbs, *Quantum mechanics and path integrals*. New York: McGraw-Hill, 1965.

[56] M. Frasca, "A modern review of the two-level approximation," *Annals of Physics*, vol. 306, no. 2, pp. 193–208, Aug. 2003, arXiv: quant-ph/0209056. [Online]. Available: http://arxiv.org/abs/quant-ph/0209056

[57] R. Friedberg and J. T. Manassah, "Dicke states and Bloch states," *Laser Physics Letters*, vol. 4, no. 12, p. 900, Aug. 2007. [Online]. Available: http://iopscience.iop.org/article/10.1002/lapl.200710073/meta

[58] K. Fujii, "Quantum Damped Harmonic Oscillator," *arXiv:1209.1437 [math-ph, physics:quant-ph]*, Sep. 2012, arXiv: 1209.1437. [Online]. Available: http://arxiv.org/abs/1209.1437

[59] ——, "Exact Solution of a Master Equation Applied to the Two Level System of an Atom," *International Journal of Geometric Methods in Modern Physics*, vol. 11, no. 10, p. 1450085, Nov. 2014, arXiv: 1405.2604. [Online]. Available: http://arxiv.org/abs/1405.2604

[60] C. Gardiner and P. Zoller, *Quantum Noise: A Handbook of Markovian and Non-Markovian Quantum Stochastic Methods with Applications to Quantum Optics*, 3rd ed., ser. Springer Series in Synergetics. Berlin Heidelberg: Springer-Verlag, 2004. [Online]. Available: //www.springer.com/de/book/9783540223016

[61] A. Garon, S. J. Glaser, and D. Sugny, "Time-optimal control of SU(2) quantum operations," *Physical Review A*, vol. 88, no. 4, Oct. 2013, arXiv: 1310.5226. [Online]. Available: http://arxiv.org/abs/1310.5226

[62] B. M. Garraway, "Nonperturbative decay of an atomic system in a cavity," *Physical Review A*, vol. 55, no. 3, pp. 2290–2303, Mar. 1997. [Online]. Available: https://link.aps.org/doi/10.1103/PhysRevA.55.2290

[63] J. M. Geremia and H. Rabitz, "Optimal Hamiltonian identification: The synthesis of quantum optimal control and quantum inversion," *The Journal of Chemical Physics*, vol. 118, no. 12, pp. 5369–5382, Mar. 2003. [Online]. Available: https://aip.scitation.org/doi/abs/10.1063/1.1538242

[64] ——, "Optimal Identification of Hamiltonian Information by Closed-Loop Laser Control of Quantum Systems," *Physical Review Letters*, vol. 89, no. 26, p. 263902, Dec. 2002. [Online]. Available: https://link.aps.org/doi/10.1103/PhysRevLett.89.263902

[65] V. Giovannetti, S. Lloyd, and L. Maccone, "Quantum-enhanced measurements: beating the standard quantum limit," *Science (New York, N.Y.)*, vol. 306, no. 5700, pp. 1330–1336, Nov. 2004.

[66] ——, "Advances in Quantum Metrology," *Nature Photonics*, vol. 5, no. 4, pp. 222–229, Apr. 2011, arXiv: 1102.2318. [Online]. Available: http://arxiv.org/abs/1102.2318

[67] S. J. Glaser, U. Boscain, T. Calarco, C. P. Koch, W. Köckenberger, R. Kosloff, I. Kuprov, B. Luy, S. Schirmer, T. Schulte-Herbrüggen, D. Sugny, and F. K. Wilhelm, "Training Schrödinger's cat: quantum optimal control," *The European Physical Journal D*, vol. 69, no. 12, p. 279, Dec. 2015. [Online]. Available: https://link.springer.com/article/10.1140/epjd/e2015-60464-1

[68] H. H. Goldstine, *A History of the Calculus of Variations from the 17th through the 19th Century*, ser. Studies in the History of Mathematics and Physical Sciences. New York: Springer-Verlag, 1980. [Online]. Available: //www.springer.com/de/book/9781461381082

[69] M. Gross and S. Haroche, *Superradiance: an essay on the theory of collective spontaneous emission.* Amsterdam: North-Holland Pub. Co., 1982, oCLC: 35402441.

[70] A. Gsponer, "A concise introduction to Colombeau generalized functions and their applications in classical electrodynamics," *arXiv:math-ph/0611069*, Nov. 2006, arXiv: math-ph/0611069. [Online]. Available: http://arxiv.org/abs/math-ph/0611069

[71] A. Gupta, T. Stait Gardner, M. J. Moghaddam, and W. S. Price, "Dipolar relaxation revisited: A complete derivation for the two spin case," *Concepts in Magnetic Resonance Part A*, vol. 44, no. 2, pp. 74–113, Sep. 2015. [Online]. Available: https://onlinelibrary.wiley.com/doi/abs/10.1002/cmr.a.21334

[72] B. C. Hall, *Lie Groups, Lie Algebras, and Representations: An Elementary Introduction*, 2nd ed., ser. Graduate Texts in Mathematics. Springer International Publishing, 2015. [Online]. Available: //www.springer.com/gp/book/9783319134666

[73] W. R. Hamilton, "On a general method of expressing the path of light, and of the planets, by the coefficients of a characteristic function," *PhiloDublin University Review and Quarterly Magazine,*, vol. 1, 1833.

[74] ——, "On a general method in dynamics," *Philosophical Transactions of the Royal Society*, vol. 2, 1834.

[75] S. Haroche and J.-M. Raimond, *Exploring the Quantum: Atoms, Cavities, and Photons*. OUP Oxford, Aug. 2006, google-Books-ID: ynwSDAAAQBAJ.

[76] T. Hida and K. Saito, Eds., *Quantum Information IV*, 1st ed. Hackensack: World Scientific Pub Co Inc, Jul. 2002.

[77] E. Hille, "Some geometric extremal problems*," *Journal of the Australian Mathematical Society*, vol. 6, no. 1, pp. 122–128, Feb. 1966. [Online]. Available: https://www.cambridge.org/core/journals/journal-of-the-australian-mathematical-society/article/some-geometric-extremal-problems/5CECC884763F91DC18867E54646DBD0D

[78] T. Holstein and H. Primakoff, "Field Dependence of the Intrinsic Domain Magnetization of a Ferromagnet," *Physical Review*, vol. 58, no. 12, pp. 1098–1113, Dec. 1940. [Online]. Available: https://link.aps.org/doi/10.1103/PhysRev.58.1098

[79] R. A. Horn and C. R. Johnson, *Matrix Analysis*, reprint edition ed. Cambridge: Cambridge University Press, Feb. 1990.

[80] T.-L. Hwang, P. C. M. van Zijl, and M. Garwood, "Fast Broadband Inversion by Adiabatic Pulses," *Journal of Magnetic Resonance*, vol. 133, no. 1, pp. 200–203, Jul. 1998. [Online]. Available: http://www.sciencedirect.com/science/article/pii/S1090780798914410

[81] C. Itzykson and J.-B. Zuber, *Quantum Field Theory*. Courier Corporation, Sep. 2012.

[82] K. Jacobs, *Quantum Measurement Theory and its Applications*. Cambridge University Press, Aug. 2014, google-Books-ID: dAhQBAAAQBAJ.

[83] E. T. Jaynes and F. W. Cummings, "Comparison of quantum and semiclassical radiation theories with application to the beam maser," *Proceedings of the IEEE*, vol. 51, no. 1, pp. 89–109, Jan. 1963.

[84] F. Jones, *Lebesgue Integration on Euclidean Space*. Jones & Bartlett Learning, 2001, google-Books-ID: 3U7tresTD1AC.

[85] B. Julsgaard and K. Mølmer, "Dynamical evolution of an inverted spin ensemble in a cavity: Inhomogeneous broadening as a stabilizing mechanism," *Physical Review A*, vol. 86, no. 6, Dec. 2012, arXiv: 1209.4167. [Online]. Available: http://arxiv.org/abs/1209.4167

[86] ——, "Fundamental limitations in spin-ensemble quantum memories for cavity fields," *Physical Review A*, vol. 88, no. 6, Dec. 2013, arXiv: 1309.5517. [Online]. Available: http://arxiv.org/abs/1309.5517

[87] N. Khaneja, T. Reiss, C. Kehlet, T. Schulte-Herbrüggen, and S. J. Glaser, "Optimal control of coupled spin dynamics: design of NMR pulse sequences by gradient ascent algorithms," *Journal of Magnetic Resonance*, vol. 172, no. 2, pp. 296–305, Feb. 2005. [Online]. Available: http://www.sciencedirect.com/science/article/pii/S1090780704003696

[88] D. E. Kirk, *Optimal Control Theory: An Introduction*. Courier Corporation, 2004.

[89] D. H. Kobe and K.-H. Yang, "Gauge transformation of the time-evolution operator," *Physical Review A*, vol. 32, no. 2, pp. 952–958, Aug. 1985. [Online]. Available: https://link.aps.org/doi/10.1103/PhysRevA.32.952

[90] K. Kobzar, T. E. Skinner, N. Khaneja, S. J. Glaser, and B. Luy, "Exploring the limits of broadband excitation and inversion pulses," *Journal of Magnetic Resonance*, vol. 170, no. 2, pp. 236–243, Oct. 2004. [Online]. Available: http://www.sciencedirect.com/science/article/pii/S1090780704001995

[91] ——, "Exploring the limits of broadband excitation and inversion: II. Rf-power optimized pulses," *Journal of Magnetic Resonance*, vol. 194, no. 1, pp. 58–66, Sep. 2008. [Online]. Available: http://www.sciencedirect.com/science/article/pii/S1090780708001936

[92] D. O. Krimer, B. Hartl, F. Mintert, and S. Rotter, "Optimal control of non-Markovian dynamics in a single-mode cavity strongly coupled to an inhomogeneously broadened spin ensemble," *Physical Review A*, vol. 96, no. 4, p. 043837, Oct. 2017. [Online]. Available: https://link.aps.org/doi/10.1103/PhysRevA.96.043837

[93] D. O. Krimer, S. Putz, J. Majer, and S. Rotter, "Non-Markovian dynamics of a single-mode cavity strongly coupled to an inhomogeneously broadened spin ensemble," *Physical Review A*, vol. 90, no. 4, Oct. 2014, arXiv: 1410.0728. [Online]. Available: http://arxiv.org/abs/1410.0728

[94] V. Krishnan and N. Murali, "Radiation damping in modern NMR experiments: Progress and challenges," *Progress in nuclear magnetic resonance spectroscopy*, vol. 68, pp. 41–57, Jan. 2013. [Online]. Available: https://www.ncbi.nlm.nih.gov/pmc/articles/PMC3644564/

[95] R. Kubo, "Generalized Cumulant Expansion Method," *Journal of the Physical Society of Japan*, vol. 17, no. 7, pp. 1100–1120, Jul. 1962. [Online]. Available: https://journals.jps.jp/doi/abs/10.1143/JPSJ.17.1100

[96] J. B. Kuipers, *Quaternions and Rotation Sequences: A Primer with Applications to Orbits, Aerospace and Virtual Reality*. Princeton, N.J: Princeton University Press, Sep. 2002.

[97] G. Kurizki, P. Bertet, Y. Kubo, K. Mølmer, D. Petrosyan, P. Rabl, and J. Schmiedmayer, "Quantum technologies with hybrid systems," *Proceedings of the National Academy of Sciences*, p. 201419326, Mar. 2015. [Online]. Available: http://www.pnas.org/content/early/2015/03/02/1419326112

[98] M. Lapert, E. Assémat, S. J. Glaser, and D. Sugny, "Optimal control of the signal-to-noise ratio per unit time of a spin 1/2 particle: The crusher gradient and the radiation damping cases," *The Journal of Chemical Physics*, vol. 142, no. 4, p. 044202, Jan. 2015. [Online]. Available: http://aip.scitation.org/doi/abs/10.1063/1.4906751

[99] M. Lapert, Y. Zhang, M. A. Janich, S. J. Glaser, and D. Sugny, "Exploring the Physical Limits of Saturation Contrast in Magnetic Resonance Imaging," *Scientific Reports*, vol. 2, p. 589, Aug. 2012. [Online]. Available: https://www.nature.com/articles/srep00589

[100] H. v. Leeuwen and H. Maassen, "A q deformation of the Gauss distribution," *Journal of Mathematical Physics*, vol. 36, no. 9, pp. 4743–4756, Sep. 1995. [Online]. Available: https://aip.scitation.org/doi/abs/10.1063/1.530917

[101] M. H. Levitt, *Spin Dynamics: Basics of Nuclear Magnetic Resonance*, 2nd ed. Chichester Hoboken, NJ San Francisco, CA: Wiley, Apr. 2008.

[102] B. Li, H. Rabitz, and J. P. Wolf, "Optimal dynamic discrimination of similar quantum systems with time series data," *The Journal of Chemical Physics*, vol. 122, no. 15, p. 154103, Apr. 2005. [Online]. Available: https://aip.scitation.org/doi/abs/10.1063/1.1883170

[103] B. Li, G. Turinici, V. Ramakrishna, and H. Rabitz, "Optimal Dynamic Discrimination of Similar Molecules through Quantum Learning Control," *The Journal of Physical Chemistry B*, vol. 106, no. 33, pp. 8125–8131, Aug. 2002. [Online]. Available: https://doi.org/10.1021/jp0204657

[104] J. Li and N. Khaneja, "Ensemble Control of Bloch Equations," *IEEE Transactions on Automatic Control*, vol. 54, no. 3, pp. 528–536, Mar. 2009.

[105] S.-K. Liao, W.-Q. Cai, J. Handsteiner, B. Liu, J. Yin, L. Zhang, D. Rauch, M. Fink, J.-G. Ren, W.-Y. Liu, Y. Li, Q. Shen, Y. Cao, F.-Z. Li, J.-F. Wang, Y.-M. Huang, L. Deng, T. Xi, L. Ma, T. Hu, L. Li, N.-L. Liu, F. Koidl, P. Wang, Y.-A. Chen, X.-B. Wang, M. Steindorfer, G. Kirchner, C.-Y. Lu, R. Shu, R. Ursin, T. Scheidl, C.-Z. Peng, J.-Y. Wang, A. Zeilinger, and J.-W. Pan, "Satellite-Relayed Intercontinental Quantum Network," *Physical Review Letters*, vol. 120, no. 3, p. 030501, Jan. 2018. [Online]. Available: https://link.aps.org/doi/10.1103/PhysRevLett.120.030501

[106] G. Lindblad, "On the generators of quantum dynamical semigroups," *Communications in Mathematical Physics*, vol. 48, no. 2, pp. 119–130, Jun. 1976. [Online]. Available: https://link.springer.com/article/10.1007/BF01608499

[107] J. Liu and H. Yuan, "Quantum parameter estimation with optimal control," *Physical Review A*, vol. 96, no. 1, p. 012117, Jul. 2017. [Online]. Available: https://link.aps.org/doi/10.1103/PhysRevA.96.012117

[108] M. Lorente, "Creation and annihilation operators for orthogonal polynomials of continuous and discrete variables," *Electr. Trans. Num. Anal. (E.T.N.A*, pp. 102–111, 1999.

[109] D. J. Lurie, "A systematic design procedure for selective pulses in NMR imaging," *Magnetic Resonance Imaging*, vol. 3, no. 3, pp. 235–243, 1985.

[110] D. Ma, V. Gulani, N. Seiberlich, K. Liu, J. L. Sunshine, J. L. Duerk, and M. A. Griswold, "Magnetic resonance fingerprinting," *Nature*, vol. 495, no. 7440, pp. 187–192, Mar. 2013. [Online]. Available: http://www.nature.com/nature/journal/v495/n7440/full/nature11971.html

[111] W.-L. Ma, G. Wolfowicz, N. Zhao, S.-S. Li, J. J. L. Morton, and R.-B. Liu, "Uncovering many-body correlations in nanoscale nuclear spin baths by central spin decoherence," *Nature Communications*, vol. 5, p. 4822, Sep. 2014. [Online]. Available: https://www.nature.com/articles/ncomms5822

[112] S. Machnes, U. Sander, S. J. Glaser, P. de Fouquieres, A. Gruslys, S. Schirmer, and T. Schulte-Herbrueggen, "Comparing, Optimising and Benchmarking Quantum Control Algorithms in a Unifying Programming Framework," *Physical Review A*, vol. 84, no. 2, Aug. 2011, arXiv: 1011.4874. [Online]. Available: http://arxiv.org/abs/1011.4874

[113] J. Maidens, A. Barrau, S. Bonnabel, and M. Arcak, "Symmetry reduction for dynamic programming," *arXiv:1801.03237 [cs, math]*, Jan. 2018, arXiv: 1801.03237. [Online]. Available: http://arxiv.org/abs/1801.03237

[114] N. Makri, "Numerical path integral techniques for long time dynamics of quantum dissipative systems," *Journal of Mathematical Physics*, vol. 36, no. 5, pp. 2430–2457, May 1995. [Online]. Available: https://aip.scitation.org/doi/abs/10.1063/1.531046

[115] E. Mangaud, R. Puthumpally-Joseph, D. Sugny, C. Meier, O. Atabek, and M. Desouter-Lecomte, "Non-Markovianity in the optimal control of an open quantum system described by hierarchical equations of motion," *New Journal of Physics*, vol. 20, no. 4, p. 043050, 2018. [Online]. Available: http://stacks.iop.org/1367-2630/20/i=4/a=043050

[116] D. Marquardt, "An Algorithm for Least-Squares Estimation of Nonlinear Parameters," *Journal of the Society for Industrial and Applied Mathematics*, vol. 11, no. 2, pp. 431–441, Jun. 1963. [Online]. Available: https://epubs.siam.org/doi/abs/10.1137/0111030

[117] C. C. McGeoch, *Adiabatic Quantum Computation and Quantum Annealing: Theory and Practice*. Morgan & Claypool, Jul. 2014.

[118] A. Messiah, *Quantum Mechanics*. Courier Corporation, Feb. 2014, google-Books-ID: voUUAwAAQBAJ.

[119] T. Meunier, A. L. Diffon, C. Rueff, P. Degiovanni, and J.-M. Raimond, "Entanglement and decoherence of N atoms and a mesoscopic field in a cavity," *Physical Review A*, vol. 74, no. 3, Sep. 2006, arXiv: quant-ph/0603191. [Online]. Available: http://arxiv.org/abs/quant-ph/0603191

[120] K. Mølmer and Y. Castin, "Monte Carlo wavefunctions in quantum optics," *Quantum and Semiclassical Optics: Journal of the European Optical Society Part B*, vol. 8, no. 1, p. 49, 1996. [Online]. Available: http://stacks.iop.org/1355-5111/8/i=1/a=007

[121] M. H. Mohammady, G. W. Morley, and T. S. Monteiro, "Bismuth Qubits in Silicon: The Role of EPR Cancellation Resonances," *Physical Review Letters*, vol. 105, no. 6, p. 067602, Aug. 2010. [Online]. Available: https://link.aps.org/doi/10.1103/PhysRevLett.105.067602

[122] J. J. L. Morton and P. Bertet, "Storing quantum information in spins and high-sensitivity ESR," *Journal of Magnetic Resonance*, vol. 287, pp. 128–139, Feb. 2018. [Online]. Available: http://www.sciencedirect.com/science/article/pii/S1090780717302896

[123] J. L. Neves, B. Heitmann, N. Khaneja, and S. J. Glaser, "Heteronuclear decoupling by optimal tracking," *Journal of Magnetic Resonance (San Diego, Calif.: 1997)*, vol. 201, no. 1, pp. 7–17, Nov. 2009.

[124] A. Nicolas, "Optical quantum memories with cold atomic ensembles: a free space implementation for multimode storage, or a nanofiber-based one for high collection efficiency," Ph.D. dissertation, PIERRE ET MARIE CURIE, 2014.

[125] N. C. Nielsen, C. Kehlet, S. J. Glaser, and N. Khaneja, "Optimal Control Methods in NMR Spectroscopy," in *eMagRes*. American Cancer Society, 2010. [Online]. Available: https://onlinelibrary.wiley.com/doi/abs/10.1002/9780470034590.emrstm1043

[126] S. Odake and R. Sasaki, "q-oscillator from the q-Hermite polynomial," *Physics Letters B*, vol. 663, no. 1, pp. 141–145, May 2008. [Online]. Available: http://www.sciencedirect.com/science/article/pii/S0370269308003833

[127] J. Pauly, P. Le Roux, D. Nishimura, and A. Macovski, "Parameter relations for the Shinnar-Le Roux selective excitation pulse design algorithm [NMR imaging]," *IEEE transactions on medical imaging*, vol. 10, no. 1, pp. 53–65, 1991.

[128] J.-S. Peng, *Introduction To Modern Quantum Optics*, 1st ed. Singapore: Wspc, Sep. 1998.

[129] H. J. Pesch and M. Plail, "The Maximum Principle of optimal control : A history of ingenious ideas and missed opportunities - Semantic Scholar," *Control and Cybernetics*, vol. 38, 2009. [Online]. Available: /paper/A-The-Maximum-Principle-of-optimal-control-%3A-A-of-Pesch-Plail/fa2168bd507cd56ebd3a0abf6a709e9c385360cc

[130] E. Y. Pierre, D. Ma, Y. Chen, C. Badve, and M. A. Griswold, "Multiscale reconstruction for MR fingerprinting," *Magnetic Resonance in Medicine*, vol. 75, no. 6, pp. 2481–2492, 2016. [Online]. Available: https://onlinelibrary.wiley.com/doi/abs/10.1002/mrm.25776

[131] V. Potoček and S. M. Barnett, "On the exponential form of the displacement operator for different systems," *Physica Scripta*, vol. 90, no. 6, p. 065208, 2015. [Online]. Available: http://stacks.iop.org/1402-4896/90/i=6/a=065208

[132] S. Probst, A. Bienfait, P. Campagne-Ibarcq, J. J. Pla, B. Albanese, J. F. Da Silva Barbosa, T. Schenkel, D. Vion, D. Esteve, K. Mølmer, J. J. L. Morton, R. Heeres, and P. Bertet, "Inductive-detection electron-spin resonance spectroscopy with 65 spins/ Hz sensitivity," *Applied Physics Letters*, vol. 111, no. 20, p. 202604, Nov. 2017. [Online]. Available: http://aip.scitation.org/doi/full/10.1063/1.5002540

[133] S. Probst, Q. Ansel, S. J. Glaser, D. Sugny, and P. Bertet, "Shaped pulses for cavity compensation in high sensitivity electron spin resonance spectroscopy," *in preparation*, 2018.

[134] N. V. Prokof'ev and P. C. E. Stamp, "Theory of the spin bath," *Reports on Progress in Physics*, vol. 63, no. 4, p. 669, 2000. [Online]. Available: http://stacks.iop.org/0034-4885/63/i=4/a=204

[135] J. Pöttinger and K. Lendi, "Generalized Bloch equations for decaying systems," *Physical Review A*, vol. 31, no. 3, pp. 1299–1309, Mar. 1985. [Online]. Available: https://link.aps.org/doi/10.1103/PhysRevA.31.1299

[136] S. Ramakrishna and T. Seideman, "Intense Laser Alignment in Dissipative Media as a Route to Solvent Dynamics," *Physical Review Letters*, vol. 95, no. 11, p. 113001, Sep. 2005. [Online]. Available: https://link.aps.org/doi/10.1103/PhysRevLett.95.113001

[137] D. Rauch, J. Handsteiner, A. Hochrainer, J. Gallicchio, A. S. Friedman, C. Leung, B. Liu, L. Bulla, S. Ecker, F. Steinlechner, R. Ursin, B. Hu, D. Leon, C. Benn, A. Ghedina, M. Cecconi, A. H. Guth, D. I. Kaiser, T. Scheidl, and A. Zeilinger, "Cosmic Bell Test Using Random Measurement Settings from High-Redshift Quasars," *Physical Review Letters*, vol. 121, no. 8, p. 080403, Aug. 2018. [Online]. Available: https://link.aps.org/doi/10.1103/PhysRevLett.121.080403

[138] P. Rebentrost, I. Serban, T. Schulte-Herbrüggen, and F. K. Wilhelm, "Optimal Control of a Qubit Coupled to a Non-Markovian Environment," *Physical Review Letters*, vol. 102, no. 9, p. 090401, Mar. 2009. [Online]. Available: https://link.aps.org/doi/10.1103/PhysRevLett.102.090401

[139] M. Reed and B. Simon, *II: Fourier Analysis, Self-Adjointness*. Elsevier, 1975, google-Books-ID: Kz7s7bgVe8gC.

[140] C. P. Robert, "The Metropolis-Hastings algorithm," *arXiv:1504.01896 [stat]*, Apr. 2015, arXiv: 1504.01896. [Online]. Available: http://arxiv.org/abs/1504.01896

[141] Roddier, *Distributions et transformation de Fourier : à l'usage des physiciens et des ingénieurs*. Auckland u.a: France Mac Graw Hill, 2000.

[142] F. Rohrlich, "Relativistic Hamiltonian dynamics I. Classical mechanics," *Annals of Physics*, vol. 117, no. 2, pp. 292–322, Feb. 1979. [Online]. Available: http://www.sciencedirect.com/science/article/pii/0003491679903579

[143] C. Rovelli, *Quantum Gravity*. Cambridge ; New York: Cambridge University Press, Nov. 2007.

[144] C. Rovelli and F. Vidotto, *Covariant Loop Quantum Gravity An Elementary Introduction to Quantum Gravity and Spinfoam Theory*, 2014. [Online]. Available: http://www.cambridge.org/fr/academic/subjects/physics/cosmology-relativity-and-gravitation/covariant-loop-quantum-gravity-elementary-introduction-quantum-gravity-and-spinfoam-theory

[145] B. Rowland and J. A. Jones, "Implementing quantum logic gates with GRAPE: principles and practicalities," *Philosophical Transactions of the Royal Society A: Mathematical, Physical and Engineering Sciences*, vol. 370, no. 1976, pp. 4636–4650, Oct. 2012, arXiv: 1203.6260. [Online]. Available: http://arxiv.org/abs/1203.6260

[146] J. C. Russ, *The Image Processing Handbook, Fifth Edition*. CRC Press, Dec. 2006, google-Books-ID: Vs2AM2cWl1AC.

[147] S. K. Saikin, W. Yao, and L. J. Sham, "Single-electron spin decoherence by nuclear spin bath: Linked-cluster expansion approach," *Physical Review B*, vol. 75, no. 12, p. 125314, Mar. 2007. [Online]. Available: https://link.aps.org/doi/10.1103/PhysRevB.75.125314

[148] K. Sandner, "Cavity quantum electrodynamics with ultracold atoms and superconducting resonators," Ph.D. dissertation, Innsbruck, Sep. 2012.

[149] S. G. Schirmer, A. Kolli, and D. K. L. Oi, "Experimental Hamiltonian identification for controlled two-level systems," *Physical Review A*, vol. 69, no. 5, p. 050306, May 2004. [Online]. Available: https://link.aps.org/doi/10.1103/PhysRevA.69.050306

[150] S. G. Schirmer and D. K. L. Oi, "Two-qubit Hamiltonian tomography by Bayesian analysis of noisy data," *Physical Review A*, vol. 80, no. 2, p. 022333, Aug. 2009. [Online]. Available: https://link.aps.org/doi/10.1103/PhysRevA.80.022333

[151] S. G. Schirmer and F. C. Langbein, "Ubiquitous problem of learning system parameters for dissipative two-level quantum systems: Fourier analysis versus Bayesian estimation," *Physical Review A*, vol. 91, no. 2, p. 022125, Feb. 2015. [Online]. Available: https://link.aps.org/doi/10.1103/PhysRevA.91.022125

[152] L. Schwartz, *Theorie des distributions*. Hermann, Jan. 1966.

[153] D. Segal, A. J. Millis, and D. R. Reichman, "Numerically exact path-integral simulation of nonequilibrium quantum transport and dissipation," *Physical Review B*, vol. 82, no. 20, p. 205323, Nov. 2010. [Online]. Available: https://link.aps.org/doi/10.1103/PhysRevB.82.205323

[154] E. A. Sete, J. M. Gambetta, and A. N. Korotkov, "Purcell effect with microwave drive: Suppression of qubit relaxation rate," *Physical Review B*, vol. 89, no. 10, Mar. 2014, arXiv: 1401.5545. [Online]. Available: http://arxiv.org/abs/1401.5545

[155] B. W. Shore and P. L. Knight, "The Jaynes-Cummings Model," *Journal of Modern Optics*, vol. 40, no. 7, pp. 1195–1238, Jul. 1993. [Online]. Available: https://doi.org/10.1080/09500349314551321

[156] L. M. Sieberer, M. Buchhold, and S. Diehl, "Keldysh Field Theory for Driven Open Quantum Systems," *Reports on Progress in Physics*, vol. 79, no. 9, p. 096001, Sep. 2016, arXiv: 1512.00637. [Online]. Available: http://arxiv.org/abs/1512.00637

[157] T. E. Skinner and N. I. Gershenzon, "Optimal control design of pulse shapes as analytic functions," *Journal of Magnetic Resonance*, vol. 204, no. 2, pp. 248–255, Jun. 2010. [Online]. Available: http://www.sciencedirect.com/science/article/pii/S1090780710000583

[158] H. Stapelfeldt and T. Seideman, "Colloquium: Aligning molecules with strong laser pulses," *Reviews of Modern Physics*, vol. 75, no. 2, pp. 543–557, Apr. 2003. [Online]. Available: https://link.aps.org/doi/10.1103/RevModPhys.75.543

[159] A. Stottmeister and T. Thiemann, "Coherent states, quantum gravity and the Born-Oppenheimer approximation, I: General considerations," *Journal of Mathematical Physics*, vol. 57, no. 6, p. 063509, Jun. 2016, arXiv: 1504.02169. [Online]. Available: http://arxiv.org/abs/1504.02169

[160] A. Strathearn, B. W. Lovett, and P. Kirton, "Efficient Real-Time Path Integrals for Non-Markovian Spin-Boson Models," *New Journal of Physics*, vol. 19, no. 9, p. 093009, Sep. 2017, arXiv: 1704.04099. [Online]. Available: http://arxiv.org/abs/1704.04099

[161] M. Suzuki, "Generalized Trotter's formula and systematic approximants of exponential operators and inner derivations with applications to many-body problems," *Communications in Mathematical Physics*, vol. 51, no. 2, pp. 183–190, 1976. [Online]. Available: http://projecteuclid.org/euclid.cmp/1103900351

[162] G. Taguchi, S. Chowdhury, and Y. Wu, "Introduction to the Signal-to-Noise Ratio," in *Taguchi's Quality Engineering Handbook*. John Wiley & Sons, Inc., 2004, pp. 221–238. [Online]. Available: http://onlinelibrary.wiley.com/doi/10.1002/9780470258354.ch11/summary

[163] M. Tavis and F. W. Cummings, "Exact Solution for an N-Molecule—Radiation-Field Hamiltonian," *Physical Review*, vol. 170, no. 2, pp. 379–384, Jun. 1968. [Online]. Available: https://link.aps.org/doi/10.1103/PhysRev.170.379

[164] V. V. Temnov and U. Woggon, "Superradiance and Subradiance in an Inhomogeneously Broadened Ensemble of Two-Level Systems Coupled to a Low-Q Cavity," *Physical Review Letters*, vol. 95, no. 24, p. 243602, Dec. 2005. [Online]. Available: https://link.aps.org/doi/10.1103/PhysRevLett.95.243602

[165] E. Theodorou, F. Stulp, J. Buchli, and S. Schaal, "An Iterative Path Integral Stochastic Optimal Control Approach for Learning Robotic Tasks," *IFAC Proceedings Volumes*, vol. 44, no. 1, pp. 11 594–11 601, Jan. 2011. [Online]. Available: http://www.sciencedirect.com/science/article/pii/S1474667016454789

[166] E. Trélat, *Contrôle optimal: théorie & applications*. Vuibert, 2005, google-Books-ID: z3KDAAAACAAJ.

[167] L. Van Damme, Q. Ansel, S. J. Glaser, and D. Sugny, "Robust optimal control of two-level quantum systems," *Physical Review A*, vol. 95, no. 6, Jun. 2017, arXiv: 1704.07653. [Online]. Available: http://arxiv.org/abs/1704.07653

[168] L. Van-Damme, D. Schraft, G. T. Genov, D. Sugny, T. Halfmann, and S. Guérin, "Robust not gate by single-shot-shaped pulses: Demonstration of the efficiency of the pulses in rephasing atomic coherences," *Physical Review A*, vol. 96, no. 2, p. 022309, Aug. 2017. [Online]. Available: https://link.aps.org/doi/10.1103/PhysRevA.96.022309

[169] L. Van Damme, Q. Ansel, S. J. Glaser, and D. Sugny, "Time-optimal selective pulses of two uncoupled spin 1/2 particles," *Submitted to Phys. Rev. A.*, 2018.

[170] J. Vanderlinde, *Classical Electromagnetic Theory*. Springer Science & Business Media, 2004, google-Books-ID: HWrMET9_VpUC.

[171] T. Vieillard, F. Chaussard, D. Sugny, B. Lavorel, and O. Faucher, "Field-free molecular alignment of CO2 mixtures in presence of collisional relaxation," *Journal of Raman Spectroscopy*, vol. 39, no. 6, pp. 694–699, 2008. [Online]. Available: https://onlinelibrary.wiley.com/doi/abs/10.1002/jrs.1976

[172] T. Vieillard, F. Chaussard, F. Billard, D. Sugny, O. Faucher, S. Ivanov, J.-M. Hartmann, C. Boulet, and B. Lavorel, "Field-free molecular alignment for probing collisional relaxation dynamics," *Physical Review A*, vol. 87, no. 2, p. 023409, Feb. 2013. [Online]. Available: https://link.aps.org/doi/10.1103/PhysRevA.87.023409

[173] D. Viennot, "Géométrie et adiabaticité des systèmes photodynamiques quantiques," phdthesis, Université de Franche-Comté, Nov. 2005. [Online]. Available: https://tel.archives-ouvertes.fr/tel-00011145/document

[174] S. Vincent and C. Zwahlen, "Chapter 1 Selective pulses in NMR," *Analytical Spectroscopy Library*, vol. 8, pp. 1–17, Jan. 1997. [Online]. Available: https://www.sciencedirect.com/science/article/pii/S092643459780003X

[175] M. S. Vinding, I. I. Maximov, Z. Tošner, and N. C. Nielsen, "Fast numerical design of spatial-selective rf pulses in MRI using Krotov and quasi-Newton based optimal control methods," *The Journal of Chemical Physics*, vol. 137, no. 5, p. 054203, Aug. 2012. [Online]. Available: https://aip.scitation.org/doi/abs/10.1063/1.4739755

[176] H. Walther, B. T. H. Varcoe, B.-G. Englert, and T. Becker, "Cavity quantum electrodynamics," *Reports on Progress in Physics*, vol. 69, no. 5, p. 1325, 2006. [Online]. Available: http://stacks.iop.org/0034-4885/69/i=5/a=R02

[177] L. Wang, Z. Zhang, C. Huang, and K. L. Tsui, "A GPU-accelerated parallel Jaya algorithm for efficiently estimating Li-ion battery model parameters," *Applied Soft Computing*, vol. 65, pp. 12–20, Apr. 2018. [Online]. Available: http://www.sciencedirect.com/science/article/pii/S1568494617307780

[178] Z.-H. Wang and S. Takahashi, "Spin decoherence and electron spin bath noise of a nitrogen-vacancy center in diamond," *Physical Review B*, vol. 87, no. 11, p. 115122, Mar. 2013. [Online]. Available: https://link.aps.org/doi/10.1103/PhysRevB.87.115122

[179] H. M. Wiseman and G. J. Milburn, *Quantum Measurement and Control*. Cambridge University Press, 2010, google-Books-ID: ZNjvHaH8qA4C.

[180] N. Wu, N. Fröhling, X. Xing, J. Hackmann, A. Nanduri, F. B. Anders, and H. Rabitz, "Decoherence of a single spin coupled to an interacting spin bath," *Physical Review B*, vol. 93, no. 3, Jan. 2016, arXiv: 1507.04514. [Online]. Available: http://arxiv.org/abs/1507.04514

[181] Q. Xie, H. Zhong, M. T. Batchelor, and C. Lee, "The quantum Rabi model: solution and dynamics," *Journal of Physics A: Mathematical and Theoretical*, vol. 50, no. 11, p. 113001, 2017. [Online]. Available: http://stacks.iop.org/1751-8121/50/i=11/a=113001

[182] I. Yang, M. Morzfeld, C. J. Tomlin, and A. J. Chorin, "Path integral formulation of stochastic optimal control with generalized costs," *arXiv:1406.7869 [math]*, Jun. 2014, arXiv: 1406.7869. [Online]. Available: http://arxiv.org/abs/1406.7869

[183] H. Yuan and C.-H. F. Fung, "Fidelity and Fisher information on quantum channels," *New Journal of Physics*, vol. 19, no. 11, p. 113039, 2017. [Online]. Available: http://stacks.iop.org/1367-2630/19/i=11/a=113039

[184] Y. Zhang, M. Lapert, D. Sugny, M. Braun, and S. J. Glaser, "Time-optimal control of spin 1/2 particles in the presence of radiation damping and relaxation," *The Journal of Chemical Physics*, vol. 134, no. 5, p. 054103, Feb. 2011. [Online]. Available: https://aip.scitation.org/doi/10.1063/1.3543796